Aus der
Klinik für Epileptologie
des Universitätsklinikums Bonn
Direktor: Univ.-Prof. Dr. med. Rainer Surges, MHBA

Zellulär auflösende Bildgebung pathologisch transformierter kortikaler Netzwerke in vivo

Habilitationsschrift
zur Erlangung der venia legendi
der Hohen Medizinischen Fakultät
der Rheinischen-Friedrich-Wilhelms-Universität Bonn
für das Lehrgebiet
‘Experimentelle Neurowissenschaften‘

Vorgelegt von
Dr. med. Michael Wenzel
Research Clinician
an der Rheinischen Friedrich-Wilhelms-Universität Bonn
Bonn 2022

Habilitationsdatum: 05.05.2022

Einmal kränkte das System den akademischen Weg
Einmal ging es nicht ohne Parteibuch
Einmal war es anders gedacht

Meinen drei Eltern

Inhaltsverzeichnis

Einleitung

Allgemeine Bemerkungen

Die Grundlage der hier vorliegenden kumulativen Habilitationsschrift bilden die unten aufgeführten fünf Originalarbeiten, deren wesentliche Resultate im Ergebnisteil zusammengefasst und diskutiert werden:

1. **Wenzel M**, Hamm JP, Peterka DS, Yuste R.
   Reliable and elastic propagation of cortical seizures in vivo.
   Cell *Reports* (2017) 19:2681–2693, doi: 10.1016/j.celrep.2017.05.090

2. Jayant K*, **Wenzel M***, Hamm JP, Bando Y, Sahin O, Shepard KL, Yuste R.
   Flexible nanopipettes for minimally invasive intracellular electrophysiology in vivo.
   Cell *Reports* (2019) 26:266–278, doi: 10.1016/j.celrep.2018.12.019

3. **Wenzel M**, Hamm JP, Peterka DS, Yuste R.
   Acute focal seizures start as local synchronizations of neuronal ensembles.
   J Neurosci (2019) 39 (43) 8562-8575, doi: 10.1523/JNEUROSCI.3176-18.2019

4. **Wenzel M***, Han S*, Smith EH*, Hoel E, Greger B, House PA, Yuste R.
   Reduced repertoire of cortical microstates and neuronal ensembles in medically induced loss of consciousness.
   Cell *Systems* (2019) 8:467–474, doi: https://doi.org/10.1016/j.cels.2019.03.007

5. **Wenzel M**, Leunig A, Han S, Peterka DS, Yuste R.
   Prolonged anesthesia alters brain synaptic architecture.
   Proc Natl Acad Sci (2021) 118 (7) e2023676118, doi: 10.1073/pnas.2023676118

   *Geteilte Autorenschaft

Die hier vorgestellten Arbeiten untersuchen, am Beispiel anästhesiologisch modulierter oder epileptischer kortikaler Mikronetzwerke, die Rolle pathologisch transformierter lokaler Neuronenverbände im lebenden Gehirn. Durch technische Neuerungen in Bereichen der Molekularbiologie, Fluoreszenzmikroskopie, Elektrophysiologie und Computertechnologie zeichnet sich in den letzten Jahren zunehmend ab, dass aberrante zelluläre Mikronetzwerke eine tragende pathophysiologische Rolle in neurologischen und psychiatrischen Erkrankungen einnehmen. Die Erforschung zellulärer Mechanismen derartiger Mikronetzwerke im lebenden Gehirn befindet sich noch in ihren Anfängen. In den hier zusammengefassten Arbeiten wurden zellulär auflösende Messmethoden neuronaler Aktivität in *in vivo* Mausmodellen angewandt, vornehmlich Kombinationen aus Zwei-Photonen-Mikroskopie, Feldelektrophysiologie

und elektrischen Einzelzellableitungen, auch aber Mikroelektroden-Array (MEA) Messungen in menschlichen Epilepsiepatienten. Die Einleitung besteht aus vier Abschnitten. Zunächst erfolgt eine Einführung in kooperative neuronale Aktivität als Grundbaustein physiologischer Hirnaktivität. Dieser folgt ein Überblick über zellulär auflösende Messmethoden neuronaler Aktivität. Die Einleitung schließt mit einer Übersicht zum Kenntnisstand neuronaler Netzwerkdynamiken in der Entstehung und Ausbreitung fokaler epileptischer Anfälle sowie in medizinisch induziertem Bewusstseinsverlust bzw. Koma. Abgesehen von den Arbeiten, die dieser Habilitationsschrift zugrunde liegen, greifen einzelne Abschnitte der Einleitung auf die Übersichtsarbeit *Identification and quantification of neuronal ensembles in optical imaging experiments* von Wenzel und Hamm zurück (Wenzel und Hamm, 2021).

Neuronale Ensembles als emergente funktionelle Einheiten des Gehirns

Santiago Ramón y Cajal und Charles S. Sherrington gehören zu den Wegbereitern der modernen Neurowissenschaft. Mittels neuartiger Färbemethoden (Golgi, 1873) im Hirnschnitt (y Cajal, 1888) und elektrophysiologischer Einzelzellmessungen (Sherrington, 1906) begründeten sie die Neuronendoktrin, welche besagt, dass die strukturelle und funktionelle Grundeinheit des Gehirns das Einzelneuron darstellt (Shepherd, 1991). Seither diente die Neuronendoktrin als konzeptionelles Fundament neurowissenschaflticher Untersuchungen, wobei ihre Lehre vom Neuron als funktioneller Grundeinheit des Gehirns gleichermaßen seit langem Gegenstand wissenschaftlicher Auseinandersetzung ist (Yuste, 2015). Bereits Cajals Schüler Lorente de Nó hypothetisierte in den 1930er Jahren, dass statt einzelner Neurone die kooperative Aktivität afferenter Gruppen von Nervenzellen eine Antwort in Effektorneuronen auslöse (Lorente de No, 1938). Spätestens seit Donald J. Hebb diese Neuronenverbände in seinem einflussreichen Werk *The Organization of Behavior* (Hebb, 1949) als *cell assemblies* (im Englischen und Deutschen heute oft: neuronale Ensembles) bezeichnete und postulierte, dass diese das Grundelement assoziativen Lernens und perzeptiver Informationsverarbeitung darstellten, gehört die Identifikation und Charakterisierung neuronaler Ensembles im Kontext physiologischer Hirnprozesse sowie neurologischer und psychiatrischer Erkrankungen zu einer Hauptambition der modernen Neurowissenschaft.

In Übereinstimmung mit Nós und Hebbs Ensemble-Hypothese ergaben einflussreiche theoretische Überlegungen, dass neuronale Netzwerke emergente kollektive Recheneigenschaften aufweisen (Hopfield, 1982). Der Systembegriff der Emergenz rührt vom Forschungsfeld der Thermodynamik her (Clausius, 1850) und besagt bei Hopfield, dass die Recheneigenschaften eines Netzwerkes nicht durch die Summe seiner Einzelteile (z.B. Neurone) erklärt werden kann. Darüber hinaus weisen theoretische Berechnungen darauf hin, dass die Kodierung von Information durch neuronale Gruppen gegenüber Einzelneuronen eine erhöhte Robustheit aufweist (Kampa et al., 2011; Pouget et al., 2000). Umgekehrt wäre ein neuronales System, das auf der Informationsverarbeitung von Einzelneuronen statt neuronaler Ensembles fußt, intuitiv anfällig für fehlerhafte Informationsübertragung im Falle lokaler Gewebeschädigungen (Buzsáki, 2010; Pouget et al., 2000).

Während die theoretische Literatur zur Funktion kooperativer Ensembleaktivität steten Zuwachs zeigte (Abeles, 1991; Braitenberg, 1978; Hopfield, 1982; Little, 1974; Palm et al., 2014), blieben experimentelle Studien zu neuronalen Ensembles in Lebendgewebe für den größten Teil des 20. Jahrhunderts aufgrund technischer Limitationen unmöglich. Frühe elektroenzephalographische (EEG) Oberflächen-ableitungen menschlicher Hirnaktivität durch Hans Berger förderten auf makroanatomischer Ebene zutage, dass neuronale Netzwerke rhythmische Oszillationen erzeugen (Berger, 1929). Wenngleich derlei rhythmische Hirnaktivität vorhersehbar Ergebnis kollektiver Aktivität neuronaler Ensembles ist (Buzsaki, 2009; Buzsáki, 2010), so ist sie jedoch primär durch zeitliche Abläufe definiert (z.B. 8-12 Hz: „Alpha-Rhythmus“). Die räumliche Auflösung des Oberflächen-EEGs hingegen ist stark begrenzt, da es typischerweise mit Hilfe von Elektroden mit niedrigem Eingangswiderstand abgeleitet wird. Entsprechend reflektiert das aufgenommene Signal einer jeden EEG Einzelelektrode Summenpotentialschwankungen von Millionen Neuronen und lässt keine Unterscheidung neuronaler Untergruppen zu, wodurch lediglich indirekte Schlussfolgerungen über neuronale Ensemble-aktivitätsmuster möglich sind.

Ein fundamentaler Wandel in der experimentellen Zugänglichkeit neuronaler Netzwerke auf mikroanatomischer Ebene vollzog sich durch die Entwicklung von Mikroelektroden-Arrays (MEA)(Bhandari et al., 2010; Bragin et al., 1999; Campbell et al., 1991; Fried et al., 1999) und synaptisch auflösenden Bildgebungsverfahren wie

der lasergestützten Zwei-Photonen-(2P-)Mikroskopie (Denk et al., 1990; Yuste und Denk, 1995), welche im folgenden Abschnitt der Einleitung näher vorgestellt werden. Diese sich seither rasch weiterentwickelnden Technologien haben es ermöglicht, neuronale Mikronetzwerke unter physiologischen und pathophysiologischen Bedingungen mit beispielloser neuroanatomischer Präzision zu untersuchen. Initiale Studien konnten mit Hilfe von 2P-Ca^{2+}-Mikroskopie in akuten Hirnschnitten zeigen, dass spontane neuronale Grundaktivität von einer begrenzten Anzahl zeitlich räumlicher Koaktivitätsmuster gekennzeichnet ist (Cossart et al., 2003; Ikegaya et al., 2004). Diese Ergebnisse wurden als erste experimentelle Hinweise auf lokal kooperative Aktivitätsmuster neuronaler Ensembles gewertet. Auch im intakten Gehirn konnten mittels 2P-Ca^{2+}-Mikroskopie in der Folge ähnliche zeitlich räumliche Aktivitätsmuster in signifikanten, unwillkürlichen Zusammenhang mit Sinneswahrnehmung, Kontextualisierung von eingehenden Sinnesreizen und Verhalten gebracht werden. Die Tatsache, dass solche Zusammenhänge im visuellen Cortex (Hamm et al., 2017, 2021; Miller et al., 2014), auditorischen Cortex (Xin et al., 2019), parietalen (Morcos und Harvey, 2016) und frontalen Cortices (Liang et al., 2018; Siniscalchi et al., 2019) sowie Hippocampus (Cai et al., 2016) nachgewiesen werden konnten, unterstreicht nicht nur die Robustheit des Phänomens *per se*, sondern auch, dass neuronale Ensembles tatsächlich emergente Recheneinheiten des Gehirns darstellen könnten. In Fortsetzung einflussreicher Arbeiten zu mikroanatomischen neuronalen Einflüssen auf Verhalten (Houweling und Brecht, 2008; Huber et al., 2008) ergaben kürzliche Studien, die 2P-Ca^{2+}-Mikroskopie mit zellulär auflösender optogenetischer Stimulation neuronaler Aktivität kombinierten (Carrillo-Reid et al., 2016, 2019), dass die gezielte Stimulation von lediglich ein bis zwei Neuronen den Rest eines zuvor optisch identifizierten neuronalen Ensembles reaktiviert (sogenannte „Mustervervollständigung“) und in Konsequenz Verhalten beeinflussen kann (Carrillo-Reid et al., 2019). Dies gilt als direkter kausaler Hinweis im intakten Gehirn, dass Ensembleaktivierungen als kortikale Attraktoren Grundbausteine kognitiver Prozesse repräsentieren (Carrillo-Reid et al., 2017).

Neueste wissenschaftliche Untersuchungen weisen ebenfalls auf eine Schlüsselrolle pathologisch transformierter neuronaler Ensembles in Krankheitsprozessen hin. In verschiedenen tierexperimentellen Krankheitsmodellen konnten auf Ebene neuronaler Ensembles zum Beispiel eine pathologisch veränderte Größe von Ensembles oder deren Anzahl pro Hirnvolumen in Mausmodellen für Autismus (Fang und Yuste, 2017),

eine unphysiologische Ensemblesynchronität und -überaktivität, pathologisch veränderte Ensembleattraktoren sowie aberrante Schaltkreismotive in der epileptischen Anfallsentstehung und -ausbreitung (Jayant und Wenzel et al., 2019; Lillis et al., 2015; Liou, Ma und Wenzel et al., 2018; Muldoon et al., 2015; Wenzel et al., 2021), eine fehlerhafte Bewertung bekannter Sinnesreize in Modellen für neurodegenerative Erkrankungen (Jáidar et al., 2010; Kuchibhotla et al., 2014; Marinković et al., 2019; Reznichenko et al., 2012), oder eine verringerte Diskriminationsfähigkeit und dyskontextuelle Kodierung von eingehenden Sinnesreizen in Modellen für Schizophrenie (Hamm et al., 2017, 2020; Zaremba et al., 2017) identifiziert werden. Eine transiente Dysfunktion neuronaler Ensembles konnte zuletzt auch unter speziellen Bedingungen wie dem medizinisch induzierten Bewusstseinsverlust (medically induced loss of consciousness: mLOC) während Generalanästhesie nachgewiesen werden (Wenzel et al., 2019b). In Zusammenschau dieser Datenerhebungen mehrt sich in den letzten Jahren die Evidenz einer maßgeblichen Rolle neuronaler Ensembles im Kontext physiologischer und pathophysiologischer Hirnaktivität, was ebenfalls das zunehmende Interesse an neuronalen Ensembles als Ziel schaltkreisbasierter Therapieansätze für neuropsychiatrische Erkrankungen erklärt (Carrillo-Reid und Yuste, 2020; Tye, 2014).

Zellulär auflösende Messmethoden neuronaler Aktivität

Die Wichtigkeit zellulär auflösender Messmethoden zur direkten funktionellen Untersuchung neuronaler Ensembles im gesunden und erkrankten Gehirn ist bereits in den vorangegangenen Absätzen angeklungen. Für den Hauptteil des 20. Jahrhunderts stellte die einzige zellulär auflösende Messmethode neuronaler Aktivität die elektrische Einzelzellmessung dar. Die Methodik solcher Messungen, von welchen die bekannteste die *Patch-clamp* Technik darstellt (Sakmann und Neher, 2009), wurde über Jahrzehnte hinweg verfeinert und stellt bis heute eine der meistgenutzten funktionellen Messmethoden in der Neurowissenschaft dar. Dementsprechend ist ihr Anteil an unserem heutigen Kenntnisstand von der Arbeitsweise des Gehirns enorm. Die Entwicklung neuartiger Elektroden zur Ableitung einzelner Neurone ist durch mittlerweile nanometergenaue Fertigungsmöglichkeiten dabei mitnichten abgeschlossen und weiter Gegenstand intensiver Forschung (Jayant et al., 2017, Jayant und Wenzel et al., 2019). Dem zweifellosen Vorteil der millisekundengenauen elektrischen Aufzeichnung einzelner Neurone, deren kommunikative Hauptwährung

Aktionspotentiale der Dauer weniger Millisekunden sind, steht hinsichtlich der Erforschung neuronaler Ensembles der Nachteil gegenüber, dass die gleichzeitige und stabile elektrische Ableitung mehrerer Neurone, insbesondere im lebenden Gehirn, mit Hilfe multipler eingebrachter Glaselektroden schon ab einer geringen Zellzahl (>4) faktisch unmöglich wird (Jouhanneau und Poulet, 2019; Noguchi et al., 2021). Auf der anderen Seite wurde es durch die Erfindung des EEG (Berger, 1929) und makroanatomische Bildgebungsverfahren wie der funktionellen Kernspintomographie (fMRT) (Ogawa et al., 1990) im 20. Jahrhundert möglich, neuronale Aktivität hirnweit zu erfassen, was fundamentale Entdeckungen nach sich zog wie die bereits oben erwähnten oszillatorischen Eigenschaften des Gehirns (Berger, 1929), oder distribuierte Hirnaktivitätsmuster wie das sogenannte Ruhezustandsnetzwerk (*Default-Mode* Netzwerk)(Bai et al., 2010; Gotman et al., 2005; Raichle et al., 2001), welches für interne reizunabhängige Denkvorgänge von Bedeutung ist (z.B. Tagträumen)(Leszczynski et al., 2017; Poerio et al., 2017). EEG und makroanatomischen funktionellen Bildgebungsverfahren wie der fMRT ist jedoch gemein, dass sie eine erheblich eingeschränkte räumliche Auflösung aufweisen (mindestens mehrere Hunderttausend Neurone per aufgezeichneter Volumeneinheit), weshalb sie für die Erforschung lokaler neuronaler Ensembles wenig geeignet sind. Vor dem Hintergrund der genannten, an gegenüberliegenden anatomischen Skalenenden verorteten, Messansätze ist es nicht verwunderlich, dass der experimentelle Wissenszuwachs zu mikroanatomischen Dynamiken von Neuronenverbänden im 20. Jahrhundert durch technische Limitationen spärlich blieb.

Hinsichtlich elektrophysiologischer Messmethoden zur Erfassung von Aktivitätsmustern lokaler Netzwerke im intakten Gehirn bedeutete das Aufkommen von Mikroelektroden-Arrays (MEA) einen bedeutenden Umschwung. MEAs ermöglichen durch eine Vielzahl miniaturisierter, zueinander angeordneter Elektroden mit hohem elektrischen Widerstand die extrazelluläre Erfassung neuronaler Aktionspotentiale (AP) und sind materialabhängig auch im menschlichen Patienten anwendbar. Durch Berechnung von beispielsweise Amplitude, Dauer und Form extrazellulär abgeleiteter APs können diese mit Hilfe sogenannter *spike sorting* Algorithmen einzelnen Neuronen und in eingeschränktem Maße gar verschiedenen neuronalen Subtypen (zum Beispiel Prinzipalzellen oder schnell feuernden Interneuronen) zugeordnet werden. So ist es möglich, dutzende bis hunderte Einzelneurone (sogenannte *single units*) innerhalb eines lokalen neuronalen Netzwerks zu identifizieren und zumindest

über mehrere Stunden zu verfolgen, solange stabile Bedingungen gewährleistet sind (Niediek et al., 2016; Sharma et al., 2015). Unter pathophysiologischen Bedingungen wie zum Beispiel epileptischen Anfällen jedoch kann eine rapide Änderung der AP Parameter aufgrund ausgeprägter Verschiebungen transmembranärer Ionenverteilungen die stabile Ableitung zuvor identifizierter *single units* mitunter enorm erschweren (Merricks et al., 2015). Typische MEAs, die ebenfalls im menschlichen Patienten genutzt werden können, stellen Mikroelektrodenbündel (variable Anzahl von Kontakten)(Bragin et al., 1999; Fried et al., 1999) und *Utah Arrays* (96 Elektroden)(Bhandari et al., 2010; Campbell et al., 1991) dar. Im Tiermodell sind in den letzten Jahren darüber hinaus neuartige MEAs mit bis zu Tausenden von Mikroelektroden, wie zum Beispiel *NeuroGrid* (Khodagholy et al., 2015), oder *Neuropixel* (Jun et al., 2017), genutzt worden. Schlagende Vorteile von MEAs liegen in der Einzelzellauflösung, einer optimalen zeitlichen Auflösung und dem möglichen Einsatz im Menschen, ihre räumliche Ableitkapazität bleibt jedoch angesichts der realweltlichen Dichte und Subklassendiversität neuronaler Netzwerke noch immer begrenzt. Stillen Zellen gegenüber sind MEAs „taub“, da sie nicht unterscheiden können, ob ein identifiziertes Neuron nicht mehr feuert, oder durch minimale Elektrodenbewegung nicht mehr stabil abgeleitet wird. Auch vorübergehend stille Zellen aber können im Kontext bestimmter Bedingungen, zum Beispiel der lokalen epileptischen Anfallsausbreitung, aufschlussreiche Informationen zur momentanen Dynamik eines lokalen Netzwerkes enthalten (Wenzel et al., 2019a).

Durch die Gangbarmachung des Zwei-Photonen-Effekts (Göppert-Mayer, 1931) für biologische Bildgebungsverfahren mit synaptischer räumlicher Auflösung (2P-Mikroskopie) (Denk et al., 1990; Yuste und Denk, 1995) wurde die optische Aufzeichnung neuronaler Ensembleaktivität Anfang der 1990er Jahre plötzlich möglich. Seither haben technische Fortschritte im Bereich der Optik (Duemani Reddy et al., 2008; Nguyen et al., 2001; Nikolenko et al., 2008; Yang und Yuste, 2017), insbesondere aber der Computer- und Datentechnologie (Hu et al., 2018; Paninski und Cunningham, 2018) sowie Molekularbiologie mit adenoviral oder transgen exprimierten, hochsensitiven, Fluoreszenzmarkerproteinen zur Erfassung neuronaler Aktivität (zum Beispiel Ca^{2+} Indikatoren wie GCaMP oder jRGECO)(Chen et al., 2013; Dana et al., 2014, 2016, 2018; Mollinedo-Gajate et al., 2019) die direkte optische Aufnahme räumlich verteilter neuronaler Aktivitätsmuster mit Einzelzellpräzision fundamental vereinfacht. Während optische Methoden zur Aufnahme neuronaler

Populationsaktivität wie die lasergestützte 2P-Mikroskopie im Gegensatz zu elektrischen Ableitungen noch immer stark von Stellvertretersignalen für neuronales Feuern (insbesondere intrazellulärer Ca^{2+} Einstrom über die neuronale Zellmembran) abhängen und eine vergleichsweise geringe zeitliche Auflösung aufweisen (mindestens Dutzende von Millisekunden pro Einzelaufnahme)(Chen et al., 2013; Helassa et al., 2016), bieten sie doch eine Reihe an Vorteilen zur Identifikation und Charakterisierung neuronaler Ensembles im lebenden Gehirn (Wenzel und Hamm, 2021; Yang und Yuste, 2017). 2P-Mikroskopie erlaubt die optische Aufzeichnung neuronaler Aktivität in nahezu realweltlicher anatomischer Dichte, was bedeutet, dass selbst benachbarte Neurone (und deren Aktivitätsmuster) eindeutig voneinander differenziert werden können. Sie weist im Vergleich zu *single unit* Ableitungen, deren Verlässlichkeit stark von der Entfernung des erfassten Neurons von der jeweiligen Elektrode sowie der Art des *spike sorting* abhängt (Pedreira et al., 2012), eine hohe Verlässlichkeit in der stabilen Identifikation von Neuronen auf und erlaubt so auf der Basis chronisch implantierter cranialer Fenster die monatelange Aufzeichnung der Aktivität desselben, eindeutig identifizierten Neuronenverbandes *in vivo* (Holtmaat et al., 2009; Wenzel et al., 2019b; Yang et al., 2009). Mit Hilfe stetig wachsender, versatiler molekularbiologischer Verfahren zur gezielten Fluoreszenzmarkierung molekular definierter Neuronenklassen können hochauflösende optische Verfahren heute eine Vielzahl erregender und hemmender Neuronentypen, insbesondere auch nicht-neuronale Zellen wie Gliazellen, oder patrouillierende Immunzellen, welche keine AP Aktivitätsmuster aufweisen, voneinander unterscheiden und monitorieren (Carrier et al., 2020; He und Huang, 2018; Progatzky et al., 2013). Ein zusammenfassender Überblick über die vorgestellten Messmethoden neuronaler Aktivität entlang des gesamten neuroanatomischen Größenspektrums findet sich in *Übersicht 1*.

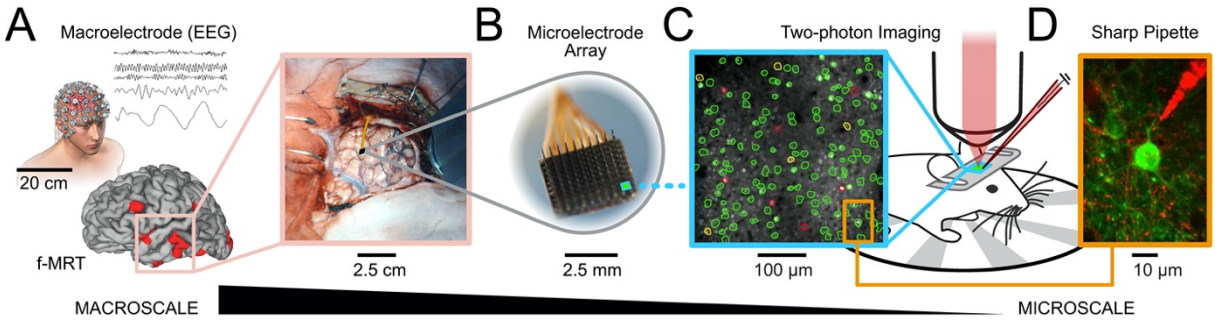

Übersicht 1: Messmethoden neuronaler Aktivität entlang des anatomischen Spektrums
Von links nach rechts, Änderung der räumlichen Auflösung von der makroanatomischen zur mikroanatomischen Ebene. **A:** Makroanatomische Messmethoden wie EEG oder fMRT erlauben hirnweite Aufnahmen, bieten jedoch eine geringe räumliche Auflösung. Hunderttausende bis Millionen Neurone tragen zu dem Signal an einer einzigen

Makroelektrode oder einem individuellen Voxel bei. Während EEG eine millisekundengenaue zeitliche Auflösung bietet, liegt sie beim fMRT im Bereich von Sekunden. Farbig gekennzeichneter Rahmen: Operationsort (Vergrößerung rechts) über dem Schläfenlappen in einem Epilepsiepatienten (Bildursprung Dr. Paul House, Utah). Makro- und Mikroelektroden-Arrays werden im Patienten zur Identifikation der Ursprungszone epileptischer Anfälle eingesetzt. **B:** Vergrößerung des implantierten Utah MEA, 4 x 4 mm, 96 Mikroelektroden, mit dessen Hilfe Aktionspotentiale von Dutzenden bis Hunderten Neuronen im menschlichen Patienten millisekundengenau extrazellulär gemessen werden können. Bemerke, dass die Anzahl der abgeleiteten Neurone über dem MEA Areal im Vgl. zur realweltlichen neuronalen Dichte gering ist. **C:** Mehrfarben *in vivo* 2P-Mikroskopie im Mausmodell, Darstellung eines typischen Sichtfensters (400 x 400 μm) im Neocortex. Das Sichtfenster macht 1% der Fläche eines Utah MEA aus (blaues Rechteck in B), erlaubt jedoch die gleichzeitige Aufzeichnung derselben oder einer höheren Anzahl von Neuronen und deren Subklassen (grün, rot, gelb). Im dargestellten Sichtfenster kann die Ca^{2+} Aktivität hunderter Neurone in hoher anatomischer Dichte mikroskopiert werden. Im Gegenzug zur mikrometergenauen räumlichen Auflösung ist die zeitliche Auflösung der 2P-Mikroskopie im Vgl. zu MEA Ableitungen gering (~30 - 120 Hz [Einzelaufnahmen pro Sekunde]). **D:** Dargestellt ist eine Pyramidalzelle (PYR), als Vergrößerung aus dem mikroskopierten Sichtfenster in C. Die PYR exprimiert den Ca^{2+} Sensor GCaMP6f (grün) und ist von einem Netz interneuronaler Zellfortsätze umgeben (rot, Interneuron Soma außerhalb des Sichtfensters). Die PYR wird gezielt von einer Nanopipette (rot, Spitze durch externe Beschichtung mit *Quantum-dots* visualisiert) angesteuert. Scharfe Mikro- oder Nanopipetten stellen den Goldstandard intrazellulärer elektrischer Ableitungen dar, da sie die millisekundengenaue Aufzeichnung neuronaler Aktionspotentiale und Subthreshold-Aktivität erlauben. Es kann jedoch jeweils nur eine Zelle pro Pipette abgeleitet werden, keine neuronale Population.
Abb. erstellt durch M. Wenzel.

Epileptische Mikronetzwerke

Den Hauptanteil dieser Habilitation machen Untersuchungen epileptischer Mikronetzwerke während der fokalen Anfallsentstehung und -ausbreitung mittels kombinierter *in vivo* 2P-Mikroskopie, Einzel- und Feldelektrophysiologie aus. Weltweit leiden etwa 50 Millionen Menschen an Epilepsie, ca. 600.000 hiervon allein in Deutschland (Beghi et al., 2019; Gavvala und Schuele, 2016; siehe ebenfalls Deutsche Gesellschaft für Epileptologie [DGfE]). Die Erkrankung hat weitreichende Auswirkungen auf das berufliche und soziale Leben von Betroffenen, da selbst alltägliche Aktivitäten wie Schwimmen oder das Fahren eines Autos nicht ohne Weiteres möglich sind (Ngugi et al., 2010; Quintas et al., 2012). Trotz einer Vielzahl verfügbarer antiepileptischer Medikamente treten bei einem Drittel aller Patienten weiterhin unkontrolliert Anfälle auf (Wiebe und Jette, 2012), weshalb das Verstehen der Entstehung und Ausbreitung von Anfällen eines der Hauptziele der Epilepsieforschung bleibt. Da sich wiederkehrende epileptische Anfälle innerhalb von Patienten mit chronischer Epilepsie semiologisch oft ähneln, bestand im 20. Jahrhundert der weithin akzeptierte konzeptionelle Rückschluss, dass dieser wiederkehrenden Semiologie schlicht jeweils dieselben iktualen („im Anfall“) neuronalen Aktivierungsmuster zugrunde lägen. Da sich die experimentelle Kenntnislage zu der Zeit jedoch, wie bereits oben ausgeführt, in überwältigender Mehrheit aus Einzelzellableitungen oder makroanatomischen Messmethoden mit

geringer räumlicher Auflösung speiste, blieben die zu epileptischen Anfällen korrelierenden Muster lokaler neuronaler Netzwerke lange unerforscht. Gerade diese lokalen Netzwerkdynamiken aber spielen wahrscheinlich eine tragende Rolle in der Entstehung und Ausbreitung fokaler Anfälle und sind deutlich komplexer als zuvor angenommen (Farrell et al., 2019; Goldberg und Coulter, 2013; Paz and Huguenard, 2015). Ein fokaler epileptischer Anfall entsteht innerhalb einer umschriebenen epileptogenen Zone („Fokus“, „intrafokal“) und breitet sich in der Folge fakultativ über weite, extrafokal gelegene Teile des Gehirns aus (Noebels et al., 2012). Aufgrund der bereits dargestellten technischen Limitationen im 20. Jahrhundert und der hierdurch über viele Jahrzehnte bestehenden Unzugänglichkeit lokaler neuronaler Netzwerke sind selbst basale Aspekte epileptischer Anfälle bis heute unzureichend geklärt. So ist zum Beispiel weiterhin unklar, was den Beginn oder das Ende eines epileptischen Anfalls im Gehirn bedingt, oder warum ein Anfall in einem Fall lokal begrenzt bleibt, während er sich im anderen über weite Teile des Gehirns ausbreitet.

Das Aufkommen zellulär auflösender MEAs und Bildgebungsverfahren hat das klassische Verständnis epilepsietypischer Hirnaktivität nachhaltig herausgefordert und faszinierende neue Einsichten in die mikroanatomischen Dynamiken anfallsproduzierender neuronaler Netzwerke ermöglicht. Es wird zum Beispiel zunehmend klar, dass sich epilepsietypische Aktivität in kleinsten Hirnvolumina (wenige hundert μm^2) abspielen kann (Bragin et al., 2000; Schevon et al., 2008; Stead et al., 2010; Wenzel et al., 2019a). Derartige mikroepileptische Aktivität lässt sich, beispielsweise in Form sogenannter Mikroanfälle, nicht nur in Patienten mit Epilepsie, sondern auch anderen neurologischen Erkrankungen, überraschenderweise zum Beispiel chronischem Kopfschmerz, finden (Stead et al., 2010). Mikroanfälle sind lokal derart begrenzt, dass sie ausschließlich mit Mikroelektroden erfasst und selbst von benachbarten Makroelektroden nicht detektiert werden (Schevon et al., 2008; Stead et al., 2010). Dieser Umstand kann paradigmatisch für die Wichtigkeit mikroanatomischer, bestenfalls zellulär auflösender Messmethoden zur Vertiefung des Verständnisses über die lokalen Ursprünge und Ausbreitung fokaler epileptischer Anfälle stehen. Neuere Untersuchungen zum mikroanatomischen neuronalen Korrelat feldelektrographisch gemessener interiktualer („zwischen Anfällen“) und iktualer Aktivität haben darüber hinaus eine bis heute andauernde Debatte angestoßen, ob das lange postulierte und weitläufig akzeptierte Konzept der ähnlichen iktualen Semiologie auf Basis ähnlicher neuronaler Aktivitätsmuster aufrecht erhalten werden

kann. Mehrere Publikationen im menschlichen Patienten und Tiermodell (*in vivo* oder im akuten Hirnschnitt) fanden gegensätzliche Hinweise für eine i) nahezu vollständige (Truccolo et al., 2011), ii) inkomplette (Schevon et al. 2012; Wenzel et al., 2017) oder iii) vollständig fehlende (Bower et al., 2012; Feldt Muldoon et al., 2013) Verlässlichkeit der Rekrutierung neuronaler Mikronetzwerke zu wiederkehrender epilepsietypischer Aktivität mit jeweils ähnlicher feldelektrographischer Signatur. Ebenfalls kontrovers diskutiert wird im Feld die Rolle bestimmter neuronaler Subklassen in der Anfallsentstehung und -ausbreitung. Bereits seit den 1960er Jahren prägt, basierend auf Einzelzellmessungen (Prince und Wilder, 1967), das Konzept der Umgebungshemmung (*inhibitory surround*) als mächtiger interneuronaler Mechanismus zur Eindämmung fokaler epilepsietypischer Aktivität das Feld der Epilepsieforschung (Jayant und Wenzel et al., 2019; Liou, Ma und Wenzel et al., 2018; Trevelyan und Schevon, 2013; Trevelyan et al., 2006; Wenzel et al., 2017, 2019b). Doch gleichermaßen wächst seit Jahrzehnten die Zahl hierzu gegensätzlicher experimenteller Studien, die eine primär kausale Rolle interneuronaler Aktivität in der Anfallsentstehung vorschlagen (Avoli, 1990; Elahian et al., 2018; Gnatkovsky et al., 2008; Shiri et al., 2016). Neuere Arbeiten im akuten Hirnschnitt fanden abhängig von der Messlokalisation gar beide Mechanismen (Sessolo et al., 2015). Zunehmend klar scheint somit, dass Interneurone wahrscheinlich keine singuläre Rolle in der Anfallsentstehung und -ausbreitung innehaben (Sessolo et al., 2015; Wenzel et al., 2019a). Zellulär auflösende Messmethoden neuronaler Ensembledynamiken, insbesondere *in vivo* 2P-Mikroskopie, haben das Potential, Antworten auf fundamentale Fragen wie „wie entsteht ein fokaler Anfall“ zu finden, weil sie die Möglichkeit bieten, eine Vielzahl von Neuronen und neuronalen Subklassen innerhalb lokaler Netzwerke im lebenden Gehirn gleichzeitig zu untersuchen. Daher bildet *in vivo* 2P-Mikroskopie auch die Grundlage der hier vorgestellten Publikationen zu epileptischen Mikronetzwerken. Ebenfalls deutlich wird durch die hier vorgestellten Arbeiten, dass das Feld der Erforschung epileptischer Mikronetzwerke im lebenden Gehirn noch am Anfang steht.

Pathologisch transformierte kortikale Mikronetzwerke während Anästhesie

Ähnlich der Erforschung epileptischer Netzwerke speiste sich die Forschung an Netzwerkmechanismen der Generalanästhesie bis kürzlich überwiegend aus theoretischen Überlegungen (Koch, 2012; Tononi, 2008; Tononi et al., 1998),

makroanatomischen Hirnaktivitätsmessungen (vornehmlich EEG und MRT)(Barttfeld et al., 2015; Hudetz et al., 2015, 2016; Lewis et al., 2012; Schroeder et al., 2016; Schröter et al., 2012), oder Einzelzellableitungen (Constantinople und Bruno, 2011; Suzuki und Larkum, 2020). Zelluläre Mechanismen der Generalanästhesie sind auf Mikronetzwerkebene bis heute aufgrund technischer Restriktionen in hohem Maße unklar geblieben (Tononi et al., 2016). Auf klinischer wie wissenschaftlicher Ebene stellen der medizinisch induzierte Bewusstseinsverlust (*medically induced loss of consciousness*, mLOC) sowie die strukturellen und funktionellen Folgen des medizinisch induzierten Komas (*medically induced coma*, MIC) zwei Hauptinteressensgebiete des Forschungsfeldes dar.

Seit der erstmaligen Anwendung der Schlafnarkose am Menschen mittels Schwefeläther im Rahmen eines operativen Eingriffs im Jahr 1846 (Dr. W. T. G. M. Morton, Boston, USA) wird intensiv an den Mechanismen von MIC und mLOC geforscht. Trotz millionenfacher jährlicher Routinedurchführung der General-anästhesie weltweit sind ihre mikroanatomischen Grundlagen jedoch nur unzureichend verstanden. Einer Reihe an Hirnarealen ist eine Schlüsselrolle im LOC zugeschrieben worden, hierunter Hypothalamus (Herrera et al., 2016), Thalamus (Castaigne et al., 1981), Basalganglien und Claustrum (Crick und Koch, 2005; Mhuircheartaigh et al., 2010), oder der Hirnstamm (Minert et al., 2017; Moruzzi und Magoun, 1949; Penfield und Jasper, 1954). Wenngleich thalamokortikale Verschaltungen einen wesentlichen Aspekt der bisherigen Forschung an LOC ausmachen (Flores et al., 2017; Herrera et al., 2016; Penfield und Jasper, 1954; Steriade, 2003), wird über die kausale Rolle kortikaler Hirnanteile seit jeher debattiert. Bereits frühe Studien im Tiermodell durch Lashley und Pavlov (Lashley, 1929; Pavlov, 1927) oder neurophysiologische Untersuchungen an Epilepsiepatienten mit Hilfe implantierter Elektroden (Penfield und Jasper, 1954) unterstrichen die fundamentale Rolle des Cortex für kognitive Prozesse, selbst extensive Entfernung kortikalen Gewebes aber führte zu keiner offensichtlichen quantitativen Bewusstseinseinschränkung (Lashley, 1929; Penfield und Jasper, 1954; Scoville und Milner, 1957). Auf der anderen Seite könnte diffus geschädigter Cortex, zum Beispiel infolge eines Sauerstoffmangels, zu LOC beitragen (Jennett, 2002).

Klar wird zunehmend, dass die Ursachen von mLOC über einzelne Hirnareale und das Konzept einer bloßen Verringerung von Hirnaktivität durch beispielsweise GABAerge

Wirkung (Hemmung neuronaler Aktivität) von Anästhetika hinausreichen. Zwar ist richtig, dass im klinischen Betrieb Routinesubstanzen wie Propofol oder inhalatorische Anästhetika (z.B. Sevofluran, oder Isofluran) zu einer Verringerung von zerebraler Aktivität, Hämodynamik und Metabolismus führen (Laaksonen et al., 2018; Pilge et al., 2014). Dies ist jedoch mitnichten für alle Anästhetika gegeben. Die Anwendung von Ketamin führt zum Beispiel zu einer sogenannten dissoziativen Anästhesie (Pender, 1971) mit einem neutralen Netto-Effekt aus zerebraler Hämodynamik und neuronaler Aktivität gegenüber dem Wachen (Cavazzuti et al., 1987; Laaksonen et al., 2018). Trotz dieser unterschiedlichen Wirkungen von Anästhetika auf Aktivitätsniveau und Stoffwechsel des Gehirns gibt es Hinweise, dass sie auf makroanatomischer Ebene ähnliche Netzwerkeffekte erzeugen. Mehrere EEG und fMRT Studien fanden kürzlich einen mit mLOC assoziierten Zusammenbruch der funktionellen Konnektivität zwischen Hirnarealen (Barttfeld et al., 2015; Hudetz et al., 2015; Lewis et al., 2012; Schroeder et al., 2016). Zwei Studien berichteten zudem, dass lokale Netzwerkdynamiken während mLOC jenen im Wachen überraschend ähnlich sind (Hudetz et al., 2016; Lewis et al., 2012). Dies wurde als Hinweis darauf gewertet, dass die Netzwerkmechanismen von LOC vornehmlich auf einer Diskoordination neuronaler Aktivität über Hirnareale hinweg fußen. Vor Erhebung der in dieser Habilitationsschrift vorgestellten Daten (Wenzel et al., 2019b) hatte jedoch keine Studie Messmethoden genutzt, die eine ausreichende räumliche Auflösung bieten, um mögliche Mikronetzwerkmechanismen von LOC mit hinreichender Präzision zu untersuchen.

Wie mLOC Mechanismen während der Einleitung und Aufrechterhaltung einer Generalanästhesie, so sind auch die Grundlagen zu strukturellen und funktionellen Folgen des medizinisch induzierten Komas (MIC) unzureichend erklärt. Insbesondere nach prolongiertem MIC (pMIC) stellen anhaltende kognitive Einschränkungen bei Überlebenden eines intensivmedizinischen Krankenhausaufenthaltes eine enorme symptombezogene und sozio-ökonomische Belastung dar (Cox und Carson, 2012; Kohler et al., 2019; Pandharipande et al., 2013; Unroe et al., 2010). Für das Kindes- und Jugendalter - während das Gehirn hoch plastisch ist und mit rapider Lerngeschwindigkeit auf äußere und innere Eingangsreize reagiert - konnte gezeigt werden, dass selbst kurz andauerndes MIC (maximale MIC Zeit im Tiermodell, unabhängig vom Alter, ca. 6 Stunden) substantielle Änderungen der synaptischen Verknüpfungen von Neuronen und kognitive Defizite nach sich ziehen kann (Briner et al., 2011; De Roo et al., 2009; Sanders et al., 2013). Ein kausaler Zusammenhang

zwischen aberranten synaptischen Verknüpfungen und kognitivem Defizit war suggestiv, da die synaptische Übertragung von Information zwischen Neuronen als einer der Grundmechanismen von Lern- und Gedächtnisprozessen anerkannt ist (Kasai et al., 2010; Segal, 2017; Yuste, 2011; Yuste und Denk, 1995). Kognitive Beschwerden nach pMIC treten jedoch auch im Erwachsenenalter in etwa einem Drittel der Patienten auf (Pandharipande et al., 2013), die zugrundeliegenden neuromorphologischen Mechanismen aber waren bis zur Durchführung der im Ergebnisteil zusammengefassten Studie unbekannt. Im Gegenteil, physiologische Grundlagenarbeiten zur altersabhängigen kortikalen synaptischen Plastizität hatten mit Hilfe hochauflösender *in vivo* 2-P-Mikroskopie gezeigt, dass kortikale Synapsen zum Erwachsenenalter hin zunehmend an Stabilität gewinnen (Grutzendler et al., 2002; Trachtenberg et al., 2002; Zuo et al., 2005). Daher schien es nicht verwunderlich, dass Anästhesiestudien (MIC Dauer 4-6 Stunden) in erwachsenen Mäusen keine Änderung funktioneller Synapsen („*dendritic spines*“) fanden (Yang et al., 2011). Die weithin akzeptierte Meinung stabiler Synapsen im Erwachsenenalter persistierte somit auch im Kontext des pMIC. Anästhesiezeiträume aber gehen im realweltlichen, intensivmedizinischen Kontext regelhaft weit über 4-6 Stunden hinaus. Demnach blieb die medizinisch bedeutsame Frage nach einer Verbindung zwischen pMIC, postanästhetischem kognitiven Defizit und einer möglichen zugrundeliegenden Veränderung der synaptischen Struktur des Gehirns im Erwachsenenalter ungeklärt.

Ebenso wie für die Erforschung epileptischer Mikronetzwerke stellt die chronische *in vivo* 2P-Mikroskopie aufgrund der bereits dargelegten Vorteile, insbesondere ihrer räumlichen Auflösung, Auflösungsdichte und stabilen Aufzeichnungskapazität optisch identifizierter Neurone, ein ideales Messinstrument zur feingradigen Aufzeichnung lokaler Ensembleaktivität während mLOC im intakten Gehirn dar. Unter maximaler Ausschöpfung der räumlichen Auflösung der 2P-Mikroskopie ist es sogar möglich, identifizierte Synapsen an einzelnen dendritischen Segmenten über Tage bis Wochen *in vivo* zu verfolgen, weshalb sie in der hier vorliegenden Habilitationsschrift ebenfalls zur Untersuchung der Auswirkungen von pMIC auf die synaptische Architektur des Gehirns genutzt wurde.

Ergebnisteil

Reliable and Elastic Propagation of Cortical Seizures in vivo

Bei dieser Arbeit (Wenzel et al., 2017) handelt es sich um die erste Studie, die die räumliche und zeitliche Rekrutierung lokaler kortikaler Neuronenverbände zu fokalen epileptischen Anfällen („iktuale Rekrutierung“) mittels kombinierter hochauflösender *in vivo* 2P-Mikroskopie (axial [L II/III] oder multi-laminär [L II/III/V] mit Hilfe implantierter Glasmikroprismen [1 x 1 mm])(Andermann et al., 2013) und Messung lokaler Feldpotenziale (LFP) untersuchte. Gegenstand der Studie waren im Forschungsfeld kontrovers diskutierte basale zeitliche und räumliche Rekrutierungsmuster von Neuronen zu wiederkehrenden epileptischen Anfällen (z.B. strukturiert, teilstrukturiert, oder willkürlich)(Bower und Buckmaster, 2008; Schevon et al., 2012; Truccolo et al., 2011) und lamina-spezifische Verzögerungen neuronaler Rekrutierung. Die Beantwortung dieser Fragen trägt eine für bestehende epilepsiechirurgische Therapien (z.B. Läsionektomie, sub-piale Resektionen) und zukünftige zielgerichtete Therapieansätze (z.B. lokale Gentherapie) fundamentale Bedeutung.

Im somatosensorischen oder visuellen Cortex wurden in zwei unabhängigen chemoconvulsiven (CC) Mausmodellen (Lokalinjektion in Lamina V: 4-AP [Vol. 500 nl; Menge insges.: 7,5 nmol] oder Ptx [500 nl; 5 nmol]) propagierende epileptische Anfälle (mikroskopiertes Sichtfeld [=FOV] ca. 400x400 μm, FOV Distanz zu Injektionsstelle ca. 1,5 – 3 mm) mit Hilfe verschiedener Calcium (Ca^{2+}) Indikatoren (OGB-1, adenoviral oder transgen exprimiertes GCaMP6s/f) mikroskopiert (Abb. 1 A-F, 3 A-B, 5 A-C). Durchgeführt wurden die Versuche mittels mikrochirurgisch etablierter kranialer Fenster und zusätzlich eingebrachter LFP Glasmikropipetten (30° Winkel: 1x LFP, 1x CC Injektion) in leicht anästhesierten (4-AP, axial: n=7, 71 Anfälle, 1402 Neurone [201 ± 25 SEM]; sagittal: n=4, 32 Anfälle, 334 Neurone [84 ± 13 SEM]) oder wachen (4-AP, axial/sagittal: n=5/1, 26/7 Anfälle, Neurone = 359 [72 ± 8 SEM]; Ptx, axial: n=3, 19 Anfälle, 182 Neurone [61 ± 1 SEM]), ausgewachsenen Mäusen (Hintergrund: C57BL/6).

Die individuell programmierte Datenanalyse (MATLAB®, MathWorks) beinhaltete nach Extraktion somatischer Ca^{2+} Transienten von Einzelneuronen ($\Delta F/F$; F = Fluoreszenz) aus den rohen Bildserien (30 Hz Bildwiederholungsrate, 512 x 512 Pixel) die Bestimmung individueller neuronaler Rekrutierungszeitpunkte zu wiederkehrenden

elektrographischen Anfällen. Dies erfolgte durch Berechnung des Maximalwertes der 1. Ableitung individueller Ca^{2+} Transienten (Abb. 1 G) während elektrographischer, in den FOV (typischerweise 400 x 400 μm) propagierender Anfälle, entsprechend der Rationale, dass die stärkste Änderung der neuronalen Feuerrate als Zeichen der iktualen Rekrutierung mit der steilsten Änderung der jeweiligen somatischen Ca^{2+} Aktivität korreliert (Trevelyan et al., 2006). Zur Evaluation der relativen Verlässlichkeit der zeitlich räumlichen Anfallsrekrutierung von Neuronen wurde primär ein relativer Rekrutierungs-Score (rr Score) etabliert, der eine Abwandlung (Median statt Mittel der Rekrutierung der Gesamtpopulation) des klassischen z Score darstellt. Auf diese Weise konnte für jedes aufgezeichnete Neuron eines Experiments in jedem Anfall ein individueller Rekrutierungszeitpunkt bestimmt werden und der hierüber erzielte Mittelwert und dessen Standardabweichung (SD) mit randomisierten Verteilungen (1000-fache Randomisierung) verglichen werden (Abb. 2 C, 3 D, 5 E). Bei Erreichen eines signifikant kleinen gemessenen SD-Werts (< 5% der randomisierten Vergleichsmasse) wurde ein Neuron als „verlässlich rekrutiert“ eingestuft (Abb. 2 E, 3 E, 5 F). Die Analyse eines möglichen zeitlich räumlichen Clustering neuronaler Rekrutierung erfolgte durch bivariate ANOVA Analyse mittlerer Distanzen räumlicher neuronaler Koordinaten (Abb. 2 F-G, 3 F, 5 G). Zur Berechnung relativer lamina-spezifischer Rekrutierungsverzögerungen (Abb. 4 A-C) wurden die Rekrutierungs-zeitpunkte vertikal übereinander liegender Neuronengruppen (L II/III versus L V) mittels Chi-Quadrat Test (gemessene versus ebenmäßige Rekrutierungsverzögerung unterschiedlicher Laminae) verglichen.

Hauptergebnis der Studie war, dass lokale kortikale Neuronenverbände unter relativen zeitlich räumlichen Gesichtspunkten (z.B. relative Berechnung der Rekrutierung von Einzelneuronen im Verhältnis zu jenem Zeitpunkt, an welchem erstmals mindestens 50% der Neurone im FOV zu einem Anfall rekrutiert worden sind) in substantiellem Umfang verlässlich in einer relativen zeitlichen Ordnung und räumlichen Clustern rekrutiert werden (Abb. 2 E-G, 3 E-G, 5 F-G). Darüber hinaus zeigte sich eine frühe supragranuläre iktuale Rekrutierung kortikaler Neurone im Vergleich zu tiefen kortikalen Laminae (Abb. 4 C). Unter Wahrung der relativen zeitlich räumlichen Rekrutierungsstruktur von Neuronenverbänden erfolgte von Anfall zu Anfall jedoch erstaunlicherweise nach absoluten Zeiteinheiten eine enorme Dehnung oder

Kompression der zeitlichen Abfolge neuronaler Rekrutierung („Elastizität“), im Bereich mehrerer Sekunden (Abb. 6 A-B). Diese Rekrutierungsstruktur wurde über Anfallsmodelle, Cortices, Wachheit, leichte Anästhesie, axiale und sagittale Bildgebung hinweg identifiziert und hing kritisch von $GABA_A$-Rezeptor vermittelter kortikaler Inhibition ab (Abb. 6 C-L). Die sekundäre Kompromittierung $GABA_A$-R vermittelter Hemmung in primär extrafokal gelegenen Territorien (Abb. 6 C) führte zu einer massiv gesteigerten Rekrutierung primär extrafokaler Neurone zu interiktualer und iktualer LFP Aktivität (Abb. 6 D-I), sowie massiven Beschleunigung und zeitlichen Uniformität iktualer neuronaler Rekrutierung (Abb. 6 J-L). Den Ergebnissen dieser Studie zufolge bestehen selbst auf mikroanatomischer Ebene wiederholte neuronale Rekrutierungsmuster zu wiederkehrenden fokalen epileptischen Anfällen, wobei die Konfiguration dieser Muster kritisch von lokaler Interneuronaktivität beeinflusst. Ein gewichtiger Grund für die in vorherigen Studien widersprüchlich erscheinenden Ergebnisse zu diesem basalen Forschungsgegenstand liegt wahrscheinlich in unterschiedlichen analytischen Herangehensweisen (z.B. festgelegte absolute Zeitfenster vs. populationsbasierte relative Kategorisierung iktualer Rekrutierung).

Cell Reports
Article

Reliable and Elastic Propagation of Cortical Seizures In Vivo

Michael Wenzel,[1,2,*] Jordan P. Hamm,[1] Darcy S. Peterka,[1] and Rafael Yuste[1]
[1]Neurotechnology Center, Department of Biological Sciences, Columbia University, New York, NY 10027, USA
[2]Lead Contact
*Correspondence: mw2946@columbia.edu
http://dx.doi.org/10.1016/j.celrep.2017.05.090

SUMMARY

Mapping the fine-scale neural activity that underlies epilepsy is key to identifying potential control targets of this frequently intractable disease. Yet, the detailed in vivo dynamics of seizure progression in cortical microcircuits remain poorly understood. We combine fast (30-Hz) two-photon calcium imaging with local field potential (LFP) recordings to map, cell by cell, the spread of locally induced (4-AP or picrotoxin) seizures in anesthetized and awake mice. Using single-layer and microprism-assisted multilayer imaging in different cortical areas, we uncover reliable recruitment of local neural populations within and across cortical layers, and we find layer-specific temporal delays, suggesting an initial supra-granular invasion followed by deep-layer recruitment during lateral seizure spread. Intriguingly, despite consistent progression pathways, successive seizures show pronounced temporal variability that critically depends on GABAergic inhibition. We propose an epilepsy circuit model resembling an elastic meshwork, wherein ictal progression faithfully follows preexistent pathways but varies flexibly in time, depending on the local inhibitory restraint.

INTRODUCTION

Epilepsy represents a wide range of pathological neural network alterations characterized by recurrent episodes of excessive brain activity. Identifying properties of seizure-producing networks (ictal networks) may enable more efficient seizure control (Baraban and Löscher, 2014; Krook-Magnuson and Soltesz, 2015). Recent advances in mapping ictal network dynamics at the microscale have unveiled unexpected complexity (Bower et al., 2012; Cymerblit-Sabba and Schiller, 2012; Feldt Muldoon et al., 2013; Keller et al., 2010; Truccolo et al., 2011, 2014), challenging the classical view of epilepsy as a condition of stereotyped ictal events (Szabo et al., 2015). In fact, the monitoring of the recruitment of neural populations to successive seizures in humans using multi-electrode arrays has led to contrasting conclusions, suggesting strict reproducibility of neuronal spiking patterns (Truccolo et al., 2011), a lack of such reproducibility close to the epileptic focus (ictal penumbra or propagation area) (Schevon et al., 2012), or completely non-repeated recruitment patterns (Bower et al., 2012). Part of the reason behind this controversy could be technical: it remains challenging for multi-electrode approaches to disambiguate the activity of densely packed neuronal circuits, especially for cells far from the electrode. Electrical recordings are inherently sparse when compared to the actual neural population density, complicating definitive conclusions. On the other hand, the few in vitro reports employing high-resolution optical imaging of ictal networks had too low a temporal resolution to uncover the true spatiotemporal dynamics of ictal networks (Badea et al., 2001; Cammarota et al., 2013; Feldt Muldoon et al., 2013; Lillis et al., 2015; Neubauer et al., 2014; Tashiro et al., 2002; Trevelyan et al., 2007).

To date, there have been only two studies using optical methods to measure the recruitment of epileptic networks at a cellular scale in vivo (Baird-Daniel et al., 2017; Muldoon et al., 2015). Baird-Daniel et al. (2017) compared the differential recruitment of glial versus neuronal populations to acute seizures at a population scale. Muldoon and colleagues (Muldoon et al., 2015) did not map seizures but interictal spikes, and they demonstrated heterogeneous recruitment of local microcircuits across seemingly stereotyped local field potential (LFP) events. Thus, despite being of great conceptual and therapeutic interest, the recruitment dynamics of densely packed neural networks during cortical seizure progression have still not been characterized in detail. In addition, it is unknown if there are layer-specific recruitment dynamics during ictal spread in vivo. However, understanding how exactly seizures progress in the living brain may hold critical new clues on how to stop their expansion.

To address these questions, we combined fast 30-Hz resonant two-photon calcium imaging with LFP recordings in two mouse models of acute seizures (4-Aminopyridine [4-AP] or picrotoxin [Ptx]) in anesthetized and awake mice, imaging both supra- and infragranular layers in different cortical areas. We find that neural recruitment to ictal activity maintains relative spatiotemporal reliability, even at the single-cell level, and that this reliability holds true across cortical areas and layers, with an initial supra-granular cortical invasion closely followed by recruitment of deep layers. However, absolute temporal micro-progression of seizures varies profoundly across events, revealing a constrained ictal network that flexibly stretches and

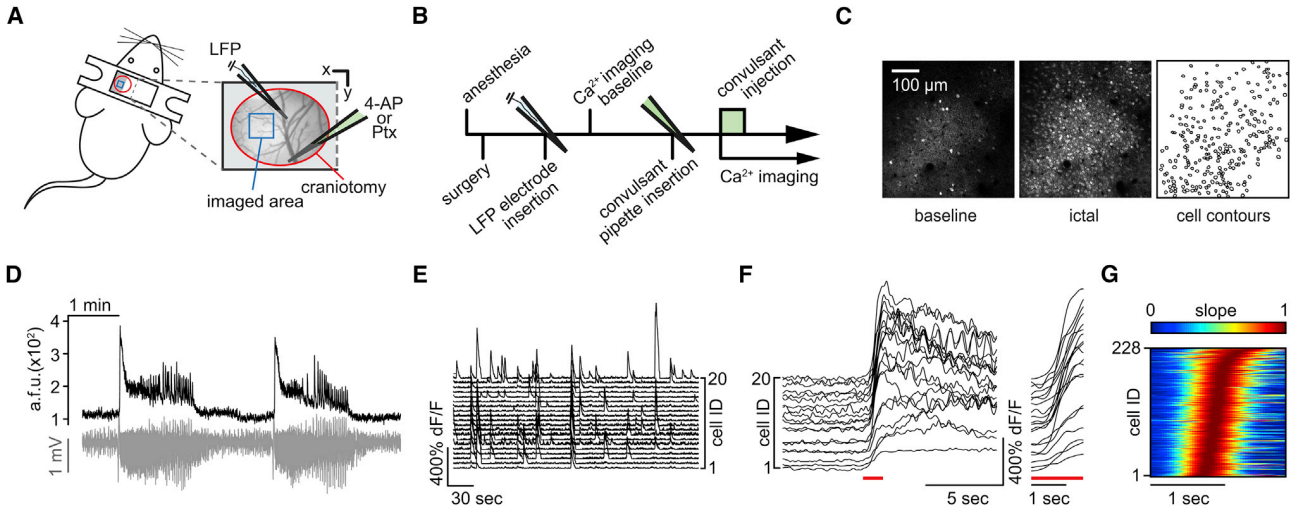

Figure 1. In Vivo Two-Photon Calcium Imaging of Seizure Spread with Single-Cell Resolution

(A) Experimental setup with surgical approach over left somatosensory cortex (craniotomy encircled in red and imaged field of view (FOV) within the seizure propagation area in blue). Each experiment (exp.) involved the insertion of two glass micropipettes, one (blue) containing a silver chloride electrode for local field potential (LFP) recording and the other (green) containing 4-AP (15 mM, injection vol. 500 nL [total amount delivered = 7.5 nmol]) or Ptx (10 mM, injection vol. 500 nL [total amount delivered = 5 nmol]).

(B) Typical experimental workflow.

(C) Propagation area in left somatosensory cortex, representative 3-s average (avg) fluorescence images of neural activity (GCaMP6s) during baseline (left) and full ictal event (middle, see also Movie S1). Contour plot of registered cells (right) is shown.

(D) Average calcium transient of FOV (black trace, GCaMP6s, imaging depth ~150 μm beneath the pial surface) and corresponding LFP (gray trace) post 4-AP.

(E) Calcium transients of 20 representative cells within FOV during baseline.

(F) The same 20 cells post 4-AP, with optical seizure break-in (underlined in red) magnified on the right.

(G) Representative example of the optical break-in of the ictal wave (normalized first derivative of ΔF/F). Cell recruitment to ictal activity was ordered in time by maximum slope.

compresses in time. We show that this progression elasticity (i.e., relative spatiotemporal reliability despite progression variability in absolute time) critically hinges on the activity of local GABAergic interneurons, as compromising their signaling results in the acceleration and invariance of ictal progression. Thus, cortical circuits, at least during seizures, can propagate activity through the same pathways with greatly variable speeds and delays, both of which depend on the strength of the local inhibitory restraint to excessive network activity.

RESULTS

To map seizure propagation, we employed two pharmacological models of acute seizures using local cortical injection of small amounts of either 4-AP (15 mM, 500 nL [total amount delivered = 7.5 nmol], layer V) or Ptx (10 mM, 500 nL [total amount delivered = 5 nmol], layer V) in mature mouse neocortex. The two drugs generate seizures through different mechanisms. While the potassium channel blocker 4-AP enhances neuronal firing through increased pre-synaptic glutamate release (Morales-Villagrán and Tapia, 1996), the disinhibitory compound Ptx acts as GABA-A receptor antagonist (Krishek et al., 1996). The models provided a two-pronged approach for studying the repeated and variant spatiotemporal details of spreading seizures at a fine scale, in a setting where intra- and extrafocal compartments are precisely defined.

Two-Photon Calcium Imaging of Neocortical Seizure Spread In Vivo

We were interested in mapping cellular recruitment during spread of ictal activity, and we used in vivo two-photon calcium imaging (OGB-1, GCaMP6s, or GCaMP6f) to monitor action potential activity in neural populations (Chen et al., 2013; Stosiek et al., 2003; Yuste and Denk, 1995; Yuste and Katz, 1991). For imaging seizure spread during mild anesthesia, a small craniotomy above the somatosensory cortex was established (Figure 1A). As a gross indicator of ictal activity within the examined area, we measured the LFP with a sharp glass microelectrode, carefully lowered into the cortex next to the imaged field of view (FOV; Figure 1A). The positioning of the LFP pipette in proximity, yet outside the seizure initiation site, did not affect the temporal signature of electrographic seizures, even though LFP signal amplitude decreased with distance to the initiation site (Figure S1A). For the induction of ictal events, a second glass micropipette containing 4-AP was inserted into the cortex to a depth of ~480 μm after baseline imaging, at a distance of ~1.5–2 mm to the FOV (Figures 1A and 1B). No epileptiform activity was induced by saline injection alone (Figure S1B).

Animals' heart rate, breath rate, and peripheral blood oxygenation were monitored via a paw sensor throughout experiments to ensure stable vital parameters (Figure S1C). Even though leading to hundreds of interictal LFP spikes (IISs), Ptx injections did not lead to full ictal events during anesthesia (data not

shown), and they were henceforth used only in experiments during wakefulness. In the absence of any chemoconvulsant, local populations in layer II/III (LII/III) displayed ongoing sparse and distributed calcium activity during baseline (Figures 1C, left and 1E). In contrast, full ictal events post 4-AP entailed sustained firing of large numbers of neurons in the FOV (Figures 1C, middle, 1D, and 1F; Figure S1D; Movies S1 and S2). Ictal invasion happened in a continuous wave of intense neuronal firing that slowly propagated across the FOV. During anesthesia, 4-AP-induced electrographic seizures and imaged calcium transients corresponded in time (Figure 1D; Figure S1D), and the rise in calcium was correlated with the typical increase in spectral power of the ictal LFP signal over a wide frequency range (1–100 Hz), reflecting massive synaptic barrages during seizures (Figure S1E). However, individual calcium deflections could only be directly related to lower frequency ictal activity toward the end of seizures (see, e.g., Movie S2), because even fast calcium indicators like OGB-1 or GCaMP6f have too low temporal kinetics to resolve individual LFP deflections during tonic ictal firing (Khoshkhoo et al., 2017). The propagation velocity of the optical invasion of the FOV was similar to the Jacksonian march described in humans and experimental seizure models where inhibition is intact (seven experiments [exp.] under anesthesia, 71 seizures, 0.64 ± 0.18 mm/s) (Jasper, 1969; Trevelyan et al., 2007; Wong and Prince, 1990). Notably, the pre-ictal neural activity in not yet invaded areas during pending seizure spread was sparse, until the sharp rise in fluorescence upon arrival of the ictal wave front (Figures 1D and 1F; Figure S1D). This activity pattern was in sharp contrast to the seizure initiation site, where locally confined, enhanced calcium activity could be imaged almost immediately after 4-AP injection (data not shown). Importantly, our temporal imaging resolution of 30 Hz was sufficient to capture individual cell recruitment to ictal activity (Figures 1F and 1G; Figure S1D).

Stereotypical Spatiotemporal Recruitment of Neural Populations by Seizures

To investigate the characteristics of local network recruitment during seizure spread, we analyzed all neurons in the FOV that showed a visible change in fluorescence upon optical break-in of ictal activity and whose somata could be followed stably across the analyzed time period (n = 7 exp. under anesthesia [OGB-1 = 4, GCaMP6s = 3], total number of seizures = 71, average number of analyzed cells = 201 ± 25 SEM). Corresponding in time to the incoming ictal wave, neurons were recruited in a continuous, sigmoid temporal curve (Figure 2A). First, we mapped temporal population recruitment patterns, specifically examining the regularity of individual cell and sub-region recruitment to seizures. Arranging cell recruitment time points (maximum slope of ΔF/F) of an individual seizure revealed that the tilt of the temporal ordering was coarsely preserved across ictal events (Figure 2B). When we tiled the imaged region instead of registering individual cells (Figure S2A), this inherent temporal structure became apparent even in unsorted data (Figure S2B).

To quantify and verify this conserved structure at the single-cell scale, we used two different analytical approaches. First, regardless of its duration, we divided every ictal break-in into three equally sized time bins (early, intermediate, and late; Figure S2C, upper panel), calculating an SD of bin membership for each cell across the entire experiment such that, if a given cell were always recruited to the seizure at the same relative time, its SD would equal zero. We additionally established a more continuous method by classifying a cell's recruitment time relative to the entire population (similar to a *Z* score), separately for each seizure (relative recruitment score [rr score]; Figure S2C, lower panel). The observed time bin or rr score distributions for each cell and their SD were compared to randomized surrogate distributions derived from a temporal reshuffling procedure (Figure S2D). Both methods revealed left-shifted SD distributions, indicating a smaller relative onset time variability in the observed dataset than would be expected by chance given population recruitment (Figure 2C). To exclude the possibility that these results were biased by the cells' indicator load (e.g., the higher the load the sooner the measured recruitment), we performed a correlation analysis between cellular baseline fluorescence and the corresponding recruitment, which showed no systematic relationship (Figure 2D; all 4 OGB-1 exp., 42 seizures, 952 cells, $r = 0.1386$, $r^2 = 0.0192$; the effect accounts for 1.9% of the variance in the data).

After obtaining cellular time bin and rr score SDs, we generated a reliability index for individual cells that were defined as reliable when their SD was smaller than 95% ($p < 0.05$) of those in the randomized dataset. Again, both approaches revealed a substantial percentage of temporally reliably recruited neurons (Figure 2E, cells). This reliability further increased with growing spatial coarseness (Figure 2E, tiles). It is noteworthy that reliability indices of time binning and rr score classification were not necessarily built of the same cells but in fact had non-overlapping sections. The combined reliability index, where a cell was called reliable if reliable in at least one of the two methods (time bin or rr score), was higher than in either individual classification (Figure 2E, right).

The fact that cell and tile analyses showed stable relative recruitment ordering to subsequent seizures implied that seizures propagate in a spatially organized manner, and, indeed, we found a coarsely maintained spatial pattern of cell recruitment (Figure 2F). To quantify this effect, we implemented a two-dimensional ANOVA approach by categorizing cells based only on their recruitment times (i.e., temporal quartiles). We compared (1) the distance of individual cells to the spatial mean of their respective quartile to (2) the distance of all cells to the spatial mean of the entire analyzed population (Figure 2G, same experiment as in Figure 2F; Figure S2E). This approach yielded significant bivariate F values for all seven experiments (F values: $F[3,48] = 11.595$, $F[3,28] = 33.260$, $F[3,36] = 11.251$, $F[3,52] = 22.208$, $F[3,36] = 12.67$, $F[3,60] = 11.64$, and $F[3,8] = 41.224$; all p values < 0.001).

Stereotypical Local Population Recruitment Patterns across Cortical Layers

To test whether network reliability holds true across cortical layers, we employed a recently introduced technique enabling multilayer imaging through implanted glass microprisms (1 × 1 × 1 mm; Figure 3A) (Andermann et al., 2013). Again, a sharp glass microelectrode was carefully lowered into the cortex close by the prism face for LFP recordings (Figure 3A), and a second

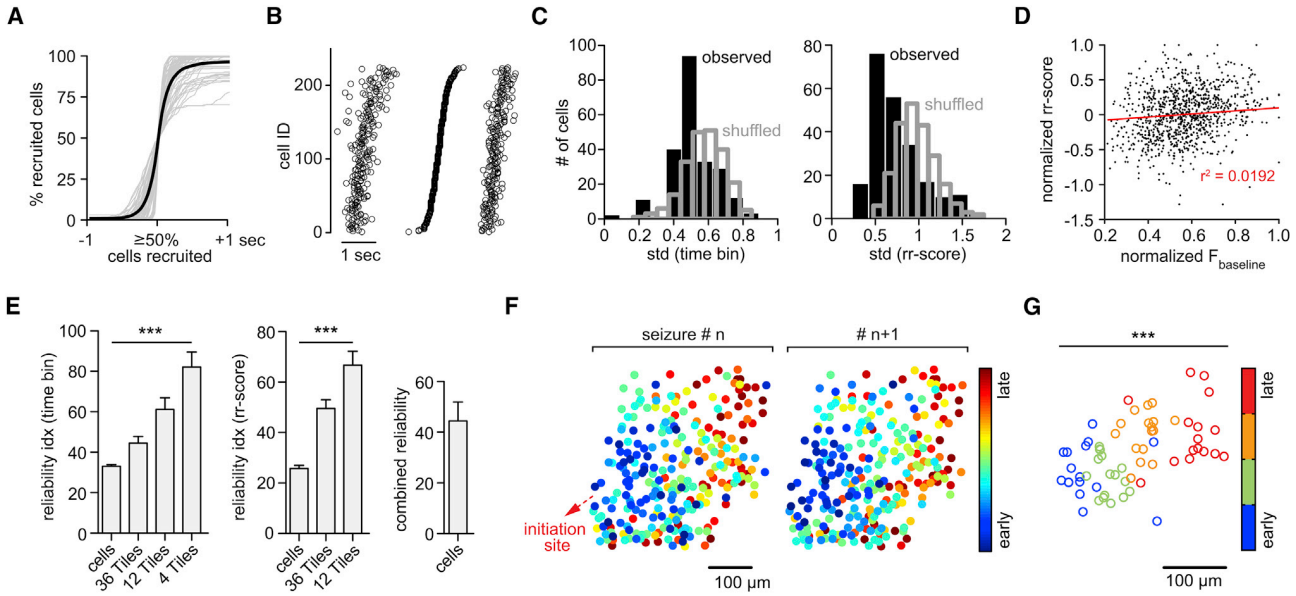

Figure 2. Stereotypical Micro-progression of Seizures

(A) Superposition of all analyzed optical seizure break-ins (gray) centered around the 50% recruitment frame. The black graph represents mean temporal recruitment (n = 7 exp., total number of seizures = 71 [11.3 ± 1.358 SEM], total number of cells analyzed = 1,402 [201 ± 25 SEM], cell number in percentage for comparability across experiments).

(B) Representative example of three consecutive optical seizure break-ins plotted next to each other. The first and third events are sorted by the temporal ordering of the second event. Each circle represents an individual cell recruitment time point.

(C) Representative experiment with observed (black) versus shuffled (gray) time bin or rr score SD distributions.

(D) Correlogram of cellular baseline fluorescence versus rr scores. Values are maximum-normalized for comparability across experiments. The relationship between the two parameters is negligible (four exp., 42 seizures, 952 cells, r = 0.1386, r^2 = 0.0192). The effect accounts for 1.9% of the variance in the data.

(E) Reliability indices displaying the percentage of cells or spatial sub-regions (tiles) whose temporal recruitment variability (time bin or rr score SD) are <5% of all shuffled values of analyzed cells or tiles ($p < 0.05$). Recruitment reliability increased with spatial coarseness (one-way ANOVA, n = 7 exp., total number of cells = 1,402; time bin and rr score classification, $p < 0.0001$). Right: combined (reliable in time bin and/or rr score classification) cell-wise reliability index is shown.

(F) Spatiotemporal maps of cell recruitment in two consecutive seizures indicating grossly preserved relative recruitment. Each dot represents an individual cell. 4-AP injection site (red arrow) is located ~1.5 mm posterior to FOV (somatosensory cortex).

(G) Same experiment. The spatial average coordinates of temporally defined population quartiles (25% earliest recruited cells, 25%–50%, 50%–75%, and 75%–100%) across 16 seizures show consistent spatiotemporal propagation (bivariate ANOVA: n = 16 seizures, F[3,60] = 11.64, $p = 0.000004$, all seven axial exp. under anesthesia, $p < 0.001$). Each circle represents the average coordinate of all cells belonging to the respective quartile.

sharp glass micropipette containing 4-AP was advanced into the cortex to a depth of ~480 μm, at a distance of ~1.5–2 mm to the implanted prism. Imaging was carried out at a distance of 180–300 μm from the vertical prism face, where no damage of the cortex was to be expected due to prism insertion (Chia and Levene, 2009b).

In accordance with previous reports (Andermann et al., 2013; Chia and Levene, 2009b), visualized vasculature and cell anatomy appeared physiological and local network activity showed sparse cell firing (Figure 3B; Movie S3), as observed during axial imaging of superficial layers (LII/III) during baseline. Correct vertical positioning of the prism was ensured by visualizing the full extent of layer V (LV) pyramidal neurons with their apical dendrites extending across layer IV (LIV) into LII/III. As observed in axial plane LII/III experiments, seizures invaded the imaged translaminar FOV in a continuous fashion (Figure S3B; Movies S4 and S5). Side-by-side plotting of individual cells' recruitment time points of consecutive seizures showed that the earlier observed coarse preservation of temporal recruitment within LII/III holds true across cortical depth (Figure 3C). Likewise, quantification of multilayer cell recruitment during lateral seizure spread revealed left-shifted SD distributions of individual cell bin memberships or rr scores (Figure 3D). Consequently, a substantial percentage of neurons in LII/III and LV was shown to occupy reliable relative temporal recruitment positions across seizures (Figure 3E). Again, spatiotemporal onset maps of successive seizures showed a maintained spatial pattern of relative cell recruitment (Figures 3F and 3G). These experiments showed that network recruitment reliability can be found across the cortical column.

Spreading Ictal Activity Recruits Superficial Cortex ahead of Deep Cortical Layers

During multilayer imaging, we noticed that relative temporal recruitment of local cell populations seemed to differ across layers (Figure 3G). To quantify layer-specific spatiotemporal recruitment delays, we located groups of neighboring neurons within spatial bins (or tiles) of 100-μm width in LII/III and LV, and we derived an average calcium population transient for every tile, for each electrographic seizure onset of an experiment

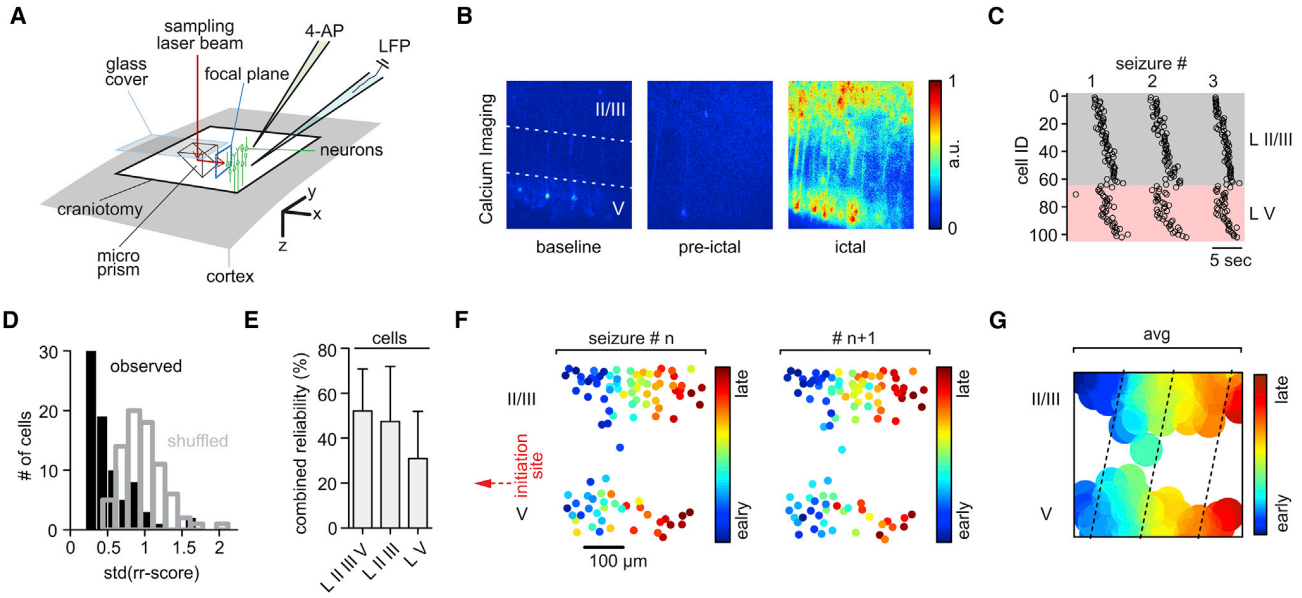

Figure 3. Stereotypical Seizure Propagation across Cortical Layers

(A) Experimental setup involving cortical microprism implant (brain surface in gray and craniotomy encircled in black). The 90-degree laser beam (red) deflection results in a vertical FOV (neurons in green); again, each experiment involved the insertion of two glass pipettes (LFP, blue and 4-AP, green).

(B) Representative 3-s average fluorescence images of multilayer neural activity, recorded under anesthesia in somatosensory cortex during baseline (left, II/III or V = layer II/III or V), directly prior to the seizure break-in (middle) and full ictal event (right, see also Movies S3, S4, and S5). The injection site of 4-AP was located ~2 mm anterolateral to the prism (in LV), aligned to the edge of the prism face.

(C) Representative example of three consecutive optical seizure break-ins plotted next to each other, indicating consistent recruitment across cortical layers. Each circle represents an individual cell recruitment time point.

(D) Representative experiment, observed (black) versus shuffled (blue) rr score SD distribution.

(E) Combined reliability index displaying the percentage of cells whose recruitment SD are <5% of all shuffled SD of all analyzed cells ($p < 0.05$, n = 4 exp., total number of seizures = 32 [8 ± 3.6 SEM], total number of cells analyzed = 334 [84 ± 13 SEM]).

(F) Spatiotemporal maps of multilayer cell recruitment in two consecutive seizures, indicating preserved cell recruitment. 4-AP injection site (red arrow) is located ~1.5 mm away from FOV.

(G) Same experiment, average contour plot of eight seizures. Note how LII/III appears to be recruited ahead of corresponding LV (dotted lines).

(Figure 4A; Figures S3C and S3D). In accordance with our results from axial imaging in LII/III (Figures 2F and 2G), tiles in LII/III being located more proximally to the seizure initiation site were consistently recruited earlier than those being situated more distant to it (Figure 4A; Figure S3C, blue traces). The same spatiotemporal pattern of progression was observed in LV (Figure 4A; Figure S3C, green traces). To our surprise, and in contrast to previous reports in disinhibited brain slices where LV led lateral spread of epileptiform activity (Telfeian and Connors, 1998), we observed an ictal recruitment of LII/III ahead of LV (Figure 4A; Figure S3). In fact, this bi-directional progression delay was already apparent to the naked eye when inspecting the raw data (Movies S4 and S5). To compare layer-specific delays across experiments, we calculated the recruitment time lags of adjacent tile pairs (lateral pairs: tile[prox] – tile[dist]; vertical pairs: tile[II/III] – tile[V]) for every seizure break-in (Figure S3D). In doing so, we did not only find significant layer-specific average negative time lags of proximal versus distal tiles in nearly all seizures but also proved a temporally variable yet consistent delay of local LV populations to their LII/III tile counterparts (Figures 4B and 4C). In sum, we found that cortical seizure spread in the intact brain involves lateral expansion within superficial and deep layers. Intriguingly, we reveal a vertical delay during lateral seizure spread, with a lead of LII/III recruitment over LV.

Mapping Cortical Seizure Micro-progression in Awake Mice

Major advancements in epilepsy research have been achieved by measurements in anesthetized animals. Yet, inherently, anesthesia alters neuronal network activity, and it does so in a non-uniform way (Adesnik et al., 2012). Therefore, we set out to investigate whether our findings hold true in the awake condition, using either local 4-AP or Ptx injection. Again, we recorded calcium activity and LFP in head-restrained yet otherwise freely moving mice, positioned on a running wheel that can tilt flexibly and therefore serve as a suspension during seizure-related motor symptoms. To maximize focal plane imaging stability in the awake state, a thin glass coverslip was positioned over the craniotomy, with a small opening established posterior to it for access of both the LFP and 4-AP or Ptx pipettes (Figure 5A).

Prior to the actual experiment, all animals were habituated to the experimenter and the experimental environment. Like in anesthetized mice, a series of full electrographic but now also behaviorally detectable seizures, including orofacial and

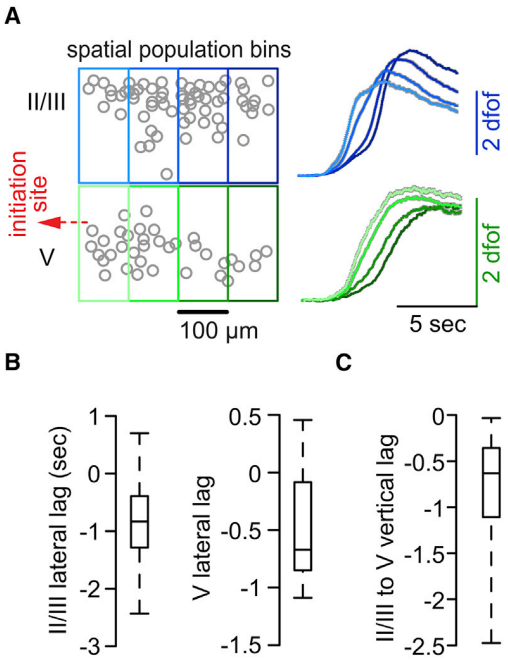

Figure 4. Supra-granular Layers Are Systematically Recruited ahead of Deep Layers

(A) Left: paradigmatic multilayer contour plot (LII/III and LV, circles represent individual cells). Small local cell populations were grouped together in spatial bins (tiles) of 100-µm width to assess lateral delays of adjacent tiles and vertical delays of tiles situated above each other. Right: population average calcium transients of individual tiles within LII/III or LV across all seizures in one experiment are shown (right, gray shades represent SEM, number of seizures = 11, number of analyzed cells = 102, number of spatial tiles = 8). Note that lateral but also vertical tile delays can be appreciated by eye.

(B) Boxplots of lateral (tile[prox] − tile[dist]) recruitment time lags of adjacent tiles within LII/III (left) or LV (right, n = 4 exp., total number of seizures = 32 [8 ± 3.6 SEM]). The boxes represent 25th–75th percentile, and the bands inside the boxes display the median recruitment time lag. In nearly all seizures, proximal tiles (lateral lag) were recruited prior to their adjacent distal tiles (for lateral lags LII/III and LV: chi-square test X2(1) = 12.7, $p < 0.001$). See also Figure S3D and Supplemental Experimental Procedures.

(C) Same 4 exp. as in (B). Boxplots of vertical recruitment time lags of adjacent tiles (tile[LII/III] − tile[LV]). In all seizures, LII/III tiles were recruited prior to their corresponding LV tiles (chi-square test X2(1) = 21.3, $p < 0.001$).

limb-related motor symptoms and, at times, alternatingly bilateral convulsions, occurred post local 4-AP or Ptx injection (Figures 5B and 5C). In spite of this, our local injection approach allowed for the study of spreading seizures under stable imaging conditions, since ictal recruitment of imaged cortical areas sufficiently often preceded seizure spread to motor cortices. In comparison to 4-AP, Ptx-induced seizures were generally short (4-AP: 71 ± 7.1 s [five exp., 26 seizures], Ptx: 19.1 ± 1.34 s [three exp., 19 seizures]). Additionally, Ptx injection commonly led to multitudes of IISs in the LFP, which, however, did not optically recruit the imaged FOV (Figure 5C). Interestingly, and consistently in awake mice, interictal periods and seizure durations displayed a rather irregular pattern. At times, ictal activity failed to invade or only incompletely penetrated the imaged territory (Figures 5B, left and 5C, left), and there was a consistent delay between the electrographic seizure onset and optical break-in on the scale of seconds (Figures 5B and 5C, magnified portions) (Khoshkhoo et al., 2017; Martinet et al., 2015). This observation could be explained by a much slower temporal seizure progression imaged during wakefulness as compared to the anesthetized condition (4-AP: 0.0215 ± 0.003 mm/s [five exp., awake] versus 0.64 ± 0.18 mm/s [seven exp., anesthetized]). Both the lack of optical penetration of IIS and the persistence of seconds of delay of optical break-in upon electrographic seizure onset present also in the Ptx model, over the duration of an entire experiment (Figure 5C, magnified portions), further supported that the injected chemoconvulsant remained local within the seizure initiation site and did not diffuse into the FOV.

During wakefulness, in line with our anesthetized recordings, neurons in the propagation area were recruited in a continuous, sigmoid temporal curve independently of the employed seizure model, yet over stretched time courses (Figure 5D; Movie S6). Cellular recruitment reliability to ictal activity persisted in awake mice, and it appeared to be even more pronounced than during anesthesia. In both 4-AP- and Ptx-induced seizures, we found a clear leftward shift of rr score SD distributions in the observed versus randomized data (Figure 5E), and, consequently, we obtained high cellular reliability indices, within and across layers (Figure 5F; 4-AP: five axial exp., one prism; Ptx: three exp.). Again, we excluded the possibility that these results were biased by the cells' indicator expression levels through a correlation analysis between cellular baseline fluorescence and the corresponding recruitment time (Figure S3E; transgenic GCaMP6f, five axial exp. [4-AP], 26 seizures, 360 cells, r = 0.1675, r^2 = 0.0281; the effect accounts for 2.8% of the variance in the data).

In agreement with our experiments in anesthetized mice, temporal population recruitment quartiles clustered into discriminable spatial domains (Figure 5G; 4-AP: 11 seizures, F[3,40] = 18.44, $p = 1.145 \times 10^{-7}$; Ptx: four seizures, F[3,12] = 52.87, $p = 1.591 \times 10^{-8}$; other 4-AP exp.: F[3,12] = 138.48, F[3,8] = 15.89, F[3,12] = 32.19, and F[3,20] = 56.5; other Ptx exp.: F[3,20] = 447.98 and F[3,28] = 91.22; all $p < 0.001$). Finally, layer-specific recruitment delays were also present in seizure spread during wakefulness. As described (Figure 4; Figure S3), we found significant layer-specific average negative time lags of proximal versus distal tiles in all seven seizures imaged through a microprism and consistent delays of local LV populations to their LII/III respective group of cells (Figure 5H). It is noteworthy that, while lateral time lags were prolonged during wakefulness, trans-laminar lags remained on par with the anesthetized condition. In conclusion, while differences in temporal seizure progression were found in awake versus anesthetized mice, relative ictal recruitment reliability of local neural networks, spatiotemporally ordered micro-progression, and layer-specific recruitment lags to spreading seizures were also present in experiments during wakefulness.

Seizure Micro-progression Is Elastic

While evaluating the spatiotemporal characteristics of local network recruitment by seizures in both the anesthetized and awake condition, we noticed that, despite the observed relative spatiotemporal stereotypy, the absolute ictal network recruitment varied profoundly in time. To further investigate this

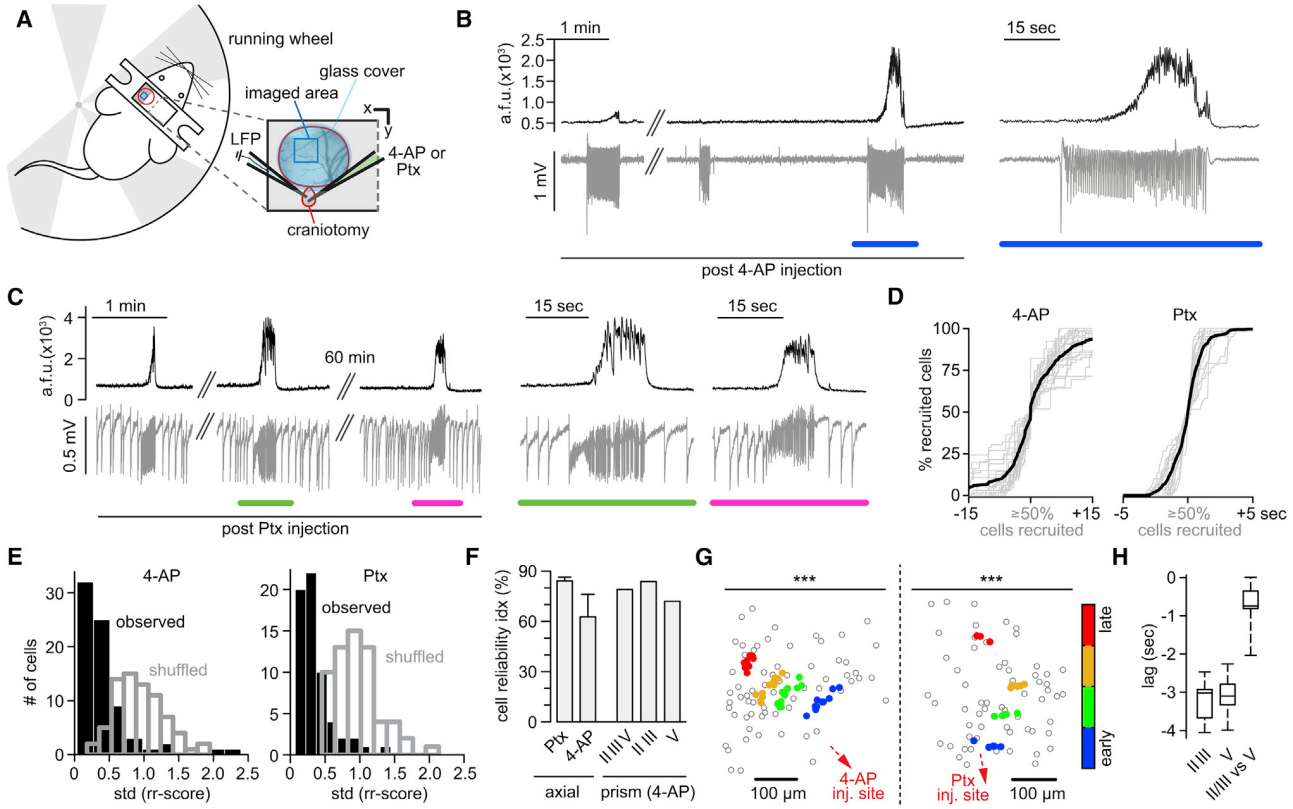

Figure 5. Stereotypical and Elastic Seizure Propagation in Awake Mice

(A) Adapted experimental setup (craniotomy outlined in red, FOV in dark blue, and glass coverslip in light blue). Two inserted glass pipettes were used (LFP [blue], 4-AP or Ptx [green, 4-AP: 500 nL, total amount delivered = 7.5 nmol; Ptx: 10 mM, 500 nL, total amount delivered = 5 nmol]).

(B) Average population calcium transient (black trace, Thy-1::GCaMP6f, LII/III) and corresponding LFP (gray trace) post 4-AP (~2 mm posterior to FOV in somatosensory cortex). Blue underscore marks magnified inset on the right.

(C) Average population calcium transient (black trace, Thy-1::GCaMP6f, LII/III) and corresponding LFP (gray trace) post Ptx (~1.5 mm posterior to FOV in somatosensory cortex). Green and magenta mark magnified insets on the right. Note the stable lack of calcium responses to IIS in the LFP and slow seizure invasion of the FOV post Ptx.

(D) Superposition of all axially imaged seizures (gray) in awake mice, post 4-AP or Ptx, centered around the 50% recruitment frame. The black graphs represent mean temporal recruitment (4-AP: n = 5 exp., total number of seizures = 26, total number of cells analyzed = 359 [72 ± 8 SEM]; Ptx: n = 3 exp., total number of seizures = 19, total number of cells analyzed = 182 [61 ± 1 SEM]; cell number in percentage for comparability across experiments).

(E) Representative experiment (4-AP or Ptx) with observed (black) versus shuffled (gray) rr score SD distributions. Both seizure models show leftward shifts of the observed versus shuffled data.

(F) Cellular reliability indices (rr score) across seizure models: Ptx (n = 3 exp., axial imaging) and 4-AP (n = 5 exp. axial imaging, n = 1 exp. multilayer imaging).

(G) Representative experiment (4-AP or Ptx). The spatial average coordinates of temporally defined population quartiles (colored dots) are plotted within the imaged population (gray circles represent individual cells); left: 4-AP (bivariate ANOVA: n = 11 seizures, $F[3,40] = 18.44$, $p = 1 \times 10^{-7}$, all five experiments in awake mice with 4-AP $p < 0.001$); right: Ptx (bivariate ANOVA: n = 4 seizures, $F[3,12] = 52.87$, $p = 1.5 \times 10^{-8}$, all three experiments in awake mice with Ptx $p < 0.001$).

(H) Multilayer imaging. Boxplots of lateral or vertical onset time lags of adjacent tiles are shown (please see also Figure S3D); boxes represent 25th–75th percentile, and bands inside boxes display the median recruitment time lag (n = 1 exp., 4-AP, total number of seizures = 7).

phenomenon, we defined the recruitment duration for each recorded seizure as the time period from the first to the last cell recruitment frame, excluding the 5% most deviant cells to the median recruitment frame to minimize outlier-related duration distortions. Across employed seizure models, population recruitment varied from hundreds of milliseconds to several seconds (Figure 6A). Strikingly, this variability was present within individual experiments too (Figure 6B; seven exp. [anesthesia], eight exp. [wakefulness]). Importantly, this phenomenon was not simply explained by a facilitating temporal compression over time, since successive seizures showed well-maintained relative spatiotemporal recruitment while their absolute time courses of recruitment compressed and stretched greatly (Figure S4A). While we could not find a systematic correlational relationship between electrographic seizure length and local population recruitment duration (Figure S4B), as has been previously described for macroscale ictal recruitment (Martinet et al., 2015), total seizure duration itself displayed temporal variability, too (Figure S4C). These results unveiled that neural recruitment to spreading seizures displays elastic features, that is, relative spatiotemporal reliability despite progression variability in absolute time.

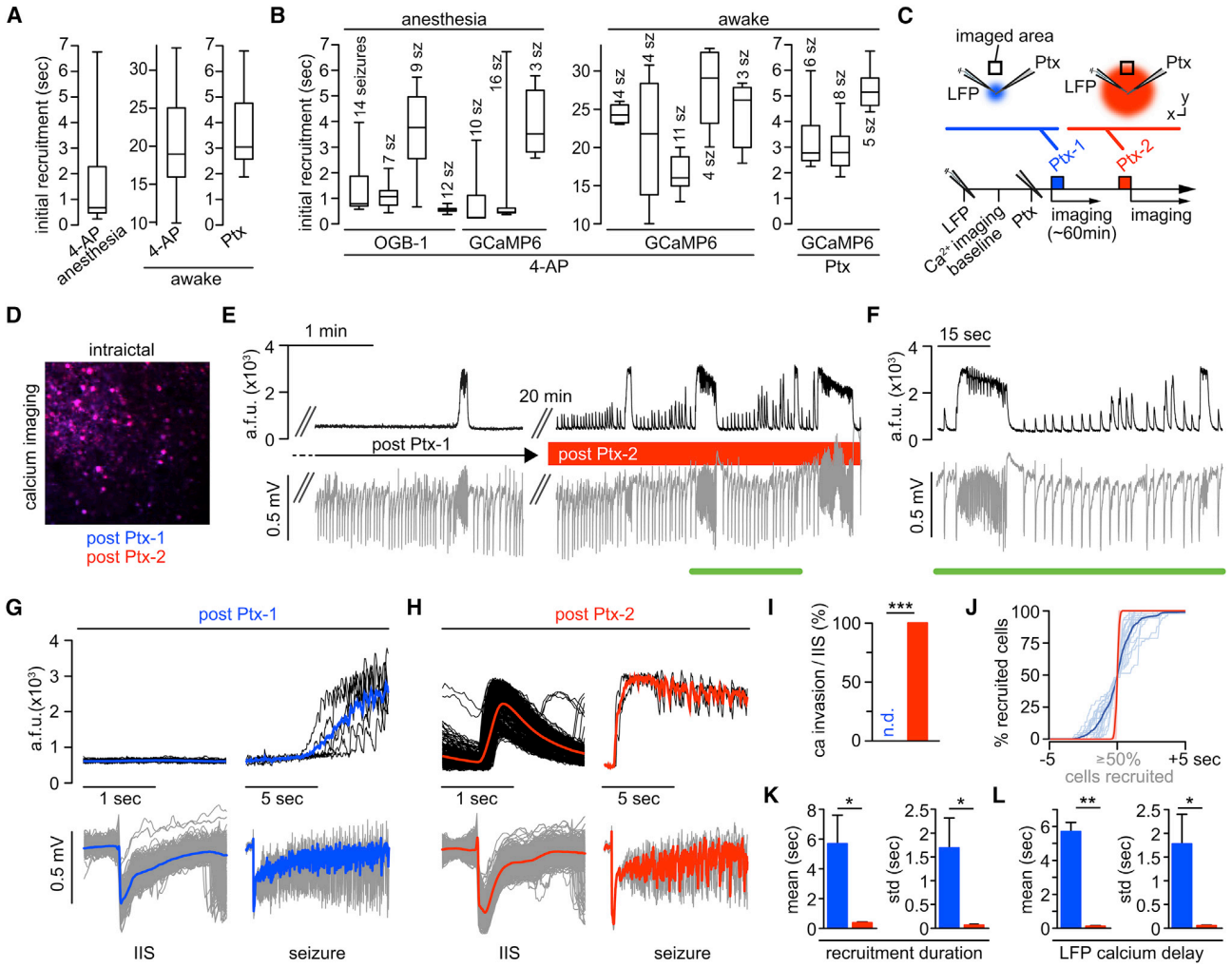

Figure 6. Elastic Recruitment Is Regulated by Local Inhibitory Neurons

(A) Absolute ictal recruitment durations vary across seizures. Boxplots display population recruitment durations analyzed for each condition; left: 4-AP under isoflurane (n = 7 exp., 71 seizures); middle: 4-AP during wakefulness (n = 5 exp., 26 seizures); right: Ptx during wakefulness (n = 3 exp., 19 seizures).

(B) Ictal recruitment durations vary within individual experiments. Boxplots of 15 exp. (n = 7 anesthesia and n = 8 wakefulness) are shown. Boxes represent 25th–75th percentile of cellular recruitment, and bands inside boxes display median cell recruitment time.

(C) Schematic depiction of experiments involving two Ptx injections during wakefulness: LFP and Ptx pipettes are located within the seizure initiation site. After LFP pipette insertion and baseline imaging, the Ptx (10-mM) pipette is inserted. The first Ptx injection (Ptx-1, blue) is volume controlled, as usual (500 nL, total amount delivered = 5 nmol]), and followed by imaging seizure spread, as described, for ~60 min. Then, a second Ptx injection (Ptx-2, red) is performed (pressure controlled, 10 psi, 10 min).

(D) Merged average images of ictal FOV post Ptx-1 (blue) and post Ptx-2 (red). Note the complete overlap of the average images (magenta); that is, the imaged focal plane remains stable beyond Ptx-2.

(E) Representative experiment; left: post Ptx-1, imaging (black) and LFP recordings (gray) of spreading seizures for >1 hr (note no calcium response to IIS in the LFP); right: ~20 min post Ptx-2.

(F) Magnification of inset in (E). Note that post Ptx-2, every IIS in the LFP coincides with a population calcium response within the FOV in the propagation area.

(G) Same experiment, post Ptx-1. Left: superimposed 2-s windows of population calcium activity are shown (top, individual traces in black, mean in blue), centered around 678 IISs recorded by LFP at the distant injection site (bottom, individual events in gray, mean in blue). Right: superimposed 10-s windows of six seizures recorded by imaging (top, individual seizures in black, mean in blue) and LFP (bottom, individual seizures in gray, mean in blue) are shown. Note the delay of several seconds between electrographic seizure onset and optical invasion.

(H) Same experiment, post Ptx-2. Left: superimposed 2-s windows of population calcium activity are shown (top, individual traces in black, mean in red), centered around 562 IISs (bottom, individual events in gray, mean in red). Right: superimposed 10-s windows of three seizures recorded by imaging (top, individual seizures in black, mean in red) and LFP (bottom, individual seizures in gray, mean in red) are shown. Note the clear population calcium response to IIS in the LFP and the immediate penetration of the imaged FOV upon electrographic seizure onset.

(I) Quantification of optical invasion per IIS (n = 4 exp., 1,327 IISs post Ptx-1 [n.d. = none detectable], 893 IISs post Ptx-2 [mean invasion rate = 100%]; Mann-Whitney test, p = 0).

(legend continued on next page)

Seizure Progression Elasticity Is Determined by Local Inhibition

To gain mechanistic insight into this phenomenon in vivo, we drew clues from previous work in acute brain slices, which provided evidence that interneuron activity governs the speed of ictal progression (Chagnac-Amitai and Connors, 1989; Trevelyan et al., 2007). To this end, we added a second part to the experiments involving local Ptx injection in awake mice. First, we injected Ptx (Ptx-1) and carried out imaging and LFP recordings as described. Then, after repeated seizure spread into our FOV under the usual condition, we pressure injected Ptx (Ptx-2) analogously to a typical OGB-1 injection (picrospritzer, ~10 psi for 10 min) (Ayzenshtat et al., 2016; Miller et al., 2014), at the same location where the first injection took place (Figure 6C). Post Ptx-2 injection, we were still able to image exactly the same FOV in the propagation area that was used post Ptx-1, without any distortion of the imaged plane (Figure 6D).

When we resumed imaging and LFP recordings post Ptx-2, we found profoundly different local population dynamics in response to IISs and during seizures (Figure 6E). Prior to Ptx-2, IISs did not coincide with optical population responses in the FOV, and optical seizure break-in happened slowly (Figures 5C, 6A, right, 6E, left, and 6G). Post Ptx-2, we started to see reliable calcium responses to IISs and rapid seizure invasion (Figures 6E, right, 6F, and 6H), suggesting that Ptx had diffused to the imaged territory. In fact, prior to complete drug diffusion across our FOV, it was possible to identify a demarcation line between tissue that had already been affected by the drug and tissue where inhibition was still intact (Figure S4D). While cells being located proximally to the said demarcation line rapidly responded to IISs, brief and prolonged ictal events, distally located cells were recruited only to prolonged seizures, in a delayed fashion and at much lower speed (Figure S4D). Importantly, the trajectory of seizure propagation across the FOV remained similar to the condition prior to Ptx-2 (compare Figures S4A, bottom and S4D).

To quantify differences in interictal and ictal network recruitment dynamics related to Ptx-1 or Ptx-2 across animals, we compared population calcium responses to electrographic IISs (recorded at the initiation site), the time delay between electrographic seizure onset and optical seizure break-in, and the local population recruitment. Indeed, post Ptx-1, IISs were never followed by a change in local population calcium, while after Ptx-2, IISs consistently evoked a response (Figure 6I; calcium response rate per IIS [Ptx-1 versus Ptx-2]: n = 4 exp., 1,327 versus 893 IISs, 0% versus 100% invasion rate, p = 0). With respect to spreading seizures, the imaged population was recruited slowly and with great temporal variability post Ptx-1, while both ictal recruitment duration and duration SD decreased strongly post Ptx-2 (Figures 6J and 6K; [Ptx-1 versus Ptx-2]: n = 4 exp., mean recruitment duration 5.696 ± 1.915 versus 0.375 ± 0.052 s, p = 0.0286; mean recruitment duration SD 1.69 ± 0.625 versus 0.068 ± 0.024 s, p = 0.0286). Similar results were obtained for the time delay between the electrographic seizure onset and optical seizure break-in (Figure 6L; [Ptx-1 versus Ptx-2]: n = 4 exp., mean delay 5.7 ± 0.538 versus 0.116 ± 0.038 s, p = 0.002; mean delay SD 1.78 ± 0.62 versus 0.055 ± 0.012 s, p = 0.0286). In conjunction with our cellular recruitment analyses, these experiments revealed that elasticity and speed of microscale seizure progression critically depends on the activity of local inhibitory interneurons.

DISCUSSION

Stereotypical Propagation of Epileptic Seizures in Cortical Microcircuits

Partly due to a lack of studies with appropriate temporal and spatial resolution, an ongoing debate has remained as to whether or not the recruitment of microscale networks to ictal activity happens in a stereotypical or random fashion. To address this question, we combined LFP recordings with fast resonant two-photon calcium imaging in mouse models of locally induced acute seizures, finding robust stereotypical and reliable recruitment. Our findings hold true across anesthesia and wakefulness, two different seizure models (4-AP or Ptx), and cortical areas. Most experiments in this study involved imaging of somatosensory cortex (LII/III) after local 4-AP or Ptx injection at 1.5–3 mm posterior to the FOV. However, we also performed experiments where we imaged in visual cortex with the injection site being located anterior, with consistent results (Figure S5). This suggests that, at the least in the setting of acute seizures, our results (1) reflect basic patterns of ictal spread, (2) are independent of the experimental model of focal onset seizures, and (3) apply across cortical areas.

Our experiments support previous work on the existence of ictal network stereotypy (Schevon et al., 2012; Truccolo et al., 2011), yet they show that local network reliability is not exact. This is consistent with previous studies that show that, under normal conditions, cortical microcircuits generate repeated patterns of multicellular activity that are, however, never exact (Cossart et al., 2003; Ikegaya et al., 2004; Miller et al., 2014). In addition, by use of multilayer imaging, we show that cellular recruitment reliability to spreading seizures is not restricted to LII/III but holds true across cortical depth. Our results do not support reports of fully non-repeated ictal recruitment patterns (Bower et al., 2012), and they further suggest that the observation of unpredictable spatiotemporal recruitment of local cell assemblies to seemingly stereotypical interictal spikes in the LFP

(J) Superposition of all optical invasions during electrographic seizures (n = 4 exp.; post Ptx-1: 21 seizures, individual events in light blue, mean in dark blue; post Ptx-2: 17 seizures, individual events in light red, mean in dark red), centered around the 50% recruitment frame of the population (cell number in percentage for comparability across experiments). Note how the slow, s-curved population recruitment curve upon Ptx-1 changes into a near step-like function post Ptx-2.
(K) Quantitative comparison of absolute population recruitment duration and duration SD of the Ptx-1 (blue) versus Ptx-2 (red) condition (n = 4 exp., Ptx-1/Ptx-2: 21/17 seizures): mean recruitment duration (5.696 ± 1.915 versus 0.375 ± 0.052 s; Mann-Whitney test, p = 0.0286) and mean recruitment duration SD (1.69 ± 0.625 versus 0.068 ± 0.024 s, p = 0.0286).
(L) Quantitative comparison of absolute time delay and delay SD of optical invasion after electrographic seizure onset of the Ptx-1 (blue) versus Ptx-2 (red) condition (n = 4 exp., Ptx-1/Ptx-2: 21/17 seizures): mean delay (5.7 ± 0.538 versus 0.116 ± 0.038 s; Mann-Whitney test, p = 0.002) and mean delay SD (1.78 ± 0.62 versus 0.055 ± 0.012 s, p = 0.0286).

(Feldt Muldoon et al., 2013; Muldoon et al., 2015) may not apply to the local recruitment dynamics during cortical seizure spread. In line with previous cellular resolution imaging studies in slices during interictal and ictal conditions (Badea et al., 2001; Feldt Muldoon et al., 2013; Trevelyan et al., 2006) and reports employing wide-field imaging (Ma et al., 2013; Rossi et al., 2016), we show that ictal recruitment of local networks occurs in a spatially ordered manner.

Interlaminar Stereotypical Propagation of Epileptic Seizures

There is evidence that deep cortical layers are crucially involved in focal ictogenesis, where they precede the recruitment of superficial neurons to ictal activity (Connors, 1984; Polack et al., 2007; Rheims et al., 2008; Telfeian and Connors, 1998; Trevelyan et al., 2006; but see also Tsau et al., 1999). However, the layer-specific neural dynamics during lateral seizure spread have not been extensively studied (Adams et al., 2015; Borbély et al., 2006; Telfeian and Connors, 1998; Tsau et al., 1999), and exclusively in vitro. Our results show an initial recruitment of superficial layers during lateral spread of ictal activity, which seems in contrast to a previous study in brain slices where deep layers were observed to lead lateral seizure spread when inhibition was moderately reduced (Telfeian and Connors, 1998). Under such conditions, seizure propagation was dependent on intact tissue bridges within LIV to LVI, and it was most effectively blocked when LVb was inactivated by local GABA administration. However, the same study showed that, under high doses of Ptx, lateral seizure propagation was possible in each layer separately.

Considering the experimental restrictions of both our study and Telfeian and Connor's report, several factors could account for the seemingly discrepant results. First, there is the inherently impaired neural connectivity in acute brain slices, which could have influenced the previously reported findings. Even though prism insertion in our experiments is expected to have affected cortical connectivity in the vicinity of the imaged FOV as well, it did so to a lesser extent, leaving most of the anatomical and functional cortical and subcortical connections intact. Second, bath application of disinhibitory drugs to brain slices leads to a global impairment of inhibition, which is unlikely to take place similarly in the intact brain. While our data point away from LV and favor LII/III as the lead layer during lateral ictal spread, it remains possible that this spread could in fact be led by LIV. This layer was consistently nearly devoid of labeled cells in our study (this has been observed in other studies as well, and cannot only be explained by injection depth; Andermann et al., 2013; Chia and Levene, 2009a). In this case, LIV neurons could suppress LV and activate superficial layers, which subsequently signal to LV (Thomson and Bannister, 2003), a scenario convergent with known connectivity motifs in mouse somatosensory cortex (Pluta et al., 2015). Our findings bear potential implications for neurosurgical intervention in epilepsy, as they indicate (e.g., regarding sub-pial resections) that the disconnection of LII/III alone could be sufficient to stop lateral seizure spread.

Clinical Relevance

This study concentrated on basic aspects of seizure spread into cortical areas that surround an acutely established epileptic focus. We capitalized on aspects that are shared between our approach and medical conditions such as brain trauma, which often present with acute seizures without the process of epileptogenesis (Beleza, 2012). Our results also carry potential implications for chronic epilepsies with focal onset seizures. There, territories outside the epileptic focus remain functionally intact, and thus they resemble the local networks imaged in this study. Instead of focusing on a specific disease pathway, we rather considered seizures as a phenomenon shared by many neurological disorders and even the healthy brain (Jirsa et al., 2014). Further, the approach of local injection of 4-AP or Ptx represents widely established models of partial onset seizures eliciting electrographic phenomena and behavioral symptoms that resemble those in naturally occurring epilepsy (Avoli et al., 2002; Szente and Pongrácz, 1979) and have contributed successfully to therapeutic research (Gajda et al., 2005; Rothman, 2009). The total amount of injected 4-AP or Ptx was small (7.5 or 5 nmol, respectively). The fact that we did not see enhanced firing in the imaged region prior to seizure break-in, neither post 4-AP nor Ptx (Ptx-1), and that particularly after local Ptx injection no change in local calcium activity was observed in response to IISs in the LFP, over the entire experiment, underscores that we imaged within the propagation area and make it unlikely that the imaged area was directly exposed to 4-AP or Ptx. Only after prolonged pressure injection of Ptx (Ptx-2) did we see a change in local calcium dynamics toward typical network activity manifestations induced by Ptx, which suggested that the drug had finally diffused to the imaged FOV.

We did not image the dynamics of precisely defined neural sub-populations during seizures. There is evidence, including the data presented here, that the local interaction of excitatory and inhibitory circuits is crucial for successful or failed ictal progression (Cammarota et al., 2013; Hunt et al., 2013; Khoshkhoo et al., 2017; Sessolo et al., 2015; Trevelyan et al., 2006; Ziburkus et al., 2006). While several recent studies have shown promising results with respect to cell sub-population-based therapeutic seizure intervention (Krook-Magnuson et al., 2013; Ledri et al., 2014), others have raised concerns about the potential seizure-promoting effects of such therapies (Avoli and de Curtis, 2011; Fujiwara-Tsukamoto et al., 2010; Gnatkovsky et al., 2008; Grasse et al., 2013; Sessolo et al., 2015). This controversy highlights that our knowledge of the basic dynamics of densely packed local ictal networks and the neural sub-types therein has remained unsatisfying. Future studies applying fast high-density recordings of neural networks and sub-populations during seizures will be important in substantiating our understanding of epileptic networks and identifying novel therapeutic targets for more efficient seizure control.

Elastic Cortical Seizure Propagation and Its Potential Relevance for Cortical Function

Finally, despite a repeated relative spatiotemporal structure of seizure progression, we found variable absolute temporal recruitment of local cell populations within and across experiments. This elastic progression, which could stretch in time over seconds, could be interpreted in light of Hebb's phase sequences (Hebb, 1949) or sequential activation of local cell assemblies and other intrinsic network dynamics (Harris, 2005)

that shape temporal activity patterns of neural cell populations (Carrillo-Reid et al., 2015; Cossart et al., 2003; Harris, 2005; Ikegaya et al., 2004; Luczak et al., 2013; MacLean et al., 2005; Schölvinck et al., 2015; Skaggs et al., 1996). Based on this model, an expanding seizure could constitute the extreme version of a phase sequence whose temporal properties are governed by *local* internal dynamics, such as the level of sustained synaptic input or efficacy of inhibition, and *global* internal dynamics, like state of arousal or global network synchrony. Testable factors likely affecting these dynamics with respect to seizures could, for example, involve the distance from the seizure initiation site, age or gender of the studied subject, different oscillatory brain states (Ewell et al., 2015), or differentially evoked firing patterns of distinct interneuronal sub-populations (Adesnik et al., 2012). Indeed, there is evidence, for example, that velocity of ictal expansion depends on the activity of inhibitory interneurons (Prince and Wilder, 1967; Trevelyan et al., 2007). We substantiate this evidence in vivo by showing that local compromising of GABAergic signaling results in the abolishment of ictal micro-progression elasticity and a speed-up of local seizure spread. However, the preexistent anatomical framework of specifically interconnected neurons restrains the possibilities of spatial seizure progression within the network.

Altogether, our finding of substantial temporal variability in combination with considerable relative spatiotemporal reliability of dense local networks during successive seizures suggests a network model of epilepsy resembling an elastic meshwork, wherein ictal progression may vary in time but cannot betray preexistent neural connectivity. Our results also carry potential implications for physiological cortical processing, and they are in agreement with previous studies investigating sequential ensemble activation (Ikegaya et al., 2004; Luczak et al., 2013; MacLean et al., 2005; Malvache et al., 2016; Schölvinck et al., 2015; Skaggs et al., 1996). Far from clock-driven machines, such as digital computers, it is fascinating to speculate how cortical circuits could function by activating specific dynamical trajectories that could be engaged elastically at different timescales. This flexible temporal environment could enable sensory stimuli to be integrated even if they have temporal variability, make possible for different areas of the cortex to interact in a flexible manner, and perhaps also influence an individual's decision-making depending on the differential temporal convergence of sensory information.

EXPERIMENTAL PROCEDURES

Further details and an outline of resources used in this work can be found in the Supplemental Experimental Procedures. All experiments were conducted with care and in accordance with the Columbia University institutional animal care guidelines. Experiments were carried out on C57BL/6 adult mice at post-natal age of 1–3 months. LFP measurements and concomitant in vivo two-photon calcium imaging were performed 1 hr after cortical Oregon Bapta Green-1 AM injection, 4–5 weeks after lentiviral transfer of GCaMP6s, or in transgenic Thy1-GCaMP6f animals. For experiments involving multilayer imaging, a small glass microprism was implanted into the cortex. A part of the craniotomy remained uncovered in front of the prism face to allow access for the LFP and 4-AP micropipettes. Seizure induction was achieved through local injection of small amounts of either 4-AP or Ptx into LV. The distance between the seizure initiation site and the imaged area ranged from 1.5 to 3 mm. Cell regions of interest (ROIs) were identified in a semi-automated fashion followed by manual confirmation. To identify the ictal recruitment time point of individual cells, we used the first discrete derivative (slope) of the ΔF/F traces following electrographic seizure onset. For assessment of individual cell recruitment reliability, a time bin or relative recruitment score (rr score) classification was used and compared to a shuffled surrogate. All data were analyzed using custom-written code in MATLAB. Error bars on bar plots and shaded areas in graph plots indicate SEM. Reliability indices of cells or tiles were compared using one-way ANOVA. Spatiotemporal clustering was assessed by bivariate ANOVA of mean distance differences. In multilayer-imaging experiments, spatial tile onset order distributions were compared to an even distribution (16 proximal/16 distal and 16 superficial/16 deep) with a 2 × 2 chi-square test. With respect to optical seizure invasion rate, cellular recruitment durations, duration SD, LFP to calcium delays, and delay SD, two experimental groups (Ptx-1 versus Ptx-2; Figures 6I, 6K, and 6L) were compared across experiments by Mann-Whitney test.

SUPPLEMENTAL INFORMATION

Supplemental Information includes Supplemental Experimental Procedures, five figures, and six movies and can be found with this article online at http://dx.doi.org/10.1016/j.celrep.2017.05.090.

AUTHOR CONTRIBUTIONS

M.W. and R.Y. conceived of the project. M.W. performed all experiments and wrote the paper. M.W. and J.P.H. analyzed the data. All authors planned experiments, discussed results, and edited the paper.

ACKNOWLEDGMENTS

We thank Dr. Yeonsook Shin and Alexa Semonche for viral injections and to members of the Yuste, Schwartz, and Schevon laboratories for comments. This work was supported by the Deutsche Forschungsgemeinschaft (DFG, grant WE 5517/1-1), NEI (DP1EY024503 and R01EY011787), NIMH (R01MH101218 and R01MH100561), and DARPA SIMPLEX N66001-15-C-4032. This material is based on work supported by, or in part by, the U.S. Army Research Laboratory and the U.S. Army Research Office under contract number W911NF-12-1-0594 (MURI).

Received: July 27, 2016
Revised: May 15, 2017
Accepted: May 28, 2017
Published: June 27, 2017

REFERENCES

Adams, C., Adams, N.E., Traub, R.D., and Whittington, M.A. (2015). Electrographic waveform structure predicts laminar focus location in a model of temporal lobe seizures in vitro. PLoS ONE *10*, e0121676.

Adesnik, H., Bruns, W., Taniguchi, H., Huang, Z.J., and Scanziani, M. (2012). A neural circuit for spatial summation in visual cortex. Nature *490*, 226–231.

Andermann, M.L., Gilfoy, N.B., Goldey, G.J., Sachdev, R.N., Wölfel, M., McCormick, D.A., Reid, R.C., and Levene, M.J. (2013). Chronic cellular imaging of entire cortical columns in awake mice using microprisms. Neuron *80*, 900–913.

Avoli, M., and de Curtis, M. (2011). GABAergic synchronization in the limbic system and its role in the generation of epileptiform activity. Prog. Neurobiol. *95*, 104–132.

Avoli, M., D'Antuono, M., Louvel, J., Köhling, R., Biagini, G., Pumain, R., D'Arcangelo, G., and Tancredi, V. (2002). Network and pharmacological mechanisms leading to epileptiform synchronization in the limbic system in vitro. Prog. Neurobiol. *68*, 167–207.

Ayzenshtat, I., Karnani, M.M., Jackson, J., and Yuste, R. (2016). Cortical Control of Spatial Resolution by VIP+ Interneurons. J. Neurosci. *36*, 11498–11509.

Badea, T., Goldberg, J., Mao, B., and Yuste, R. (2001). Calcium imaging of epileptiform events with single-cell resolution. J. Neurobiol. *48*, 215–227.

Baird-Daniel, E., Daniel, A.G., Wenzel, M., Li, D., Liou, J.Y., Laffont, P., Zhao, M., Yuste, R., Ma, H., and Schwartz, T.H. (2017). Glial Calcium Waves are Triggered by Seizure Activity and Not Essential for Initiating Ictal Onset or Neurovascular Coupling. Cereb. Cortex *27*, 3318–3330.

Baraban, S.C., and Löscher, W. (2014). What new modeling approaches will help us identify promising drug treatments? Adv. Exp. Med. Biol. *813*, 283–294.

Beleza, P. (2012). Acute symptomatic seizures: a clinically oriented review. Neurologist *18*, 109–119.

Borbély, S., Halasy, K., Somogyvári, Z., Détári, L., and Világi, I. (2006). Laminar analysis of initiation and spread of epileptiform discharges in three in vitro models. Brain Res. Bull. *69*, 161–167.

Bower, M.R., Stead, M., Meyer, F.B., Marsh, W.R., and Worrell, G.A. (2012). Spatiotemporal neuronal correlates of seizure generation in focal epilepsy. Epilepsia *53*, 807–816.

Cammarota, M., Losi, G., Chiavegato, A., Zonta, M., and Carmignoto, G. (2013). Fast spiking interneuron control of seizure propagation in a cortical slice model of focal epilepsy. J. Physiol. *591*, 807–822.

Carrillo-Reid, L., Miller, J.-E.K., Hamm, J.P., Jackson, J., and Yuste, R. (2015). Endogenous sequential cortical activity evoked by visual stimuli. J. Neurosci. *35*, 8813–8828.

Chagnac-Amitai, Y., and Connors, B.W. (1989). Horizontal spread of synchronized activity in neocortex and its control by GABA-mediated inhibition. J. Neurophysiol. *61*, 747–758.

Chen, T.W., Wardill, T.J., Sun, Y., Pulver, S.R., Renninger, S.L., Baohan, A., Schreiter, E.R., Kerr, R.A., Orger, M.B., Jayaraman, V., et al. (2013). Ultrasensitive fluorescent proteins for imaging neuronal activity. Nature *499*, 295–300.

Chia, T.H., and Levene, M.J. (2009a). In vivo imaging of deep cortical layers using a microprism. J. Vis. Exp. (*30*), 1509.

Chia, T.H., and Levene, M.J. (2009b). Microprisms for in vivo multilayer cortical imaging. J. Neurophysiol. *102*, 1310–1314.

Connors, B.W. (1984). Initiation of synchronized neuronal bursting in neocortex. Nature *310*, 685–687.

Cossart, R., Aronov, D., and Yuste, R. (2003). Attractor dynamics of network UP states in the neocortex. Nature *423*, 283–288.

Cymerblit-Sabba, A., and Schiller, Y. (2012). Development of hypersynchrony in the cortical network during chemoconvulsant-induced epileptic seizures in vivo. J. Neurophysiol. *107*, 1718–1730.

Ewell, L.A., Liang, L., Armstrong, C., Soltész, I., Leutgeb, S., and Leutgeb, J.K. (2015). Brain State Is a Major Factor in Preseizure Hippocampal Network Activity and Influences Success of Seizure Intervention. J. Neurosci. *35*, 15635–15648.

Feldt Muldoon, S., Soltesz, I., and Cossart, R. (2013). Spatially clustered neuronal assemblies comprise the microstructure of synchrony in chronically epileptic networks. Proc. Natl. Acad. Sci. USA *110*, 3567–3572.

Fujiwara-Tsukamoto, Y., Isomura, Y., Imanishi, M., Ninomiya, T., Tsukada, M., Yanagawa, Y., Fukai, T., and Takada, M. (2010). Prototypic seizure activity driven by mature hippocampal fast-spiking interneurons. J. Neurosci. *30*, 13679–13689.

Gajda, Z., Szupera, Z., Blazsó, G., and Szente, M. (2005). Quinine, a blocker of neuronal cx36 channels, suppresses seizure activity in rat neocortex in vivo. Epilepsia *46*, 1581–1591.

Gnatkovsky, V., Librizzi, L., Trombin, F., and de Curtis, M. (2008). Fast activity at seizure onset is mediated by inhibitory circuits in the entorhinal cortex in vitro. Ann. Neurol. *64*, 674–686.

Grasse, D.W., Karunakaran, S., and Moxon, K.A. (2013). Neuronal synchrony and the transition to spontaneous seizures. Exp. Neurol. *248*, 72–84.

Harris, K.D. (2005). Neural signatures of cell assembly organization. Nat. Rev. Neurosci. *6*, 399–407.

Hebb, D.O. (1949). The Organization of Behavior (New York: Wiley).

Hunt, R.F., Girskis, K.M., Rubenstein, J.L., Alvarez-Buylla, A., and Baraban, S.C. (2013). GABA progenitors grafted into the adult epileptic brain control seizures and abnormal behavior. Nat. Neurosci. *16*, 692–697.

Ikegaya, Y., Aaron, G., Cossart, R., Aronov, D., Lampl, I., Ferster, D., and Yuste, R. (2004). Synfire chains and cortical songs: temporal modules of cortical activity. Science *304*, 559–564.

Jasper, H.H. (1969). Mechanisms of propagation: extracellular studies. In Basic mechanisms of the epilepsies, H.H. Jasper, A.A. Ward, and A. Pope, eds. (New York: Little, Brown).

Jirsa, V.K., Stacey, W.C., Quilichini, P.P., Ivanov, A.I., and Bernard, C. (2014). On the nature of seizure dynamics. Brain *137*, 2210–2230.

Keller, C.J., Truccolo, W., Gale, J.T., Eskandar, E., Thesen, T., Carlson, C., Devinsky, O., Kuzniecky, R., Doyle, W.K., Madsen, J.R., et al. (2010). Heterogeneous neuronal firing patterns during interictal epileptiform discharges in the human cortex. Brain *133*, 1668–1681.

Khoshkhoo, S., Vogt, D., and Sohal, V.S. (2017). Dynamic, Cell-Type-Specific Roles for GABAergic Interneurons in a Mouse Model of Optogenetically Inducible Seizures. Neuron *93*, 291–298.

Krishek, B.J., Moss, S.J., and Smart, T.G. (1996). A functional comparison of the antagonists bicuculline and picrotoxin at recombinant GABAA receptors. Neuropharmacology *35*, 1289–1298.

Krook-Magnuson, E., and Soltesz, I. (2015). Beyond the hammer and the scalpel: selective circuit control for the epilepsies. Nat. Neurosci. *18*, 331–338.

Krook-Magnuson, E., Armstrong, C., Oijala, M., and Soltesz, I. (2013). On-demand optogenetic control of spontaneous seizures in temporal lobe epilepsy. Nat. Commun. *4*, 1376.

Ledri, M., Madsen, M.G., Nikitidou, L., Kirik, D., and Kokaia, M. (2014). Global optogenetic activation of inhibitory interneurons during epileptiform activity. J. Neurosci. *34*, 3364–3377.

Lillis, K.P., Wang, Z., Mail, M., Zhao, G.Q., Berdichevsky, Y., Bacskai, B., and Staley, K.J. (2015). Evolution of Network Synchronization during Early Epileptogenesis Parallels Synaptic Circuit Alterations. J. Neurosci. *35*, 9920–9934.

Luczak, A., Bartho, P., and Harris, K.D. (2013). Gating of sensory input by spontaneous cortical activity. J. Neurosci. *33*, 1684–1695.

Ma, H., Zhao, M., and Schwartz, T.H. (2013). Dynamic neurovascular coupling and uncoupling during ictal onset, propagation, and termination revealed by simultaneous in vivo optical imaging of neural activity and local blood volume. Cereb. Cortex *23*, 885–899.

MacLean, J.N., Watson, B.O., Aaron, G.B., and Yuste, R. (2005). Internal dynamics determine the cortical response to thalamic stimulation. Neuron *48*, 811–823.

Malvache, A., Reichinnek, S., Villette, V., Haimerl, C., and Cossart, R. (2016). Awake hippocampal reactivations project onto orthogonal neuronal assemblies. Science *353*, 1280–1283.

Martinet, L.E., Ahmed, O.J., Lepage, K.Q., Cash, S.S., and Kramer, M.A. (2015). Slow Spatial Recruitment of Neocortex during Secondarily Generalized Seizures and Its Relation to Surgical Outcome. J. Neurosci. *35*, 9477–9490.

Miller, J.E., Ayzenshtat, I., Carrillo-Reid, L., and Yuste, R. (2014). Visual stimuli recruit intrinsically generated cortical ensembles. Proc. Natl. Acad. Sci. USA *111*, E4053–E4061.

Morales-Villagrán, A., and Tapia, R. (1996). Preferential stimulation of glutamate release by 4-aminopyridine in rat striatum in vivo. Neurochem. Int. *28*, 35–40.

Muldoon, S.F., Villette, V., Tressard, T., Malvache, A., Reichinnek, S., Bartolomei, F., and Cossart, R. (2015). GABAergic inhibition shapes interictal dynamics in awake epileptic mice. Brain *138*, 2875–2890.

Neubauer, F.B., Sederberg, A., and MacLean, J.N. (2014). Local changes in neocortical circuit dynamics coincide with the spread of seizures to thalamus in a model of epilepsy. Front. Neural Circuits *8*, 101.

Pluta, S., Naka, A., Veit, J., Telian, G., Yao, L., Hakim, R., Taylor, D., and Adesnik, H. (2015). A direct translaminar inhibitory circuit tunes cortical output. Nat. Neurosci. *18*, 1631–1640.

Polack, P.O., Guillemain, I., Hu, E., Deransart, C., Depaulis, A., and Charpier, S. (2007). Deep layer somatosensory cortical neurons initiate spike-and-wave discharges in a genetic model of absence seizures. J. Neurosci. *27*, 6590–6599.

Prince, D.A., and Wilder, B.J. (1967). Control mechanisms in cortical epileptogenic foci. "Surround" inhibition. Arch. Neurol. *16*, 194–202.

Rheims, S., Represa, A., Ben-Ari, Y., and Zilberter, Y. (2008). Layer-specific generation and propagation of seizures in slices of developing neocortex: role of excitatory GABAergic synapses. J. Neurophysiol. *100*, 620–628.

Rossi, L.F., Wykes, R.C., Kullman, D., and Carandini, M. (2016). Cortical seizure propagation respects functional connectivity underlying sensory processing. bioRxiv. http://dx.doi.org/10.1101/080598.

Rothman, S.M. (2009). The therapeutic potential of focal cooling for neocortical epilepsy. Neurotherapeutics *6*, 251–257.

Schevon, C.A., Weiss, S.A., McKhann, G., Jr., Goodman, R.R., Yuste, R., Emerson, R.G., and Trevelyan, A.J. (2012). Evidence of an inhibitory restraint of seizure activity in humans. Nat. Commun. *3*, 1060.

Schölvinck, M.L., Saleem, A.B., Benucci, A., Harris, K.D., and Carandini, M. (2015). Cortical state determines global variability and correlations in visual cortex. J. Neurosci. *35*, 170–178.

Sessolo, M., Marcon, I., Bovetti, S., Losi, G., Cammarota, M., Ratto, G.M., Fellin, T., and Carmignoto, G. (2015). Parvalbumin-Positive Inhibitory Interneurons Oppose Propagation But Favor Generation of Focal Epileptiform Activity. J. Neurosci. *35*, 9544–9557.

Skaggs, W.E., McNaughton, B.L., Wilson, M.A., and Barnes, C.A. (1996). Theta phase precession in hippocampal neuronal populations and the compression of temporal sequences. Hippocampus *6*, 149–172.

Stosiek, C., Garaschuk, O., Holthoff, K., and Konnerth, A. (2003). In vivo two-photon calcium imaging of neuronal networks. Proc. Natl. Acad. Sci. USA *100*, 7319–7324.

Szabo, G.G., Schneider, C.J., and Soltesz, I. (2015). Resolution revolution: epilepsy dynamics at the microscale. Curr. Opin. Neurobiol. *31*, 239–243.

Szente, M., and Pongrácz, F. (1979). Aminopyridine-induced seizure activity. Electroencephalogr. Clin. Neurophysiol. *46*, 605–608.

Tashiro, A., Goldberg, J., and Yuste, R. (2002). Calcium oscillations in neocortical astrocytes under epileptiform conditions. J. Neurobiol. *50*, 45–55.

Telfeian, A.E., and Connors, B.W. (1998). Layer-specific pathways for the horizontal propagation of epileptiform discharges in neocortex. Epilepsia *39*, 700–708.

Thomson, A.M., and Bannister, A.P. (2003). Interlaminar connections in the neocortex. Cereb. Cortex *13*, 5–14.

Trevelyan, A.J., Sussillo, D., Watson, B.O., and Yuste, R. (2006). Modular propagation of epileptiform activity: evidence for an inhibitory veto in neocortex. J. Neurosci. *26*, 12447–12455.

Trevelyan, A.J., Sussillo, D., and Yuste, R. (2007). Feedforward inhibition contributes to the control of epileptiform propagation speed. J. Neurosci. *27*, 3383–3387.

Truccolo, W., Donoghue, J.A., Hochberg, L.R., Eskandar, E.N., Madsen, J.R., Anderson, W.S., Brown, E.N., Halgren, E., and Cash, S.S. (2011). Single-neuron dynamics in human focal epilepsy. Nat. Neurosci. *14*, 635–641.

Truccolo, W., Ahmed, O.J., Harrison, M.T., Eskandar, E.N., Cosgrove, G.R., Madsen, J.R., Blum, A.S., Potter, N.S., Hochberg, L.R., and Cash, S.S. (2014). Neuronal ensemble synchrony during human focal seizures. J. Neurosci. *34*, 9927–9944.

Tsau, Y., Guan, L., and Wu, J.Y. (1999). Epileptiform activity can be initiated in various neocortical layers: an optical imaging study. J. Neurophysiol. *82*, 1965–1973.

Wong, B.Y., and Prince, D.A. (1990). The lateral spread of ictal discharges in neocortical brain slices. Epilepsy Res. *7*, 29–39.

Yuste, R., and Denk, W. (1995). Dendritic spines as basic functional units of neuronal integration. Nature *375*, 682–684.

Yuste, R., and Katz, L.C. (1991). Control of postsynaptic Ca2+ influx in developing neocortex by excitatory and inhibitory neurotransmitters. Neuron *6*, 333–344.

Ziburkus, J., Cressman, J.R., Barreto, E., and Schiff, S.J. (2006). Interneuron and pyramidal cell interplay during in vitro seizure-like events. J. Neurophysiol. *95*, 3948–3954.

Acute Focal Seizures Start As Local Synchronizations of Neuronal Ensembles

Die soeben zusammengefasste Studie beinhaltete die räumlich hochauflösende Analyse der zeitlich räumlichen iktualen Rekrutierung extrafokal (außerhalb des epileptischen Anfallsfokus) lokalisierter neuronaler Populationen während der Anfallspropagation. Die nun folgende Studie (Wenzel et al., 2019a) nahm sich zum Ziel, intrafokale (Anfallsursprungszone) und extrafokale neuronale Populationsdynamiken während der Anfallsentstehung und -ausbreitung zu untersuchen und miteinander in Beziehung zu setzen. Darüber hinaus erfolgte erstmals in diesem Kontext die simultane Untersuchung erregender (Pyramidalzellen; „PYR“) und spezifischer hemmender Neuronen (Parvalbumin positive Interneurone; „PVs“) mittels *in vivo* Zweifarben-2-P-Mikroskopie in eigens gezüchteten, transgenen GCaMP6::PV-Cre::LSL-td-Tomato Mäusen (Hintergrund: C57BL/6). Dieser Ansatz wurde verfolgt, da die lokale Interaktion erregender und hemmender Neuronenklassen in der Anfallsentstehung und -ausbreitung wahrscheinlich eine Schlüsselrolle spielt (Paz und Huguenard, 2015; Trevelyan und Schevon, 2013).

Im somatosensorischen Kortex (ca. 150 μm subpial) wurden, wie bereits im vorherigen Abschnitt beschrieben, durch Lokalinjektion von 4-AP (Lamina V [ca. 480 μm subpial], Vol. 500 nl; Menge insges.: 7,3 nmol]) chemoconvulsiv (CC) fokale epileptische Anfälle ausgelöst (mikroskopiertes Sichtfeld [=FOV] ca. 400 x 400 μm), wobei neben LFP Messungen zellulär auflösende neuronale Ca^{2+} Netzwerkaktivität (GCaMP6, Laser-Exzitation mit 940 nm) in Lamina II/III nun entweder über der Injektionsstelle aufgenommen wurde („intrafokal“, n = 3 Exp., insges. 439 PYR, 20 PVs), oder in der bereits beschriebenen Distanz zur Injektionsstelle (ca. 1,5 - 2 mm, („extrafokal“, n = 4 Exp., insges. 620 PYR, 59 PVs) (Abb. 1 A-E). Durchgeführt wurden die Versuche mittels verschiedener mikrochirurgisch etablierter kranialer Fenster in Kombination mit zusätzlich eingebrachten Glasmikropipetten (30° Einführwinkel: 1x LFP, 1x CC Injektion) in leicht anästhesierten, ausgewachsenen Mäusen (Abb. 1 A).

Die individuell programmierte Datenanalyse (MATLAB®, MathWorks) beinhaltete nach Extraktion somatischer Ca^{2+} Transienten von Einzelneuronen ($\Delta F/F$) aus den rohen Bildserien (30 Hz Bildwiederholungsrate, 512 x 512 Pixel) die Bestimmung individueller neuronaler Rekrutierungszeitpunkte zu wiederkehrenden elektrographischen Anfällen.

Dies erfolgte durch Berechnung des Maximalwertes der 1. Ableitung individueller Ca^{2+} Transienten von individuellen Neuronen im FOV (Abb. 1 E). Die Analyse eines möglichen zeitlich räumlichen Clustering neuronaler Rekrutierung erfolgte durch bivariate ANOVA Analyse mittlerer Distanzen räumlicher neuronaler Koordinaten (Abb. 2 G). In der Analyse neuronaler Subklassenaktivität erfolgte die Identifikation von PVs durch das zusätzliche Auslesen des PV-spezifischen, rotverschobenen (Laser-Exzitation mit 990 nm), strukturellen td-Tomato Fluoreszenz-signals (Abb. 4 A, D und 5 A, D). Zur Darstellung und Analyse multizellulärer Netzwerkdynamiken in einem niedrig-dimensionalen Raum wurde eine Prinzipalkomponentenanalyse (PCA) des Ca^{2+} Populationssignals verschiedener experimenteller Zeitabschnitte (Baseline, präiktual und früh-iktual) durchgeführt und die Anzahl der Komponenten, die für >90% der Varianz des Ca^{2+} Populationssignals verantwortlich zeichneten, für die jeweiligen Abschnitte quantifiziert (Abb. 3 A-E).

Ein Hauptergebnis der Studie stellte dar, dass intrafokale und extrafokale iktuale Rekrutierung lokaler Neuronenverbände unterschiedliche zeitlich räumliche Dynamiken aufweisen. Während extrafokale Neuronenverbände durch eine kontinuierliche, s-kurven-förmige iktuale Invasion rekrutiert wurden, geschah dies im intrafokalen Kompartiment in einer sprunghaften, stufenartigen Weise (Abb. 2 A-D). Darüber hinaus unterschieden sich die absolut gemessenen iktualen Rekrutierungszeiträume intrafokaler und extrafokaler Neuronenverbände und die Varianz dieser Zeiträume über wiederkehrende Anfälle hinweg jeweils signifikant (Abb. 2 E-F), im Sinne einer intrafokal im Gegensatz zu extrafokal nochmals stark gesteigerten „Elastizität“ neuronaler Rekrutierung. Nichtsdestotrotz konnten im intrafokalen wie extrafokalen Kompartiment Cluster zeitlich räumlicher iktualer Rekrutierung festgestellt werden (Abb. 2 G-H). Interessanterweise wiesen intra- und extrafokale präiktuale (40-Sekundenintervall vor dem elektrographischen Anfallsbeginn) Netzwerkdynamiken eine ausgeprägte Dimensionalitätsreduktion auf (Abb. 3 E), wobei dies mit einer frühen und eskalierenden intrafokalen Überaktivität bei gleichzeitiger Suppression extrafokaler Umgebungsnetzwerkaktivität einherging (Abb. 3 A, B). Korrelierend mit dieser Dimensionalitätsreduktion wurde präiktual extrafokal eine im Vergleich zur PYR Subklasse erhöhte PV Aktivität nachgewiesen (Abb. 4 B-C), wohingegen im selben Zeitintervall intrafokal PYR dominierten (Abb. 5 B-C). Wir

werteten dies auf dem Fundament vorheriger Studien als sukzessiven Zusammenbruch PV-vermittelter Hemmung und eskalierend synchroner PYR Aktivität im intrafokalen Kompartiment bei gleichzeitig PV-vermittelter extrafokaler Umgebungshemmung von PYR (Jayant und Wenzel et al., 2019; Liou, Ma und Wenzel et al., 2018; Prince und Wilder, 1967; Schevon et al., 2012; Trevelyan et al., 2006). Erstaunlicherweise wiesen lokale PV-Rekrutierungsmuster ein heterogenes zeitlich räumliches Muster auf, mit teils völlig verschiedenen zeitlichen Rekrutierungen selbst direkt benachbarter PVs (Abstand < 50 μm) (Abb. 4 D-F, 5 D). Dies weist auf komplexe Schaltkreismotive innerhalb identifizierter interneuronaler Subklassen während der Anfallsmikroprogression hin, z.B. durch teils gegenseitig hemmende Interaktionen unter PVs (Karnani et al., 2016). Die Wichtigkeit der räumlichen Auflösung von *in vivo* 2P-Mikroskopie für die hier zusammengefasste Studie wird dadurch unterstrichen, dass die soeben aufgeführten Dynamiken lokaler Neuronenverbände sich in einem räumlich teils derart begrenzten Raum abspielten (z.B. < 100 x 100 μm), dass diese von lokalen LFP Messungen mittels Glasmikroelektroden (2 - 5 MΩ) selbst in der Nähe von wenigen hundert μm nicht detektiert wurden. So wiesen intrafokale, lokale, optisch gemessene neuronale Populationdynamiken bereits eindeutige iktuale Merkmale auf (pathologisch erhöhte Aktivität und Synchronität, räumliche und zeitliche Evolution), obwohl feldelektrographisch noch kein Anfall detektiert worden war (Abb. 2 C). Durch die hohe räumliche Auflösung und Aufzeichnungsdichte erlaubten die Ergebnisse dieser Studie daher erstmals eine empirische Rekonstruktion der fokalen Anfallsevolution, vom intrafokalen Ursprung bis zur extrafokalen Propagation (Abb. 6).

Neurobiology of Disease

Acute Focal Seizures Start As Local Synchronizations of Neuronal Ensembles

Michael Wenzel, Jordan P. Hamm, Darcy S. Peterka, and Rafael Yuste
Neurotechnology Center, Department of Biological Sciences, Columbia University, New York, New York 10027

Understanding seizure formation and spread remains a critical goal of epilepsy research. We used fast *in vivo* two-photon calcium imaging in male mouse neocortex to reconstruct, with single-cell resolution, the dynamics of acute (4-aminopyridine) focal cortical seizures as they originate within a spatially confined seizure initiation site (intrafocal region), and subsequently propagate into neighboring cortical areas (extrafocal region). We find that seizures originate as local neuronal ensembles within the initiation site. This abnormal hyperactivity engages increasingly larger areas in a saltatory fashion until it breaks into neighboring cortex, where it proceeds smoothly and is then detected electrophysiologically (LFP). Interestingly, PV inhibitory interneurons have spatially heterogeneous activity in intrafocal and extrafocal territories, ruling out a simple role of inhibition in seizure formation and spread. We propose a two-step model for the progression of focal seizures, where neuronal ensembles activate first, generating a microseizure, followed by widespread neural activation in a traveling wave through neighboring cortex during macroseizures.

Key words: **calcium imaging; epilepsy; interneurons; microseizures; seizures; two-photon**

Significance Statement

We have used calcium imaging in mouse sensory cortex *in vivo* to reconstruct the onset of focal seizures elicited by local injection of the chemoconvulsant 4-aminopyridine. We demonstrate at cellular resolution that acute focal seizures originate as increasingly synchronized local neuronal ensembles. Because of its spatial confinement, this process may at first be undetectable even by nearby LFP electrodes. Further, we establish spatial footprints of local neural subtype activity that correspond to consecutive steps of seizure microprogression. Such footprints could facilitate determining the recording location (e.g., inside/outside an epileptogenic focus) in high-resolution studies, even in the absence of a priori knowledge about where exactly a seizure started.

Introduction

Understanding the properties of seizure-producing cortical circuits ("epileptic networks") may enable more efficient seizure control. Although cortical circuits are complex in terms of cell types and connectivity, little is known about the neural subpopulation dynamics within epileptic networks *in vivo* (Muldoon et al., 2015; Neumann et al., 2017), especially in relation to the seizure initiation site and surrounding brain tissue. However, how exactly seizures progress from microscale to macroscale in the intact brain may hold critical new clues on how to stop their expansion.

Seizures often emerge at locally confined epileptic foci, from where they can secondarily spread across the brain. But, due to technical limitations, our knowledge about the precise dynamics of local brain networks in and outside such foci is still scarce. Recent technology advances have enabled more fine-scaled studies of these dynamics leading for example to the identification of "microseizures" (Goldensohn, 1975; Schevon et al., 2008; Worrell et al., 2008; Stead et al., 2010). Microseizures display field-electrographic features similar to seizures detected in the EEG, yet are clinically silent and territorially too confined to be detectable by conventional macroelectrodes (Stead et al., 2010). Thus, a deeper understanding of seizure emergence and spread at a neural circuit level requires techniques with high spatiotemporal resolution. Although multielectrode arrays have pushed our understanding of fine-scale epileptic network dynamics, most common configurations (96 electrodes, 4 × 4 mm) do not allow measurements of complete neural circuits. In fact, such arrays usually record from several dozen (at best up to ~180) neurons from patches of cortex or hippocampus (Truccolo et al., 2011;

Received Dec. 17, 2018; revised July 27, 2019; accepted Aug. 9, 2019.

Author contributions: M.W. and R.Y. designed research; M.W. performed research; M.W., J.P.H., and D.S.P. analyzed data; M.W., J.P.H., D.S.P., and R.Y. edited the paper; M.W. wrote the paper.

This work was supported by the Deutsche Forschungsgemeinschaft (DFG, Grant WE 5517/1-1), NEI (DP1EY024503, R01EY011787), NIMH (R01MH101218, R01MH100561, R01MH115900), and DARPA SIMPLEX N66001-15-C-4032. This material is based upon work supported by, or in part by, the U.S. Army Research Laboratory and the U.S. Army Research Office under contract number W911NF-12-1-0594 (MURI). We thank Yeonsook Shin, Alexa Semonche, Reka Recinos, Mari Bando, and Azadeh Hamzei for viral injections and members of the Yuste laboratory for useful comments.

M. Wenzel's present address: Department of Epileptology, University of Bonn, 53127 Bonn, Germany.
Correspondence should be addressed to Michael Wenzel at michaelwenzel2946@gmail.com.

https://doi.org/10.1523/JNEUROSCI.3176-18.2019

Neumann et al., 2017), which, however, contain hundreds of thousands of neurons. Due to this, and the usually spatially poor identification of seizure initiation sites before electrode implantation in patients or animals, it has remained unclear how seizures emerge and transition from focal epileptic discharges to secondarily generalized seizures. As an alternative to electrophysiology, calcium imaging can monitor action potential activity with single cell resolution (Yuste and Katz, 1991; Smetters et al., 1999), so it seems as an ideal method to map seizures and epileptic spread, cell by cell, at the anatomical microscale (Badea et al., 2001). However, calcium imaging studies of epileptic activity have traditionally suffered from a temporal resolution too low to investigate sizable population dynamics during seizures (Badea et al., 2001; Tashiro et al., 2002; Trevelyan et al., 2007; Cammarota et al., 2013; Feldt Muldoon et al., 2013; Neubauer et al., 2014; Lillis et al., 2015; Muldoon et al., 2015). To improve the temporal resolution of calcium imaging, we recently introduced a fast (30 Hz) resonant scanning method to study cortical seizure propagation *in vivo* (Wenzel et al., 2017). In that initial study, general local network recruitment patterns to spreading acute seizures were investigated at a distance ("propagation area") to a spatially confined seizure initiation site. We found that in the propagation area, seizure spread occurs in a continuous fashion, through stereotypical circuits, and that this spread is elastic in time and regulated by the activity of GABAergic interneurons.

Here, we turn our attention to the initiation site ('intrafocal') of cortical seizures, and compare the findings to recruitment patterns within the propagation area ("surround cortex" or "extrafocal"). To compare seizure progression at the anatomical microscale ('microprogression') in both these compartments, we use fast (30 Hz) two-photon calcium imaging of GCaMP6-labeled neuronal populations of mouse somatosensory cortex and LFP recordings in the 4-aminopyridine (4-AP) mouse model of acute focal onset seizures *in vivo*. The approach combines high temporal and single cell resolution to unveil the local population activity underlying seizures with unequivocal anatomical precision. With a precisely defined focal seizure onset zone by local cortical 4-AP injection (Nagappan et al., 2018, see also methods), we image cortical circuits within the seizure initiation site as well as the propagation area that is invaded only during seizures detected by nearby microelectrodes. Further, we perform subpopulation calcium imaging of td-Tomato labeled PV interneurons within those territories during seizure emergence and spread, and find spatially heterogeneous PV recruitment. Our data represent a complete reconstruction of seizure progression from their microepileptic origins, and have potential implications for the early detection of pending seizures through the establishment of local footprints of neuronal subpopulation activity patterns throughout seizure evolution.

Materials and Methods

Experiments. All experiments were performed with care and in compliance with the Columbia University institutional animal care guidelines. Experiments were performed on either male C57BL/6 wild-type mice (Jackson Laboratories; RRID:IMSR_JAX:000064) or male PV-Cre::LSL-tdTomato mice (Jackson Laboratories; PV-Cre mice: RRID:IMSR_JAX:017320; LSL-tdTomato mice: RRID:IMSR_JAX:007908) at a postnatal age of 1–3 months. Animals were never used for previous or subsequent experiments. Food and water was provided *ad libitum*. Mice were housed at a 12 h light/dark cycle. Calcium transients and LFP signals from three GCaMP6s monolabeled animals, in which general, extrafocal seizure progression was compared with intrafocal dynamics in this paper, were also used in our previous study that exclusively investigated seizure progression in extrafocal territories ("propagation area") (Wenzel et al., 2017). All intrafocal imaging experiments and double-labeled animals for subpopulation imaging were exclusively used for the study presented here.

Specification of terms related to epileptic activity used in this study. This paper contains numerous different terms referring to epileptic activity. We would like to specify here how particular terms were used:

"Ictal activity": the Latin term "ictus" refers to a sudden attack, and is used for epileptic seizures in clinical epileptology. We used the adjective "ictal" exclusively in the context of seizure activity. The term 'interictal' refers to epileptic activity in between seizures. We made use of the term "pre-ictal" (as part of the interictal period) with reference to the time period immediately preceding the electrographic seizure onset in the LFP.

"Epileptic activity": The term "epilepsy" comprises both interictal and ictal activity. The adjective "epileptic" was used here as an umbrella term for both pre-ictal and ictal neural activity. For escalatory aberrant intrafocal calcium activity patterns during pending LFP seizure onset at the nearby microelectrode, we used the term 'epileptic' activity, as in our dual (calcium imaging, LFP) recordings the delineation between pre-ictal and ictal activity became less clear. We used the term "micro-epileptic" to emphasize the spatial dimension of our calcium imaging at the anatomical scale of dozens to hundreds of micrometers.

"Microseizures": Microseizures display field-electrographic features similar to seizures detected in the EEG, yet are clinically silent and territorially too confined to be detectable by conventional macroelectrodes, or even nearby microelectrodes (e.g., at 1 mm distance; Stead et al., 2010). Macroseizures represent seizures that can be detected by microelectrodes and macroelectrodes across wider portions of the brain.

Virus injections and surgical procedures. Before actual experiments, animals were injected with AAV1-Syn-GCaMP6s-WPRE-SV40 (purchased from the University of Pennsylvania Vector Core). Mice were anesthetized with isoflurane (initial dose 2–3% partial pressure in air, then reduction to 1–1.5%). A small cranial aperture was established above left somatosensory cortex (coordinates from bregma: x 2.5 mm, y −0.24 mm, z −0.2 mm) using a dental drill. A glass capillary pulled to a sharp micropipette was stereotactically lowered into cortical layer 2/3. An 800 nl solution of 1:1 diluted AAV1-Syn-GCaMP6s (Chen et al., 2013) was slowly injected over 5 min at a depth of 200 μm from the pial surface using a microinjector (World Precision Instruments). Four to 5 weeks after virus injection, on the day of the experiment, mice were anesthetized with isoflurane (initial dose 2–3% partial pressure in air, then reduction to 1.0%). A small flap of skin above the skull was removed and a titanium head plate with a central foramen (7 × 7 mm) was attached to the skull with dental cement above the left hemisphere (Fig. 1*A*). Then, a small craniotomy similar to previous descriptions (Miller et al., 2014) was carried out. Specifically, posterior to the virus injection site, the skull was circularly thinned using a dental drill until a small piece (~2 mm in diameter) of skull could be removed effortlessly with fine forceps.

Two-photon calcium imaging. Activity of cortical neurons was recorded by imaging changes of fluorescence with a two-photon microscope (Bruker Instruments) and a Ti:Sapphire laser (Chameleon Ultra II; Coherent) at 940 nm through a 25× objective (water-immersion, numerical aperture 1.05, Olympus). Resonant galvanometer scanning and image acquisition (frame rate 30 fps, 512 × 512 pixels, 100–170 μm beneath the pial surface) were controlled by Prairie View Imaging software. Multiple datasets were acquired consecutively over the course of an experiment (90,000–150,000 frames in total, with several momentary breaks interspersed for reasons of practicality). During the entire experiment, the head-restrained animals were kept under light isoflurane anesthesia (0.8–1% partial pressure in air) via a nose piece while body temperature was maintained with a warming pad (37.5°C).

Ictal model and electrophysiology. The local 4-AP model of acute cortical seizures was used in this study, as it allowed the precise localization of the seizure initiation site and propagation area. We primarily defined the seizure initiation site as the location of 4-AP injection (15 mM, 500 nl, layer 4 or 5, total amount delivered = 7.5nmol), and the propagation area as an area at 1.5–2 mm distance, which is primarily unaffected by 4-AP (Nagappan et al., 2018), but invaded during secondary lateral seizure spread as described previously (Wenzel et al., 2017). In the context

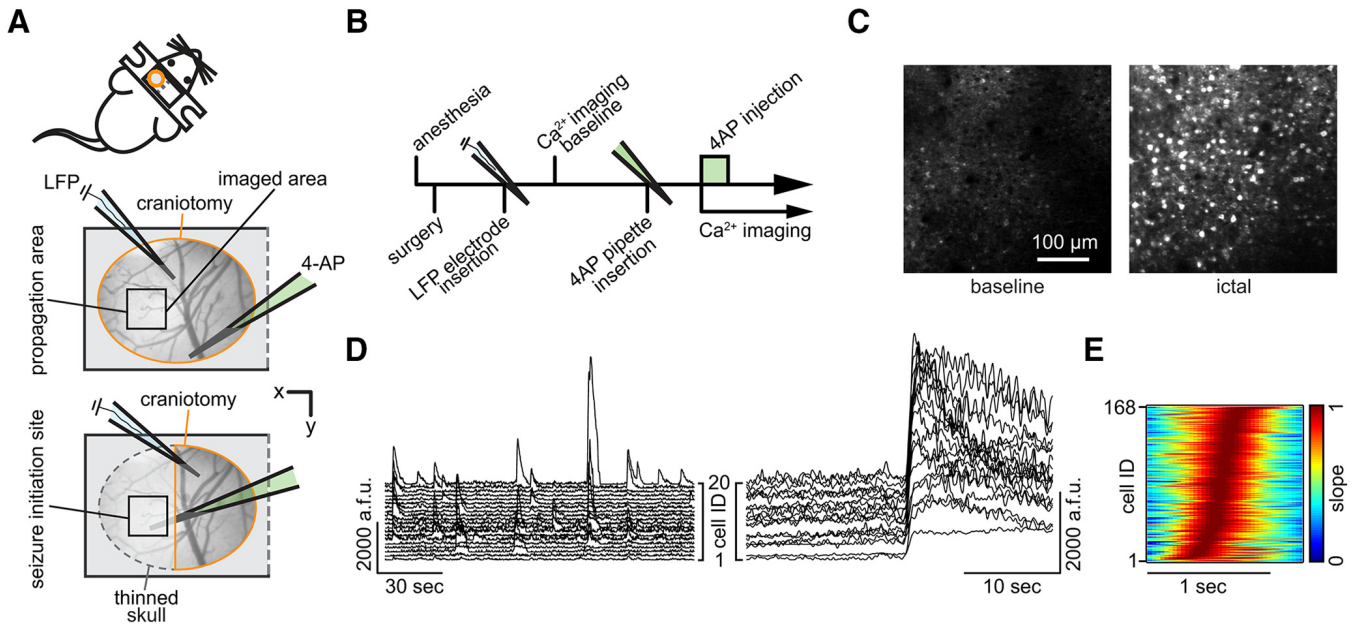

Figure 1. Imaging in the seizure initiation site and propagation area. ***A***, Experimental setup. Two surgical approaches over left somatosensory cortex; craniotomy encircled in orange, thinned skull in dotted gray, black squares indicate imaged FOV; each experiment (exp.) involved the insertion of two glass micropipettes, one (blue) containing a silver chloride silver for LFP recording, the other (green) containing 4-AP (15 mM, injection vol. 500 nl, total amount delivered = 7.5nmol). ***B***, Experimental workflow. ***C***, Propagation area, representative 3 s average (avg) fluorescence images of neural activity (GCaMP6s) during baseline and ictal break-in. ***D***, Calcium (Ca^{2+}) transients of 20 representative cells during baseline conditions (left) and during ictal invasion of the propagation area (right). a.f.u., Arbitrary fluorescent units. ***E***, Propagation area, representative example of the arriving ictal wavefront. Normalized first derivative of each registered neuron's fluorescent trace during electrographic seizure onset is shown. Cell recruitment to ictal activity ordered in time by maximum slope. Note the s-curved shape of cell recruitment highlighting sufficient temporal imaging resolution for individual cellular recruitment.

of the 4-AP model used here, it is further noteworthy that seizure occurrence in chronic animal models of epilepsy is usually low (Arida et al., 1999; Ewell et al., 2015; Muldoon et al., 2015). It would require either multiple fortunate or prohibitively long imaging sessions of infrequently occurring spontaneous seizures to capture a sufficient number of seizures, along with reasons concerned with potential tissue photo-damage, fluophore bleaching and hardware limitations. For LFP recordings, a sharp glass micropipette (2–5 MΩ) filled with saline and containing a silver chloride wire was carefully advanced into the cortex (30° angle) under visual control to a depth of ~100 μm beneath the pial surface. The pipette tip was positioned close by the imaged area (Fig. 1*A*). A reference electrode was positioned over the contralateral prefrontal cortex. In the context of this paper, the term "electrographic" specifically refers to LFP signals recorded by sharp glass micro-electrodes as described above. LFP signals were amplified using a Multiclamp 700B amplifier (Molecular Devices), low-pass filtered (300 Hz, Multiclamp 700B commander software, Molecular Devices), digitized at 1 kHz (Bruker Instruments) and recorded using Prairie View Voltage Recording Software alongside with calcium imaging. For induction of seizures, another sharp glass micropipette containing 4-AP (15 mM, 0.5 μl) was slowly lowered (30° angle) into the cortex to a depth of 420–480 μm. The pipette tip was positioned at a distance of ~1.5–2 mm caudally to the imaged area. Correct positioning of the pipette tip was ensured by a diagonal dry-run within saline above the cortex preceding actual insertion. 4-AP was injected over the course of 10–15 min by use of a Micro4 Micro Syringe Pump Controller (World Precision Instruments). Electrographic seizure onset time points were determined mathematically by mean and SD of LFP recordings. The first time point exceeding > 5 SD from the interictal LFP mean power was defined as the electrographic seizure onset and confirmed by visual inspection. We did not determine seizure onsets based on calcium imaging, but analyzed neural calcium transients with reference to the electrographic seizure onset in the LFP, as field electrophysiology represents the most widely accepted method to detect the temporal onset of seizures.

Focality of the local cortical 4-AP model. It is difficult to prove that no 4-AP reached the imaged field of view in the propagation area ("extrafocal") throughout our experiments. However, a number of points support that this area was indeed not primarily affected by 4-AP in our setting. We locally injected small amounts of 4-AP (7.3 nmol) into deep layers, and imaged in layer 2/3 at a distance of 1.5–2 mm. We only found enhanced extrafocal pyramidal activity during secondary seizure spread. By contrast, we immediately observed increased neural firing upon 4-AP injection in the initiation site. One could argue that our observed network compartmentalization might be driven by a 4-AP concentration gradient, for example, preferentially activating extrafocal PVs leading to surround network suppression. However, Nagappan et al. (2018) recently showed in the identical seizure model that fluorescently labeled 4-AP hardly diffuses beyond 1 mm from the injection site over 2 h. At the same time, Liou et al. (2018) found enhanced PV firing even at an ~4 mm distance to ongoing focal cortical seizures. Finally, we recently showed slow seizure propagation in the disinhibitory local picrotoxin (Ptx) model (Wenzel et al., 2017), where, if the propagation area had primarily experienced Ptx, seizure progression would have been rapid, and interictal LFP spikes would have recruited local pyramidal neurons. However, such recruitment only occurred upon a second Ptx injection in the initiation site (picospritzer, 10 psi, 10 min).

Image analysis. Cell regions of interest (ROIs) were identified in a semiautomated fashion by using custom written software in MATLAB (Caltracer 3 β, available on the Yuste laboratory website at https://blogs.cuit.columbia.edu/rmy5/) followed by manual confirmation. Because of pronounced and synchronous fluorescence changes of surround neuropil during epileptic conditions, halo subtraction procedures could lead to distortions of calcium transients of individual cells. Therefore, we applied ROI shrinkage (ROI soma outline minus 1.5 pixels radially), which has been successfully used to minimize bleed-in of surround neuropil fluorescence (Hofer et al., 2011). Cells with low signal-to-noise ratio or no apparent calcium transients were excluded from further analysis. Individual cells that were lost over the course of the experiment due to at times discrete axial movement of the imaged focal plane during local 4-AP injection were also excluded from further analysis. Individual cell fluorescence was calculated as the average across all pixels within the ROI.

Cell recruitment analyses. To determine the recruitment time-point of individual cells to ictal activity, we used the first discrete derivative (slope) of the individual fluorescent traces assuming that the sharpest

change in fluorescence correlates best with maximal recruitment to seizure activity (Trevelyan et al., 2006; Wenzel et al., 2017). Population recruitment durations were calculated as the time from the first to the last recruited registered cell, excluding the 5% most deviant cells to reduce outlier-induced duration distortions. Specific time lags of PV neural recruitment compared with local network recruitment to seizure activity were calculated as previously described (Wenzel et al., 2017): First, we derived the median frame Y_{50} wherein the cumulative number of recruited cells first equaled or exceeded 50% of all registered neurons. Then, relative to this Y_{50}, each PV was assigned a temporal recruitment lag by subtracting Y_{50} from its individual recruitment frame X_N ($X_n - Y_{50}$, a negative result would indicate an early recruitment of the respective PV ahead of the median population recruitment for a given seizure event).

Spatiotemporal clustering. To identify spatio-temporo-progressive network activity motifs during seizure microprogression, we ordered cell recruitment points in time (from early to late recruitment) during each individual ictal event of an experiment and divided each dataset into four groups (1–25%, 26–50%, 51–75%, 76–100%), as previously described (Wenzel et al., 2017). Then, the mean distance of cell coordinates (x, y within imaged area) of individual quartiles were calculated to either the mean coordinate of the respective quartile, or the mean coordinate of all recorded cells, for each seizure. These distances were compared with each other. If cells' recruitment time points are similar and cells cluster spatially, their distance to the mean coordinate of their respective quartile should be significantly shorter than the mean distance to the mean coordinate of all cells that are distributed over the entire field of view (Fig. 2*G*).

PCA and state space. We sought to parsimoniously describe multicellular network dynamics in a lower rank subspace amenable to visual display and linear comparisons. Using in-house written MATLAB routines and standard functions, we calculated a principle components analysis (PCA) on cells × time points activity matrices (i.e., cells were variables) separately for baseline (preinjection) activity, the 40 s period before LFP seizure onset, and 3 s after seizure onset. We examined scree plots to quantify the proportion of variance accounted for by each component (Cattell, 1966), comparing root eigenvalues between conditions to assess an indication of dataset dimensionality. In all three cases, the scree-test suggested 2 components (although the variance of network activity at baseline was ostensibly spread across more components than preictal and postictal periods). For plotting and visualizing the nature of the multicellular propagation patterns (i.e., similarities, differences, and the periodic structure of their build up; Fig. 3*A*,*B*), we performed a VARIMAX rotation (Kaiser, 1958) to limit PCA solutions to two components (based on scree test; a 2D solution is also conveniently easier to visualize). This approach simplifies the PCA solution to include fewer components (in this case, two, which remain orthogonal) by rotating factor weights in a manner that maximizes the summed variances of the squared loadings.

Statistics. All data were analyzed using custom written code in MATLAB (The MathWorks). Error bars on bar plots and shaded areas in graph plots indicate SEM. To determine statistical significance for analyses regarding cell recruitment, Mann–Whitney tests were applied unless stated otherwise. For statistical analysis of spatio-temporal clustering, we used bivariate ANOVA analysis of mean distance differences (df = 3). High activity subtype comparison (Figs. 4, 5) was determined by χ^2 test (1 degree of freedom [df]).

Additional resources. MOCO (ImageJ plugin for motion correction) is available online on the Yuste laboratory website.

Results

This study used optical and electrical techniques to record focal seizure emergence and spread, and contains the terms "electrographic," "microseizure," "macroseizure," "micro-epileptic," "epileptic," "pre-ictal," and "ictal." To avoid confusion as to how these terms were used in the context of this work, respective definitions are provided in the methods section. The data shown here represent a total of 13 experiments. Six animals were studied for general intrafocal or extrafocal recruitment to epileptic activity (898 distinctly registered neurons), and seven animals were used for subpopulation imaging (1059 distinctly registered neurons, of which 79 were PVs). We used an *in vivo* mouse model of acute cortical seizures applying local injection of 4-AP (15 mM, 500 nl, layer 4 or 5, total amount delivered = 7.5 nmol) in lightly anesthetized mice. We performed experiments under light anesthesia to reduce the animal burden of a series of prolonged tonic-clonic seizures and given that seizures in humans do not only happen during wakefulness, but are also encountered in seizure-susceptible individuals even during deeper anesthesia on the intensive care unit or in the operation room (Howe et al., 2016; Ulkatan et al., 2017). Further, we and others have previously provided some evidence that despite differences such as seizure threshold or propagation speed, general neural recruitment patterns during cortical seizure progression share fundamental characteristics across anesthesia and wakefulness (Uva et al., 2013; Wenzel et al., 2017). The 4-AP model was chosen for several reasons (see the Materials and Methods). First, local injection of small amounts of 4-AP establishes a territorially well defined acute epileptic focus surrounded by primarily unperturbed cortex that is invaded during electrographic seizures (Wenzel et al., 2017; Nagappan et al., 2018). Although not recapitulating chronic epilepsy, the acute situation established by focal 4-AP resembles real world medical conditions such as intracerebral bleeding, local brain trauma or ischemic stroke, in which acute seizures often occur shortly after the injury (Beleza, 2012). The model also shares some similarities with chronic conditions such as epilepsy with focal onset seizures, where spatially confined epileptic discharges secondarily spread into otherwise functionally intact brain tissue (Milton et al., 2007). Moreover, unlike disinhibitory chemoconvulsants such as picrotoxin or bicuculline, 4-AP leaves inhibitory circuits intact, and elicits electrographic and behavioral phenomena that are similar to seizures in chronic epilepsy (Szente and Pongrácz, 1979; Avoli et al., 2002). Instead of addressing a specific disease pathway but rather considering epileptic seizures as a phenomenon shared by many neurological disorders and even the healthy brain, our model focused on understanding the phenomena of epileptic states (Jirsa et al., 2014).

Two-photon calcium imaging within the local seizure initiation site *in vivo*

Two experimental setups were used including either a craniotomy for imaging within the propagation area or a craniotomy combined with adjacently thinned skull for intrafocal imaging (Fig. 1*A*). In both setups, imaging was performed in layers 2/3 (L2/3, ~150 μm beneath the cortical surface) of mouse primary somatosensory cortex. The experimental workflow is depicted in Figure 1*B*. For LFP measurements, which served as the electrographic indicator of seizures within the investigated cortical territory, a sharp glass microelectrode was carefully lowered into the cortex close by the imaged area. Whenever the term "electrographic" is used throughout this paper, it refers to the recorded LFP signal. For induction of seizures, a second glass micropipette containing 4-AP (total amount delivered = 7.5 nmol) was slowly advanced to a cortical depth of ~480 μm. The tip of the 4-AP pipette was either positioned at a distance of ~1.5–2 mm caudally to the field of view (propagation area) or directly underneath the imaged area (initiation site). During baseline conditions, local populations in L2/3 displayed ongoing sparse and distributed calcium activity (Fig. 1*C*,*D*, left; Miller et al., 2014), contrasted by sustained firing of large numbers of neurons in the field of view

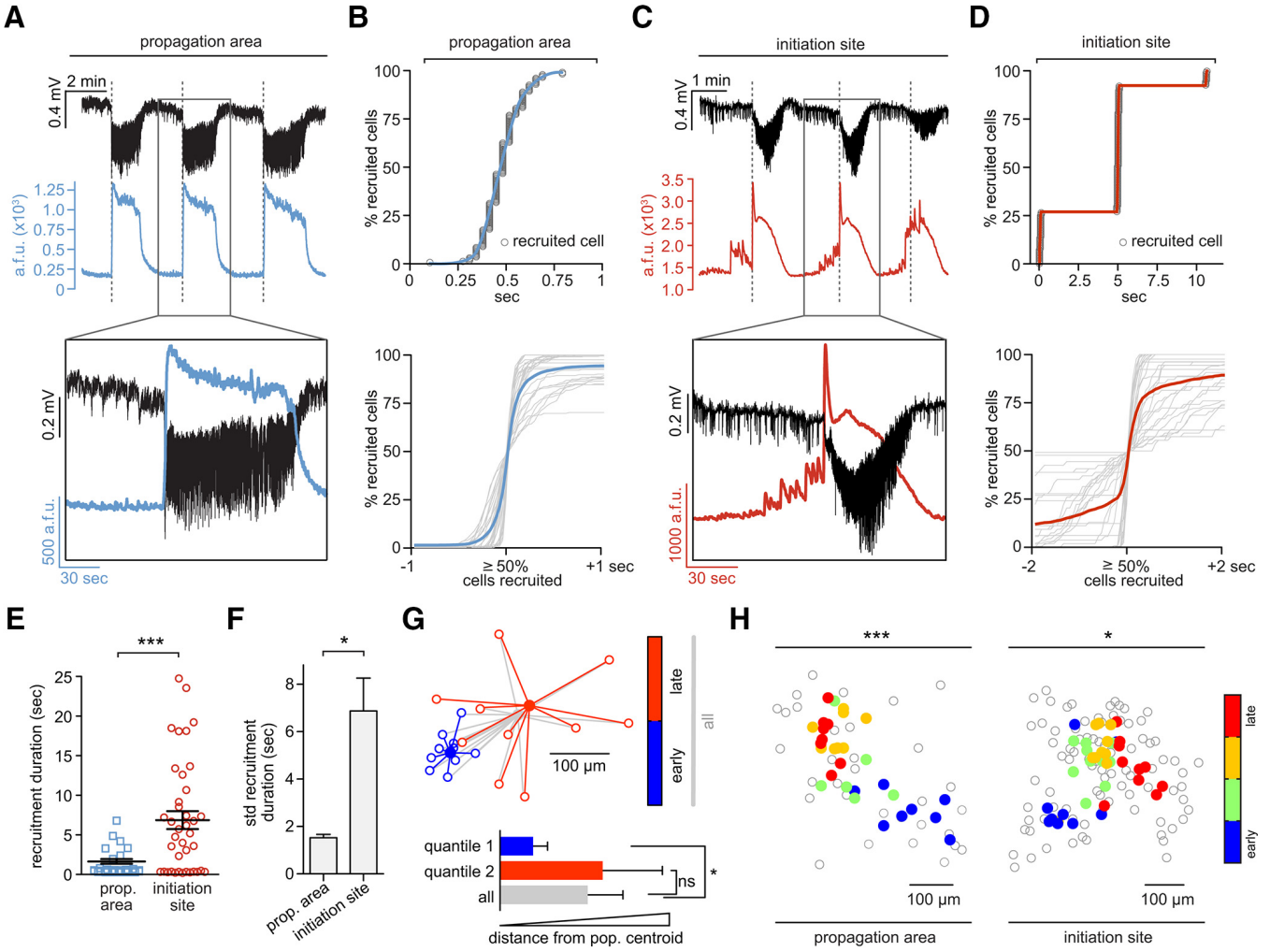

Figure 2. Differential intrafocal and extrafocal neuronal recruitment during seizure micro-progression. ***A***, Propagation area: LFP signal (black), and corresponding population avg. Ca^{2+} transient (blue) of three consecutive seizures, detailed depiction of second event (inset, see also Movie 1). Note how electrographic seizure onsets (dotted lines) correspond to the sudden rise of the population Ca^{2+} signal. a.f.u., Arbitrary fluorescent units (***B***) Propagation area. Top, Representative example of smooth, s-shaped cell recruitment during ictal break-in. Bottom, Superposition of neural recruitment curves across all analyzed ictal break-ins (gray) centered around the 50% recruitment frame; blue graph represents mean [$n = 3$ exp., total number of seizures = 31 (10.3 ± 1.5275 SEM)], cell number in percentage for comparability across exp.). ***C***, Initiation site: LFP recording (black) and corresponding avg. population Ca^{2+} transient (red) of three consecutive seizures, detailed depiction of second event (inset, see also Movie 2). Note the temporal mismatch of electrographic seizure onsets and intrafocal population Ca^{2+} events. Large pre-ictal population bursts are visible before the electrographic seizure onset (dotted line). ***D***, Top, Representative example of stepwise cell recruitment during intrafocal micro-epileptic progression. Bottom, Superposition of all analyzed intrafocal epileptic recruitment (gray) centered around the 50% cell recruitment frame; red graph represents mean (3 exp., total number of seizures = 39 [13 ± 1.55 SEM]). ***E***, Comparison of extrafocal vs intrafocal cell recruitment durations ($n = 31$ vs 39 durations; mean 1.83 ± 0.3 s vs 6.82 ± 1.1 s, Mann–Whitney test $p < 0.001$). Determination of recruitment durations was done by calculating the time period from the first to last recruited registered cell, excluding the 5% most deviant cells. ***F***, Comparison of extrafocal versus intrafocal recruitment duration variability (mean SD ± SEM, Mann–Whitney test $p < 0.05$). ***G***, Schematic depiction of bivariate cluster analysis. For practical visualization, only 2 quantiles (blue = 50% earliest, red = 50% latest recruited cells) are displayed for an individual seizure (actual exp. contained 4 quantiles). Each quantile contains 10 cells. Each outlined circle corresponds to the spatial coordinate of an individual cell, each filled circle to the respective quantile centroid (blue, first quantile; red, second quantile; gray, all; centroid, mean spatial coordinate). Note: quantiles were calculated based only on temporal onset, regardless of space. Bottom panel: Arbitrary mean distance + SD for each quantile for the single seizure shown on top (actual analysis contained all seizures of an individual experiment). Cells belonging to the early 50th percentile (blue) cluster spatially, cells belonging to the late 50 percentile (red) do not. ***H***, Left, Spatial analysis of propagation area: Spatiotemporal quartile clustering (quartiles calculated as mean coordinate of 1–25% earliest cells, 25–50%, 50–75% and 75–100%, see Materials and Methods) across 8 consecutive seizures (bivariate ANOVA $p < 0.001$, all extrafocal exp. $p < 0.05$). Right, Spatial analysis of initiation site: Spatiotemporal quartile clustering (each quartile coordinate = spatial mean of 25% recruited cells) clustering across 10 consecutive seizures (bivariate ANOVA $p = 0.0145$, all intrafocal exp. $p < 0.05$). Depiction of statistical significance for Figure 2: $^*p < 0.05$; $^{***}p < 0.001$.

during electrographic seizures post 4-AP injection (Fig. 1*C*,*D*, right). Within the propagation area, seizure invasion happened in a wave of burst neuronal firing advancing slowly (Wong and Prince, 1990; Trevelyan et al., 2007; Wenzel et al., 2017) across the field of view (see Movie 1). The temporal imaging resolution of 30 Hz was sufficient to capture individual cell recruitment to epileptic activity (Fig. 1*E*). We focused on early seizure cell recruitment and recruitment immediately preceding electrographic seizures (time window 40 s before and 10 s into individual electrographic seizures), since this window represents a critical time for potential therapeutic interventions. To systematically investigate general temporal characteristics of microprogression of epileptic activity, we analyzed the activity of all neurons in the field of view that showed visible calcium transients during epileptic activity and whose somata could be followed across the entire experiment. Individual cell recruitment time-points were derived by calculating the first discrete derivative (slope) of the fluorescent traces assuming that the steepest rise in fluorescence correlates best with maximal recruitment to epileptic activity (Badea et al., 2001; Trevelyan et al., 2006; Wenzel et al., 2017).

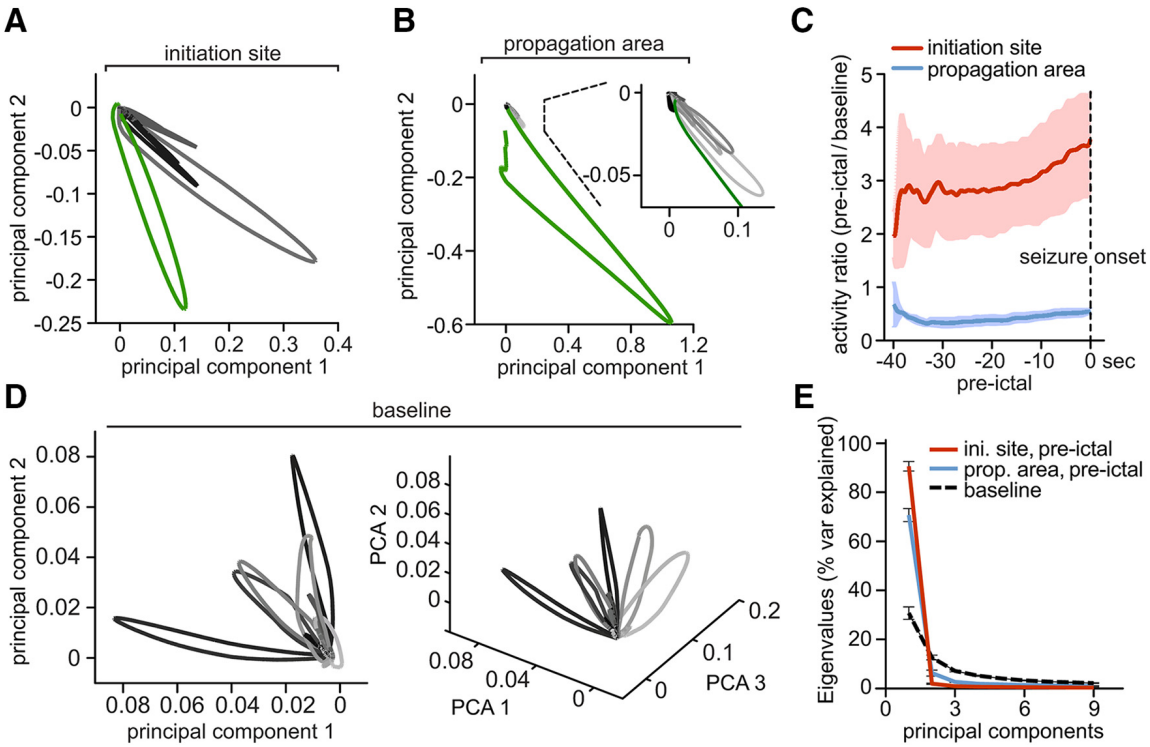

Figure 3. Pre-ictal local networks compartmentalize and decline into lower dimensional attractors. ***A***, Representative network state spaces [40 s pre-ictal state changes in grayscale (black = earliest change), electrographic seizure onset in green] within the seizure initiation site and (***B***) the propagation area, with a magnified inset. Every data point along a given trajectory corresponds to the imaged population activity at a single time point (for details on PCA component space visualization please see methods). Note two important local network features visualized in ***A*** and ***B*** at once: pre-ictal network activity dimensionality is reduced in both initiation site and propagation area; however, intrafaocal network activity shows large trajectories before electrographic seizure onset while extrafocal activity appears to be suppressed. ***C***, Cumulative frame-population-averaged positive change of fluorescence, normalized to baseline (set to 1), as indicator of general relative network activity changes over time (GCaMP6s, 3 extrafocal/3 intrafocal exp., 29/39 pre-ictal periods). Pre-ictal intrafocal vs extrafocal network activity was compared by a running *t* test ($p < 0.001$ from −34 to 0 s). ***D***, Representative network state space (2D on the left, same space in 3D on the right) with individual network events (in gray scale) over a 40 s period during baseline. In contrast to the pre-ictal condition displayed in ***A*** and ***B***, activity trajectories reach out into all plotted dimensions. ***E***, Scree plot of principial components of baseline network activity versus pre-ictal intrafocal vs extrafocal activity. Note the reduced number of principal components in both pre-ictal conditions. Displayed components accounted for >90% of the variance, respectively.

Seizure initiation and propagation areas display differential spatiotemporal dynamics

In the propagation area, electrographic seizures and calcium transients corresponded well and neurons in the propagation area were recruited in a continuous fashion (Fig. 2*A* and *B*, top) (Wenzel et al., 2017). Before ictal invasion during electrographic seizures, little to no calcium activity was visible in the propagation area. To analyze this, we superimposed the calcium activity for all experiments in the propagation area around the frame where the proportion of neurons recruited to ictal activity reached 50%. The superimposed graphs lined up consistently, describing a continuous s-shaped curve (Fig. 2*B*, bottom, $n = 3$ experiments; GCaMP6s; total number of seizures = 31; average number of seizures = 10.3 ± 1.5275; total number of analyzed cells = 576; average number of analyzed cells = 192 ± 58.9237), as previously described (Neumann et al., 2017; Wenzel et al., 2017).

The seizure initiation site, however, displayed strikingly different activity patterns (Fig. 2*C*) (Warren et al., 2010). Unlike the propagation area, we observed here locally restricted, pronounced bursts of activity, sometimes long before electrographic seizure onset (Fig. 2*C*, Movie 2). These events reflected sustained, abnormal local population activity that evolved in space and time, which are typical EEG hallmarks of seizure activity. Further, intrafocal epileptic buildup consistently occurred before electrographic seizure onset. Moreover, neurons within the seizure initiation site were recruited in a stepwise pattern (Fig. 2*D*, top). When we superimposed all imaged intrafocal neuronal activity around the 50% recruitment frame, a discontinuous pattern emerged from highly variable individual recruitment graphs (Fig. 2*D*, bottom, $n = 3$ experiments, GCaMP6s, total number of seizures = 39, average number of seizures 13 ± 1.55, total number of analyzed cells = 272, average number of analyzed cells = 91 ± 23 cells). Neuronal recruitment was temporally stretched, up to dozens of seconds ahead of the LFP seizure onset (Fig. 2*E*), and significantly surpassed the already considerable variability of neuronal activation across seizures within the surround cortex (Wenzel et al., 2017) (Fig. 2*F*).

We compared the spatiotemporal maps of successive seizures between the propagation area and the seizure initiation site and found that, despite the different types of seizure progression, a conserved spatial pattern of relative cell recruitment was evident in both compartments across seizures (Fig. 2*G*,*H*) (Trevelyan et al., 2006; Truccolo et al., 2014; Neumann et al., 2017; Wenzel et al., 2017). To quantify and compare these observed spatiotemporal patterns, we used a 2-dimensional ANOVA (Wenzel et al., 2017), categorizing cells into temporal quartiles and comparing the variance of the distance of each cell with the quartile spatial mean and with the variance of the distance to the spatial mean of all cells (Fig. 2*G*). The analysis yielded significant differences between distributions, with bivariate F-values for all experiments in the propagation area ($F = 12.67, 11.64, 41.22$; all $p < 0.001$) and in the seizure initiation site ($F = 22.15, 4.02, 3.43$; $p = 1.4 \times 10–9, 0.0145, 0.024$) (Fig. 2*H*).

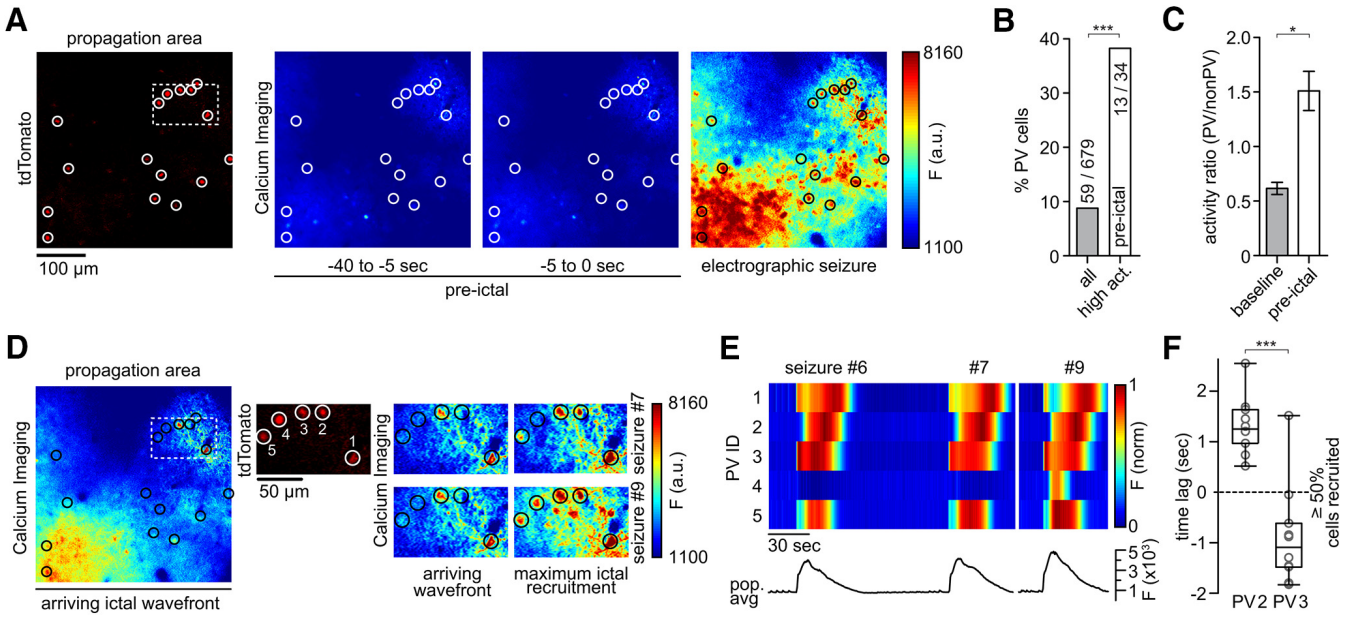

Figure 4. Ictal recruitment of PV interneurons in the propagation area. ***A***, Left to right, tdTomato-positive parvalbumin-containing interneurons (PVs, encircled), imaged at 990 nm; Ca^{2+} imaging (at 940 nm): fluorescence avg. images during pre-ictal period and ictal activity. ***B***, PV percentage among highest active neurons during pre-ictal period ($n = 4$ experiments, total number of pre-ictal periods = 30 [7.5 ± 1.85 SEM], all imaged non-PVs = 620, PVs = 59, top 5% activity cells = 34) compared with general subtype distribution (χ^2 test $p(\chi^2 > 39.381) < 0.001$). ***C***, Activity ratio of PV versus non-PV subpopulations during baseline and the 40 s period before seizure onset. Activity ratios were obtained by dividing frame-subpopulation-averaged positive change of Ca^{2+} fluorescence. During baseline (left), PVs continually display lower values than non-PVs. During the pre-ictal period (right), this relationship is inverted ($n = 4$ exp., GCaMP6s, 30 pre-ictal periods, Mann–Whitney test $p = 0.0286$). ***D***, Same exp. as in A, during ictal break-in (left); middle and right side: insert shown in ***A*** and ***D*** (dotted box). Displayed are 5 immediately neighboring PVs and their Ca^{2+} transients during ictal break-in and sustained ictal activity across 2 successive seizures (upper and lower panel, see also Movies 4 and 5). Note the diverse PV recruitment to ictal activity with PV #1 and #3 bursting ahead of the arriving ictal wavefront, PV #2 and #5 showing delayed recruitment (intraictal section), and one nonparticipant PV (#4) during the first seizure. The latter cell is clearly recruited to a successive ictal event. ***E***, Bottom, Population avg. Ca^{2+} fluorescence signal of all 124 registered cells from exp. shown in A and D across 3 seizures (#6, 7,and 9). Top, Max-normalized Ca^{2+} fluorescence for the 5 PVs highlighted in D, shown across 3 seizures. Note the differential recruitment on the order of seconds of even immediately neighboring PVs. PV #4 does only show a clear Ca^{2+} signal in the last seizure displayed (***F***) Differential relative recruitment (Time lag with respect to the 50% recruitment frame) of immediately neighboring PV #2 and #3 (intercell distance <50 μm, both cells are located far from the arriving ictal wavefront within the imaged area) across all seizures of the exp. (10 seizures, Mann–Whitney test $p < 0.001$). Boxes represent 25th to 75th percentile of cellular recruitment, bands inside boxes display median cell recruitment time points, circles represent cell recruitment time lag for individual seizures. Depiction of statistical significance for Figure 4: *$p < 0.05$; ***$p < 0.001$.

In sum, we found a saltatory expansion of abnormal neural population hyperactivity within the seizure initiation site followed by a continuous invasion of surround cortex. Within the seizure initiation site, spatially restricted bursts of population activity occur up to dozens of seconds before LFP seizure onset, with highly variable, stretched courses of neural recruitment in absolute time. In stark contrast, in the surround cortex, preseizure activity is low and neural recruitment occurs only during electrographic seizures. Despite differential types of microprogression of epileptic activity, the relative spatiotemporal activity patterns of local networks show consistency across seizures in both intrafocal and extrafocal compartments.

Preseizure subnetwork compartmentalization and critical state transitions

The differential intrafocal and extrafocal subnetwork activity before LFP seizure onset prompted us to further investigate the mechanisms underlying these population dynamics. To this end, we analyzed the neuronal correlation in the calcium imaging data by applying principal component analysis (PCA; Materials and Methods, Fig. 3*A–C*) to 40 s preseizure periods. PCA weights were calculated within an experiment across all seizures and applied in time to simplify the "state-space" of multidimensional population activity occurring before and during LFP seizure onset (Fig. 3*A*,*B*). Compared with extrafocal network activity (Fig. 3*B*, grayscale, electrographic seizure onset in green), which was sparse (Bower and Buckmaster, 2008; Schevon et al., 2012) and correspondingly did not show clear excursions in state space before LFP seizure onset, intrafocal population dynamics showed large state space trajectories (Fig. 3*A*, grayscale) corresponding to sustained abnormal hyperactivity evolving in time and space toward the electrographic seizure onset (green). Accordingly, during the 40 s before electrographic seizure onset, intrafocal average population activity was persistently higher than during baseline and escalated noticeably toward seizure onset (Fig. 3*C*, red trace). On the contrary, at the same time, extrafocal population activity in surround cortex was in fact steadily lower than during baseline conditions (Fig. 3*C*, blue trace).

However, compared with baseline conditions, where a great diversity of network states stretching out in multiple dimensions was present (Fig. 3*D*), both intrafocal and extrafocal local networks shared a significantly reduced set of discernible states during the 40 s before LFP seizure onset [Fig. 3*A*, *B* (magnified portion), *E*]. Therefore, whereas intrafocal average population activity escalated toward electrographic seizure onset and extrafocal average population activity was much reduced, the transition toward electrographic seizures involved a reduced dimensionality in population activity in both compartments (Fig. 3*E*). Such a transition suggests a decline of the network into lower dimensional attractors (or semistable, theoretically recurrent population states) which has been proposed by computational simulations and EEG analysis (Mehta et al., 1993; Lopes da Silva

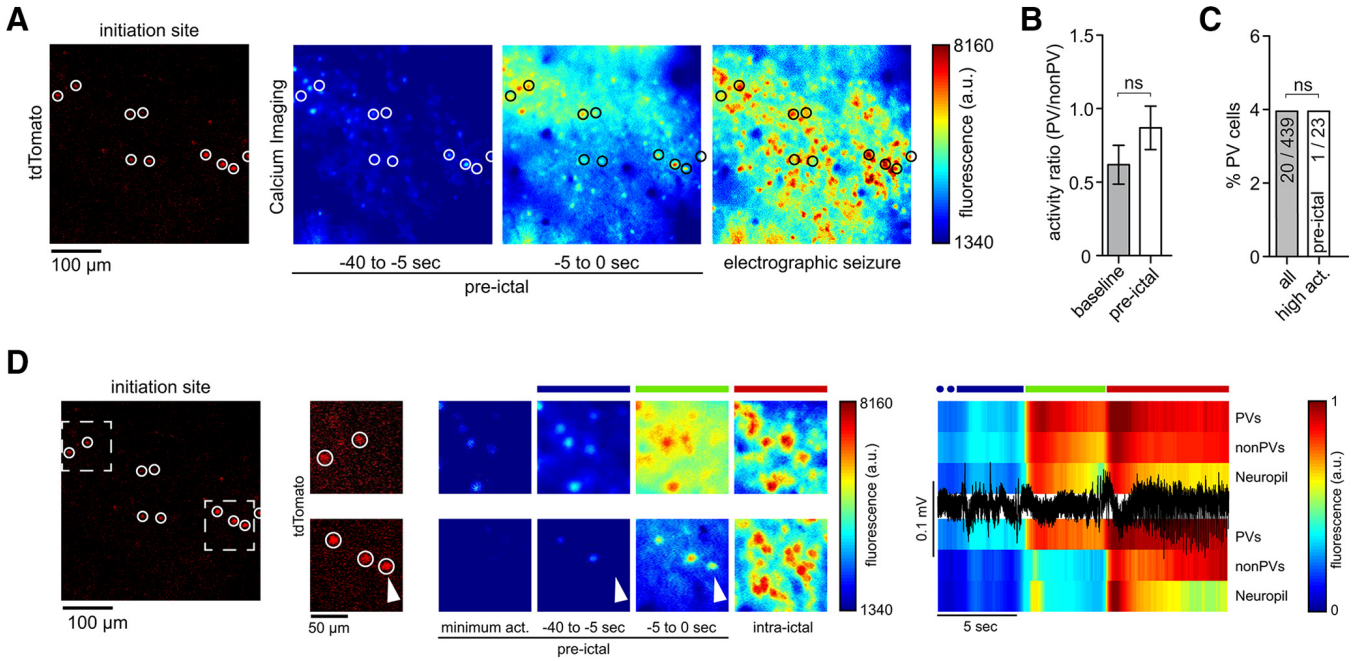

Figure 5. Ictal recruitment of PV interneurons in the seizure initiation site. ***A***, Left, tdTomato-positive parvalbumin containing interneurons (PVs, red, encircled) imaged at 990 nm; Ca^{2+} imaging (at 940 nm): fluorescence avg. images of pre-ictal and ictal neural activity. ***B***, Activity ratio of PV versus non-PV subpopulations during baseline and the 40 s period before LFP seizure onset. Activity ratios were obtained by dividing frame-subpopulation-averaged positive change of Ca^{2+} fluorescence ($n = 3$ exp., all imaged non-PVs = 439, all PVs = 20, 23 pre-ictal periods). During baseline (left), PVs continually displayed lower values than non-PVs. This relationship was preserved during the pre-ictal period (right, Mann–Whitney test $p = 0.4$). ns = not significant. ***C***, PV percentage among highest active neurons during pre-ictal period ($n = 3$ exp., 23 pre-ictal periods, top 5% activity cells = 23) compared with general subtype distribution (χ^2 test $P(\chi 2 > 0.002) = 1.0151$). ns = not significant. ***D***, Same exp. as in ***A*** with 2 magnified inserts (see also Movies 6 and 7) within distinct intrafocal subterritories. Ca^{2+} imaging during saltatory micro-epileptic progression (middle); note again the diverse recruitment of PVs to ictal activity (arrowhead). Colored bars above the Ca^{2+} avg. images correspond to the colored bars above the LFP trace (black) and population avg. Ca^{2+} traces (PVs, non-PVs and Neuropil) on the right.

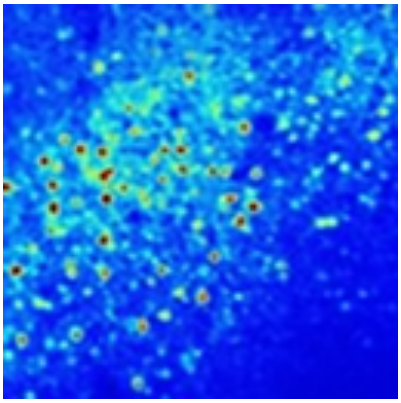

Movie 1. GCaMP6s calcium imaging of representative full ictal event within propagation area, left somatosensory cortex, layer II/III (depth ~150 μm beneath pial surface). The incoming wave corresponds to the electrographic seizure onset. Imaging wave length = 940 nm, acquisition speed = 30 frames/sec. Movie played at 2x acquisition speed.

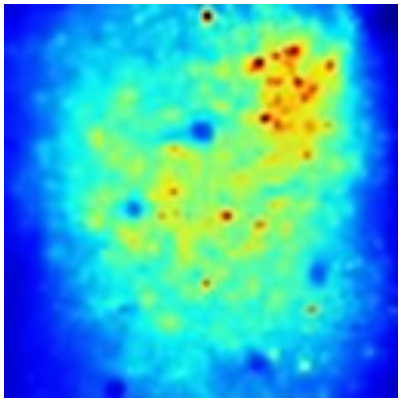

Movie 2. GCaMP6s calcium imaging of representative full ictal event within seizure initiation site, left somatosensory cortex, layer II/III (depth ~150 μm beneath pial surface). The final saltatory displayed step of microseizure expansion corresponds to the electrographic seizure onset. Note the striking difference in network recruitment duration, directionality, and continuity as compared to Movie 1. Imaging wave length = 940 nm, acquisition speed = 30 frames/sec. Movie played at 3x acquisition speed.

et al., 2003) to occur during ictal transition, but not directly documented at this spatiotemporal scale.

Together, we show that during epileptic expansion, intrafocal and extrafocal subnetworks of neurons activate differently. Although intrafocal population activity escalates toward LFP seizure onset, surround cortical subnetwork activity drops below baseline level. In both compartments, subnetwork activity declines into lower dimensional attractors during ictal transition.

Local PV interneuron populations enhance epileptic network compartmentalization

Recent *in vitro* and *in vivo* studies involving functional interference with interneuronal subtypes (especially fast-spiking PVs) have led to controversial results regarding the role of fast-spiking interneurons in seizure promotion or restraint (Avoli et al., 1993; Gnatkovsky et al., 2008; Avoli and de Curtis, 2011; Cammarota et al., 2013; Krook-Magnuson et al., 2013; Ledri et al., 2014; Shiri et al., 2015). With regard to interneuronal recruitment dynamics

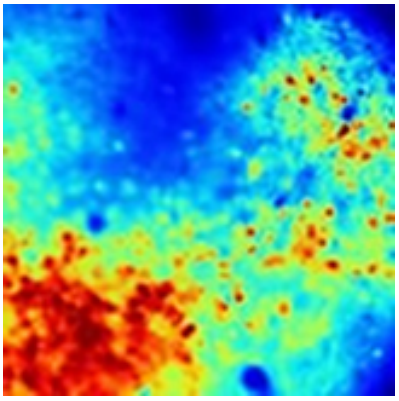

Movie 3. GCaMP6s calcium imaging of representative full ictal event within propagation area, left somatosensory cortex, layer II/III (depth ~150 μm beneath pial surface). The incoming wave corresponds to the electrographic seizure onset. Imaging wave length = 940 nm, acquisition speed = 30 frames/sec. Movie played at 3x acquisition speed.

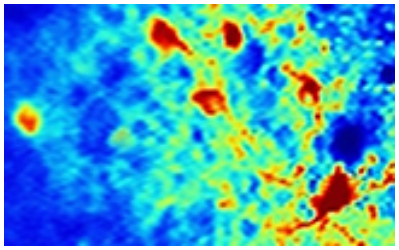

Movie 4. Magnified portion from Movie 3. GCaMP6s calcium imaging of representative full ictal event within propagation area, left somatosensory cortex, layer II/III (imaging depth ~150 μm beneath pial surface). Imaging wave length = 940 nm, acquisition speed = 30 frames/sec. Movie played at 4x acquisition speed.

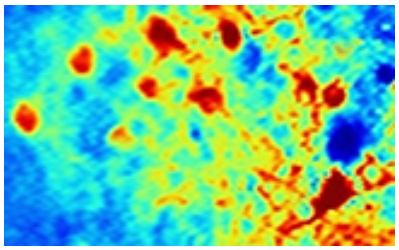

Movie 5. Magnified portion from Movie 3. GCaMP6s calcium imaging of representative successive full ictal event (in comparison to the earlier one displayed in Movie 4) within propagation area, left somatosensory cortex, layer II/III (imaging depth ~150 μm beneath pial surface). Imaging wave length = 940 nm, acquisition speed = 30 frames/sec. Movie played at 4x acquisition speed.

during epileptic activity, a recent study showed reliable recruitment of putative fast-spiking interneurons to epileptic activity (Neumann et al., 2017) echoing the finding of neural recruitment reliability at the general population level (Truccolo et al., 2011; Wenzel et al., 2017). Consistent with Muldoon et al. (2015), Neumann et al. (2017) also found that epileptic activity predominantly entrained PVs, not pyramidal cells. However, it remains unclear, whether these studies recorded inside the seizure initiation site, or surround cortex.

To understand the role of local GABAergic interneuron populations during seizure formation and spread, we studied calcium dynamics of PV interneurons in both intrafocal and extrafocal compartments by using transgenic mice that express the red fluorescent protein td-Tomato in parvalbumin containing interneurons (Madisen et al., 2010). First, we simultaneously imaged PV and non-PV calcium dynamics during seizure spread into the propagation area (extrafocal, Fig. 4*A*, Movie 3). Interestingly, PVs were consistently among the neurons displaying the strongest calcium activity during the 40 s time period leading up to an electrographic seizure (Fig. 4*B*). Population-level analyses further supported this finding. Although absolute activity (e.g., firing rates) could not be directly compared between PV cells and non-PV cells given known differences in cell calcium dynamics, bursting patterns, and baseline rates (Hofer et al., 2011), the relative ratio of PV versus non-PV population calcium transients was inverted during the 40 s period before electrographic seizures compared with baseline conditions (Fig. 4*C*), suggesting that PVs comprise a functionally distinct subpopulation in the propagation area during seizure formation (Neumann et al., 2017; Liou et al., 2018). During epileptic invasion of extrafocal territories during electrographic seizures, we encountered surprisingly eclectic PV population dynamics with several striking features. In accordance with previous reports, we identified PVs that reliably showed strong calcium transients just ahead of the arriving seizure wavefront (Fig. 4*D*, cells 1 and 3) (Kawaguchi, 2001; Timofeev et al., 2002; Trevelyan et al., 2006; Ziburkus et al., 2006; Schevon et al., 2012; Cammarota et al., 2013). At the same time however, we found at times immediately neighboring PVs displaying delayed recruitment (Cell 2 and 5 in Fig. 4*D*,*E*). Consistent with the electrophysiological data by Neumann and colleagues (Neumann et al., 2017), these sequential PV calcium dynamics were conserved across seizures (Fig. 4*E*). Surprisingly, we also identified transiently nonparticipant PVs (cell 4 in Fig. 4*D*, top; Fig. 4*E*, Movie 4). Clear recruitment to later seizures (cell 4 in Fig. 4*D*, bottom; Fig. 4*E*, Movie 5) excluded the possibility of a lack of GCaMP expression.

Finally, we went on to image subpopulation dynamics within the seizure initiation site (Fig. 5*A*). Consistent with our results in extrafocal territories, PVs showed less population average calcium activity than non-PVs at baseline (Fig. 5*B*, left). By contrast, after 4-AP injection, this relationship was not inverted in the 40 s before electrographic seizure onset (Fig. 5*B*, right). We also did not encounter an increased percentage of intrafocal PVs among the neurons displaying highest calcium activity during the final 40 s before electrographic seizure onset. This does not indicate that intrafocal PVs were less active but rather that they were surrounded by enhanced local firing of non-PV cells (Fig. 5*C*). Interestingly, similar to our results in extrafocal territories, in small intrafocal patches of cortex during epileptic expansion before LFP seizure onset, we found diverse local recruitment of PVs as well (Fig. 5*D*, arrowheads). During intrafocal epileptic microprogression, we observed stepwise failure of the inhibitory surround (Trevelyan et al., 2006; Cammarota et al., 2013) (Fig. 5*A*,*D*; Fig. 5*D*, blue bars, Movies 6 and 7).

We conclude that PVs display spatially heterogeneous recruitment patterns within epileptic networks. Before electrographic seizure onset, a hypoactive surround cortex, and even small hypoactive regions ($<100\ \mu m^2$) within the seizure initiation site, are observed together with increased local PV population activity. On an average population level, PVs increase their firing during ictal transition, consistent with previous studies (Prince and Wilder, 1967; Schwartz and Bonhoeffer, 2001; Timofeev et al., 2002; Gnatkovsky et al., 2008; Cammarota et al., 2013; Miri et al.,

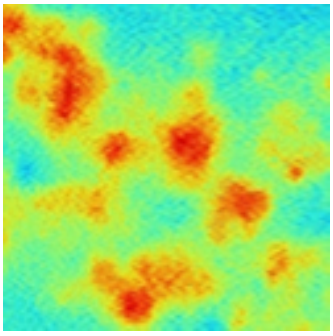

Movie 6. Magnified portion imaged field of view as displayed in Figure 5 *A* and *D* (upper left). GCaMP6s calcium imaging of step-wise microepileptic expansion within the seizure initiation site, left somatosensory cortex, layer II/III (imaging depth ~150 μm beneath pial surface). Imaging wave length = 940 nm, acquisition speed = 30 frames/sec. Movie is played 4x acquisition speed.

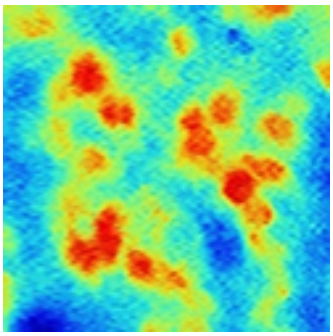

Movie 7. Magnified portion imaged field of view as displayed in Figure 5 *A* and *D* (lower right). GCaMP6s calcium imaging of step-wise microepileptic expansion within the seizure initiation site, left somatosensory cortex, layer II/III (imaging depth ~150 μm beneath pial surface). Imaging wave length = 940 nm, acquisition speed = 30 frames/second. Movie is played at 4x acquisition speed.

2018). However, at the single-cell level, we find side-by-side early and late PV recruitment in a spatially heterogeneous fashion, and even nonparticipant PVs. The temporal patterns of sequential PV activation repeat across seizures (Neumann et al., 2017).

Discussion

To better understand how seizures originate, we used an *in vivo* mouse model of acute pharmacological seizures induced by local cortical 4-AP injection (Zhao et al., 2011; Ma et al., 2013; Wenzel et al., 2017; Liou et al., 2018), a widely established model of focal onset seizures that enables the establishment of a precisely defined seizure initiation site. We used calcium imaging to study cortical circuit activity within the seizure initiation site, and in primarily unperturbed surround cortex at a distance of 1.5–2 mm during secondary seizure spread (Nagappan et al., 2018, please also see methods).

We find aberrant intrafocal activity that occurs before LFP seizure detection, which in our view corresponds to seizure initiation at the anatomical microscale (Goldensohn, 1975; Schevon et al., 2008; Worrell et al., 2008; Stead et al., 2010). Studies using multielectrode arrays (MEA) have suggested that sustained micro-epileptic activity represents the earliest step during seizure emergence (Goldensohn, 1975; Bragin et al., 2000; Schevon et al., 2008; Worrell et al., 2008; Stead et al., 2010). However, this has been difficult to definitely prove using MEAs in humans, as the most common arrays cover a cortical area of 4 × 4 mm and contain 96 electrodes spaced 400 μm apart. As a consequence, full temporal seizure evolution will likely be missed, since the seizure initiation site can be as small as 0.04 mm^3 (Schevon et al., 2008). Our intrafocal imaging with single-cell resolution supports the hypothesis that the hyperactivity of pathologically interconnected neuronal clusters (PINs) serve as a prerequisite of seizures that are then detected by field electrophysiology (Bragin et al., 2000). This spatially confined, evolving intrafocal population activity preceding the electrographic seizure onset may be described as ictal activity that is 'electrographically silent', like an electrographic seizure in the surface EEG that occurs in the absence of clinical symptoms is typically called 'clinically silent' in medical practice. Naturally, there can be no epileptic activity of any sort that is electrically silent, as it is inherently based on neural activity. However, this does not preclude the notion that an electrical signal can be electrographically 'silent' depending on the resolution of the recording technique (e.g., a single neuron's activity cannot be detected by an EEG macroelectrode). However, as our intrafocal experiments did not include simultaneous optical and electrical recordings at the exact same location, our data does not unambiguously prove that neuronal ensemble activation before electrographic seizure onset (detected by the nearby microelectrode) corresponds to initial microseizure activity. Thus, it is also possible that the calcium data corresponded to pre-ictal population bursts recruiting increasingly large ensembles over time (Huberfeld et al., 2011). However, consistent with a recent case report of a microseizure (LFP) preceding macroseizure onset (intracranial EEG, or iEEG) in a patient (Weiss et al., 2016), it remains plausible that our intrafocal imaging indeed captured seizure initiation, as the escalating intrafocal population activity consistently transitioned over into the electrographic seizure, was sustained, aberrant, and evolved in time and space. The latter activity features are essential parameters in identifiying seizure activity in EEG recordings in clinical routine.

To our knowledge, no *in vivo* study to date has captured the very first step of a seizure on the scale of local microcircuits. In fact, due to the potentially miniscule neural starter population and the rapid decay of LFP signal strength with distance, it was recently hypothesized that it might be impossible to precisely capture seizure initiation in humans using field electrophysiology (Schevon et al., 2019).

Our approach, using fast two-photon calcium imaging *in vivo*, enabled us to follow acute seizure evolution from its earliest time point in the intact brain. We observed differential modes of spatiotemporal microprogression of epileptic activity inside the seizure initiation site compared with epileptic invasion of the propagation area. Inside the initiation site, we found a saltatory (i.e., "stepwise," "modular," or "discontinuous") expansion of epileptic activity on the time scale of seconds (Trevelyan et al., 2006). Consistent with studies on extrafocal seizure propagation in animals (Schwartz and Bonhoeffer, 2001; Ma et al., 2013) and humans (Schevon et al., 2012), intrafocal expansion of aberrant activity was followed by a more continuous seizure spread into nearby cortex during electrographic seizures, which suggests that seizure evolution consists of different consecutive types of progression across anatomical scales (Fig. 6, schematic overview).

Even though pathological local networks (Mehta et al., 1993; Bower et al., 2015) and local interaction of excitatory and inhibitory neurons within epileptic networks (Bragin et al., 2000) have been suggested to play a pivotal role in the progression of ictal activity (for review, see Trevelyan and Schevon, 2013), little is known about their fine-scale *in vivo* subpopulation dynamics

within cortical microcircuits. Our data indicate that interneuron activity compartmentalizes local cortical networks before electrographic seizures, and throughout seizure evolution, with distinct local footprints of neural subpopulation dynamics. In the 40 s leading up to the electrographic seizure, intrafocal population average dynamics comprised pathologically high and escalating pyramidal cell firing in the presence of enhanced interneuron population average activity while at the same time yet-to-be-invaded ("penumbral") extrafocal territories displayed enhanced interneuron firing and suppressed pyramidal activity. At an even finer anatomical scale (dozens of micrometers), the described local subpopulation footprints of activity could be observed also within the seizure initiation site. In studies on ictal neural recruitment in the context of chronic epilepsy, the precise spatial origin of a recorded seizure cannot be experimentally controlled. As a consequence, the exact location of recording with regards to the seizure initiation site at the anatomical microscale remains usually vague. Our subpopulation imaging results could facilitate the retroactive determination of the recording location (e.g., intrafocal vs extrafocal) in studies investigating seizures in humans or animal models of chronic epilepsy, even in the absence of a priori knowledge about where exactly a seizure started. For example, in a recent study investigating LVF seizures using microwires and macroelectrodes in patients with temporal lobe epilepsy, it was reported that putative interneurons in the mesial temporal lobe increase their firing seconds ahead of putative excitatory neurons within both the macroanatomically defined SOZ (ipsilateral) and propagation areas (contralateral) (Elahian et al., 2018). Based on the microanatomical data presented here, and a previous report of a single LVF seizure in a human (Weiss et al., 2016), where the macroelectrographic (intracranial EEG) seizure onset was preceded by an LFP microseizure, it could be reasonably assumed that the areas sampled by Elahian et al. (2018) within the macroanatomical SOZ were exclusively located outside the microanatomical seizure initiation site, and invaded only during seizure spread (which was discussed by the authors themselves).

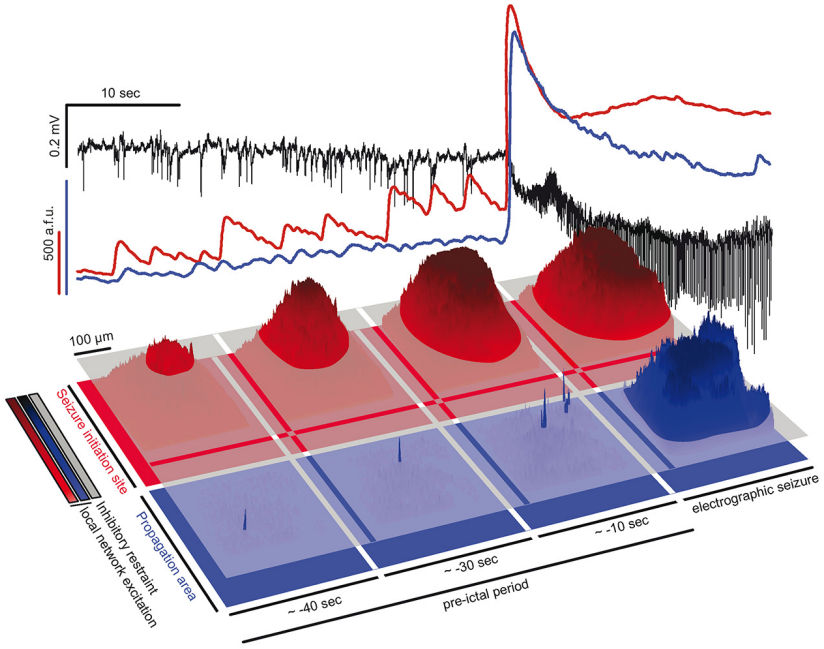

Figure 6. Two-step seizure progression model. Top panel: Depicted is a 40 s pre-ictal period before electrographic seizure onset, and initial 20 s of a full ictal event. LFP (black), and corresponding intrafocal (red) and extrafocal (blue) avg. population Ca^{2+} transient. Note how during the pre-ictal period, increasingly escalating population Ca^{2+} events are only detected inside the seizure initiation site, not in extrafocal territories. Bottom, Corresponding to the population avg. signals shown above, 3-D surface Ca^{2+} activity plots of imaged fields of view inside the seizure initiation site (red), and in extrafocal territory (blue). The gray layer schematically represents local interneuron population activity. During intrafocal micro-epileptic build-up in the pre-ictal period, inhibition fails at the level of local ensembles only inside the seizure initiation site. Small patches of excitatory ensemble activity break through the layer of local inhibition. Microepileptic expansion over the 40 s pre-ictal period occurs in a saltatory fashion taking over increasingly large areas where inhibition has failed to restrain epileptic activity. Due to the yet highly spatially confined epileptic build-up, it is at first electrographically silent, and not detected even by nearby LFP microelectrodes. Once a local threshold is reached (whose nature remains unclear), seizures spread into neighboring territories outside the seizure initiation site in a continuous fashion, and become detectable by microelectrodes and macroelectrodes across wider portions of the brain. Before this ictal expansion, little population activity can be detected in surround cortex, as opposed to intrafocal territories. This is likely due to increased feedforward inhibition in extrafocal areas that is driven by locally confined pathological activity inside the seizure initiation site. Thus, seizure progression consists of at least two consecutive steps, and may display differential spatiotemporal local network and subpopulation dynamics highly depending on the localization of recording.

Does interneuron activity restrain, or promote seizures? Consistent with previous work *in vivo*, we found enhanced local interneuron activity immediately before electrographic seizures (Prince and Wilder, 1967; Miri et al., 2018). Although some studies suggest that it is this enhanced pre-ictal interneuronal firing that triggers seizures by pathological entrainment of excitatory neurons (Shiri et al., 2015; Avoli et al., 2016; Miri et al., 2018), there is also *in vitro* (Ziburkus et al., 2006; Sessolo et al., 2015) and *in vivo* (Jayant et al., 2019) evidence based on intracellular recordings that local progression of epileptic activity coincides with interneuronal depolarization block. Our data rather support the latter studies in that we find enhanced pre-ictal interneuronal activity while at the same time immediate surround pyramidal cell firing is not increasingly synchronized, but in fact suppressed. Still, sustained interneuronal activity may support network synchronization by rebound excitation upon inhibitory failure (Grenier et al., 1998; Sessolo et al., 2015). Along these lines, it is possible that the LFP paroxysmal depolarization shift observed during electrographical seizures in our experiments, corresponds to tonic firing of excitatory neurons upon inhibitory failure at the anatomical macroscale (Baldino et al., 1986; Traub et al., 1993; Stiglbauer et al., 2017). It is of important note that seizure promoting, restraining, or sustaining effects of interneuronal activity likely highly depend on the microanatomical location (e.g., seizure initiation site vs propagation area) (Sessolo et al., 2015; Khoshkhoo et al., 2017; Codadu et al., 2019), timing and regularity of interneuronal activity (Uva et al., 2013; Khoshkhoo et al., 2017; Shiri et al., 2017; Miri et al., 2018), and interneuronal subtype (Khoshkhoo et al., 2017). Further, findings on seizure promoting or restraining interneuron dynamics may be restricted to the used experimental model (i.e., local 4-AP model). Notably, it never occurred in our experiments that all PVs in the field of view (~400 × 400 µm) showed simultaneous preseizure calcium transients indicating that the elicitation of epileptic discharges by simultaneous optogenetic activation of large PV populations might not reflect the *in vivo* situation (Shiri et al., 2015).

Echoing our and other research groups' recent analyses of local ictal network recruitment in time (Truccolo et al., 2014; Rossi et al., 2017; Wenzel et al., 2017), we found that temporal activation of local PVs is conserved across seizures (Neumann et al., 2017). Although seemingly at odds with previous reports on temporal heterogeneity of neural recruitment to seizures (Bower et al., 2012), we find it important to note that this discrepancy might be based on a missing distinction between absolute and relative time scales. Although our data indicate substantial reliability (or "stereotypy" or "homogeneity") of neural recruitment on relative time scales, that is, order of recruitment, we found, at the same time, profound recruitment heterogeneity (or "variability" or "elasticity") on absolute time scales (Wenzel et al., 2017).

A main finding of the present study is that spatial recruitment of local PVs during seizures is highly diverse, extending from previous studies showing that interneurons fire ahead of the propagating seizure wave front (Kawaguchi, 2001; Timofeev et al., 2002; Trevelyan et al., 2006; Ziburkus et al., 2006; Schevon et al., 2012; Cammarota et al., 2013). At times, immediately neighboring PVs (intercell distance $<20\ \mu m$) showed completely different temporal activation during seizure break-in indicating that the PV subfamily does not activate homogeneously during seizures. It seems intuitive that one main reason for this should be rooted in within-class molecular PV subtypes (e.g., chandelier cells vs basket cells), and their differential connectivity. However, due to a lack of spatial resolution in most studies, and current constraints in molecular targeting of within-class interneuron subtypes, this diversity of spatial recruitment of local PVs to seizures has been largely overlooked. Intriguingly, because of double fluorescent labeling and the high spatial resolution of our imaging approach, we also found nonparticipant PVs during seizures. Since PVs can synapse onto each other and are also targets of other interneuronal classes (Sik et al., 1995; Bezaire and Soltesz, 2013; Pfeffer et al., 2013; Pi et al., 2013), nonparticipant PVs, and potentially other inhibitory subtypes as well, may be actively inhibited during seizures (Paz and Huguenard, 2015). This finding might help understand why *in vivo* optogenetic activation of PVs during seizures still suspended epileptic activity (Krook-Magnuson et al., 2013), in a circumstance where one would assume PVs to be strongly active anyway. In those experiments, light activation might have recruited predominantly "nonexhausted" PVs.

In summary, we provide novel insights into the microcircuit dynamics across seizure evolution from its earliest time point *in vivo*, demonstrating how local synchronization of neuronal ensembles evolves into electrographically detectable seizures. Our experiments help viewing differential modes of seizure microprogression within a larger context of seizure evolution, and show that PV population dynamics during seizures in extrafocal and intrafocal regions are spatially more diverse than previously thought. Our results also underscore that the precise location of recording is critical to any one experiment investigating seizure microprogression. Here, we establish spatiotemporal subtype activity footprints that correspond to consecutive steps of seizure microprogression. As in chronic focal epilepsy the precise seizure initiation site is often unclear, such footprints could instruct high-resolution recordings in determining the recording location (e.g., intrafocal vs extrafocal) even in the absence of *a priori* knowledge about where exactly a seizure started.

References

Arida RM, Scorza FA, Peres CA, Cavalheiro EA (1999) The course of untreated seizures in the pilocarpine model of epilepsy. Epilepsy Res 34: 99–107.

Avoli M, de Curtis M (2011) GABAergic synchronization in the limbic system and its role in the generation of epileptiform activity. Prog Neurobiol 95:104–132.

Avoli M, Psarropoulou C, Tancredi V, Fueta Y (1993) On the synchronous activity induced by 4-aminopyridine in the CA3 subfield of juvenile rat hippocampus. J Neurophysiol 70:1018–1029.

Avoli M, D'Antuono M, Louvel J, Köhling R, Biagini G, Pumain R, D'Arcangelo G, Tancredi V (2002) Network and pharmacological mechanisms leading to epileptiform synchronization in the limbic system in vitro. Prog Neurobiol 68:167–207.

Avoli M, de Curtis M, Gnatkovsky V, Gotman J, Kohling R, Lévesque M, Manseau F, Shiri Z, Williams S (2016) Specific imbalance of excitatory/inhibitory signaling establishes seizure onset pattern in temporal lobe epilepsy. J Neurophysiol 115:3229–3237.

Badea T, Goldberg J, Mao B, Yuste, R (2001) Calcium imaging of epileptiform events with single-cell resolution. J Neurobiol 215–227.

Baldino F Jr, Wolfson B, Heinemann U, Gutnick MJ (1986) An N-methyl-D-aspartate (NMDA) receptor antagonist reduces bicuculline-induced depolarization shifts in neocortical explant cultures. Neurosci Lett 70: 101–105.

Beleza P (2012) Acute symptomatic seizures: a clinically oriented review. Neurologist 18:109–119.

Bezaire MJ, Soltesz I (2013) Quantitative assessment of CA1 local circuits: knowledge base for interneuron-pyramidal cell connectivity. Hippocampus 23:751–785.

Bower MR, Buckmaster PS (2008) Changes in granule cell firing rates precede locally recorded spontaneous seizures by minutes in an animal model of temporal lobe epilepsy. J Neurophysiol 99:2431–2442.

Bower MR, Stead M, Meyer FB, Marsh WR, Worrell GA (2012) Spatiotemporal neuronal correlates of seizure generation in focal epilepsy. Epilepsia 53:807–816.

Bower MR, Stead M, Bower RS, Kucewicz MT, Sulc V, Cimbalnik J, Brinkmann BH, Vasoli VM, St Louis EK, Meyer FB, Marsh WR, Worrell GA (2015) Evidence for consolidation of neuronal assemblies after seizures in humans. J Neurosci 35:999–1010.

Bragin A, Wilson CL, Engel J Jr (2000) Chronic epileptogenesis requires development of a network of pathologically interconnected neuron clusters: a hypothesis. Epilepsia 41:S144–S152.

Cammarota M, Losi G, Chiavegato A, Zonta M, Carmignoto G (2013) Fast spiking interneuron control of seizure propagation in a cortical slice model of focal epilepsy. J Physiol 591:807–822.

Cattell RB (1966) The scree test for the number of factors. Multivariate Behavioral Research 1:245–276.

Chen TW, Wardill TJ, Sun Y, Pulver SR, Renninger SL, Baohan A, Schreiter ER, Kerr RA, Orger MB, Jayaraman V, Looger LL, Svoboda K, Kim DS (2013) Ultrasensitive fluorescent proteins for imaging neuronal activity. Nature 499:295–300.

Codadu NK, Parrish RR, Trevelyan AJ (2019) Region-specific differences and areal interactions underlying transitions in epileptiform activity. J Physiol 597:2079–2096.

Elahian B, Lado NE, Mankin E, Vangala S, Misra A, Moxon K, Fried I, Sharan A, Yeasin M, Staba R, Bragin A, Avoli M, Sperling MR, Engel J Jr, Weiss SA (2018) Low-voltage fast seizures in humans begin with increased interneuron firing. Ann Neurol 84:588–600.

Ewell LA, Liang L, Armstrong C, Soltész I, Leutgeb S, Leutgeb JK (2015) Brain state is a major factor in preseizure hippocampal network activity and influences success of seizure intervention. J Neurosci 35:15635–15648.

Feldt Muldoon S, Soltesz I, Cossart R (2013) Spatially clustered neuronal assemblies comprise the microstructure of synchrony in chronically epileptic networks. Proc Natl Acad Sci U S A 110:3567–3572.

Gnatkovsky V, Librizzi L, Trombin F, de Curtis M (2008) Fast activity at seizure onset is mediated by inhibitory circuits in the entorhinal cortex in vitro. Ann Neurol 64:674–686.

Goldensohn ES (1975) Initiation and propagation of epileptogenic foci. Adv Neurol 11:141–162.

Grenier F, Timofeev I, Steriade M (1998) Leading role of thalamic over

cortical neurons during postinhibitory rebound excitation. Proc Natl Acad Sci U S A 95:13929–13934.
Hofer SB, Ko H, Pichler B, Vogelstein J, Ros H, Zeng H, Lein E, Lesica NA, Mrsic-Flogel TD (2011) Differential connectivity and response dynamics of excitatory and inhibitory neurons in visual cortex. Nat Neurosci 14:1045–1052.
Howe J, Lu X, Thompson Z, Peterson GW, Losey TE (2016) Intraoperative seizures during craniotomy under general anesthesia. Seizure 38:23–25.
Huberfeld G, Menendez de la Prida L, Pallud J, Cohen I, Le Van Quyen M, Adam C, Clemenceau S, Baulac M, Miles R (2011) Glutamatergic pre-ictal discharges emerge at the transition to seizure in human epilepsy. Nat Neurosci 14:627–634.
Jayant K, Wenzel M, Bando Y, Hamm JP, Mandriota N, Rabinowitz JH, Plante IJ, Owen JS, Sahin O, Shepard KL, et al. (2019) Flexible nanopipettes for minimally invasive intracellular electrophysiology in vivo. Cell Rep *26* 266–278 e265.
Jirsa VK, Stacey WC, Quilichini PP, Ivanov AI, Bernard C (2014) On the nature of seizure dynamics. Brain 137:2210–2230.
Kaiser HF (1958) The varimax criterion for analytic rotation in factor analysis. Psychometrika 23:187–200.
Kawaguchi Y (2001) Distinct firing patterns of neuronal subtypes in cortical synchronized activities. J Neurosci 21:7261–7272.
Khoshkhoo S, Vogt D, Sohal VS (2017) Dynamic, cell-type-specific roles for GABAergic interneurons in a mouse model of optogenetically inducible seizures. Neuron 93:291–298.
Krook-Magnuson E, Armstrong C, Oijala M, Soltesz I (2013) On-demand optogenetic control of spontaneous seizures in temporal lobe epilepsy. Nat Commun 4:1376.
Ledri M, Madsen MG, Nikitidou L, Kirik D, Kokaia M (2014) Global optogenetic activation of inhibitory interneurons during epileptiform activity. J Neurosci 34:3364–3377.
Lillis KP, Wang Z, Mail M, Zhao GQ, Berdichevsky Y, Bacskai B, Staley KJ (2015) Evolution of network synchronization during early epileptogenesis parallels synaptic circuit alterations. J Neurosci 35:9920–9934.
Liou JY, Ma H, Wenzel M, Zhao M, Baird-Daniel E, Smith EH, Daniel A, Emerson R, Yuste R, Schwartz TH, Schevon CA (2018) Role of inhibitory control in modulating spread of focal ictal activity. Brain 141: 2083–2097
Lopes da Silva F, Blanes W, Kalitzin SN, Parra J, Suffczynski P, Velis DN (2003) Epilepsies as dynamical diseases of brain systems: basic models of the transition between normal and epileptic activity. Epilepsia 44:72–83.
Ma H, Zhao M, Schwartz TH (2013) Dynamic neurovascular coupling and uncoupling during ictal onset, propagation, and termination revealed by simultaneous in vivo optical imaging of neural activity and local blood volume. Cereb Cortex 23:885–899.
Madisen L, Zwingman TA, Sunkin SM, Oh SW, Zariwala HA, Gu H, Ng LL, Palmiter RD, Hawrylycz MJ, Jones AR, Lein ES, Zeng H (2010) A robust and high-throughput cre reporting and characterization system for the whole mouse brain. Nat Neurosci 13:133–140.
Mehta MR, Dasgupta C, Ullal GR (1993) A neural network model for kindling of focal epilepsy: basic mechanism. Biol Cybern 68:335–340.
Miller JE, Ayzenshtat I, Carrillo-Reid L, Yuste R (2014) Visual stimuli recruit intrinsically generated cortical ensembles. Proc Natl Acad Sci U S A 111:E4053–4061.
Milton JG, Chkhenkeli SA, Towle VL (2007) Brain connectivity and the spread of epileptic seizures. In: Handbook of brain connectivity, pp 477–503. Heidelberg: Springer.
Miri ML, Vinck M, Pant R, Cardin JA (2018) Altered hippocampal interneuron activity precedes ictal onset. Elife 7:e40750.
Muldoon SF, Villette V, Tressard T, Malvache A, Reichinnek S, Bartolomei F, Cossart R (2015) GABAergic inhibition shapes interictal dynamics in awake epileptic mice. Brain 138:2875–2890.
Nagappan S, Liu L, Fetcho R, Nguyen J, Nishimura N, Radwanski RE, Lieberman S, Baird-Daniel E, Ma H, Zhao M, Schaffer CB, Schwartz TH (2018) In vivo femtosecond laser subsurface cortical microtransections attenuate acute rat focal seizures. Cereb Cortex. In press.
Neubauer FB, Sederberg A, MacLean JN (2014) Local changes in neocortical circuit dynamics coincide with the spread of seizures to thalamus in a model of epilepsy. Front Neural Circuits 8:101.
Neumann AR, Raedt R, Steenland HW, Sprengers M, Bzymek K, Navratilova Z, Mesina L, Xie J, Lapointe V, Kloosterman F, Vonck K, Boon PAJM, Soltesz I, McNaughton BL, Luczak A (2017) Involvement of fast-spiking cells in ictal sequences during spontaneous seizures in rats with chronic temporal lobe epilepsy. Brain 140:2355–2369.
Paz JT, Huguenard JR (2015) Microcircuits and their interactions in epilepsy: is the focus out of focus? Nat Neurosci 18:351–359.
Pfeffer CK, Xue M, He M, Huang ZJ, Scanziani M (2013) Inhibition of inhibition in visual cortex: the logic of connections between molecularly distinct interneurons. Nat Neurosci 16:1068–1076.
Pi HJ, Hangya B, Kvitsiani D, Sanders JI, Huang ZJ, Kepecs A (2013) Cortical interneurons that specialize in disinhibitory control. Nature 503:521–524.
Prince DA, Wilder BJ (1967) Control mechanisms in cortical epileptogenic foci. "Surround" inhibition. Arch Neurol 16:194–202.
Rossi LF, Wykes RC, Kullmann DM, Carandini M (2017) Focal cortical seizures start as standing waves and propagate respecting homotopic connectivity. Nat Commun 8:217.
Schevon CA, Ng SK, Cappell J, Goodman RR, McKhann G Jr, Waziri A, Branner A, Sosunov A, Schroeder CE, Emerson RG (2008) Microphysiology of epileptiform activity in human neocortex. J Clin Neurophysiol 25:321–330.
Schevon CA, Weiss SA, McKhann G Jr, Goodman RR, Yuste R, Emerson RG, Trevelyan AJ (2012) Evidence of an inhibitory restraint of seizure activity in humans. Nat Commun 3:1060.
Schevon CA, Tobochnik S, Eissa T, Merricks E, Gill B, Parrish RR, Bateman LM, McKhann GM Jr, Emerson RG, Trevelyan AJ (2019) Multiscale recordings reveal the dynamic spatial structure of human seizures. Neurobiol Dis 127:303–311.
Schwartz TH, Bonhoeffer T (2001) In vivo optical mapping of epileptic foci and surround inhibition in ferret cerebral cortex. Nat Med 7:1063–1067.
Sessolo M, Marcon I, Bovetti S, Losi G, Cammarota M, Ratto GM, Fellin T, Carmignoto G (2015) Parvalbumin-positive inhibitory interneurons oppose propagation but favor generation of focal epileptiform activity. J Neurosci 35:9544–9557.
Shiri Z, Manseau F, Lévesque M, Williams S, Avoli M (2015) Interneuron activity leads to initiation of low-voltage fast-onset seizures. Ann Neurol 77:541–546.
Shiri Z, Lévesque M, Etter G, Manseau F, Williams S, Avoli M (2017) Optogenetic low-frequency stimulation of specific neuronal populations abates ictogenesis. J Neurosci 37:2999–3008.
Sik A, Penttonen M, Ylinen A, Buzsáki G (1995) Hippocampal CA1 interneurons: an in vivo intracellular labeling study. J Neurosci 15:6651–6665.
Smetters D, Majewska A, Yuste R (1999) Detecting action potentials in neuronal populations with calcium imaging. Methods 18:215–221.
Stead M, Bower M, Brinkmann BH, Lee K, Marsh WR, Meyer FB, Litt B, Van Gompel J, Worrell GA (2010) Microseizures and the spatiotemporal scales of human partial epilepsy. Brain 133:2789–2797.
Stiglbauer V, Hotka M, Ruiß M, Hilber K, Boehm S, Kubista H (2017) Cav 1.3 channels play a crucial role in the formation of paroxysmal depolarization shifts in cultured hippocampal neurons. Epilepsia 58:858–871.
Szente M, Pongrácz F (1979) Aminopyridine-induced seizure activity. Electroencephalogr Clin Neurophysiol 46:605–608.
Tashiro A, Goldberg J, Yuste R (2002) Calcium oscillations in neocortical astrocytes under epileptiform conditions. J Neurobiol 50:45–55.
Timofeev I, Grenier F, Steriade M (2002) The role of chloride-dependent inhibition and the activity of fast-spiking neurons during cortical spike-wave electrographic seizures. Neuroscience 114:1115–1132.
Traub RD, Miles R, Jefferys JG (1993) Synaptic and intrinsic conductances shape picrotoxin-induced synchronized after-discharges in the guinea-pig hippocampal slice. J Physiol 461:525–547.
Trevelyan AJ, Schevon CA (2013) How inhibition influences seizure propagation. Neuropharmacology 69:45–54.
Trevelyan AJ, Sussillo D, Watson BO, Yuste R (2006) Modular propagation of epileptiform activity: evidence for an inhibitory veto in neocortex. J Neurosci 26:12447–12455.
Trevelyan AJ, Sussillo D, Yuste R (2007) Feedforward inhibition contributes to the control of epileptiform propagation speed. J Neurosci 27:3383–3387.
Truccolo W, Donoghue JA, Hochberg LR, Eskandar EN, Madsen JR, Anderson WS, Brown EN, Halgren E, Cash SS (2011) Single-neuron dynamics in human focal epilepsy. Nat Neurosci 14:635–641.

Truccolo W, Ahmed OJ, Harrison MT, Eskandar EN, Cosgrove GR, Madsen JR, Blum AS, Potter NS, Hochberg LR, Cash SS (2014) Neuronal ensemble synchrony during human focal seizures. J Neurosci 34:9927–9944.

Ulkatan S, Jaramillo AM, Téllez MJ, Kim J, Deletis V, Seidel K (2017) Incidence of intraoperative seizures during motor evoked potential monitoring in a large cohort of patients undergoing different surgical procedures. J Neurosurg 126:1296–1302.

Uva L, Trombin F, Carriero G, Avoli M, de Curtis M (2013) Seizure-like discharges induced by 4-aminopyridine in the olfactory system of the in vitro isolated guinea pig brain. Epilepsia 54:605–615.

Warren CP, Hu S, Stead M, Brinkmann BH, Bower MR, Worrell GA (2010) Synchrony in normal and focal epileptic brain: the seizure onset zone is functionally disconnected. J Neurophysiol 104:3530–3539.

Weiss SA, Alvarado-Rojas C, Bragin A, Behnke E, Fields T, Fried I, Engel J Jr, Staba R (2016) Ictal onset patterns of local field potentials, high frequency oscillations, and unit activity in human mesial temporal lobe epilepsy. Epilepsia 57:111–121.

Wenzel M, Hamm JP, Peterka DS, Yuste R (2017) Reliable and elastic propagation of cortical seizures in vivo. Cell Rep 19:2681–2693.

Wong BY, Prince DA (1990) The lateral spread of ictal discharges in neocortical brain slices. Epilepsy Res 7:29–39.

Worrell GA, Gardner AB, Stead SM, Hu S, Goerss S, Cascino GJ, Meyer FB, Marsh R, Litt B (2008) High-frequency oscillations in human temporal lobe: simultaneous microwire and clinical macroelectrode recordings. Brain 131:928–937.

Yuste R, Katz LC (1991) Control of postsynaptic Ca2+ influx in developing neocortex by excitatory and inhibitory neurotransmitters. Neuron 6:333–344.

Zhao M, Nguyen J, Ma H, Nishimura N, Schaffer CB, Schwartz TH (2011) Pre-ictal and ictal neurovascular and metabolic coupling surrounding a seizure focus. J Neurosci 31:13292–13300.

Ziburkus J, Cressman JR, Barreto E, Schiff SJ (2006) Interneuron and pyramidal cell interplay during in vitro seizure-like events. J Neurophysiol 95:3948–3954.

Flexible Nanopipettes for Minimally Invasive Intracellular Electrophysiology in vivo

Einen optimalen experimentellen Ansatz zur Erfassung der Dynamiken verschiedener neuronaler Subklassen im Kontext lokaler Netzwerke stellt die gezielte elektrische Messung visuell identifizierter Neurone im Vergleich zur umgebenden neuronalen Populationsaktivität im intakten Gehirn dar. Diese Art von Experiment, welche prototypisch *in vivo* Patch-clamp Aufzeichnungen und gleichzeitige lokale Netzwerkmessungen (per LFP, oder hochauflösender Mikroskopie) beinhaltet, sind jedoch von hohem Schwierigkeitsgrad und traditionell wenigen, spezialisierten Forschungsgruppen weltweit vorbehalten (Constantinople und Bruno, 2011; Lee et al., 2006, 2009; Long und Lee, 2012; Margrie et al., 2002, 2003; Pala und Petersen, 2015; Pernía-Andrade und Jonas, 2014; Petersen, 2017; Polack et al., 2013; Suzuki und Larkum, 2020; Svoboda et al., 1997). In der hier vorgestellten Studie (Jayant und Wenzel et al., 2019) wurden neuartige, laser-fabrizierte Quartzglas-Nanopipetten für stabile intrazelluäre *in vivo* Ableitungen etabliert (Seal Resistance 500-800 MΩ) (Abb. 1 A-B). Diese Nanosharps weisen aufgrund eines mehrere Millimeter langen schlanken Halses flexible Eigenschaften (bis zu 90° ohne Bruch flexibel, mit stabilen elektrischen Pipetteneigenschaften) auf (Abb. 1 B), welche für stabile *in vivo* Ableitungen aufgrund von Gewebspulsationen und -bewegungen im intakten Gehirn vorteilhaft sein können (Lee et al., 2006). Die äußerst kleine Pipettenspitzenöffnung von ca. 10-25 Nanometern (Abb. 1 A) minimiert darüber hinaus das für Patch-clamp Mikropipetten gängige Problem des Verstopfens der Pipettenöffnung beim Navigieren durch Hirngewebe und ermöglicht die serielle Ableitung mehrere Neurone hintereinander ohne zwischenzeitlichen Pipettenwechsel (im Schnitt 5-10 Neurone/Nanopipette)(Abb. 3 A, B und 4 D). Der intrazelluläre Zugang zur Zelle erfolgt mittels Etablierung einer Nanopore in der Zellmembran des Zielneurons durch Elektroporation (Abb. 1 F) und ist auf diese Weise zellschonend.

Die etablierten Nanopipetten wurden in dieser Studie für *in vitro* Ableitungen und *in vivo* Messungen in anästhesierten und wachen Mäusen (n=14) für verschiedenartige Experimente genutzt: blinde Ableitungen in wachen Mäusen (insges. 50 Zellen), visuell gesteuerte Ableitungen (externe Markierung von Nanosharps durch fluoreszente *Quantum-dots*) unter 2P-Mikroskopie (12 Somata [PYR und PV], 6 Dendriten) bis zu

einer kortikalen Tiefe von ca. 800 μm (Abb. 2 A-C), in Kombination mit LFP Messungen (Abb. 2 E-F und 6) sowie in vivo 2P-Ca^{2+}-Mikroskopie neuronaler Populationen (Abb. 5 A-E und 6) innerhalb einzelner kortikaler Laminae oder multilaminär (mikroprismengestützt, Abb. 5 und 6), unter physiologischen Bedingungen (Ableitdauer bis max. 3,5 h) und infolge chemoconvulsiver Auslösung (4-AP, wie in den beiden vorherigen Studien beschrieben; 8 Zellen in 3 Mäusen) akut epileptischer Anfälle genutzt (Abb. 6).

Durch die oben beschriebenen Eigenschaften der neu etablierten und charakterisierten Nanosharps konnte in einer Vielzahl verschiedener *in vivo* Experimente gezeigt werden, dass diese aufgrund der vergleichsweise simplen Implementierbarkeit das Potential für eine breite Anwendung in der neurobiologischen Forschung haben, selbst in Laboren, die nicht auf *in vivo* Einzelzellableitungen spezialisiert sind. Vor dem Hintergrund pathologisch transformierter neuronaler Zellverbände wurden zur Untersuchung neuronaler Subklassendynamiken während der epileptischen Anfallsausbreitung abermals eigens gezüchtete transgene GCaMP6::PV-Cre::LSL-td-Tomato Mäuse (Hintergrund: C57BL/6) genutzt (Abb. 6 B). Durch Kombination mikroprismengestützter multilaminärer 2-Kanal *in vivo* 2-Photonenmikroskopie von lokalen Populationsdynamiken (Ca^{2+} Aktivität) und gleichzeitiger LFP Messung (per Glasmikropipette) sowie visuell gesteuerter, gezielter elektrischer Ableitung von PV Interneuronen (per Nanosharp)(Abb. 6 A-C) konnte erstmals im intakten Gehirn gezeigt werden, dass die iktuale Invasion lokaler Neuronenverbände zeitlich mit einem Depolarisationsblock von PV Interneuronen zusammenfällt (Abb. 4 C-E).

OPEN ACCESS
CellPress

Cell Reports
Resource

Flexible Nanopipettes for Minimally Invasive Intracellular Electrophysiology *In Vivo*

Krishna Jayant,[1,2,6,7,8,9,*] Michael Wenzel,[2,6,7,8] Yuki Bando,[2,6,7] Jordan P. Hamm,[2,6,7] Nicola Mandriota,[2] Jake H. Rabinowitz,[1] Ilan Jen-La Plante,[3,6] Jonathan S. Owen,[3,6] Ozgur Sahin,[2,4,6] Kenneth L. Shepard,[1,5,6,7] and Rafael Yuste[2,6,7]

[1]Department of Electrical Engineering, Columbia University, New York, NY 10027, USA
[2]Department of Biological Sciences, Columbia University, New York, NY 10027, USA
[3]Department of Chemistry, Columbia University, New York, NY 10027, USA
[4]Department of Physics, Columbia University, New York, NY 10027, USA
[5]Department of Biomedical Engineering, Columbia University, New York, NY 10027, USA
[6]NeuroTechnology Center, Columbia University, New York, NY 10027, USA
[7]Kavli Institute for Brain Science, Columbia University, New York, NY 10027, USA
[8]These authors contributed equally
[9]Lead Contact
*Correspondence: kj2346@columbia.edu
https://doi.org/10.1016/j.celrep.2018.12.019

SUMMARY

Intracellular recordings *in vivo* remains the best technique to link single-neuron electrical properties to network function. Yet existing methods are limited in accuracy, throughput, and duration, primarily via washout, membrane damage, and movement-induced failure. Here, we introduce flexible quartz nanopipettes (inner diameters of 10–25 nm and spring constant of ~0.08 N/m) as nanoscale analogs of traditional glass microelectrodes. Nanopipettes enable stable intracellular recordings (seal resistances of 500 to ~800 MΩ, 5 to ~10 cells/nanopipette, and duration of ~1 hr) in anaesthetized and awake head-restrained mice, exhibit minimal diffusional flux, and facilitate precise recording and stimulation. When combined with quantum-dot labels and microprisms, nanopipettes enable two-photon targeted electrophysiology from both somata and dendrites, and even paired recordings from neighboring neurons, while permitting simultaneous population imaging across cortical layers. We demonstrate the versatility of this method by recording from parvalbumin-positive (Pv) interneurons while imaging seizure propagation, and we find that Pv depolarization block coincides with epileptic spread. Flexible nanopipettes present a simple method to procure stable intracellular recordings *in vivo*.

INTRODUCTION

Intracellular electrophysiological recordings *in vivo* are widely used to study synaptic integration (Petersen and Crochet, 2013; Svoboda et al., 1999), decipher local circuit interactions (Adesnik et al., 2012; Pluta et al., 2015; Polack et al., 2013), and elucidate the relationship between single-neuron dynamics and behavior (Houweling and Brecht, 2008). Yet limitations to this versatile technique have hindered more widespread use *in vivo*. The first pertains to electrode compliance, specifically the mechanical mismatch at the micropipette-neuron interface. Traditionally, single-cell electrophysiology *in vivo* is performed using sharp microelectrodes (Long et al., 2010; McIlwain and Creutzfeldt, 1967; Schneider et al., 2014; Svoboda et al., 1997, 1999; Yazaki-Sugiyama et al., 2009) or whole-cell patch pipettes (Kodandaramaiah et al., 2012; Lee et al., 2006, 2009; Margrie et al., 2002). Both techniques use glass microelectrodes, which have approximate tip diameters of ≥100 nm (sharp electrode) and 1–2 μm (patch electrode), as well as an abrupt conical taper with an outer diameter approaching ~1 mm within a few hundred microns of the tip. This geometry and design make the pipette stiff, which leads to low experimental throughput because of mechanical disruption, a critically important aspect when recording from soft tissues in awake moving animals (Lee et al., 2006). Furthermore, the large tip openings, coupled with the method of cell entry, can cause intracellular washout over time or, in the case of sharp microelectrodes, a permanent membrane shunt. Moreover, patch pipettes are not easily reusable *in vivo*, require continuous application of pressure while navigating through the brain, and exhibit variable access resistances with increased recording depths.

Another major limitation relates to the ability to perform targeted intracellular recordings from visually identified neurons deep in the living brain (Muñoz et al., 2014), a key requirement in modern circuit neuroscience (Petersen, 2017). Although targeted recordings can be performed using whole-cell patching under two-photon visual guidance, they are mainly relegated to superficial cortical regions because of scattering of light in deep tissue (Packer et al., 2015). However, conventional sharp electrodes are generally difficult to use under two-photon guidance due to poor visualization of the tip and inefficient pressure application, and they have only been used under two-photon visualization for targeted recordings in superficial brain regions and with

larger pipette diameters (Svoboda et al., 1997). Furthermore, it is becoming increasingly important to be able to couple targeted recordings with simultaneous population calcium (Ca^{2+}) imaging across layers, because it can help decode how single-neuron dynamics relates to network activity (Carrillo-Reid et al., 2016; Yuste and Katz, 1991). However, performing targeted *in vivo* electrophysiology applicable across any depth, along with multilayer population Ca^{2+} imaging (Yang et al., 2016), remains an unresolved technical challenge. Methods to overcome this limitation have treated these two components in isolation, solely focused on either improving the throughput of blind and targeted intracellular recordings *in vivo* (Kitamura et al., 2008; Kodandaramaiah et al., 2012; Long et al., 2015; Muñoz et al., 2014) or imaging neural activity in deeper regions of the cortex (Andermann et al., 2013; Horton et al., 2013; Theer et al., 2003; Tischbirek et al., 2015), but they have never sought to optimize them simultaneously, which is needed.

Ideally, to accomplish high-throughput intracellular electrophysiology *in vivo*, especially in awake animals, microelectrodes should be flexible, minimally invasive, and immune to movement, yet they also should be stiff enough to enter the brain, exhibit stable and high SNR (signal-to-noise ratio) recordings, be reusable, and be easily visualized under two-photon excitation to enable targeted recordings *in vivo*. Nanoelectrodes in the tens of nanometers range have gained widespread attention as minimally invasive intracellular voltage probes *in vitro* (Angle and Schaefer, 2012; Hai et al., 2010; Robinson et al., 2012; Tian et al., 2010). The nanoscale size, coupled with unique material properties, has been exploited to gain intracellular access with tight seals. However, measuring signals with stable resting membrane potentials (RMPs), negating the high impedance artifact (Brette et al., 2008; Jayant et al., 2017), and enabling precise stimulation is challenging, particularly *in vivo*. Flexible electrodes are mechanically more compatible with soft tissue and can be used to record for long periods *in vivo*, but they have only been realized for extracellular measurements to date because of their planar nature (Viventi et al., 2010). So could intracellular microelectrodes be modified to obtain a nanoscale flexible probe suitable *in vivo*? To address this challenge, we introduced electrolyte-filled quartz nanopipettes *in vitro* (Jayant et al., 2017), which have tips an order of magnitude smaller than conventional glass microelectrodes, exhibit stable and high SNR recordings, allow the measurement of direct current (DC) RMPs, and can be optimally compensated for electrode artifacts (electrode capacitance of ~8–10 pF). Here, we exploit the ultra-flexible property of these electrodes for *in vivo* use and demonstrate robust and stable measurements in the presence of animal movements. The ability to make long stable recordings, coupled with the benefit of being reusable, improves experimental throughput by allowing multiple cells to be probed by a single electrode without becoming clogged or causing washout. Furthermore, we demonstrate that flexible nanopipettes, in conjunction with quantum-dot labels and microprism-assisted two-photon imaging (Andermann et al., 2013), enable targeted recordings across all cortical layers, applicable in both the awake and the anaesthetized animal, with the advantage of being compatible with simultaneous population Ca^{2+} imaging.

RESULTS

Flexible Nanopipettes: Design and Characterization

From classical beam theory, the stiffness k of a hollow cylindrical tube of radius R and height h can be approximated by $k = 3EI/L^3$ (cantilever approximation). Here, $I \approx \pi R^3 t$ signifies the geometric moment of inertia at the tip, L signifies the length of the taper, and E signifies Young's modulus of the material. The product EI, which is the bending modulus, is a measure of how easily the structure will flex in response to a load. The stiffness k is directly proportional to the bending modulus and, through this, the cube of the radius, the thickness of pipette tip t, and inversely proportional to the cube of the length of the cylinder or taper. We used this relationship to optimize the form factor of fabricated quartz nanopipettes (each with an inner diameter [I.D.] of ~10–20 nm) (Figure 1A; STAR Methods) with long (7–10 mm), thin, and extremely flexible tapers (Figure 1B, left; Figure S1A) (radius curvature of ~2 mm and a bend of ~90° at the stem) that were nonetheless axially stiff to enter the brain without any change in tip resistance. Furthermore, the pipettes did not show signs of permanent deformation when bent (Figure 1B, middle) and were able to immediately regain their original shape thereafter (Figure 1B, right). We then scanned an atomic force microscope (AFM) tip across the long and narrow taper (Figure 1C) to measure the bending stiffness from the force distance curve (Figure S1B). We found bending stiffness values of ~0.08 N/m near the tip (black trace, Figure 1C) a value much lower than conventional flexible extracellular electrodes (Liu et al., 2015) and identical to the stiffness of cantilever probes used in AFM analysis of cell membranes (Qi et al., 2015). We compared this pipette design against quartz microelectrodes with shorter tapers but a nearly similar tip size (~50–100 nm outer diameter) (pink trace, Figure 1C) and found an order of magnitude difference in bending stiffness, which suggests that cone angle and taper length are key parameters in deciding flexibility. Because of material limitations, conventional borosilicate glass microelectrodes yield shorter tapers, wider cone angles, and larger tips, which render them less compliant than our long quartz nanopipette. Moreover, because of the nanoscale tip and the associated geometries achieved (Figure 1D), these electrodes are reusable, do not easily clog, and minimize intracellular washout. In addition, simulations based on the coupled Poisson-Nernst-Planck and Navier-Stokes equations (Lan et al., 2016) suggested minimal diffusional flux of ~0.1–1 fM/s for the geometries realized with resistances dependent on taper geometry and cytoplasmic diffusion constants (Figure 1E; Figure S1C; Methods S1). Electrolyte-filled (3 M KCl) nanopipettes were optimally compensated (wall capacitance of ~9–10 pF) in the extracellular bath before cell entry to reduce signal attenuation due to filtering (STAR Methods). Transmembrane entry was elicited either through complete tip insertion (type A entry, fully intracellular) (Figure 1F, left) or through an electroporation-induced nanopore (type B entry, quasi-intracellular) (Figure 1F, right) as previously described (Jayant et al., 2017). Clogging did not occur, and we hypothesize this resulted from the low flux and the presence of vortex flows at the tip of the nanopipette (Figure S1D), which preclude lipids from flowing into the orifice. Type B recordings can be characterized as one of two forms.

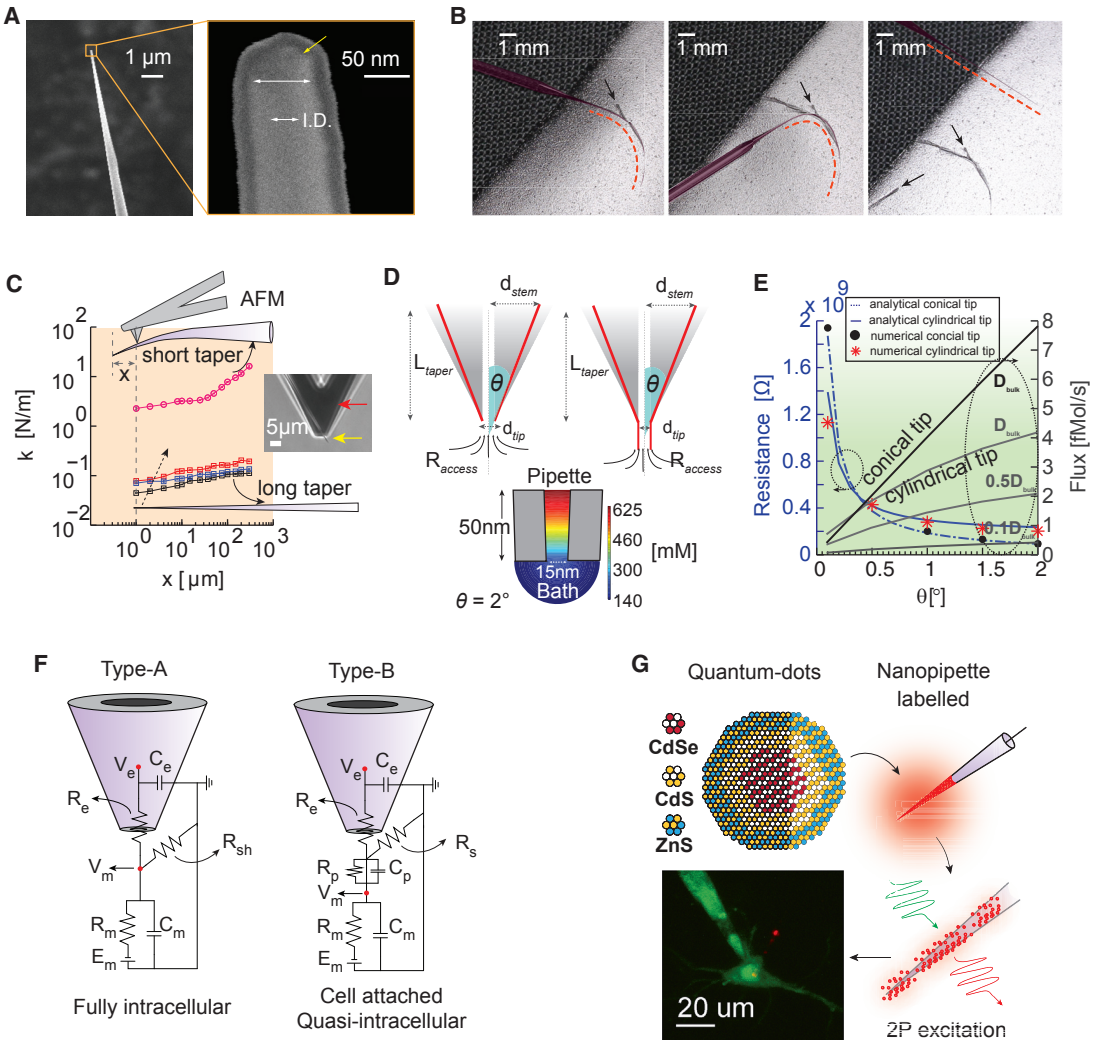

Figure 1. Flexible Nanopipette Design Characteristics

(A) SEM of the nanopipette (left) and magnified view of the tip (right). The outer diameter-to-inner diameter (I.D.) ratio is 2:1. Note the outer 10 nm platinum coating layer required for SEM imaging.

(B) Images depicting the degree of nanopipette flexibility (left, middle, and right). The nanopipette (false colored; red dotted line) is immobilized on tape, and the taper is subsequently bent (left). The taper is bent farther (>60°) (middle) and subsequently recovers to a taut axially stiff pipette (right) when removed from the tape without damage. The black arrows indicate imprints of the taper in the tape.

(C) AFM-based stiffness measurements of nanopipettes for varying taper lengths (black, blue, and red indicate a long nanopipette with small variations in taper length (~8 mm), and pink represents a short tapered conventional sharp microelectrode design). The inset depicts the AFM tip (red) scanning the tip of the nanopipette (yellow). The spring constant (stiffness) of the long tapered nanopipette close to the tip (~0.08 N/m) reveals a highly compliant structure.

(D) Geometry of the two types of nanopipettes commonly used: conical tip (upper left) and cylindrical tip with conical taper (upper right). The half cone angle (theta), length of the taper (L_{taper}), diameter of the tip (d_{tip}), and access resistance (R_{access}) influence the net resistance, concentration gradient, and flux. Simulated heatmap of the concentration gradient at the tip of a purely conical nanopipette (bottom). Note the large gradient close to the tip.

(E) Numerical simulations of resistance versus theta (left y axis) and flux versus theta (right y axis) for the two geometries shown in (D) for a fixed diameter of 15 nm and 3 M KCl filling solution. Low flux values (<1 fM/s) can be achieved when the pipette tip is cylindrical (theta of ~0) near the end and the diffusion constant of ions at the tip (cytoplasmic fluid) is lower than bulk. Resistance versus theta was calculated analytically and corroborated numerically (see text for details).

(F) Equivalent circuit models showing the nanopipette cell membrane interface under full tip impalement (left, type A) and electroporation-induced or cell-attached entry (right, type B). Here, R_e and C_e denote the distributed pipette resistance and capacitance, respectively. R_{sh}, R_s, and R_p represent the shunt, seal, and pore resistance, respectively. R_m represents the membrane resistance, C_m represents the membrane capacitance, C_p represents the pore capacitance, and E_m represents the reversal potential of the leak channels. Depending on whether R_p or C_p dominates the junction contribution, and under a moderate to high R_s, the recorded signal V_e could reflect either a purely capacitive extracellular signal (C_p dominates, similar to cell-attached recording) or a tightly coupled and scaled intracellular signal (R_p dominates, similar to quasi-intracellular or in-cell recordings).

(G) CdSe/Cds/ZnS QDs label nanopipettes through adsorption, allowing clear visualization of the nanopipette relative to the patch pipette under two-photon visualization (bottom).

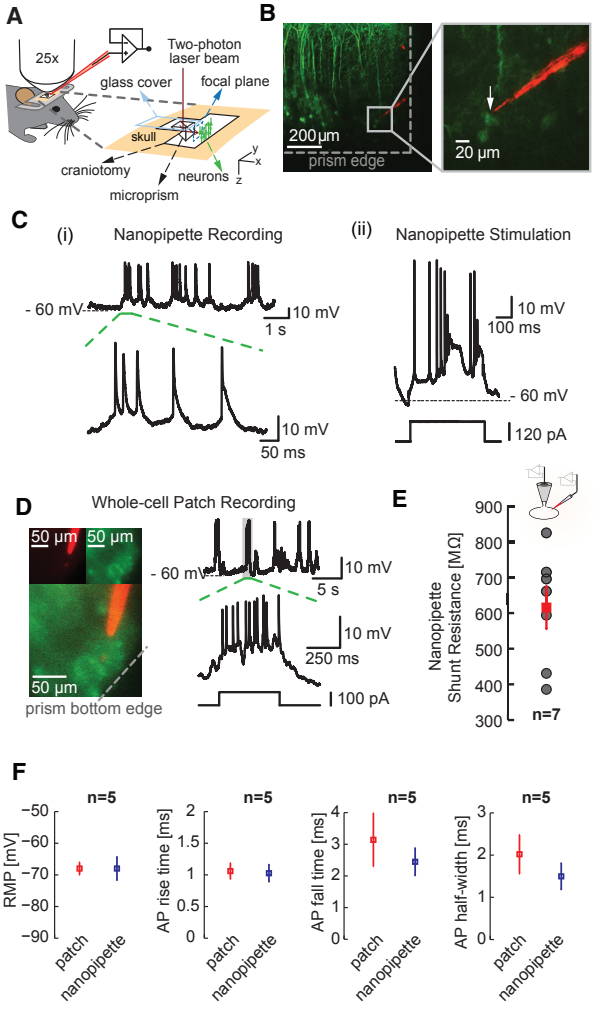

Figure 2. Targeted Intracellular Recordings from Layer 5 Neurons in the Visual Cortex of Lightly Anaesthetized Mice

(A) Illustration showing the targeted intracellular recordings technique applicable across all cortical layers. A glass microprism (height, 1 mm; width, 1 mm) with a reflective coating along the slanted edge is implanted into the brain of a head-fixed mouse. Two-photon imaging through the prism allows the visualization of labeled neurons and enables the precise guidance of the quantum-dot-coated sharp nanopipette to the target cell.

(B) Targeted nanopipette recordings (type A entry) from thy1-YFP-labeled layer 5 pyramidal neurons (top, left) using the technique outlined in (A). The prism enables the precise guidance of the nanopipette to the target cell (inset, right) and simultaneous visualization of the entire cortical column up to layer 1.

(C) (i) Intracellular measurements from the targeted pyramidal shown in (B) and typical AP characteristics (dotted green section). (ii) Membrane depolarization elicited through current injection across the sharp nanopipette in bridge mode. The electrode artifact is extremely low.

(D) Targeted whole-cell patch-clamp recordings from layer 5 pyramidal neurons. Note the high access resistances.

(E) Nanopipette shunt resistance (red) of 615.29 ± 59.69 MΩ (mean ± SEM, n = 7) measured using simultaneous whole-cell patch and nanopipette recordings (type A) from somas of neurons (inset) *in vitro* (see text for details). Gray dots reflect all measured values.

(F) Comparison of RMP, AP rise time, decay, and half-width measured using whole-cell patch pipettes (red) and nanopipettes (blue). Plots reflect mean ± SEM.

In the first case, the recordings are similar to the quasi-intracellular or in-cell recording approach (Hai et al., 2010; Moore et al., 2017), in which the cell membrane engulfs the electrode tip, creating high seal resistance. Upon electroporation, the pore resistance (R_p) drops and thus dominates the capacitive contribution to the overall impedance of the membrane junction (i.e., C_p). The recordings in this case reflect attenuated intracellular signals, because the membrane voltage gets divided across the seal resistance (R_s) and R_p (Figure 1F, right). This attenuated signal can, if needed, be deconvolved or reestimated offline using measured equivalent circuit parameters (Jayant et al., 2017) (STAR Methods; Figure S2; Methods S1). However, in the absence of an electropore, and provided R_s is high, the waveform recorded by the nanopipette reflects a high-seal extracellular signal. This is because the C_p contribution to the impedance (Figure 1F, right) dominates over R_p (i.e., C_p dV_m/dt dominates and R_p is very large). This form is similar to the cell-attached configuration in which the signal looks like the time derivative of the intracellular signal. The relative advantages of both forms of type B recording will be discussed in later sections, in which we describe recordings from dendrites and cell bodies with concomitant intracellular Ca^{2+} imaging. In this manuscript, we explicitly mention the particular cases in which type B recordings were employed and deconvolution or reestimation was used. All data presented in this manuscript are raw.

One important aspect that has traditionally precluded sharp microelectrodes from being used for targeted recordings *in vivo* is the poor visibility of the tip. Conventionally, whole-cell patch pipettes are filled with a dye, which allows the localization of the tip under two-photon illumination. Unfortunately, such dyes do not label the nanopipette shank and tip due to the miniature lumen, and they are prone to photobleaching, which makes it hard to visualize the tip (K.J., unpublished data). However, quantum dots (QDs) have a high two-photon absorption cross-section and are less prone to photobleaching, which renders them suitable labels for deep-layer *in vivo* studies (Andrásfalvy et al., 2014; Jayant et al., 2017). In this study, QD labeling of the nanopipette from the outside (Figure 1G; STAR Methods) enabled precise tip localization.

Targeted Recordings from Pyramidal Cells

To visualize the target cell and nanopipette in deep cortical layers and to enable precise registry of the QD-coated nanopipette to the target cell of interest, we used two-photon imaging through implanted microprisms (Figure 2A; Figure S3). We first targeted a layer 5 pyramidal cell in a lightly anesthetized thy1-YFP transgenic mouse (Feng et al., 2000) (STAR Methods) using flexible nanopipettes. Layer 5 somata with their main apical dendrites were visualized, and a target cell was identified by two-photon imaging through the prism (Figure 2B, left; Figures S3B and S3C). The QD-coated nanopipette was then guided to the target neuron under dual-color imaging (Figure 2B, right, inset; STAR Methods). Transmembrane access was elicited through type A, in which we clearly observed spontaneous action potentials (APs), sub-threshold activity, and cortical up states (Figure 2C, left, i) for durations routinely lasting more than 1 hr (statistics on recording durations are discussed in the section describing data from awake animals). Membrane

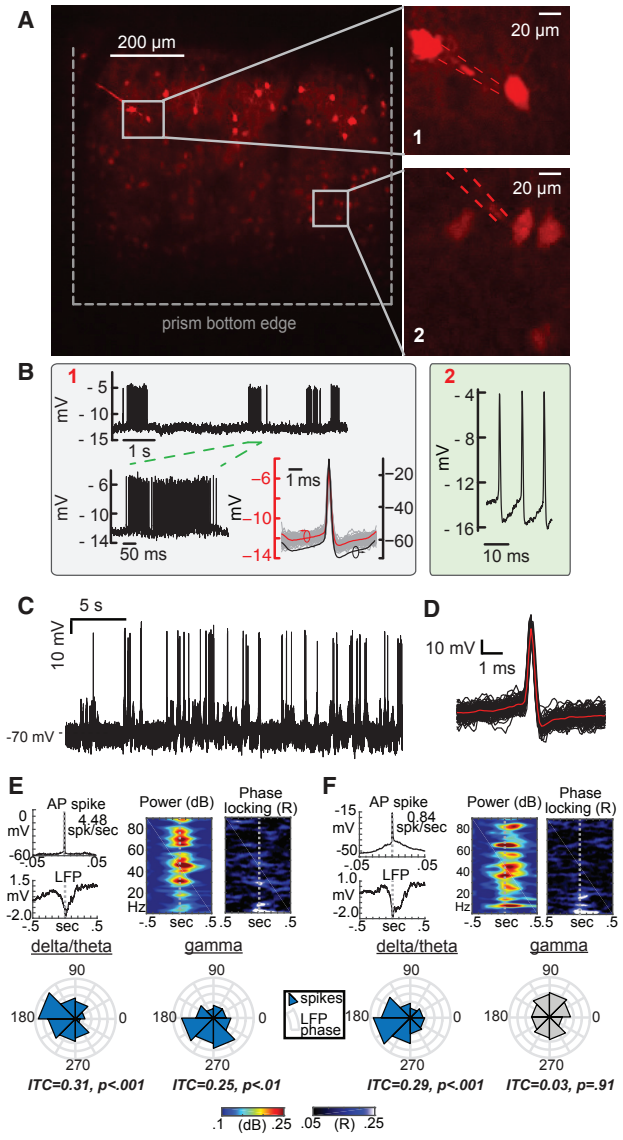

Figure 3. Targeted Intracellular Recordings from Pv Interneurons in the Visual Cortex of Lightly Anaesthetized Mice

(A) Targeted recordings from tdTomato-labeled Pv interneurons (top, left). Inset 1 (top, right, Pv1) depicts targeted contact to a layer 2/3 Pv, while inset 2 (bottom, right, Pv2) depicts image-guided access to a layer 5 Pv using the same nanopipette. The nanopipette was advanced to layer 5 once the recordings in layer 2/3 were terminated. Here, nanopipette entry was elicited through electroporation (type B, see text for details) as opposed to full penetration (mechanical advancement with electrical stimulation). Electroporation-induced entry typically lasted several minutes until the pore resealed. Then, entry into the cell could again be evoked by application of an electroporation pulse.

(B) Raw type B recordings from the Pv interneurons shown in (A): layer 2/3 Pv (left box, marked 1) and layer 5 Pv (right box, marked 2). The steady-state potentials measured via electroporation from Pv1 and Pv2 are nearly identical, indicating little or no change in the tip potential of the nanopipette. Raw waveforms reflect scaled intracellular signals due to the high impedance junction (membrane voltage is divided across seal resistance and pore resistance). Deconvolved (reestimated) APs using the measured time constants and electroporation transients (see text for details) revealed full-scale AP spikes with a 0.5 ms half-width (bottom right of left box).

shunting was negligible upon entry, which allowed unfiltered measurements of action potential (AP) amplitude with high temporal resolution. Moreover, with optimally compensated electrodes, we were able to induce AP firing activity via brief current injection (Figure 2C, right, ii). As a comparison, we imaged through the prism to guide whole-cell patch pipettes toward layer 5 pyramidal cells (850 μm below the surface of the pia) and performed stable (1.5 hr) targeted whole-cell patch-clamp recordings (Figure 2D). The SNR of whole-cell recordings (not corrected for junction potentials) was comparable in amplitude and timescale to nanopipette recordings (Figure S4), including similar baseline RMP values. Access resistances with whole-cell recordings in deep layers typically ranged between 13 and 80 MΩ. Using simultaneous whole-cell patch and nanopipette recordings from somata of layer 5 pyramidal neurons in cortical slices, we measured the effective shunting-seal resistance of the nanopipette neuron interface. The input resistance of the cell was measured using the whole-cell patch electrode before and after nanopipette penetration (Figure 2E; STAR Methods). We found a mean seal resistance of ~600 MΩ (maximum of ~820 MΩ, n = 7 cells) (Figure 2E), a value much larger than the input resistance of most neurons. Such RMPs were obtained readily during entry *in vivo* (Figure 2C; Figure S4A); hence, measurement using type A entry did not need deconvolution or reestimation. We also found that AP properties—namely, RMP, AP rise time, decay time, and AP half-width recorded using nanopipettes—were nearly identical to those measured with whole-cell patch recordings *in vivo* (n = 5 cells) (Figure 2F). Specifically, the RMP and AP half-width measured using sharp nanopipettes (−67.99 ± 3.6 mV; 1.5 ± 0.3 ms; n = 5, mean ± SEM) were similar to those measured with whole-cell patch recordings (−68 ± 2 mV; 2.02 ± 0.46 ms; n = 5, mean ± SEM) indicating negligible shunting and the formation of a tight seal. Extending the application space and demonstrating the versatility of our flexible nanopipettes, we performed paired recordings from two pyramidal cells located one above the other in layer 5 (labeled 1 and 2) (Figure S4C).

Targeted Recordings from Pv Interneurons

To expand the experimental repertoire of our combined flexible nanopipettes and microprism technique, we targeted superficial and deep-layer parvalbumin-positive (Pv) interneurons. We first recorded from layer 2/3 Pv interneurons (Pv1 and Pv2) (Figure 3A) and elicited entry via weak electroporation (type B). This mode of recording is easy to establish; occurs almost instantaneously upon contact with the cell membrane due to tight seals (either

(C) Typical sharp nanopipette recordings (raw) from Pv interneurons *in vivo* elicited via type A entry.

(D) Spike-triggered average (STA) of the measured APs from (C).

(E) STA (left) of APs from a layer 4/5 Pv (raw, top) and simultaneously recorded local field potentials (LFPs; bottom; 150 μm depth) demonstrate that spikes coincided with brief extracellular potentials or putative network-wide up states. LFP recordings display a spike-locked increase in broadband power (middle) but specific phase locking in both theta-alpha (3–10 Hz) and gamma (35 Hz) bands (right and bottom, 100 trials; p values reflect Rayleigh statistics).

(F) Recordings from a layer 5 pyramidal neuron (raw) demonstrate similar spike-locked potentials and spectral power changes in the LFP, but phase locking was only present in the delta-theta band.

quasi-intracellular or extracellular); allows long recordings (the longest recording was ~2.5 hr), especially in the presence of movement or brain tissue pulsation; and can be easily reestablished in the event of recording loss. Specifically, the electroporated pore tends to reseal, evidenced by a return of the baseline to the prerecording condition, which can be electroporated again to achieve repeated intracellular access. However, type B entry, as described earlier, results in signal attenuation due to the voltage divider between the seal and the pore resistance (Figure 1F, right). This voltage divider will affect the absolute steady-state value but still permit detection of the AP transient (alternating current; AC). We clearly observed fast spiking activity of a labeled Pv interneuron (Pv1) (Figure 3B, gray box, top), based on the measured time constants and steady-state transients. These quasi-intracellular signals could be easily deconvolved or reestimated to reflect ~70 mV amplitudes (Pv1) (Figure 3B, gray box, bottom; Figure S2; Methods S1). We then used the same electrode and proceeded to record from another visually identified Pv interneuron along the same diagonal axis but located in a deeper layer. We again elicited transmembrane access via type B entry (Pv2) (Figure 3B, green box, right) and were able to observe fast spiking activity. The steady-state potentials (i.e., baseline) measured upon entry by the nanopipette were nearly identical in both cells (about −12 mV). This shows that the pipette did not clog, electroporation resulted in similar pore diameters, seal resistances were identical, and the tip potential (i.e., offsets due to charge at the tip, nominally about −2 to −4 mV) was unchanged across the traversed distance. The concept of a liquid junction potential does not affect these recordings, because the K^+ and Cl^- mobilities are nearly the same. A constant tip potential (due to the charge of the glass wall right at the tip and the nearly constant flux of ions) can be easily measured and subtracted from the overall RMP recording.

How do type B recordings compare with impalement-based (type-A) entry, and does electrolyte diffusion from the nanopipette affect Pv interneuron dynamics? To test this, we impaled Pv interneurons *in vivo* (Figure 3C). We observed that the AP amplitude, rise, decay, and RMPs were typical of Pv interneurons (Figure 3D) and were identical to the reestimated results in the cell-attached configuration (Pv1) (Figure 3B, gray box, bottom). This shows that type B recordings are physiological and can be used when full membrane impalement is not possible. Stable intracellular recording properties for ~1 hr and a calculated diffusional flux of ~0.1–1 fM/s proved that diffusion of KCl across the nanometer opening of the pipette does not affect cell physiology. Yet the lack of diffusion precludes diffusion of dye across the pipette tip, which makes it hard to backfill a neuron. To complete the overall characterization of the method, we studied the relation between intracellular Pv signals and network activity. To this effect, we combined intracellular recordings with local field potential (LFP) measurements (Figures 3E and 3F). We found that Pv intracellular APs clearly coincided with the LFP, demonstrating a spike-locked increase in broadband power (Figure 3E, top). Specific phase locking (Siapas et al., 2005; Womelsdorf et al., 2014) (Figure 3E, bottom) was clearly observed in both the theta-alpha band (3–12 Hz) and the gamma band (35 Hz), which is a hallmark of cortico-hippocampal Pv interneuron activity. In contrast, although intracellular recordings from targeted pyramidal cells showed similar spike-locked potentials and spectral power trends (Figure 3F, top), phase locking was only present in the delta-theta band (1–8 Hz) (Figure 3F, bottom), confirming that our targeted approach was specific to the cell visualized.

Robust and Stable Intracellular Recordings in Awake-Behaving Mice

We next performed intracellular recordings using flexible nanopipettes from awake head-fixed mice, allowed to move on a running wheel (Figure 4A). Although targeted recordings have been performed in awake head-fixed animals (Polack et al., 2013) and freely moving animals (Lee et al., 2006; Long and Lee, 2012), the mechanical mismatch between patch pipette and cell is a major contributor to recording disruption. Specifically, and as in the case of mice, body movements such as crouching, swaying from side to side, walking, and running are common (Figure 4A) and can easily lead to loss of recording. It is paramount that the electrode be able to both stimulate and record without loss of seal under these conditions. We first recorded from neurons ~800 μm below the pia (Figure 4B) using our flexible nanopipettes blindly. We elicited break-in (type A), with a stable baseline RMP (Figure 4B, black). Intracellular entry was established, and the movement of the mouse was monitored via a motion sensor on the wheel (Figure 4B, gray). A single transition in the motion sensor trace indicates subtle movement or single steps, while multiple transitions indicate running. We then injected brief current (Figure 4B, red) pulses into the cell to evoke an AP response and observed normal AP amplitude, rise time, and decay without loss of signal quality (Figure 4B, inset). Once the mouse stopped moving, spontaneous AP activity continued with the same stable RMP, demonstrating that the nanopipette was able to maintain a stable seal both upon entry and in the presence of locomotion. In a separate experiment we targeted Pv interneurons 600 μm below the surface of the pia, using flexible nanopipettes and microprisms (Figure 4C). We found a stable baseline, even during running (Figure 4C, gray), without loss of recording. We observed that the AP firing rate increased while running (Figure 4C, red), reduced when motion stopped (Figure 4C, blue), and increased again during subtle motion (Figure 4C, green). We clearly observed a slight depolarization in the RMP just as locomotion started (Figure 4C, green), which has been shown to influence brain state-dependent signal processing (Polack et al., 2013). The AP amplitude was nearly constant throughout the time the mouse was running, again indicative of stable and high seal resistance.

We then proceeded to demonstrate the stability (i.e., of RMP and AP amplitude), repeatability (i.e., number of cells per nanopipette), and robustness (i.e., duration of recordings) of the nanopipette under such conditions. We demonstrated repeatability concomitantly by recording blindly from multiple cells using a single nanopipette across ~900 μm of the cortex with both type A entry (n = 4 mice, 5–10 cells/pipette) (Figure 4D) and type B entry (Figure S5). We considered a recording successful if the RMP was more negative than −55mV and AP potential amplitude was at least 50–70mV. The stability of the RMPs indicated an unclogged pipette and healthy seal formation in every cell entered. This ability of the pipette to remain unclogged as

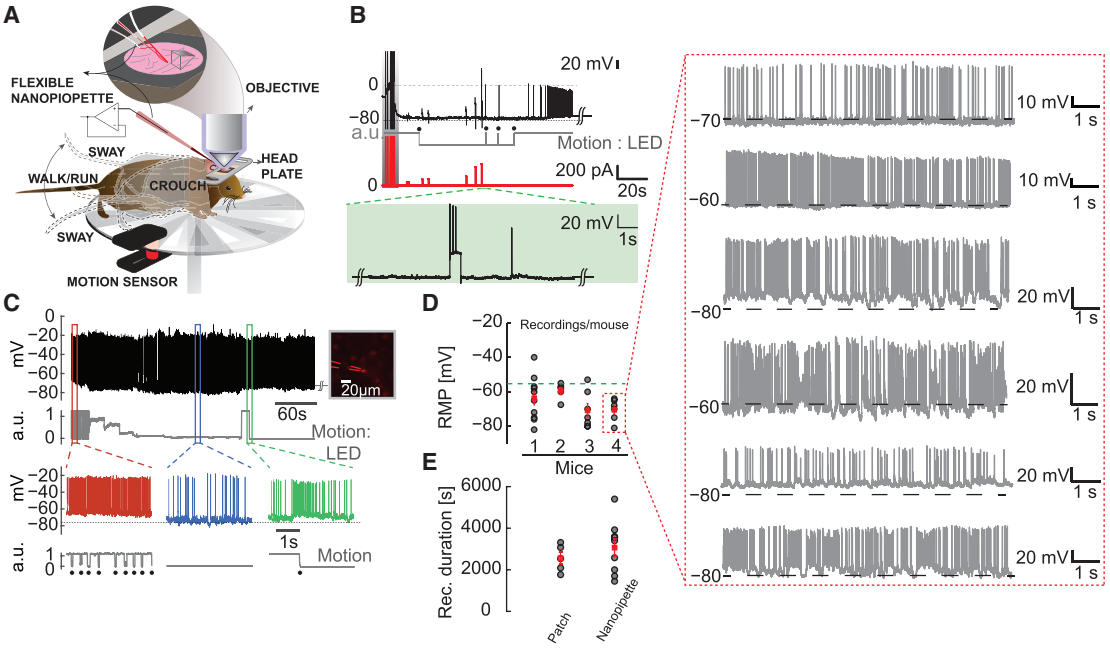

Figure 4. Targeted Intracellular Recordings from the Somatosensory Cortex in Awake Moving Mice

(A) Schematic depicting blind and targeted intracellular recording using flexible nanopipettes in the awake head-fixed animal. The mouse is allowed to move on a circular wheel. The mouse exhibits various body movements: sway, crouch, walk, and run. The flexible nanopipette bends with this motion while maintaining intracellular access (inset).

(B) Typical blind recording performed ~800 μm deep in the visual cortex (V1). Intracellular break-in (type A) is elicited upon nanopipette stimulation (dark gray, shaded region) with a stable RMP of about −78 mV. Running and rest conditions (gray trace, black dots, digitized for clarity) are monitored by the motion sensor. Current injection (red trace) elicits clear AP activity (green dotted lines, shaded region) with a minimal increase in pipette resistance (residual unbridged resistance after cell entry). Note the stable intracellular baseline even in the presence of movement.

(C) Targeted intracellular recording (type A, black trace, top) from a layer 2/3 Pv interneuron (right, inset) in the motor cortex showing stable AP amplitude and steady RMP. Recordings last ~10 min to 1 hr in the presence of locomotion. Motion sensor (gray, raw data) indicates a rapid running movement (red region) followed by a gradual decrease, eventually coming to rest (blue region), and a subsequent movement again (green region, walk or run). Note the strong correlation between onset of movement and increase in AP firing rate (green trace).

(D) RMP for ten consecutive cells measured using a single nanopipette in each mouse. Entry in all cases was type A. Note the consistency in RMPs measured across multiple cells using the same electrode. The green dotted line indicates the −55 mV mark. This result clearly demonstrates that nanopipettes do not clog and can be repeatedly reused. The red dotted box shows the amplitude and stability of each recording from mouse 4 as an example.

(E) Duration of nanopipette recordings across 7 awake mice (n = 9 cells) compared to duration of recordings achieved using the whole-cell patch recordings in anaesthetized mice.

Data reflect mean ± SEM. Note the similarity in mean and maximal durations.

it traverses across the brain was tested by recording both in the neocortex and in sub-cortical regions. We found that the pipette was essentially unchanged in resistance across depth and was able to record full-length APs, even 5 mm deep (Figure S6). The red dotted box (data from mouse 4 in Figure 4D) shows the waveforms recorded during this experiment in which every cell entered had stable baseline and AP characteristics. We held each of these cells for at least 3 min before proceeding to the next cell. This was done to demonstrate the reusable nature of the electrode. To demonstrate the stability of our recordings (i.e., the duration), we compared recording durations procured using the nanopipette across 4 awake mice with whole-cell recordings procured in anaesthetized animals. Whole-cell recordings in anaesthetized conditions present the best-case scenario in terms of recording durations, because they should be relatively immune to movement-induced failure. We were able to consistently maintain nanopipette intracellular access up to ~1 hr when exclusively testing for duration alone (n = 7 mice, 9 cells, and 6 nanopipettes) (Figure 4E). These durations performed in awake locomoting animals matched whole-cell patch recordings from anaesthetized mice (n = 5 mice and 5 cells), suggesting that the nanopipette recordings are similar in terms of stability. In contrast, type B recordings could last between 2.5 and 3.5 hr in an awake running animal and across multiple animals without loss of SNR (n = 9 cells from 4 mice) (Figure S5). Altogether, these results suggest that flexible nanopipettes can ensure minimally invasive recordings (if type B is used), facilitate high-throughput experimentation, and permit stable recordings.

Targeted Recordings from Dendrites and Simultaneous Ca^{2+} Imaging from Somata

In combination with Ca^{2+} imaging *in vivo*, intracellular recordings can potentially elucidate signal integration properties in neurons and sub-cellular dendritic processes (Palmer et al., 2014) and tie

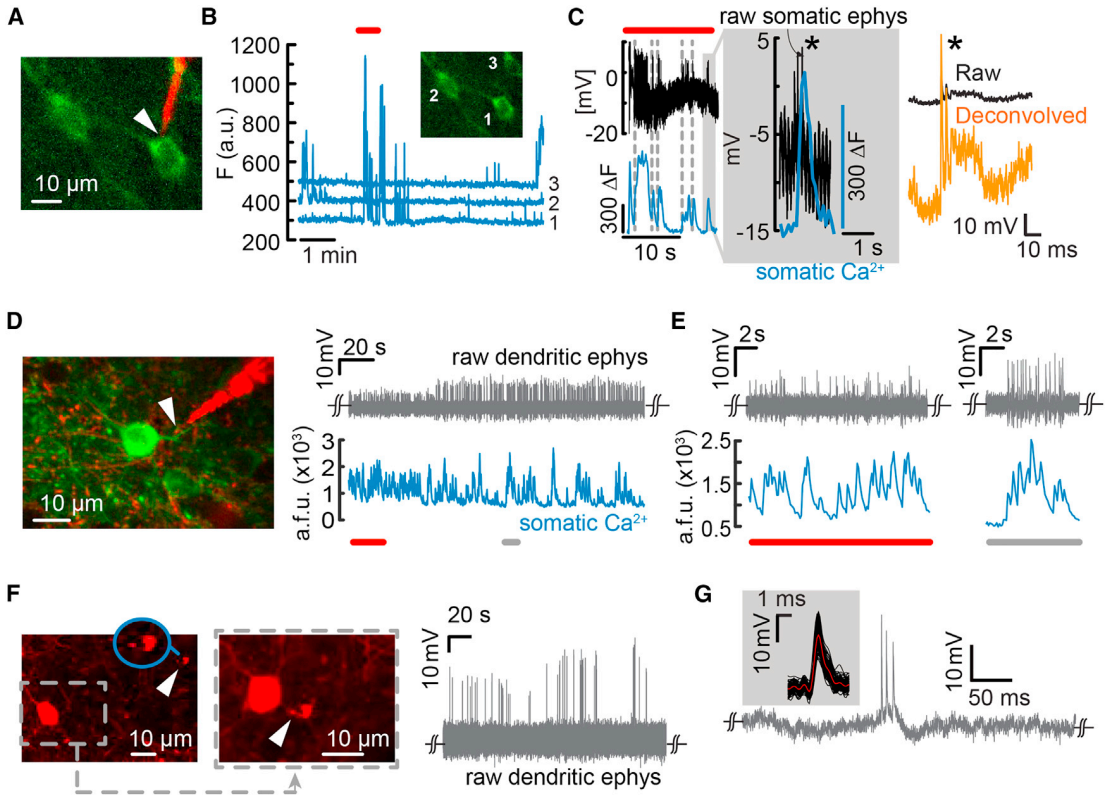

Figure 5. Simultaneous Two-Photon Ca^{2+} Imaging and Targeted Recordings from Somata and Dendrites in the Visual Cortex of Lightly Anaesthetized Mice

(A) Simultaneous Ca^{2+} imaging and targeted intracellular recordings from GCaMP6f-labeled layer 5 pyramidal cells.

(B) Raw cellular Ca^{2+} transients for both the targeted cell and the two neighboring neurons.

(C) Simultaneous Ca^{2+} transients and intracellular potential dynamics from cell 1 (region outlined by a box in B). Intracellular entry was elicited through electroporation (type B, in-cell recordings), rather than impalement, to avoid shunting. Note the clear registry of Ca^{2+} transients to APs (inset, gray shaded region). Single APs could be reestimated offline (right, orange trace).

(D) Targeted electrical recordings from a basal dendrite of a GCaMP6f-labeled layer 2/3 pyramidal neuron (left). The raw waveforms reflect a type B recording (right) in which the nanopipette forms a tight seal with the dendrite and measures a capacitively coupled signal. Simultaneous Ca^{2+} transients recorded from the soma show a high degree of correlation with the AP spikes (bottom). The extracellular SNR improved over time, indicating better seal formation.

(E) Sections of the trace shown in (D), underlined in red or gray. The nanopipette is sensitive enough to measure single dendritic spikes that coincide with somatic Ca^{2+} transients.

(F) Targeted dendritic recordings from Pv interneurons (left and middle, white arrow, and inset). The two images show the nanopipette first approaching the target Pv (left, tip magnified in blue inset) and then in contact with the dendrite (middle). Raw AP waveforms reflect a type B entry (in-cell recordings) with a high seal. The steady-state voltage measured was close to the potential measured before contact with the dendrite, indicating no intracellular access. Here, the waveform resembles an attenuated intracellular signal, indicating a stronger resistive contribution at the junction between the pipette and the membrane.

(G) Typical dendritic AP waveform and STA of the waveforms (inset) recorded from the Pv dendrite.

intracellular dynamics to population activity (Carrillo-Reid et al., 2016; Stosiek et al., 2003). To demonstrate the efficacy of the nanopipette, and the usefulness of the type B mode of recording, we performed simultaneous intracellular recordings and Ca^{2+} imaging from the soma and dendrites of labeled cells. As mentioned previously, depending on the nature of the pipette-membrane interface, type B recordings can result in either pure extracellular recordings (membrane capacitance dominates) or quasi-intracellular recordings (pore resistance dominates the capacitance contribution). First, we performed prism-assisted targeted electrophysiology from a pyramidal neuron 850 µm below the pial surface (Figure 5A) and simultaneous Ca^{2+} imaging from neighboring cell bodies in transgenic mice expressing GCaMP6f (Dana et al., 2014) (Figure 5B). Intracellular access was elicited using type B entry to avoid the formation of transmembrane shunt (Figure 5C, left). This approach resulted in attenuated spikes but could be easily reestimated offline (Figure 5C, right; Figure S2; Methods S1). Although these intracellular spikes were attenuated, the SNR was sufficiently high to observe a clear correspondence between individual APs and Ca^{2+} transients. Moreover, with electroporation-induced entry, reentry upon pore resealing could be reestablished without causing apparent damage to the cell. Then, in a separate experiment, we used our flexible nanopipettes to probe oblique dendrites close to the soma in both pyramidal cells and Pv interneurons (Figures 5D–5F). Targeted dendritic recordings were

performed similarly to the targeted somatic recordings except that the pipette was moved more slowly when close to the membrane, readjusted by slow retraction if needed, and then renavigated to the dendrite. In GCaMP6f-expressing pyramidal neurons from layer 2/3, upon contact with the proximal basal dendrite (Figure 5D, left), which measured ~1 μm in diameter, we immediately noticed high SNR extracellular spikes (Figure 5D, right), which were accompanied by corresponding Ca^{2+} transients in the soma (Figures 5D and 5E). The SNR of these recordings increased as the recording ensued, suggesting that seal formation is a dynamic process. Such recordings typically lasted several minutes (n = 6 dendrites, maximum duration of ~9 min) before we lost contact due to motion, but contact could be reestablished by subsequent pipette readjustment. With recordings made from apical dendritic segments (Figure S7), we achieved better stability and were able to clearly procure type B quasi-intracellular signals along with Ca^{2+} transients. Thus, this approach can be considered a nanoscale analog of the classical cell-attached configuration using patch pipettes. With Pv interneurons exclusively labeled by tdTomato (Figure 5F, left), dendritic recordings (Figure 5F, right) also reflected a quasi-intracellular type B interface in which the recorded waveforms resembled attenuated intracellular potentials (Figure 5G). These signals were characterized by their faster rise times and half-widths typical of Pv dendritic recordings (Hu et al., 2010). Altogether, these results indicate that nanopipettes are minimally invasive and allow targeted recording from small, sub-cellular dendritic processes.

Targeted Recordings from Pv Interneurons during Epileptic Seizures

Finally, to demonstrate the applicability of flexible nanopipettes to answer biological questions, we measured Pv interneuron dynamics in a pharmacological seizure model. Studies in brain slices and the intact brain have suggested that epileptiform activity is restrained by feedforward inhibition, the failure of which results in ictal progression (Trevelyan et al., 2006). Of the different inhibitory cell classes, Pv interneurons are considered an important source of this inhibition and have been reported to undergo firing impairment during propagation of epileptiform activity *in vitro* (Cammarota et al., 2013). However, how Pv interneurons affect local seizure progression and how they tie to ictal network activity *in vivo* remain poorly understood (Neumann et al., 2017; Wenzel et al., 2018). To address these questions, we performed prism-assisted targeted intracellular recordings from Pv interneurons, simultaneously measuring the LFP, and performed imaging Ca^{2+} activity in the local cortical network during seizure spread (Figure 6; STAR Methods). We induced epileptic seizures via brief surface application of 4-aminopyridine (4-AP) (1 mM), a well-established chemoconvulsive that leads to the acute formation of seizures, which are electrographically and behaviorally similar to focal onset seizures observed in humans (Wenzel et al., 2017). We found that the optical break-in of epileptiform activity into our field of view (Video S1) coincided with both the electrographic seizure and a Pv depolarization block (Figures 6C–6E). Moreover, before the cessation of firing, Pv neurons displayed sustained enhanced average firing rates (2 animals, 5 Pv interneurons, 15 preictal periods each, and 10.27 ± 1.956 spikes/s during the 5 s before seizure onset versus 2 animals, 5 Pv interneurons, 15 ictal periods, and 0.26 ± 0.13 spikes/s during the 5 s after seizure onset; p = 0.006) (Figure 6E). Confirming the inverse relation between Pv firing and ictal spread, toward the end of an electrographic seizure, the firing rate and RMP again stabilized (Figure 6D). Steady intracellular conditions were maintained even though the mouse at times experienced convulsions during seizures, an aspect we attribute to the flexible nature of the nanopipette. These results emphasize the critical role of Pv interneurons in restraining epileptic activity in the intact mammalian brain. Moreover, the recovery of Pv interneuron activity toward the end of seizures carries potential implications for the importance of Pv interneurons in seizure termination. For details on success rate and drawbacks, refer the Quantification and Statistical Analysis section.

DISCUSSION

Intracellular electrophysiology is a 6-decade-old foundational neuroscience technique (McIlwain and Creutzfeldt, 1967), and its basic methodology, because of its uncomplicated approach and elegance, has essentially remained unchanged. Traditionally performed using ~100 nm tip sharp glass microelectrodes (Denk and Detwiler, 1999; McIlwain and Creutzfeldt, 1967), a simple geometric modification of the pipette led to the whole-cell patch-clamp electrode widely used *in vivo* and *in vitro* (Margrie et al., 2003). Yet both types of electrodes are mechanically mismatched when applied to pliable and flexible cell membranes, which makes them susceptible to a loss of recordings in the presence of movement. Furthermore, intracellular dialysis, pipette clogging, and variable access resistances preclude high-throughput experimentation with a single pipette. Moreover, conventional sharp microelectrodes, with tip dimensions in the range of hundreds of nanometers, do not form high seals, cause a permanent shunt (Brette et al., 2008), and are prone to electrolyte leakage from the tip (Geisler et al., 1972). All these factors affect cell physiology and recording throughput and have prevented the widespread use of intracellular recordings *in vivo* from awake-behaving animals and more specifically with sharp electrodes. Here, we introduce and demonstrate the usability of flexible quartz nanopipettes, which alleviate these limitations and enable high SNR and high-throughput intracellular electrophysiology in the anaesthetized and the awake animal.

The nanopipette, a nanoscale analog of the glass sharp microelectrode, has small tips (~10–25 nm I.D.) with long narrow tapers that enable high seal resistances and tight cell-electrode coupling. As a consequence of the nanoscale form factor, these nanopipettes are ultra-flexible (~0.08 N/m), with stiffness values identical to the stiffness of soft AFM probes used to study cell mechanics (Qi et al., 2015). The narrow electrode profile also causes low electrolyte flux rates (0.1–1 fM/s) and renders the electrode reusable, thus improving recording throughput tremendously (5–10 cells/electrode) in awake moving animals. In addition to the nanopipette, and to enable targeted electrophysiology (Denk and Detwiler, 1999; Kitamura et al., 2008; Margrie et al., 2003) with single-cell resolution *in vivo* across any cortical depth, we combined it with two-photon microprism

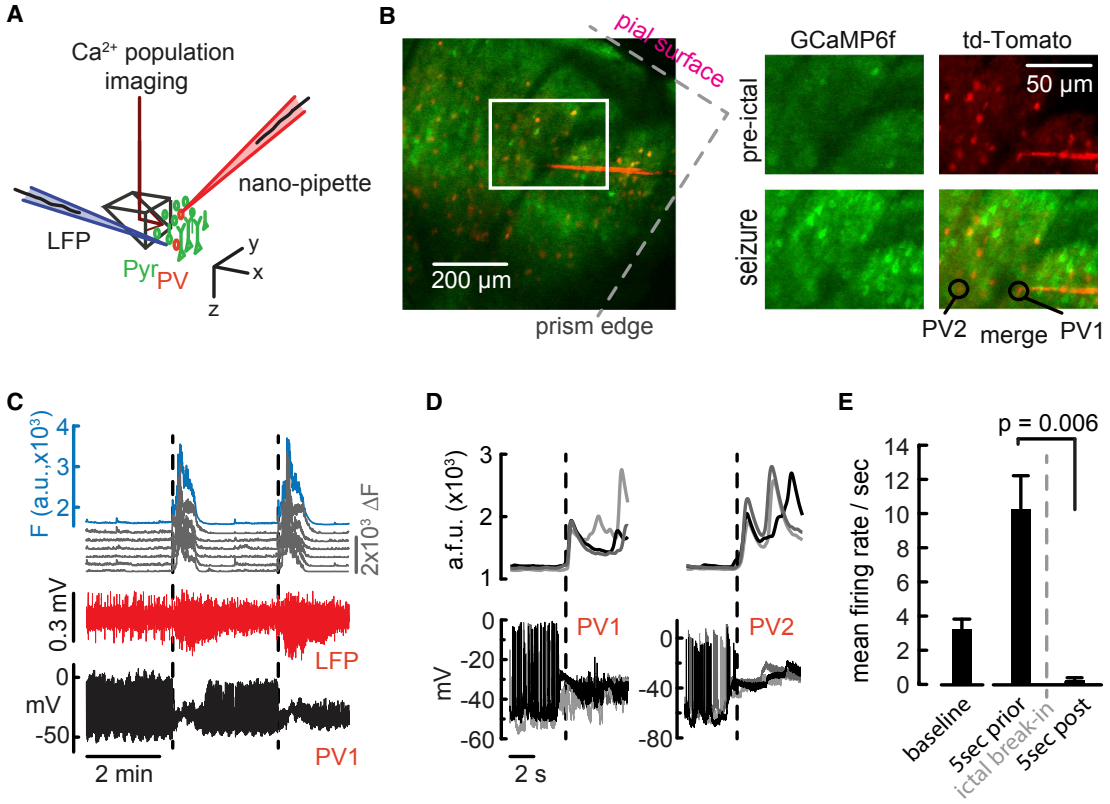

Figure 6. Simultaneous Two-Photon Population Imaging and Targeted Intracellular Recordings during Epileptic Seizure Spread

(A) Illustration showing simultaneous LFP recording, targeted intracellular recording, and dual-color two-photon imaging of both tdTomato-labeled Pv and GCaMP6f-expressing pyramidal cells from both the visual and the somatosensory cortex.

(B) Simultaneous intracellular (type A) recording from Pv interneurons (Pv1 and Pv2, red) approximately 400 µm below the surface of the pial layer, and population Ca^{2+} imaging (green) across the cortical column. The nanopipette was unchanged between recordings.

(C) Population Ca^{2+} transients from pyramidal cells (top, 5 individual cells in gray, population mean in blue) corresponded well with 4-AP-induced electrographic seizures (middle, LFP in red). Note the abrupt depolarization block in the Pv1 intracellular recording (bottom, black trace), which coincides with a sharp rise in population Ca^{2+} activity during seizure propagation into the field of view.

(D) Six consecutive seizures while recording from Pv1 and Pv2 (bottom, left and right, respectively, type A) depict the trend shown in (C). For each Pv, three consecutive optical break-ins of epileptic activity are superimposed (top, left and right, average population Ca^{2+} transient). Both Pv interneurons show consistent, immediate cessation of firing upon optical break-in of seizure activity, consistent with entering depolarization block. The intracellular membrane dynamics returned to the same baseline after each seizure period. No current was injected during voltage recordings. AP waveforms were not distorted, but firing rates changed after ictal break-in.

(E) Compared to baseline, Pv average firing rates increased during pending electrographic seizures (2 animals, 5 Pv interneurons, 15 preictal periods each, and 10.27 ± 1.956 spikes/s during the 5 s before seizure onset) but ceased upon optical break-in of ictal activity during electrographic seizure occurrence (2 animals, 5 Pv interneurons, 15 ictal periods, and 0.26 ± 0.13 spikes/s during the 5 s after seizure onset) ($p = 0.006$).

The concomitant RMP shift in (D) suggests a depolarization block.

imaging. Our approach integrates two-photon guidance through an implanted microprism and intracellular recordings using QD-labeled nanopipettes. QDs coat the nanopipette from the outside, are not prone to photobleaching, and exhibit a high cross-section of absorption, thereby allowing easy visualization of a nanoscale tip that otherwise would be impossible to locate. Intracellular recordings are facilitated by QD-coated nanopipettes that are visually guided to the target cell via two-photon microprism imaging. Two-photon targeted patching (TPTP) has predominantly been performed in superficial cortical layers (Kitamura et al., 2008; Naka and Adesnik, 2016). This is partly because of the poor visualization of target cells and the recording patch pipette in deep scattering tissue. The microprism's hypotenuse is coated with aluminum, which results in the laser beam being deflected by 90° and helps overcome two limitations that restrict *in vivo* imaging and cell targeting: visualizing deep cortical layers without scattering-imposed imaging limitations and concomitant imaging across cortical layers within a continuous, single field of view (Figure 6B; Figures S3B and S3C; Videos S1 and S2). Microprisms are inexpensive, easy to implant, and fully compatible with standard epifluorescence microscopy, two-photon imaging, and emerging methods, such as spatial light modulators (Yang et al., 2016), three-photon microscopy (Horton et al., 2013), and acousto-optic deflectors

(Grewe et al., 2010). Moreover, prisms can be used with gradient index (GRIN) lenses, which are widely employed and well suited for deep-layer imaging (Ghosh et al., 2011).

Other methods have been developed for targeted whole-cell recordings *in vivo*. Shadow patching (Kitamura et al., 2008) was introduced to allow targeted electrophysiological recordings from unlabeled cells *in vivo* based on the negative contrast of the cell body. In principle, this method could be applicable to deeper regions of the cortex, but it becomes difficult when one is interested in recording from genetically defined cell populations, like interneurons subtypes, and still suffers from scattering in deep tissue. Moreover, because a large amount of dye is continuously perfused into the extracellular space to create clearly visible shadows—which has implications for tissue health with increasing experimental time—this approach often leads to large background fluorescence signals that can affect population imaging in deep cortical areas and limits the number of times a pipette can enter the brain. Options such as automated whole-cell patching have solely focused on improving the throughput of whole-cell recordings and have not yet demonstrated concomitant population Ca^{2+} imaging or suitability in awake moving animals. Moreover, automated TPTP still suffers from the known limitations related to light scattering in brain tissue. One viable approach, in contrast to TPTP, is optogenetically assisted whole-cell patching (Muñoz et al., 2014), which requires neurons to be transfected with channelrhodopsin-2 (ChR2) under a suitable promoter. Using the standard blind patching approach, glass electrodes (carrying an optical fiber inside for light stimulus delivery) are slowly advanced through the brain until a cell is encountered. ChR2-expressing neurons fire reliably upon light stimulation. Once a time-locked firing is recorded, whole-cell recordings are established using standard procedures. While this approach is technically not limited to any depth, the lack of optical monitoring makes it difficult to ascertain the precise location of the pipette relative to the cell. Moreover, a sparse target population will adversely affect the efficiency in finding the target cell of interest. In addition, because all preceding methods use conventional patch pipettes, intracellular recordings will still suffer from throughput limitations, clogging, and high access resistances with increased depth. Recently, tetrodes were used to record quasi-intracellular signals from dendrites in a moving animal (Moore et al., 2017). Although such an approach suffers from low success rates, is blind, and cannot be used at present for targeted intracellular recordings or with two-photon imaging, it suggests flexibility and a narrow profile as key design parameters to be considered when long-duration intracellular or quasi-intracellular recordings are paramount.

Using flexible nanopipettes and microprisms, we alleviate the preceding limitations. Specifically, we perform targeted recordings from mice under different brain states (locomotion and low anesthesia). We show that nanopipettes form a tight seal with neurons exhibiting either a purely intracellular or a quasi-intracellular mode (Jayant et al., 2017; McIlwain and Creutzfeldt, 1967; Moore et al., 2017). In addition, we demonstrate six advantages: (1) a flexible, reproducible, and stable intracellular nanoelectrode; (2) an ability to perform targeted recordings using nanopipettes across any depth in the brain; (3) an ability to perform targeted recordings from dendrites; (4) an ability to perform simultaneous recordings from pairs of neurons (Figure S4C); (5) an ability to perform simultaneous targeted recordings and cellular Ca^{2+} imaging across cortical layers; and (6) an ability to record in awake moving animals. In closing, the nanoelectrode and associated methods presented in this study improve the sharp microelectrode technique and can make intracellular electrophysiology routine in awake animals, where motion-invariant recordings are paramount, enabling its widespread use in circuit neuroscience *in vivo*.

STAR★METHODS

Detailed methods are provided in the online version of this paper and include the following:

- KEY RESOURCES TABLE
- CONTACT FOR REAGENT AND RESOURCE SHARING
- EXPERIMENTAL MODEL AND SUBJECT DETAILS
  - Mice
  - Slice preparation
- METHOD DETAILS
  - *In vivo* whole-cell electrophysiology
  - Nanopipette electrophysiology
  - Slice electrophysiology
  - Quantum-dot synthesis and pipette coating
  - Local field potential (LFP) measurement
  - Two-photon imaging *in vivo*
- QUANTIFICATION AND STATISTICAL ANALYSIS
  - Image processing
  - Instantaneous amplitude/phase decomposition
  - Average power and phase locking characterization
  - Atomic Force Microscopy (AFM) measurements
  - Multiphysics Simulations
  - Success rate, drawbacks of flexible nanopipette blind and targeted recordings, and overall experimental 'n'

SUPPLEMENTAL INFORMATION

Supplemental Information includes seven figures, two videos, and one methods files and can be found with this article online at https://doi.org/10.1016/j.celrep.2018.12.019.

ACKNOWLEDGMENTS

This work was supported by the NIMH (R01MH101218 and R01MH100561), NEI (DP1EY024503 and R01EY011787), and the DFG (WE 5517/1-1). This material is also based upon work supported by, or in part by, the U.S. Army Research Office under contract W911NF-12-1-0594 (MURI) and contract DARPA-BAA-16-17. K.J. was supported by the Kavli Institute of Brain Science at Columbia. We thank all members of the Yuste lab for help and useful comments.

AUTHOR CONTRIBUTIONS

K.J. conceptualized the overall method. K.J. and M.W. designed the study and performed the experiments. Y.B. assisted with whole-cell patch recordings. K.J., M.W., and J.P.H. analyzed the data. I.J-L.P. and J.S.O. synthesized QDs. K.J. and J.H.R. performed simulations. N.M. performed AFM experiments. O.S., K.L.S., and R.Y. advised on experiments. R.Y. assembled and directed the team, provided overall supervision, and secured equipment and

funding. K.J. and M.W. wrote the manuscript. K.J., M.W., and R.Y. edited the manuscript. All authors provided comments.

DECLARATION OF INTERESTS

The authors declare no competing interests.

Received: September 14, 2017
Revised: October 23, 2018
Accepted: December 4, 2018
Published: January 2, 2019

REFERENCES

Adesnik, H., Bruns, W., Taniguchi, H., Huang, Z.J., and Scanziani, M. (2012). A neural circuit for spatial summation in visual cortex. Nature *490*, 226–231.

Andermann, M.L., Gilfoy, N.B., Goldey, G.J., Sachdev, R.N., Wölfel, M., McCormick, D.A., Reid, R.C., and Levene, M.J. (2013). Chronic cellular imaging of entire cortical columns in awake mice using microprisms. Neuron *80*, 900–913.

Andrásfalvy, B.K., Galiñanes, G.L., Huber, D., Barbic, M., Macklin, J.J., Susumu, K., Delehanty, J.B., Huston, A.L., Makara, J.K., and Medintz, I.L. (2014). Quantum dot-based multiphoton fluorescent pipettes for targeted neuronal electrophysiology. Nat. Methods *11*, 1237–1241.

Angle, M.R., and Schaefer, A.T. (2012). Neuronal recordings with solid-conductor intracellular nanoelectrodes (SCINEs). PLoS ONE *7*, e43194.

Brette, R., Piwkowska, Z., Monier, C., Rudolph-Lilith, M., Fournier, J., Levy, M., Frégnac, Y., Bal, T., and Destexhe, A. (2008). High-resolution intracellular recordings using a real-time computational model of the electrode. Neuron *59*, 379–391.

Cammarota, M., Losi, G., Chiavegato, A., Zonta, M., and Carmignoto, G. (2013). Fast spiking interneuron control of seizure propagation in a cortical slice model of focal epilepsy. J. Physiol. *591*, 807–822.

Carrillo-Reid, L., Yang, W., Bando, Y., Peterka, D.S., and Yuste, R. (2016). Imprinting and recalling cortical ensembles. Science *353*, 691–694.

Chen, T.-W., Wardill, T.J., Sun, Y., Pulver, S.R., Renninger, S.L., Baohan, A., Schreiter, E.R., Kerr, R.A., Orger, M.B., Jayaraman, V., et al. (2013). Ultrasensitive fluorescent proteins for imaging neuronal activity. Nature *499*, 295–300.

Dana, H., Chen, T.-W., Hu, A., Shields, B.C., Guo, C., Looger, L.L., Kim, D.S., and Svoboda, K. (2014). Thy1-GCaMP6 transgenic mice for neuronal population imaging *in vivo*. PLoS ONE *9*, e108697.

Denk, W., and Detwiler, P.B. (1999). Optical recording of light-evoked calcium signals in the functionally intact retina. Proc. Natl. Acad. Sci. USA *96*, 7035–7040.

Dubbs, A., Guevara, J., and Yuste, R. (2016). moco: Fast motion correction for calcium imaging. Front. Neuroinform. *10*, 6.

English, D.F., Peyrache, A., Stark, E., Roux, L., Vallentin, D., Long, M.A., and Buzsáki, G. (2014). Excitation and inhibition compete to control spiking during hippocampal ripples: intracellular study in behaving mice. J. Neurosci. *34*, 16509–16517.

Feng, G., Mellor, R.H., Bernstein, M., Keller-Peck, C., Nguyen, Q.T., Wallace, M., Nerbonne, J.M., Lichtman, J.W., and Sanes, J.R. (2000). Imaging neuronal subsets in transgenic mice expressing multiple spectral variants of GFP. Neuron *28*, 41–51.

Geisler, C.D., Lightfoot, E.N., Schmidt, F.P., and Sy, F. (1972). Diffusion effects of liquid-filled micropipettes: a pseudobinary analysis of electrolyte leakage. IEEE Trans. Biomed. Eng. *19*, 372–375.

Ghosh, K.K., Burns, L.D., Cocker, E.D., Nimmerjahn, A., Ziv, Y., Gamal, A.E., and Schnitzer, M.J. (2011). Miniaturized integration of a fluorescence microscope. Nat. Methods *8*, 871–878.

Grewe, B.F., Langer, D., Kasper, H., Kampa, B.M., and Helmchen, F. (2010). High-speed *in vivo* calcium imaging reveals neuronal network activity with near-millisecond precision. Nat. Methods *7*, 399–405.

Hai, A., Shappir, J., and Spira, M.E. (2010). In-cell recordings by extracellular microelectrodes. Nat. Methods *7*, 200–202.

Horton, N.G., Wang, K., Kobat, D., Clark, C.G., Wise, F.W., Schaffer, C.B., and Xu, C. (2013). *In vivo* three-photon microscopy of subcortical structures within an intact mouse brain. Nat. Photonics *7*, 205–209.

Houweling, A.R., and Brecht, M. (2008). Behavioural report of single neuron stimulation in somatosensory cortex. Nature *451*, 65–68.

Hu, H., Martina, M., and Jonas, P. (2010). Dendritic mechanisms underlying rapid synaptic activation of fast-spiking hippocampal interneurons. Science *327*, 52–58.

Jayant, K., Hirtz, J.J., Plante, I.J., Tsai, D.M., De Boer, W.D., Semonche, A., Peterka, D.S., Owen, J.S., Sahin, O., Shepard, K.L., and Yuste, R. (2017). Targeted intracellular voltage recordings from dendritic spines using quantum-dot-coated nanopipettes. Nat. Nanotechnol. *12*, 335–342.

Kitamura, K., Judkewitz, B., Kano, M., Denk, W., and Häusser, M. (2008). Targeted patch-clamp recordings and single-cell electroporation of unlabeled neurons *in vivo*. Nat. Methods *5*, 61–67.

Kodandaramaiah, S.B., Franzesi, G.T., Chow, B.Y., Boyden, E.S., and Forest, C.R. (2012). Automated whole-cell patch-clamp electrophysiology of neurons *in vivo*. Nat. Methods *9*, 585–587.

Lan, W.-J., Edwards, M.A., Luo, L., Perera, R.T., Wu, X., Martin, C.R., and White, H.S. (2016). Voltage-rectified current and fluid flow in conical nanopores. Acc. Chem. Res. *49*, 2605–2613.

Lee, A.K., Manns, I.D., Sakmann, B., and Brecht, M. (2006). Whole-cell recordings in freely moving rats. Neuron *51*, 399–407.

Lee, A.K., Epsztein, J., and Brecht, M. (2009). Head-anchored whole-cell recordings in freely moving rats. Nat. Protoc. *4*, 385–392.

Liu, J., Fu, T.-M., Cheng, Z., Hong, G., Zhou, T., Jin, L., Duvvuri, M., Jiang, Z., Kruskal, P., Xie, C., et al. (2015). Syringe-injectable electronics. Nat. Nanotechnol. *10*, 629–636.

Long, M.A., and Lee, A.K. (2012). Intracellular recording in behaving animals. Curr. Opin. Neurobiol. *22*, 34–44.

Long, M.A., Jin, D.Z., and Fee, M.S. (2010). Support for a synaptic chain model of neuronal sequence generation. Nature *468*, 394–399.

Long, B., Li, L., Knoblich, U., Zeng, H., and Peng, H. (2015). 3D image-guided automatic pipette positioning for single cell experiments *in vivo*. Sci. Rep. *5*, 18426.

Margrie, T.W., Brecht, M., and Sakmann, B. (2002). *In vivo*, low-resistance, whole-cell recordings from neurons in the anaesthetized and awake mammalian brain. Pflugers Arch. *444*, 491–498.

Margrie, T.W., Meyer, A.H., Caputi, A., Monyer, H., Hasan, M.T., Schaefer, A.T., Denk, W., and Brecht, M. (2003). Targeted whole-cell recordings in the mammalian brain *in vivo*. Neuron *39*, 911–918.

McIlwain, J.T., and Creutzfeldt, O.D. (1967). Microelectrode study of synaptic excitation and inhibition in the lateral geniculate nucleus of the cat. J. Neurophysiol. *30*, 1–21.

Moore, J.J., Ravassard, P.M., Ho, D., Acharya, L., Kees, A.L., Vuong, C., and Mehta, M.R. (2017). Dynamics of cortical dendritic membrane potential and spikes in freely behaving rats. Science *355*, eaaj1497.

Muñoz, W., Tremblay, R., and Rudy, B. (2014). Channelrhodopsin-assisted patching: *in vivo* recording of genetically and morphologically identified neurons throughout the brain. Cell Rep. *9*, 2304–2316.

Naka, A., and Adesnik, H. (2016). Inhibitory circuits in cortical layer 5. Front. Neural Circuits *10*, 35.

Neumann, A.R., Raedt, R., Steenland, H.W., Sprengers, M., Bzymek, K., Navratilova, Z., Mesina, L., Xie, J., Lapointe, V., Kloosterman, F., et al. (2017). Involvement of fast-spiking cells in ictal sequences during spontaneous seizures in rats with chronic temporal lobe epilepsy. Brain *140*, 2355–2369.

Packer, A.M. (2011). Understanding the nervous system as an information processing machine: dense, nonspecific, canonical microcircuit architecture of inhibition in neocortex and A neural circuit for angular velocity computation (Columbia University), PhD thesis.

Packer, A.M., Russell, L.E., Dalgleish, H.W.P., and Häusser, M. (2015). Simultaneous all-optical manipulation and recording of neural circuit activity with cellular resolution *in vivo*. Nat. Methods *12*, 140–146.

Palmer, L.M., Shai, A.S., Reeve, J.E., Anderson, H.L., Paulsen, O., and Larkum, M.E. (2014). NMDA spikes enhance action potential generation during sensory input. Nat. Neurosci. *17*, 383–390.

Petersen, C.C.H. (2017). Whole-cell recording of neuronal membrane potential during behavior. Neuron *95*, 1266–1281.

Petersen, C.C., and Crochet, S. (2013). Synaptic computation and sensory processing in neocortical layer 2/3. Neuron *78*, 28–48.

Pluta, S., Naka, A., Veit, J., Telian, G., Yao, L., Hakim, R., Taylor, D., and Adesnik, H. (2015). A direct translaminar inhibitory circuit tunes cortical output. Nat. Neurosci. *18*, 1631–1640.

Pnevmatikakis, E.A., Soudry, D., Gao, Y., Machado, T.A., Merel, J., Pfau, D., Reardon, T., Mu, Y., Lacefield, C., Yang, W., et al. (2016). Simultaneous denoising, deconvolution, and demixing of calcium imaging data. Neuron *89*, 285–299.

Polack, P.-O., Friedman, J., and Golshani, P. (2013). Cellular mechanisms of brain state-dependent gain modulation in visual cortex. Nat. Neurosci. *16*, 1331–1339.

Qi, Y., Andolfi, L., Frattini, F., Mayer, F., Lazzarino, M., and Hu, J. (2015). Membrane stiffening by STOML3 facilitates mechanosensation in sensory neurons. Nat. Commun. *6*, 8512.

Robinson, J.T., Jorgolli, M., Shalek, A.K., Yoon, M.H., Gertner, R.S., and Park, H. (2012). Vertical nanowire electrode arrays as a scalable platform for intracellular interfacing to neuronal circuits. Nat. Nanotechnol. *7*, 180–184.

Schneider, D.M., Nelson, A., and Mooney, R. (2014). A synaptic and circuit basis for corollary discharge in the auditory cortex. Nature *513*, 189–194.

Siapas, A.G., Lubenov, E.V., and Wilson, M.A. (2005). Prefrontal phase locking to hippocampal theta oscillations. Neuron *46*, 141–151.

Stosiek, C., Garaschuk, O., Holthoff, K., and Konnerth, A. (2003). *In vivo* two-photon calcium imaging of neuronal networks. Proc. Natl. Acad. Sci. USA *100*, 7319–7324.

Svoboda, K., Denk, W., Kleinfeld, D., and Tank, D.W. (1997). *In vivo* dendritic calcium dynamics in neocortical pyramidal neurons. Nature *385*, 161–165.

Svoboda, K., Helmchen, F., Denk, W., and Tank, D.W. (1999). Spread of dendritic excitation in layer 2/3 pyramidal neurons in rat barrel cortex *in vivo*. Nat. Neurosci. *2*, 65–73.

Theer, P., Hasan, M.T., and Denk, W. (2003). Two-photon imaging to a depth of 1000 microm in living brains by use of a Ti:Al2O3 regenerative amplifier. Opt. Lett. *28*, 1022–1024.

Tian, B., Cohen-Karni, T., Qing, Q., Duan, X., Xie, P., and Lieber, C.M. (2010). Three-dimensional, flexible nanoscale field-effect transistors as localized bioprobes. Science *329*, 830–834.

Tischbirek, C., Birkner, A., Jia, H., Sakmann, B., and Konnerth, A. (2015). Deep two-photon brain imaging with a red-shifted fluorometric Ca2+ indicator. Proc. Natl. Acad. Sci. USA *112*, 11377–11382.

Trevelyan, A.J., Sussillo, D., Watson, B.O., and Yuste, R. (2006). Modular propagation of epileptiform activity: evidence for an inhibitory veto in neocortex. J. Neurosci. *26*, 12447–12455.

Viventi, J., Kim, D.H., Moss, J.D., Kim, Y.S., Blanco, J.A., Annetta, N., Hicks, A., Xiao, J., Huang, Y., Callans, D.J., et al. (2010). A conformal, bio-interfaced class of silicon electronics for mapping cardiac electrophysiology. Sci. Transl. Med. *2*, 24ra22.

Wenzel, M., Hamm, J.P., Peterka, D.S., and Yuste, R. (2017). Reliable and elastic propagation of cortical seizures *in vivo*. Cell Rep. *19*, 2681–2693.

Wenzel, M., Hamm, J.P., Peterka, D.S., and Yuste, R. (2018). Seizures start as silent microseizures by neuronal ensembles. bioRxiv. https://doi.org/10.1101/358903.

Womelsdorf, T., Valiante, T.A., Sahin, N.T., Miller, K.J., and Tiesinga, P. (2014). Dynamic circuit motifs underlying rhythmic gain control, gating and integration. Nat. Neurosci. *17*, 1031–1039.

Yang, W., Miller, J.E., Carrillo-Reid, L., Pnevmatikakis, E., Paninski, L., Yuste, R., and Peterka, D.S. (2016). Simultaneous multi-plane imaging of neural circuits. Neuron *89*, 269–284.

Yazaki-Sugiyama, Y., Kang, S., Câteau, H., Fukai, T., and Hensch, T.K. (2009). Bidirectional plasticity in fast-spiking GABA circuits by visual experience. Nature *462*, 218–221.

Yuste, R., and Katz, L.C. (1991). Control of postsynaptic Ca2+ influx in developing neocortex by excitatory and inhibitory neurotransmitters. Neuron *6*, 333–344.

Reduced Repertoire of Cortical Microstates and Neuronal Ensembles in Medically Induced Loss of Consciousness

Die zuvor erfolgte Etablierung multimodaler Versuchsaufbauten mit chronischer *in vivo* 2P-Mikroskopie und Elektrophysiologie (Feld- und Einzelzellmessungen) in wachen Mäusen, sowie Korrelation mit Verhaltensparametern ermöglichte ein feingradiges Studium lokaler neuronaler Zellverbände unter physiologischen sowie pathologischen Bedingungen. In der folgend zusammengefassten Studie (Wenzel et al., 2019b) wurde dieser experimentelle Ansatz zur Erfassung mikroanatomischer Dynamiken lokaler neuronaler Ensembles genutzt, um erstmals ihren möglichen Einfluss auf den medizinisch induzierten Bewusstseinsverlust (*medically induced loss of consciousness*; mLOC) zu untersuchen. Die hier zusammengefasste Studie basierte auf Harry Nyquists Berechnungen zur Telegraphie (Nyquist, 1924), welchen zufolge die Transmission von Information (y; in Bits) logarithmisch vom zur Verfügung stehenden Symbolrepertoire (x) abhängt ($y = \log_2(x)$), sowie theoretischen neurowissenschaftlichen Überlegungen, wonach eine sinnvolle Diskrimination und Verarbeitung eines spezifischen Sinnesreizes die zerebrale Fähigkeit erfordert, diesen von einer Vielzahl alternativer Sinnesreize zu unterscheiden (Tononi, 2008). Demzufolge wurde nun hier hypothetisiert, dass sich die notwendige neuronale Repräsentanz dieser Fähigkeit in einer messbaren Anzahl unterscheidbarer lokaler Hirnaktivitätsmuster auf Ebene lokaler neuronaler Ensembles widerspiegelt und dass dieses Musterrepertoire über quantitative Bewusstseinsebenen (z.B. Wachheit, Generalanästhesie) hinweg verschiedene Ausmaße aufweist.

Im primären und sekundären visuellen Kortex (ca. 150 μm subpial) sowie in der CA1 Region des Hippocampus (ca. 100 μm unter der Kapsel) wurde in ausgewachsenen Mäusen, in welchen ein chronisch neokortikales oder hippokampales Fenster etabliert worden war, mittels *in vivo* 2P-Mikroskopie über fünf verschiedene quantitative Bewusstseinsstufen (Wachheit, milde / chirurgische / tiefe Anästhesie, Aufwachen) zellulär auflösende neuronale Ca^{2+} Netzwerkaktivität (GCaMP6) gemessen (Abb. 1 A, B, E, F). Die nahtlose Einleitung der Anästhesie mittels Isofluran aus dem Wachen heraus erfolgte über ein eigens entworfenes Ventilationssystem, das direkt vor der Maus angebracht und an welches diese vor der Durchführung des Experiments habituiert worden war (Abb. 1 A). Neben der Bildgebung wurden gleichzeitig

Messungen lokaler Feldpotenziale (LFP) sowie der Lokomotion (Infrarotsensor am Laufrad) durchgeführt (Abb. 1 A, C, D). Die LFP Messungen dienten neben klinischen Parametern (z.B. Lokomotion, Atemfrequenz, Schmerzreaktion) dazu, die Tiefe der Anästhesie zu objektivieren und so die verschiedenen quantitativen Bewusstseinszustände nach empirischen Maßstäben über Mäuse hinweg vergleichbar zu machen (Abb. 1 C). Vier der fünf genannten experimentellen Bedingungen (abgesehen vom inhärent dynamischen Aufwachprozess) wurden jeweils in einem *steady state* aufgezeichnet. Soweit technisch möglich, wurden die experimentellen Ergebnisse in Mäusen sodann intraoperativ in 2 Epilepsiepatienten, bei welchen im Rahmen der prä-epilepsiechirurgischen Diagnostik zusätzlich zu klinisch indizierten Tiefenelektroden ebenfalls Mikroelektroden-Arrays mit Einzelzellauflösung im Gyrus temporalis medius implantiert wurden (Abb. 2 A-B), über drei verschiedene Anästhesietiefen (Propofol, milde / chirurgische / tiefe Anästhesie) nachvollzogen.

Die individuell programmierte Datenanalyse (MATLAB®, MathWorks) beinhaltete nach Extraktion somatischer Ca^{2+} Transienten von Einzelneuronen (ΔF/F) aus den rohen Bildserien (30 Hz Bildwiederholungsrate, 512 x 512 Pixel, FOV typischerweise 400 x 400 μm) und algorithmischer Binarisierung (Abb. 1 B) der neuronalen Aktivität mehrere Ansätze zur Identifikation unterscheidbarer lokaler neuronaler Aktivitätsmuster über die fünf genannten experimentellen Bedingungen hinweg. Im Sinne einer Minimierung algorithmenspezifischer Ergebniseinflüsse wurden unterscheidbare neuronale Populationsaktivitätsmuster (Ca^{2+}: Maus, n=7; Single Units: Mensch, n=2) mittels 4 komplett unterschiedlicher Berechnungsarten, *t-distributed stochastic neighbor embedding* und konsekutiver Wasserscheidensegmentation (t-SNE/WS, Abb. 1 G)(Van Der Maaten und Hinton, 2008), *affinity propagation clustering* (APC) (Frey und Dueck, 2007), Hauptkomponentenanalyse (PCA), oder *Lempel-Ziv-Welch Complexity* (LZWC)(Welch, 1984; Ziv und Lempel, 1978) berechnet. Zum Ausschluss willkürlich identifizierter Ensemble-Aktivitätsmuster wurden für jede experimentelle Bedingung gemessene Muster mit randomisierten Mustern in statistischen Bezug gesetzt (Abb. 1 L, 2 L). Die LFP Analyse diente der möglichst objektiven Bestimmung der fünf (drei im Menschen) genannten experimentellen Bedingungen (jeweils 10 min): Wachheit (Maus), leichte Sedierung (Maus/Mensch; Verlangsamung des LFP Signals, jedoch

der Wachheit ähnlich), chirurgische Anästhesie (Maus/Mensch; kontinuierlich erhöhte Spektralleistung im Delta-Frequenzbereich [1-4 Hz]), tiefe Anästhesie (Maus/Mensch; Burst-suppression Muster) und Aufwachen (Maus; Isofluran aus)(Abb. 1 C, 2 C).

Die zwei wesentlichen, in Mäusen sowie menschlichen Patienten erzielten Ergebnisse der Studie ergaben einerseits eine anästhesietiefenabhängige reversible Reduktion des Repertoires lokal diskriminierbarer neuronaler Populationsaktivitätsmuster (Abb. 1 K, 2 G-K), andererseits eine Fragmentierung lokaler neuronaler Koaktivität, also einen Zerfall neuronaler Ensembleaktivität hin zu Einzelneuronaktivität (Abb. 1 M-N, 2 M-N). Beide Ergebnisse sprechen dafür, dass lokale Neuronenverbände eine Rolle im mLOC spielen, da beide diese Formen neuronaler Aktivität fundamental wichtig sind für sinnvolle kognitive Hirnoperationen und effizienter Aktivierung nachgeschalteter neuronaler Gruppen im kognitiven Prozess (Buzsáki, 2010; Carrillo-Reid und Yuste, 2020; Harris et al., 2003; Hebb, 1949; Hopfield, 1982; Lorente de No, 1938; Yuste, 2015). Die Ergebnisse dieser Studie legen entgegen der verbreiteten Meinung eines primär makroanatomischen Verlusts der Informationsintegration während mLOC nahe (Barttfeld et al., 2015; Hudetz et al., 2015, 2016; Lewis et al., 2012; Schroeder et al., 2016), dass der Zusammenbruch von Information über makroanatomische Hirnareale hinweg während mLOC eine Folge des Zusammenbruchs lokaler Informationsstrukturen im Gehirn darstellt. Die hier gewonnenen Ergebnisse waren über Spezies (Maus, Mensch), primäre sensorische und höhergeordnete Cortices sowie typische Generalanästhetika (Isofluran [Maus], Propofol [Mensch]) und Analysearten (t-SNE/WS, APC, PCA, LZWC) hinweg konsistent.

Cell Systems
Brief Report

Reduced Repertoire of Cortical Microstates and Neuronal Ensembles in Medically Induced Loss of Consciousness

Michael Wenzel,[1,2,6,7,8,*] Shuting Han,[1,2,6] Elliot H. Smith,[3,6] Erik Hoel,[1,2] Bradley Greger,[4] Paul A. House,[5] and Rafael Yuste[1,2]
[1]Department of Biological Sciences, Columbia University, New York, NY 10027, USA
[2]NeuroTechnology Center, Columbia University, New York, NY 10027, USA
[3]Department of Neurological Surgery, Columbia University Medical Center, New York, NY 10032, USA
[4]School of Biological and Health Systems Engineering, Arizona State University, Tempe, AZ 85287, USA
[5]Department of Neurosurgery, University of Utah, Salt Lake City, UT 84132, USA
[6]These authors contributed equally
[7]Present address: Department of Epileptology, University of Bonn, Bonn, 53127 Bonn, Germany
[8]Lead Contact
*Correspondence: michaelwenzel2946@gmail.com
https://doi.org/10.1016/j.cels.2019.03.007

SUMMARY

Medically induced loss of consciousness (mLOC) during anesthesia is associated with a macroscale breakdown of brain connectivity, yet the neural microcircuit correlates of mLOC remain unknown. To explore this, we applied different analytical approaches (t-SNE/watershed segmentation, affinity propagation clustering, PCA, and LZW complexity) to two-photon calcium imaging of neocortical and hippocampal microcircuit activity and local field potential (LFP) measurements across different anesthetic depths in mice, and to micro-electrode array recordings in human subjects. We find that in both cases, mLOC disrupts population activity patterns by generating (1) fewer discriminable network microstates and (2) fewer neuronal ensembles. Our results indicate that local neuronal ensemble dynamics could causally contribute to the emergence of conscious states.

INTRODUCTION

Medically induced loss of consciousness (mLOC) is generated via general anesthesia enabling life-saving surgical procedures or critical care and is also a hallmark of incompletely understood disorders such as vegetative state. Despite its fundamental importance, the neural circuit and network mechanisms underlying LOC have remained unclear. Several brain areas have been implicated in causing the loss or recovery of consciousness, such as the hypothalamus (Herrera et al., 2016), thalamus (Castaigne et al., 1981), basal ganglia and claustrum (Crick and Koch, 2005; Mhuircheartaigh et al., 2010), or the brain stem (Minert et al., 2017; Moruzzi and Magoun, 1949; Penfield and Jasper, 1954). Although thalamocortical connections have been central in LOC research (Flores et al., 2017; Herrera et al., 2016; Penfield and Jasper, 1954; Steriade, 2003), the role of the cortex itself remains debated (Merker, 2007). Early on, animal studies by Lashley (1929) and Pavlov (1927) or surgical procedures on epilepsy patients (Penfield and Jasper, 1954) described the pivotal role of the cortex in cognition, yet the removal of even expansive cortical areas resulted in no apparent quantitative change of consciousness (Lashley, 1929; Pavlov, 1927; Penfield and Jasper, 1954; Scoville and Milner, 1957). However, diffusely damaged cortex, for example after hypoxia, might contribute to LOC (Jennett, 2002). Recently, fMRI studies investigating large-scale networks during mLOC have identified a breakdown of functional connectivity between cortical areas (Barttfeld et al., 2015; Hudetz et al., 2015; Lewis et al., 2012). In addition, it has been reported that local network dynamics during mLOC remain surprisingly similar to those found in the conscious state (Hudetz et al., 2016; Lewis et al., 2012), implying that LOC arises mainly from discoordination of neural activity across brain areas. Yet, to date, no study has employed techniques with sufficient spatial resolution to properly examine the basic neural signatures of LOC at the scale of cortical microcircuits (Tononi et al., 2016).

A theoretical framework suggests that consciousness depends on the brain's ability to discriminate between a specific sensory input and a large set of alternatives (Tononi, 2008). In agreement with this, several studies have identified a rich set of discriminable resting states of cortical activity at the macroscale (Barttfeld et al., 2015; Hudetz et al., 2015). With this in mind, along with the transmission rate of information depending logarithmically on the set of symbols used (Nyquist, 1924), we hypothesized that an individual's ability to discriminate between a set of alternatives at any moment should be rooted in discriminable micro-patterns of activity (microstates) at the level of local neuronal ensembles, i.e., groups of coactive neurons which have been postulated to represent functional building blocks of neural circuits (Hebb, 1949; Hopfield, 1982). If this is the case, LOC could arise from alterations in the local microcircuit, which would secondarily and unavoidably generate macroscale connectivity deficits. As a consequence, microstate dynamics across anesthetic depth and recovery could provide mechanistic insights into the basis of LOC. Using *in-vivo* two-photon calcium (Ca^{2+})

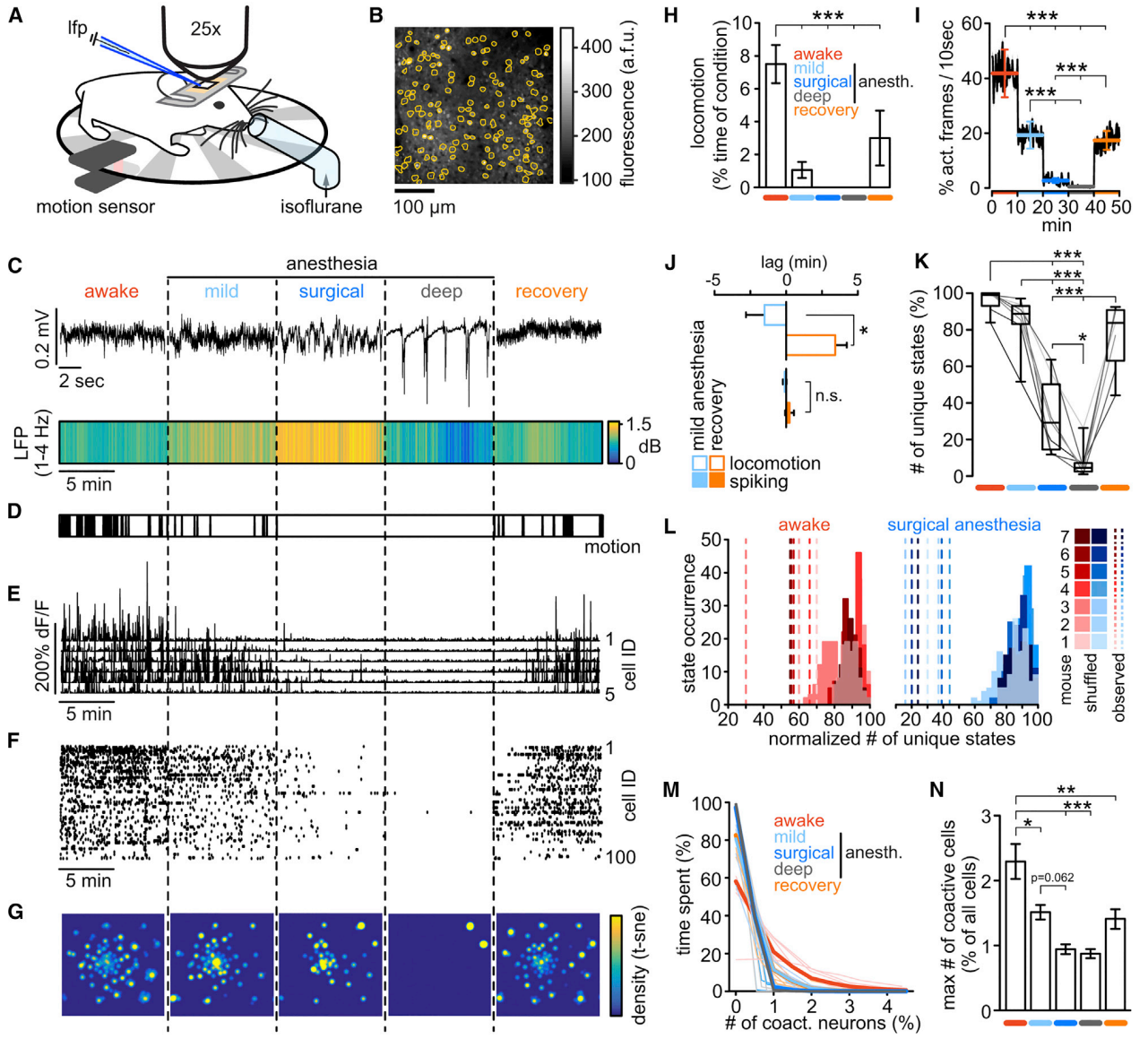

Figure 1. Reduced Repertoire of Microstates in Mice during mLOC

(A) Awake, head-restrained mouse on a running wheel. Locomotion was measured by an infrared sensor. For seamless transitions across conditions, isoflurane was delivered through a custom tube placed right in front of the mouse. For LFP recordings, a pulled glass micro-electrode was carefully inserted into the cortex at around 250 µm depth through a small burr hole next to an implanted glass cover. Through the glass, two-photon calcium imaging was performed.

(B) Image of typical field of view and registered neuronal somata outlines (orange).

(C) Upper panel: representative brief raw LFP traces across five conditions. Lower panel: avg LFP delta range [1–4 Hz] spectral power across all five 10 min long conditions (n = 7 animals). Note the continuously increased delta power during surgical anesthesia.

(D) Superimposed locomotion of all 7 mice across conditions. Note that movement is absent in surgical and burst-suppression anesthesia.

(E) Calcium transients of 5 representative registered neurons across all five conditions.

(F) Corresponding raster plot of all registered neurons.

(G) Density map of microcircuit states, visualized by t-SNE for the entire experiment, displayed per condition. Vectors representing the population activity at each time point were transformed into a two-dimensional space while preserving local structures, and a density map was generated from the scatter plot.

(H) Quantification of locomotion across the entirety of each experiment (exp.), displayed as % locomotion per condition (10 min each); anesth., anesthesia.

(I) Neural activity level across conditions, quantified as probability of detecting activity within a moving 10 s window in a yes or no fashion; conditions colored as in Figure 1H.

(J) Relationship between LOC and neural activity during mild anesthesia versus recovery. Shown are the mean lags (n = 7 mice) of events (motion or spiking) with respect to the first (5 min) and second halves (5 min) of mild anesthesia or recovery. If motion or activity were evenly distributed throughout conditions mean lags would be 0. Note how locomotion consistently stopped in the first half of the mild anesthesia condition, while it re-emerged exclusively in the second half of the recovery condition (−90.6 ± 77.6 s versus 205 ± 48.6 s, Mann Whitney test [n = 7]; p = 0.0105). Importantly, in both conditions neural activity levels were much more evenly distributed across both conditions (−6.2 ± 7.8 s versus 14.2 ± 18.3 s, Mann Whitney test [n = 7]; p = 0.62).

(legend continued on next page)

imaging in mice, we find that, across primary sensory and higher-order cortex, isoflurane-induced mLOC is indeed associated with a decreased cortical repertoire of discriminable microstates. Our results further indicate that local ensemble activity patterns undergo fragmentation during anesthesia. In addition, using micro-electrode array (MEA) single unit recordings in two human subjects, we find that a decrease in microstates also occurs during propofol-induced LOC Our results are consistent with the hypothesis that coactive neuronal ensembles are building blocks of cortical function and, in conjunction with previous studies at coarser anatomical scales (Barttfeld et al., 2015; Hudetz et al., 2015; Lewis et al., 2012; Schroeder et al., 2016), they suggest that functional connectivity of the cortex breaks down across both micro- and macroscale during mLOC.

RESULTS

Reduction of Cortical Microstates during mLOC in Mice

We first monitored the activity of neuronal populations by combining local field potential (LFP) and fast two-photon Ca^{2+} imaging in primary sensory cortex (Yang and Yuste, 2017; Yuste and Denk, 1995; Yuste and Katz, 1991) in head-restrained Thy1-GCaMP6F mice (Dana et al., 2014) allowed to move on a running wheel (Figures 1A and 1B). To ensure seamless transitions between anesthetic depths, we used a custom tube for delivery of the inhalatory anesthetic isoflurane. In 7 mice, we assessed 5 consecutive conditions (10 min each) matched across animals based on hallmark LFP patterns (Figure 1C): wakefulness, light sedation (slowed LFP yet similar to wakefulness), surgical anesthesia (continuously increased LFP delta [1–4 Hz] spectral power), deep anesthesia (burst-suppression LFP), and recovery from anesthesia (isoflurane off). To further index the animals' level of consciousness, we assessed clinical parameters (breath rate and reaction to tail pinching) and locomotion recorded by an infra-red sensor at the running wheel (Figure 1D). During surgical or burst-suppression anesthesia, mice were unresponsive to tail-pinching. Ca^{2+} transients of imaged neurons were extracted from frame series (Figures 1B and 1E) and binarized (Figure 1F, see methods). To detect similar patterns of population activity from the spike raster matrices, we performed t-distributed stochastic neighbor embedding (t-SNE) (van der Maaten and Hinton, 2008; Figure 1G) leading to a 2D embedding space from which clusters of groups of neurons with similar neural activity, or "microstates," could be identified by watershed segmentation (WS) (Figure S1A). Identified clusters were confirmed by comparing intra- and inter-cluster distances (Figure S1B). Across 7 mice, a total of 851 neurons (122 ± 12 SEM) and 34,321 active frames (4,903 ± 929 SEM) participating in 425 microstates (61 ± 9 SEM) were analyzed. To rule out spontaneous fluctuation of microstate presence as an experimental bias, we first examined their stability. We found that identified discriminable microstates remained present over at least 24 h (n = 4 exp.; microstates per exp. [d1 versus d2]: 55 versus 54, 61 versus 61, 75 versus 63, and 55 versus 51; MW test [100 ± 0% versus 93.73 ± 3.59%]: p = 0.143; Figure S1C). Across all mice, locomotion was strongly reduced during mild anesthesia and recovery, and no locomotion was detected during surgical or burst-suppression anesthesia (Figure 1H). To examine if locomotion acts as a bias by increasing the number of microstates, we determined the fraction of locomotion frames contributing to each identified microstate. Out of the 425 microstates across 7 mice, merely one state (0.24%) exclusively and one additional state (0.24%) predominantly contained activity during locomotion (Figures S1D and S1E). While not in disagreement with evidence that locomotion changes cortical gain (stimulus-driven response amplitude) (Fu et al., 2014; Niell and Stryker, 2010; Polack et al., 2013; Saleem et al., 2013), this finding is in line with previous work showing stimulus-driven ensemble activity patterns to recur spontaneously, also in the absence of any stimulus (Han et al., 2008; Kenet et al., 2003; Miller et al., 2014).

Consistent with previous studies, neural firing decreased promptly during mLOC (Figure 1I) (Ishizawa et al., 2016; Lewis et al., 2012). In line with Lewis et al., who investigated non-steady state anesthesia in humans using propofol boluses (Lewis et al., 2012), locomotion and response to tail pinching lagged behind neural activity levels during the recovery period, while, inversely, neural activity outlasted the arrest of locomotion during mLOC (Figure 1J). In contrast to recent reports (Hudetz et al., 2016; Lewis et al., 2012), the number of discriminable microstates was strongly reduced during surgical and burst-suppression anesthesia (Figure 1K). To investigate the potential influence of neuronal coactivity on the microstate classification, we repeated the analysis only using frames that contained no more than the maximum number of coactive cells observed during surgical anesthesia (2.6 ± 0.4 SEM, n = 7 mice), finding consistent results (Figure S2A).

To explore if the effect of microstate reduction during deeper anesthesia could be explained by random coactivation of sparsely active neurons, we repeated t-SNE/WS on 100 randomized datasets derived from observed data through within-frame shuffling. This procedure preserved total per-frame activity while disrupting within-frame patterns (Figures S2B and S2C). Importantly, in all mice and conditions, the number of randomly generated microstates was significantly higher than that found in the corresponding observed data (Figures 1L, S2C, and S2D), except for the wake-up period in one experiment and burst-suppression anesthesia. This lack of significant difference could be explained by a critically low overall activity. These results

(K) Boxplots of number of unique microstates (t-SNE/WS) across conditions as % of all identified unique microstates in a given experiment; line plots are individual experiments (grayscale).

(L) Total number of observed unique microstates (dashed lines) during wakefulness (red) or surgical anesth. (blue) versus corresponding distributions of values from 100 randomized datasets. (n = 7 mice, each exp. max-normalized for purpose of visualization). No overlap of observed versus random data ($p < 0.01$).

(M) Number of co-active neurons (in %, for purpose of visualization) versus the relative time spent by imaged population containing such co-activity, displayed per condition. Thick lines represent means, thin lines individual exp. conditions (N) Maximum number of co-active neurons (as % of all neurons per exp.) participating in a specific microstate, across conditions (colors as in M). Borderline statistical significance mild vs. surgical anesthesia p=0.062.

Figures 1H–1N show data from n = 7 mice; all error bars represent mean ± SEM; all boxes in boxplots represent 25–75 percentile of the data, bars within boxes represent means. Except comparison between observed and randomized data (Figure 1L) and comparison of two groups (Figure 1J), all statistical analyses represent one-way ANOVA with Bonferroni post-test. *$p < 0.05$, **$p < 0.01$, ***$p < 0.001$.

indicated that observed microstates were non-random, given sufficient activity, and that they represented a much smaller set compared to all possible states.

To rule out that our results could be due to the t-SNE/WS approach, we applied several additional analytical approaches based on different algorithms. Affinity propagation clustering (APC) (Frey and Dueck, 2007) and principal-component analysis (PCA) also showed a progressive and non-random reduction of discriminable patterns of microciruit activity across anesthetic depth (Figures S3A–S3C). Further, consistent results were obtained by calculating Lempel-Ziv-Welch complexity (LZWC) (Figures S3D and S3E; Welch, 1984; Ziv and Lempel, 1978) and the number of unique features (“words” or, collectively, “dictionary”) encountered by LZW across conditions (Figure S3F). Expectedly, the number of discriminable activity patterns was not identical across approach. The intention here was not to test if our data fit a certain algorithm’s assumption the best or not but instead to prove that the results can be reproduced from multiple algorithmic angles.

Microstate Reduction during mLOC in Mice Is Not Restricted to Primary Sensory Cortex

To exclude the possibility that our finding could be restricted to primary sensory areas, we repeated the experiments in higher order visual cortex (anterolateral, rostrolateral visual cortex) (Marshel et al., 2011) and hippocampal CA1 (stratum pyramidale) (Figures S4A and S4B; Eichenbaum, 2017). As in our experiments in primary sensory cortex, mLOC was associated with a striking reduction of discriminable microstates with increasing depth of anesthesia and recovery of states during the wake-up period (Figure S4C). Again, in both secondary visual cortex and hippocampus, observed microstates were non-random given sufficient activity (data not shown), and the results were similar across analytical approaches (Figure S4C). These experiments showed that microstate reduction during mLOC in mice is not restricted to primary sensory cortex but can be found across cortical areas.

Neuronal Ensemble Fragmentation during mLOC in Mice

While collecting data for this study, we became aware that changes in ensemble co-activity seemed to be associated with mLOC. To study this, we operationally defined an ensemble as a group of neurons that are coactive in any given frame (Miller et al., 2014). Indeed, neural co-activity within identified microstates was also consistently decreased with anesthetic depth (Figures 1M, 1N, and S5A). These neuronal ensembles were also not due to chance firing of cells, as within-cell shuffling, disrupting co-activity patterns while maintaining the same total activity per condition (Figure S2B, lower panel) led to random distributions significantly smaller than the observed data (Figures S5B and S5C). These results indicated a reduction of local ensembles (Miller et al., 2014) during mLOC, with a progression toward independent single neuron activity patterns during deeper anesthesia.

Reduction of Cortical Microstates and Ensemble Fragmentation during mLOC in Humans

To investigate whether our mouse findings hold true in humans, we studied discriminable microstates and neural coactivity across anesthetic depth in two neurosurgical patients with pharmacoresistant epilepsy undergoing pre-surgical evaluation. In addition to subdural macro-electrode implantation for epileptic focus identification in the temporal lobe (Figure 2A), these patients were implanted with a Utah MEA (4 × 4 mm, 96 electrodes, Figures 2A and 2B) measuring both LFP (Figure 2C) and single unit activity (SUA) in infragranular layers (Schevon et al., 2012) of the anterior middle temporal gyrus (Figure 2D). This higher cortical area has been shown to be involved in semantic processing (Faroqi-Shah et al., 2018), retrieval of conceptual knowledge (Davey et al., 2015), or intersensory conflict detection (van Kemenade et al., 2018). In both patients, 3 anesthetic conditions (mild, surgical, and deep [burst-suppression] anesthesia) were examined by applying intravenous propofol. Again, anesthetic depth was matched across patients based on LFP signals (Figure 2C). Since MEAs were implanted on the day clinical electrodes were removed, neither wakefulness nor the wake-up period could be recorded. As with the mouse analysis, neural firing was binarized (Figure 2D) and microstates were first identified using t-SNE/WS (Figures 2E and S1A). In the two human subjects, a total of number of 145 single units (72.5 ± 18.5 SEM) and 6,950 active frames (3,475 ± 1147 SEM, 1 frame = 100 ms epoch) participating in 89 microstates (44.5 ± 5.5 SEM) were identified. As in mice, a general drop of neural activity was observed with increasing anesthetic depth (Figure 2F). Likewise, our finding of a decrease of the number of discriminable t-SNE/WS microstates during anesthesia in mice held true in both patients (Figure 2G). Again, applying AP clustering (Figure 2H), PCA analysis (Figure 2I), LZWC, or LZW dictionary size (Figures 2J and 2K) to the data as complementary analytical approaches led to consistent results. As before, the effects could not only be explained by a random coactivation of neurons, as observed results were significantly different from randomized datasets (Figure 2L). Thus, in line with our results in mice, the local population drew from an increasingly reduced repertoire of microstates with increasing anesthetic depth. Finally, in both patients, neural coactivity patterns non-randomly disappeared with increasing depth of anesthesia (Figures 2M, 2N, and S5D).

DISCUSSION

We used cellular scale population recording techniques in mice and humans to investigate changes in microscale activity patterns across anesthetic depth and recovery from anesthesia. Our results appear at odds with a recent report (Schroeder et al., 2016), where mLOC occurred despite unchanged levels of overall activity during ketamine-induced dissociative anesthesia (Pender, 1971). But, whereas most first-line anesthetics decrease cerebral metabolism (Laaksonen et al., 2018; Pilge et al., 2014), ketamine differentially affects cerebral hemodynamics and neural firing with a net neutral effect (Cavazzuti et al., 1987; Laaksonen et al., 2018). Keeping in mind that functional brain imaging in the clinical setting relies on changes in cerebral metabolism as a proxy for neural firing (e.g., FDG-PET CT or BOLD signal in fMRI), it is not surprising that Schroeder et al. (2016) found a preserved overall firing rate. Importantly, our analysis of discriminable patterns of local network activity focused on the general presence of microstates, regardless of overall population activity. Thus, both the anesthetic and the analysis that we used are significantly different

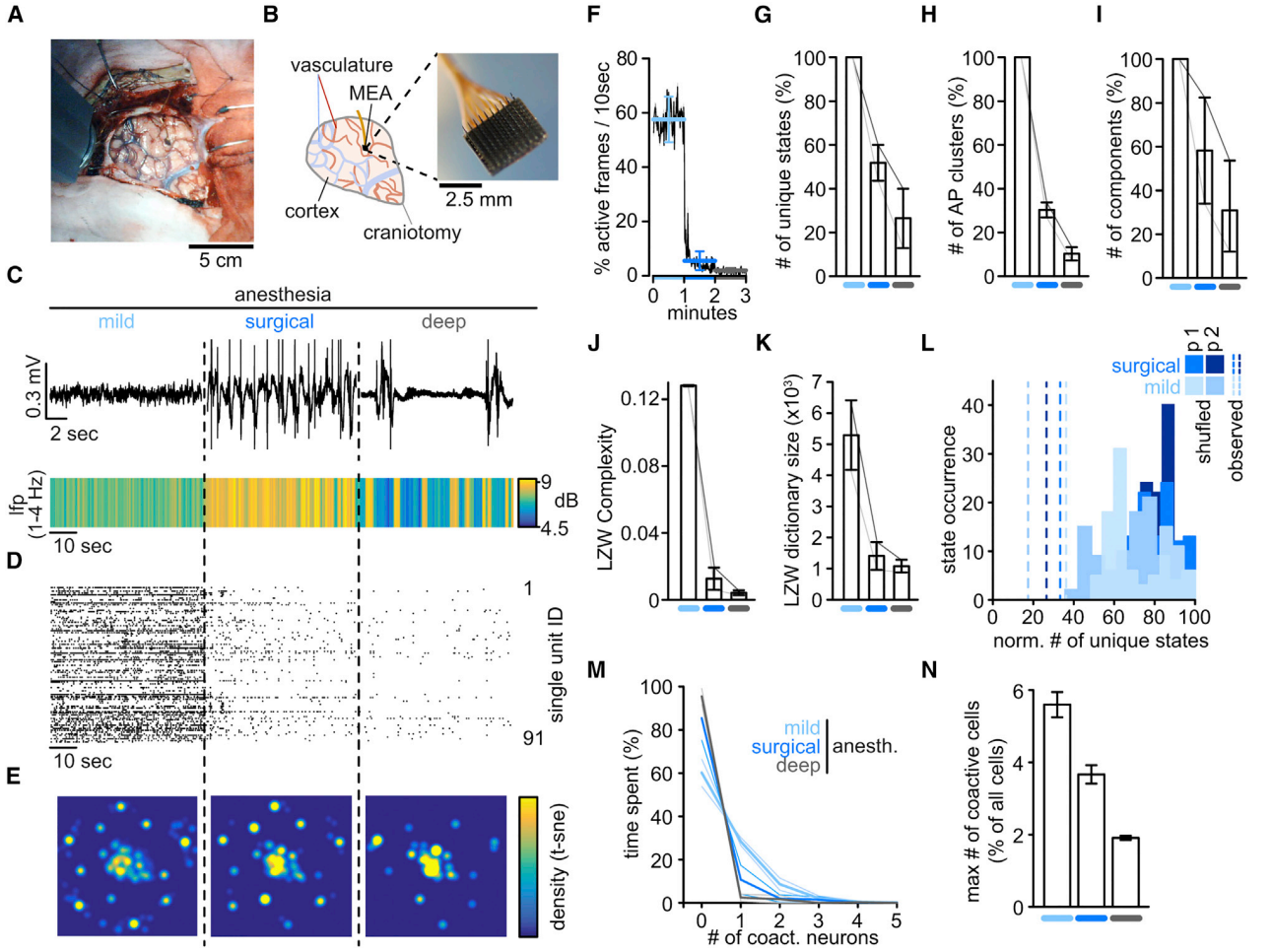

Figure 2. Reduced Repertoire of Cortical Microstates and Ensembles during mLOC in Humans

All error bars in Figure 2 represent mean ± SEM (n = 2 patients).

(A) Photo of the craniotomy carried out on one patient in this study.

(B) Left: drawing of craniotomy in (A). Craniotomy (gray); arteries (red); veins (blue), multielectrode micro-array (MEA, black). Right: close-up photo of micro-electrode array (4 x 4 mm, 96 electrodes).

(C) Upper panel: representative brief raw LFP traces across three anesthetic conditions in one patient. Lower panel: avg LFP delta range [1–4 Hz] spectral power across conditions and patients.

(D) Raster plot of all single units in one patient.

(E) Two-dimensional density plot of same data after t-SNE, displayed per condition. Every dot represents a time point containing neural activity.

(F) Neural activity level across conditions, quantified as probability of detecting activity within a moving 10 s window in a yes or no fashion; conditions colored as in (C).

(G) Number of unique microstates (t-SNE/WS) across conditions as % of all identified microstates per exp.; line plots are individual patients.

(H) Number of unique microstates (APC) across conditions as % of all identified microstates per exp.; line plots are individual patients.

(I) Number of PCA components across conditions as % of all identified components per exp.; line plots are individual patients.

(J) LZW complexity across conditions; line plots are individual patients.

(K) LZW dictionary size across conditions; line plots are individual patients.

(L) Number of observed unique microstates (dashed lines) during mild anesth. (light blue) or surgical anesth. (dark blue) versus corresponding distributions of values from 100 randomized datasets, max-normalized for purpose of visualization. No overlap of observed versus random data, equal to $p < 0.01$; p1 and p2 represent patient 1 and 2.

(M) Number of co-active neurons versus the time spent by population in time points containing such co-activity per condition, displayed as mean across patients (thick lines). Thin lines represent conditions in individual patients.

(N) Maximum number of co-active neurons (as % of all neurons per exp.) participating in a specific microstate across conditions.

from Schoeder et al., making it difficult to directly compare the studies.

The discrepancy between our findings and previous studies using similar anesthetics (Hudetz et al., 2016; Lewis et al., 2012) might be partly explained by the difference in recording techniques and signal analysis. Using a 64-electrode microarray, Hudetz et al. (Hudetz et al., 2016) described that the repertoire of mesoscale cortical activity is not altered during anesthesia. But,

importantly, analysis was carried out on LFPs filtered at 4–60 Hz, which are dominated not by neural firing itself but the summed-up synaptic activity from thousands to millions of neurons. Hudetz et al. used negative LFP deflections as a proxy for local population activity. It is important to keep in mind that while such LFP deflections may correspond to local population firing, identical negative LFP deflections may not necessarily correspond to the firing of the identical local population, as dendritic arbors are much more spatially distributed and overlapping with dendritic arbors of neighboring neurons than neural somata. As a consequence, the spatial resolution blurs and, with it, the detectable diversity of activity dynamics within local neural networks becomes hard to discern. In contrast, two-photon Ca^{2+} imaging and MEA unit recordings capture somatic firing of local groups of neurons in a spatially precise manner. Indeed, in a separate recent study using two-photon imaging of interictal epileptiform activity indicated that seemingly identical LFP deflections (filtered similarly to Hudetz et al., 2016) may be composed of varied patterns of local ensemble firing (Feldt Muldoon et al., 2013).

In addition, using a 96-electrode MEA, Lewis and colleagues (Lewis et al., 2012) reported that, while macroscale connectivity broke down during mLOC, microscale activity persisted similarly to the conscious state. This conclusion was based on pairwise correlation of a small fraction (<15%) of recorded single units showing the highest firing rate in one human subject. This preselection is debatable, given that sparse neural firing (e.g., reviewed in Barth and Poulet, 2012) and weak pairwise correlation between local neurons (Cohen and Kohn, 2011) represent elementary constituents of cortical activity. These aspects preclude neither synchronous network states (Schneidman et al., 2006) nor powerful computational dynamics of the network (Hopfield, 1982). In our human recordings, all units belonging to the recorded local network were included in the analysis across anesthetic depth.

To conclude, extending previous studies at the macroscale (Barttfeld et al., 2015; Hudetz et al., 2015; Lewis et al., 2012), our results provide evidence that during mLOC, functional connectivity of the cortex also breaks down at the microscale. Regarding general brain function, a number of mechanistic studies on local cortical circuit activity (Afraz et al., 2006; Carrillo-Reid et al., 2018; Houweling and Brecht, 2008; Huber et al., 2008; Salzman et al., 1990) have substantiated the hypothesis that local neural ensembles are functional building blocks of cognition (Hebb, 1949; Hopfield, 1982). Indeed, in a recent study, the precisely controlled simultaneous holographic activation of as few as two cortical neurons with pattern completion capabilities could trigger an entire local neural ensemble and alter performance in a visual task (Carrillo-Reid et al., 2018). This implies that behavior, which is inherently based on the integration of information processed across cortical areas, can be altered by fine-scaled local neural activity. It remains currently technically difficult to test whether the same microscale-macroscale circuit mechanisms hold true for mLOC as well, as one would need to locally interfere with a vast number of neural ensembles across the entire cortex simultaneously in order to induce mLOC or rescue it. Our results nevertheless demonstrate that, during mLOC, local microstates reversibly disappear, and neural ensembles undergo fragmentation. This implies that functional connectivity and integration of information at the macroscale should be altered, too, since it is built with these smaller functional building blocks. In sum, our study provides a micro-anatomical basis for how the cortex, along with subcortical areas in a distributed complex cerebral system, could contribute to the generation, loss, or re-gain of consciousness (Koch, 2012).

STAR★METHODS

Detailed methods are provided in the online version of this paper and include the following:

- KEY RESOURCES TABLE
- CONTACT FOR REAGENT AND RESOURCE SHARING
- EXPERIMENTAL MODEL AND SUBJECT DETAILS
  - Animal subjects
  - Human Subjects, and Ethics Statement
- METHOD DETAILS
  - Animals, Surgical Procedures, and Setup Acclimatization
  - Experimental Timeline in Mice
  - Infrared Locomotion Detection in Mice
  - Two-Photon Calcium Imaging in Mice
  - Two-Photon Image Processing
  - Local Field Potential Recordings in Mice
  - Single Unit Activity and LFP Data Acquisition and Preprocessing in Humans
  - Analysis of LFP Spectral Power in Mice or Human Subjects
  - T-SNE and Watershed Segmentation (t-SNE/WS)
  - Affinity Propagation Clustering (APC)
  - Lempel-Ziv-Welch Complexity (LZWC)
- QUANTIFICATION AND STATISTICAL ANALYSIS
  - Additional Resources
  - Code Availability

SUPPLEMENTAL INFORMATION

Supplemental Information can be found online at https://doi.org/10.1016/j.cels.2019.03.007.

ACKNOWLEDGMENTS

This work was supported by the NIMH (R01MH101218 and R01MH100561) and NEI (DP1EY024503 and R01EY011787). This material is also based upon work supported by, or in part by, the U.S. Army Research Laboratory and the U.S. Army Research Office under contract number W911NF-12-1-0594 (MURI). S.H. is a Howard Hughes Medical Institute International Student Research Fellow. We thank the Yuste lab members for input and constructive discussions.

AUTHOR CONTRIBUTIONS

M.W. conceived the study, designed, and performed all experiments in mice and wrote the manuscript. All authors discussed data, wrote the materials and methods section, and edited the manuscript. M.W. and S.H. pre-processed and analyzed data (calcium data, LFP, t-SNE/WS, AP clustering, and PCA). E.H.S. processed and spike-sorted human data. E.H. independently examined microstate alterations during LOC and provided LZW analysis for rodent and human data. B.G. and P.A.H. obtained and provided human data. R.Y. assembled and directed the team, supervised the study, and provided guidance and funding.

DECLARATION OF INTERESTS

The authors declare no competing interests.

Received: June 14, 2018
Revised: October 20, 2018
Accepted: March 14, 2019
Published: May 1, 2019

REFERENCES

Afraz, S.R., Kiani, R., and Esteky, H. (2006). Microstimulation of inferotemporal cortex influences face categorization. Nature *442*, 692–695.

Barth, A.L., and Poulet, J.F. (2012). Experimental evidence for sparse firing in the neocortex. Trends Neurosci. *35*, 345–355.

Barttfeld, P., Uhrig, L., Sitt, J.D., Sigman, M., Jarraya, B., and Dehaene, S. (2015). Signature of consciousness in the dynamics of resting-state brain activity. Proc. Natl. Acad. Sci. USA *112*, 887–892.

Carrillo-Reid, L., Han, S., Yang, W., Akrouh, A., and Yuste, R. (2018). Triggering Visually Guided Behavior by Holographic Activation of Pattern Completion Neurons in Cortical Ensembles. Biorxiv.

Castaigne, P., Lhermitte, F., Buge, A., Escourolle, R., Hauw, J.J., and Lyon-Caen, O. (1981). Paramedian thalamic and midbrain infarct: clinical and neuropathological study. Ann. Neurol. *10*, 127–148.

Cavazzuti, M., Porro, C.A., Biral, G.P., Benassi, C., and Barbieri, G.C. (1987). Ketamine effects on local cerebral blood flow and metabolism in the rat. J. Cereb. Blood Flow Metab. *7*, 806–811.

Cohen, M.R., and Kohn, A. (2011). Measuring and interpreting neuronal correlations. Nat. Neurosci. *14*, 811–819.

Crick, F.C., and Koch, C. (2005). What is the function of the claustrum? Philos. Trans. R. Soc. Lond. B Biol. Sci. *360*, 1271–1279.

Dana, H., Chen, T.W., Hu, A., Shields, B.C., Guo, C., Looger, L.L., Kim, D.S., and Svoboda, K. (2014). Thy1-GCaMP6 transgenic mice for neuronal population imaging in vivo. PLoS One *9*, e108697.

Davey, J., Cornelissen, P.L., Thompson, H.E., Sonkusare, S., Hallam, G., Smallwood, J., and Jefferies, E. (2015). Automatic and controlled semantic retrieval: TMS reveals distinct contributions of posterior middle temporal gyrus and angular gyrus. J. Neurosci. *35*, 15230–15239.

Dombeck, D.A., Harvey, C.D., Tian, L., Looger, L.L., and Tank, D.W. (2010). Functional imaging of hippocampal place cells at cellular resolution during virtual navigation. Nat. Neurosci. *13*, 1433–1440.

Eichenbaum, H. (2017). On the integration of space, time, and memory. Neuron *95*, 1007–1018.

Faroqi-Shah, Y., Sebastian, R., and Woude, A.V. (2018). Neural representation of word categories is distinct in the temporal lobe: an activation likelihood analysis. Hum. Brain Mapp. *39*, 4925–4938.

Feldt Muldoon, S., Soltesz, I., and Cossart, R. (2013). Spatially clustered neuronal assemblies comprise the microstructure of synchrony in chronically epileptic networks. Proc. Natl. Acad. Sci. USA *110*, 3567–3572.

Flores, F.J., Hartnack, K.E., Fath, A.B., Kim, S.E., Wilson, M.A., Brown, E.N., and Purdon, P.L. (2017). Thalamocortical synchronization during induction and emergence from propofol-induced unconsciousness. Proc. Natl. Acad. Sci. USA *114*, E6660–E6668.

Frey, B.J., and Dueck, D. (2007). Clustering by passing messages between data points. Science *315*, 972–976.

Fu, Y., Tucciarone, J.M., Espinosa, J.S., Sheng, N., Darcy, D.P., Nicoll, R.A., Huang, Z.J., and Stryker, M.P. (2014). A cortical circuit for gain control by behavioral state. Cell *156*, 1139–1152.

Han, F., Caporale, N., and Dan, Y. (2008). Reverberation of recent visual experience in spontaneous cortical waves. Neuron *60*, 321–327.

Hebb, D.O. (1949). The Organization of Behavior (Wiley).

Herrera, C.G., Cadavieco, M.C., Jego, S., Ponomarenko, A., Korotkova, T., and Adamantidis, A. (2016). Hypothalamic feedforward inhibition of thalamocortical network controls arousal and consciousness. Nat. Neurosci. *19*, 290–298.

Hopfield, J.J. (1982). Neural networks and physical systems with emergent collective computational abilities. Proc. Natl. Acad. Sci. USA *79*, 2554–2558.

House, P.A., MacDonald, J.D., Tresco, P.A., and Normann, R.A. (2006). Acute microelectrode array implantation into human neocortex: preliminary technique and histological considerations. Neurosurg. Focus *20*, E4.

Houweling, A.R., and Brecht, M. (2008). Behavioural report of single neuron stimulation in somatosensory cortex. Nature *451*, 65–68.

Huber, D., Petreanu, L., Ghitani, N., Ranade, S., Hromádka, T., Mainen, Z., and Svoboda, K. (2008). Sparse optical microstimulation in barrel cortex drives learned behaviour in freely moving mice. Nature *451*, 61–64.

Hudetz, A.G., Liu, X., and Pillay, S. (2015). Dynamic repertoire of intrinsic brain states is reduced in propofol-induced unconsciousness. Brain Connect *5*, 10–22.

Hudetz, A.G., Vizuete, J.A., Pillay, S., and Mashour, G.A. (2016). Repertoire of mesoscopic cortical activity is not reduced during anesthesia. Neuroscience *339*, 402–417.

Ishizawa, Y., Ahmed, O.J., Patel, S.R., Gale, J.T., Sierra-Mercado, D., Brown, E.N., and Eskandar, E.N. (2016). Dynamics of propofol-induced loss of consciousness Across primate neocortex. J. Neurosci. *36*, 7718–7726.

Jennett, B. (2002). The Vegetative State: Medical Facts, Ethical and Legal Dilemmas (Cambridge University Press).

Kenet, T., Bibitchkov, D., Tsodyks, M., Grinvald, A., and Arieli, A. (2003). Spontaneously emerging cortical representations of visual attributes. Nature *425*, 954–956.

Koch, C. (2012). In Which I Argue That Consciousness Is a Fundamental Property of Complex Things… (MIT Press).

Laaksonen, L., Kallioinen, M., Långsjö, J., Laitio, T., Scheinin, A., Scheinin, J., Kaisti, K., Maksimow, A., Kallionpää, R.E., Rajala, V., et al. (2018). Comparative effects of dexmedetomidine, propofol, sevoflurane, and S-ketamine on regional cerebral glucose metabolism in humans: a positron emission tomography study. Br. J. Anaesth. *121*, 281–290.

Lashley, K.S. (1929). Brain Mechanisms and Intelligence: A Quantitative Study of Injuries to the Brain (University of Chicago Press).

Lewis, L.D., Weiner, V.S., Mukamel, E.A., Donoghue, J.A., Eskandar, E.N., Madsen, J.R., Anderson, W.S., Hochberg, L.R., Cash, S.S., Brown, E.N., et al. (2012). Rapid fragmentation of neuronal networks at the onset of propofol-induced unconsciousness. Proc. Natl. Acad. Sci. USA *109*, E3377–E3386.

Marshel, J.H., Garrett, M.E., Nauhaus, I., and Callaway, E.M. (2011). Functional specialization of seven mouse visual cortical areas. Neuron *72*, 1040–1054.

Merker, B. (2007). Consciousness without a cerebral cortex: a challenge for neuroscience and medicine. Behav. Brain Sci. *30*, 63–81.

Mhuircheartaigh, R.N., Rosenorn-Lanng, D., Wise, R., Jbabdi, S., Rogers, R., and Tracey, I. (2010). Cortical and subcortical connectivity changes during decreasing levels of consciousness in humans: a functional magnetic resonance imaging study using propofol. J. Neurosci. *30*, 9095–9102.

Miller, J.E., Ayzenshtat, I., Carrillo-Reid, L., and Yuste, R. (2014). Visual stimuli recruit intrinsically generated cortical ensembles. Proc. Natl. Acad. Sci. USA *111*, E4053–E4061.

Minert, A., Yatziv, S.L., and Devor, M. (2017). Location of the mesopontine neurons responsible for maintenance of anesthetic loss of consciousness. J. Neurosci. *37*, 9320–9331.

Moruzzi, G., and Magoun, H.W. (1949). Brain stem reticular formation and activation of the EEG. Electroencephalogr. Clin. Neurophysiol. *1*, 455–473.

Niell, C.M., and Stryker, M.P. (2010). Modulation of visual responses by behavioral state in mouse visual cortex. Neuron *65*, 472–479.

Nyquist, H. (1924). Certain factors affecting telegraph speed. Bell Syst. Tech. J. *3*, 324–346.

Pavlov, P.I. (1927). Conditioned Reflexes: an Investigation of the Physiological Activity of the Cerebral Cortex (Oxford University Press).

Pender, J.W. (1971). Dissociative anesthesia. JAMA *215*, 1126–1130.

Penfield, W.J., and Jasper, H. (1954). Epilepsy and the Functional Anatomy of the Human Brain (Little, Brown).

Pilge, S., Jordan, D., Kreuzer, M., Kochs, E.F., and Schneider, G. (2014). Burst suppression-MAC and burst suppression-CP(5)(0) as measures of cerebral effects of anaesthetics. Br. J. Anaesth. *112*, 1067–1074.

Pnevmatikakis, E.A., Soudry, D., Gao, Y., Machado, T.A., Merel, J., Pfau, D., Reardon, T., Mu, Y., Lacefield, C., Yang, W., et al. (2016). Simultaneous denoising, deconvolution, and demixing of calcium imaging data. Neuron *89*, 285–299.

Polack, P.O., Friedman, J., and Golshani, P. (2013). Cellular mechanisms of brain state-dependent gain modulation in visual cortex. Nat. Neurosci. *16*, 1331–1339.

Saleem, A.B., Ayaz, A., Jeffery, K.J., Harris, K.D., and Carandini, M. (2013). Integration of visual motion and locomotion in mouse visual cortex. Nat. Neurosci. *16*, 1864–1869.

Salzman, C.D., Britten, K.H., and Newsome, W.T. (1990). Cortical microstimulation influences perceptual judgements of motion direction. Nature *346*, 174–177.

Schevon, C.A., Weiss, S.A., McKhann, G., Jr., Goodman, R.R., Yuste, R., Emerson, R.G., and Trevelyan, A.J. (2012). Evidence of an inhibitory restraint of seizure activity in humans. Nat. Commun. *3*, 1060.

Schneider, C.A., Rasband, W.S., and Eliceiri, K.W. (2012). NIH Image to ImageJ: 25 years of image analysis. Nat. Methods *9*, 671–675.

Schneidman, E., Berry, M.J., 2nd, Segev, R., and Bialek, W. (2006). Weak pairwise correlations imply strongly correlated network states in a neural population. Nature *440*, 1007–1012.

Schroeder, K.E., Irwin, Z.T., Gaidica, M., Nicole Bentley, J., Patil, P.G., Mashour, G.A., and Chestek, C.A. (2016). Disruption of corticocortical information transfer during ketamine anesthesia in the primate brain. Neuroimage *134*, 459–465.

Scoville, W.B., and Milner, B. (1957). Loss of recent memory after bilateral hippocampal lesions. J. Neurol. Neurosurg. Psychiatry *20*, 11–21.

Shoham, S., Fellows, M.R., and Normann, R.A. (2003). Robust, automatic spike sorting using mixtures of multivariate t-distributions. J. Neurosci. Methods *127*, 111–122.

Steriade, M. (2003). The corticothalamic system in sleep. Front. Biosci. *8*, d878–d899.

Tononi, G. (2008). Consciousness as integrated information: a provisional manifesto. Biol. Bull. *215*, 216–242.

Tononi, G., Boly, M., Massimini, M., and Koch, C. (2016). Integrated information theory: from consciousness to its physical substrate. Nat. Rev. Neurosci. *17*, 450–461.

van der Maaten, L., and Hinton, G. (2008). Visualizing Data using t-SNE. J. Mach. Learn. Res. *9*, 2579–2605.

van Kemenade, B.M., Arikan, B.E., Podranski, K., Steinsträter, O., Kircher, T., and Straube, B. (2018). Distinct roles for the cerebellum, angular gyrus, and middle temporal gyrus in action-feedback monitoring. Cereb. Cortex *29*, 1520–1531.

Welch, T.A. (1984). A technique for high-performance data-compression. Computer *17*, 8–19.

Yang, W., Miller, J.E., Carrillo-Reid, L., Pnevmatikakis, E., Paninski, L., Yuste, R., and Peterka, D.S. (2016). Simultaneous multi-plane imaging of neural circuits. Neuron *89*, 269–284.

Yang, W., and Yuste, R. (2017). In vivo imaging of neural activity. Nat. Methods *14*, 349–359.

Yuste, R., and Denk, W. (1995). Dendritic spines as basic units of synaptic integration. Nature *375*, 682–684.

Yuste, R., and Katz, L.C. (1991). Control of postsynaptic Ca2+ influx in developing neocortex by excitatory and inhibitory neurotransmitters. Neuron *6*, 333–344.

Ziv, J., and Lempel, A. (1978). Compression of individual sequences via variable-rate coding. IEEE Trans. Inform. Theory *24*, 530–536.

Prolonged Anesthesia Alters Brain Synaptic Architecture

In der soeben zusammengefassten Studie wurden reversible Änderungen neuronaler Ensembleaktivität während kurzzeitigem, medizinisch induziertem Bewusstseinsverlust untersucht. Unter maximaler Ausschöpfung der räumlichen Auflösung der *in vivo* 2P-Mikroskopie wurde in der im Folgenden zusammengefassten Studie (Wenzel et al., 2021) untersucht, ob prolongiertes medizinisch induziertes Koma (pMIC) anhaltende Auswirkungen auf die synaptische Architektur des Gehirns hat. Im Kindesalter sind synaptische Änderungen infolge von bereits kurzzeitiger Generalanästhesie seit Langem beschrieben und ein Zusammenhang dieser Änderungen mit kognitiven Einschränkungen bekannt (Briner et al., 2011; De Roo et al., 2009; Sanders et al., 2013). Im Erwachsenenalter stellt sich die Erkenntnislage jedoch grundsätzlich anders dar. Zwar leiden circa ein Drittel der Überlebenden von Intensivstationsaufenthalten unter teils jahrelangen kognitiven Defiziten (Pandharipande et al., 2013), ein Zusammenhang von pMIC und Änderungen der synaptischen Struktur des erwachsenen Gehirns war bis zur hier zusammengefassten Studie jedoch ungeklärt.

Zur verlässlichen Durchführung von pMIC in Mäusen wurde eine Miniaturintensivstation etabliert, mit welcher kontinuierliches pMIC erfolgreich bis zu einer Dauer von max. 40 Stunden durchgeführt wurde (Abb. 1 A). Zu jedem Zeitpunkt eines Experiments war ein Experimentierender zur klinischen Überwachung der Versuchstiere im Labor zugegen. In transgenen Thy1-YFP Mäusen (strukturell fluoreszente Markierung von kortikalen Pyramidalneuronen)(Feng et al., 2000) wurde in minimal invasivem Vorgehen ein chronisch kraniales Fenster durch Verdünnung des Schädelknochens mit Hilfe eines Dentalbohrers auf 10-20 μm etabliert (Drew et al., 2010; Xu et al., 2007). Nach einer mindestens zweiwöchigen Erholungszeit wurden kortikale Dendriten, Synapsen und deren Dynamik mittels chronischer 2P-Mikroskopie (4 Zeitpunkte über 8 Tage) sowie wiederholte basale kognitive Testungen (*novel object recognition* Test [NOR]) (Leger et al., 2013) nach einem ineinander greifenden Versuchsschema durchgeführt (Abb. 1 A-D). Jede Mikroskopie-Session nahm hierbei ~15-30 min in Anspruch und beinhaltete die Aufnahme von hochauflösenden z-Schichtungen (unter milder Isoflurananästhesie zur Verringerung von Bewegungsartefakten) in bis zu 4 verschiedenen kortikalen Arealen (FOV typischerweise 50 x 50 μm, Schichtabstände in z = 1,5 μm, Aufnahmetiefe bis zu 150 μm subpial) (Abb. 2 A,

B, D, J). Die mikrometergenaue Koregistrierung initial identifizierter Synapsen erfolgte jeweils über mikrovaskuläre Landmarken und mehrfache optische Vergrößerungsstufen (Drew et al., 2010; Holtmaat et al., 2009)(Abb. 2 A, B).

Es wurde pMIC (Isofluran, 0,5-1,5% ppa) in 6 erwachsenen Mäusen (Alter: 7,7 ± 1,5 Monate SEM) mit einer mittleren Dauer von 18 h (17,96 ± 0,74 SEM) durchgeführt (Abb. 1 F). Während der gesamten pMIC Dauer wurden kontinuierlich Atem- (65 ± 3 / min SEM) und Herzfrequenz (435 ± 14 / min SEM), Atmungs-/Pulsdistension (1,75 ± 0,16 SEM) und periphere O_2-Sättigung (96,96 ± 0,32 % SEM) sowie der klinische Zustand (direkte klinische Überwachung, sowie *remote* Video-Monitoring) monitoriert (Abb. 1 A, F). Durch ein *closed-loop* System wurde mittels rektaler Körperkerntemperaturmessung und Wärmeplatte eine konstante Körpertemperatur von 37,5°C sichergestellt. Ausreichende Flüssigkeits- und Energiezufuhr während pMIC wurden über eine perfusorgesteuerte subkutane Verabreichung von 1% Glukose-Kochsalzlösung (3,46 ± 0,35 ml SEM) sichergestellt. Zu jedem Zeitpunkt während pMIC war ein Experimentierender der zusammengefassten Studie in den Laborräumen für etwaige notwendige Versuchsanpassungen (z.B. Änderung Anästhesietiefe, Flüssigkeitsszufuhr, O_2-Anteil in der Beatmungsluft etc.) zugegen.

Im Kontext von pMIC ergab sich in der wiederholten kognitiven Testung erwartungsgemäß im Vergleich zur Baseline Periode eine signifikante Verschlechterung der Rekognitionsleistung (NOR) im Anschluss an pMIC (Abb. 1 H). Ein Einfluss einer möglichen postanästhetisch verringerten Lokomotion konnte hierbei ausgeschlossen werden, da die Tiere in der Testung vor und nach pMIC ähnliche Gesamtlaufdistanzen zeigten (Abb. 1 I). Die mikroskopierte dendritische Stuktur erwies sich in allen anästhesierten Tieren über pMIC hinweg als vollständig stabil (Fig. 2 B-C). Im Gegensatz zum synaptischen 1-Tages-Umsatz (Umsatz [%] = gebildete + verlorene Synapsen / Gesamtzahl Synapsen) in erwachsenen Kontrollmäusen (n = 6; Gesamt-synapsenzahl: 1.113 [185,5 ± 50 SEM]) zeigte sich jedoch der synaptische Umsatz in Assoziation mit pMIC (n = 6, Gesamtsynapsenzahl: 1.254 [209 ± 40 SEM]) mehr als verdoppelt (Abb. 2 D-E). Synaptischer Zuwachs und Verlust waren während pMIC jeweils signifikant erhöht, wobei der Zuwachs den Verlust überwog (Abb. 2 F). Nach pMIC blieb der 3-Tages-Umsatz an Synapsen im Vergleich zu Baseline (3-Tages-Umsatz vor pMIC) signifikant erhöht (Abb. 2 G), wobei der synaptische Verlust

die postanästhetische Periode dominierte (Abb. 2 H). Erstaunlicherweise zeigten sich knapp die Hälfte der während pMIC neu gebildeten Synapsen in der postanästhetischen Periode stabil (42,69 ± 10.87% SEM [Gesamtzahl gebildeter Synapsen: 59 in 6 Mäusen]). Durch Bezugsetzung des prä- und postanästhetischen synaptischen Umsatzes mit gemessenen Änderungen der NOR Testleistung ergab sich eine signifikante inverse Beziehung des erhöhten postanästhetischen synaptischen Umsatzes mit einer verminderten NOR Testleistung (Abb. 2 I).

Diese Experimente wurden nun ebenfalls in adoleszenten Tieren (Alter 30 Tage) durch-geführt, da prolongiertes MIC auch in diesem Alter bislang nicht untersucht worden war (Abb. 2 J-N). Ähnlich den Resultaten im Erwachsenenalter ergab sich in Jungtieren (n = 4, pMIC Dauer = 18,5 ± 1,26 h SEM, Gesamtsynapsenzahl: 284 [71 ± 12 SEM]) im Vergleich zu Kontrollen (n = 5; Gesamtsynapsenzahl: 587 [117.4 ± 15 SEM]) ein signifikant erhöhter pMIC-assoziierter synaptischer 1-Tages-Umsatz (Abb. 2 J, K), der von einem synaptischen Zuwachs dominiert wurde (Abb. 2 L). Prä- und postanästhetischer synaptischer Umsatz zeigten sich in Jungtieren im Überblick gleichbleibend (Abb. 2 M), wobei die postanästhetische Phase in adoleszenten Tieren noch deutlicher von einem Verlust an Synapsen geprägt war als in erwachsenen Tieren (Abb. 2 N). Analog zu den Ergebnissen in erwachsenen Tieren zeigten sich auch in Jungtieren die Hälfte der während pMIC neu gebildeten Synapsen im Anschluss an pMIC stabil (50,57 ± 9.09% SEM [[Gesamtzahl gebildeter Synapsen: 36 in 4 Mäusen]). Zusammenfassend konnte durch diese Experimente erstmals eine altersunabhängige Verknüpfung zwischen pMIC-assoziiertem kognitiven Defizit und einer hiermit korrelierenden, nachhaltigen Veränderung der - ehemals als im Erwachsenenalter stabil erachteten - synaptischen Architektur des Gehirns nachgewiesen werden.

Prolonged anesthesia alters brain synaptic architecture

Michael Wenzel[a,1,2], Alexander Leunig[a], Shuting Han[a], Darcy S. Peterka[a], and Rafael Yuste[a]

[a]Neurotechnology Center, Department of Biological Sciences, Columbia University, New York, NY 10027

Edited by Emery N. Brown, Massachusetts General Hospital, Boston, MA, and approved December 19, 2020 (received for review November 20, 2020)

Prolonged medically induced coma (pMIC) is carried out routinely in intensive care medicine. pMIC leads to cognitive impairment, yet the underlying neuromorphological correlates are still unknown, as no direct studies of MIC exceeding ~6 h on neural circuits exist. Here, we establish pMIC (up to 24 h) in adolescent and mature mice, and combine longitudinal two-photon imaging of cortical synapses with repeated behavioral object recognition assessments. We find that pMIC affects object recognition, and that it is associated with enhanced synaptic turnover, generated by enhanced synapse formation during pMIC, while the postanesthetic period is dominated by synaptic loss. Our results demonstrate major side effects of prolonged anesthesia on neural circuit structure.

anesthesia | dendritic spines | synaptic plasticity | memory deficit | two-photon imaging

Cognitive impairment due to prolonged medically induced coma (pMIC) represents an enormous clinical and socioeconomic burden affecting millions of patients worldwide (1–3). In adulthood, clinical trials have proven that intensive care unit (ICU) survivors frequently suffer from lasting cognitive impairment (2, 4), yet the neuromorphopathological underpinnings of this impairment have remained elusive. In early life, when the brain is highly plastic, MIC (maximum of 6 h tested in rodents to date) has been shown to result in synaptic changes and long-term cognitive impairment (5–7). However, basic animal research suggests that, during later adolescence and adulthood, dendrites and dendritic spines are stable under physiological conditions (8–10) and short-term MIC (11). Whether this notion holds true for pMIC is unknown.

Results

There has been a paucity of experimental studies of structural and functional consequences of pMIC, so we first created a robust pMIC experimental protocol for mice. We combined an anesthesia setup (Fig. 1*A*), chronic two-photon imaging of cortical synapses (Fig. 1*B*), and repeated behavioral assessment (Fig. 1*C*) into an integrated experimental framework (Fig. 1*D* and *Materials and Methods*). Two imaging sessions were carried out to determine baseline 3-d synaptic turnover (day 1, day 4). Immediately after day 4 imaging, pMIC was initiated. To document synaptic changes across pMIC, a third imaging session was performed immediately upon pMIC discontinuation (day 5). Three days post pMIC, mice were imaged once again to determine postanesthetic 3-d synaptic turnover (day 8). Additionally, a novel object recognition test was performed during baseline conditions (day 4), and repeated after recovery from pMIC (day 7) (Fig. 1*C*).

We used the inhalatory anesthetic isoflurane due to its fast kinetics and thus maximal adjustability of anesthetic depth (12). We tried to avoid an FiO_2 (fraction of inspired oxygen) >50%, as this has been associated with increased mortality in human intensive care (13). Vital parameters (peripheral O_2 saturation, heart rate, breath rate, pulse/breath distention) were continually monitored using an infrared thigh sensor (Fig. 1*E*). When developing the protocol, we successfully performed pMIC in mice for up to 40 h, yet for reasons of feasibility (continuous presence of an experimenter required), we performed pMIC on 12 adult mice (age: 7.7 ± 1.5 mo SEM) with a mean duration of 18 h (17.96 ± 0.74 SEM). Cardiorespiratory instability (after exclusion of possible sensor or detection errors: sustained non-hypovolemic hypotonic bradyarrhythmia [pulse curve, pulse/breath distension], repeated hypotonic tachycardia [self-limited], unexplained drop in O_2 saturation <90% for >30 s, sustained breath rate <30/min, repeated unexplained gasping [self-limited]) or maximum pMIC duration of 24 h were chosen as primary pMIC discontinuation criteria. Fluid and nutritional supply were ensured by administration of glucose solution (1% in phosphate-buffered saline [PBS]) via a subcutaneous line at 0.1 to 0.2 mL/hr (total volume 3.46 ± 0.35 mL SEM). Under steady-state isoflurane concentrations of 0.5 to 1.5% partial pressure in air (ppa), mice displayed continuously high peripheral oxygen saturation (96.96 ± 0.32% SEM), heart rates between 350 and 500 beats per minute (435 ± 14 SEM), breath rates of 50 to 80 excursions per minute (65 ± 3 SEM), and a pulse/breath distension ratio above 1 (1.75 ± 0.16 SEM) (Fig. 1 *E* and *F*). Oxygenation >90% was maintained with little variance across a wide range of covarying heart and breath rates (Fig. 1*E*–*G*). Breath rate showed the largest variance among monitored vital parameters (Fig. 1*G*), and most accurately clinically reflected anesthetic depth. Upon pMIC discontinuation, mice rapidly displayed accelerated heart and breath rates, and soon reacted to tactile stimulation. We defined the period between isoflurane discontinuation and first appearance of the righting reflex as wake-up time (9.65 ± 1.41 min SEM). After waking up, all mice soon showed apparently normal movement and body coordination, typical grooming, and feeding behavior. To evaluate pMIC-associated behavioral changes, mice were subjected to a novel object recognition test (14) (NOR) prior to and post pMIC (Fig. 1*C*). Expectedly, mice spent significantly

Significance

In human patients, prolonged medically induced coma (pMIC) is associated with significant cognitive deficits. Yet, a synapse-level neuromorphological correlate has been demonstrated experimentally only in early life, when the brain is highly plastic. The current notion is that synapses become increasingly stabilized and that MIC has no effect on synaptic dynamics in adulthood. Yet, the longest experimental study of MIC-associated synaptic changes has been only ~6 h. We established a pMIC experimental protocol in mice and found that pMIC alters synaptic brain architecture and object recognition at all ages. Our results ring an alarm bell to the medical community and call for the development of individually tailored anesthetic regimens and intensified research on adjuvant therapeutic strategies to maintain brain structure and function during pMIC.

Author contributions: M.W. conceived the project and designed experiments; M.W. and A.L. performed experiments; M.W., A.L., D.S.P., and S.H. analyzed data; M.W. wrote the paper; M.W., A.L., S.H., D.S.P., and R.Y. discussed results; and R.Y. assembled and directed the team.

The authors declare no competing interest.

This article is a PNAS Direct Submission.

[1]Present address: Department of Epileptology, University of Bonn, 53127 Bonn, Germany.

[2]To whom correspondence may be addressed. Email: michaelwenzel2946@gmail.com.

Published February 10, 2021.

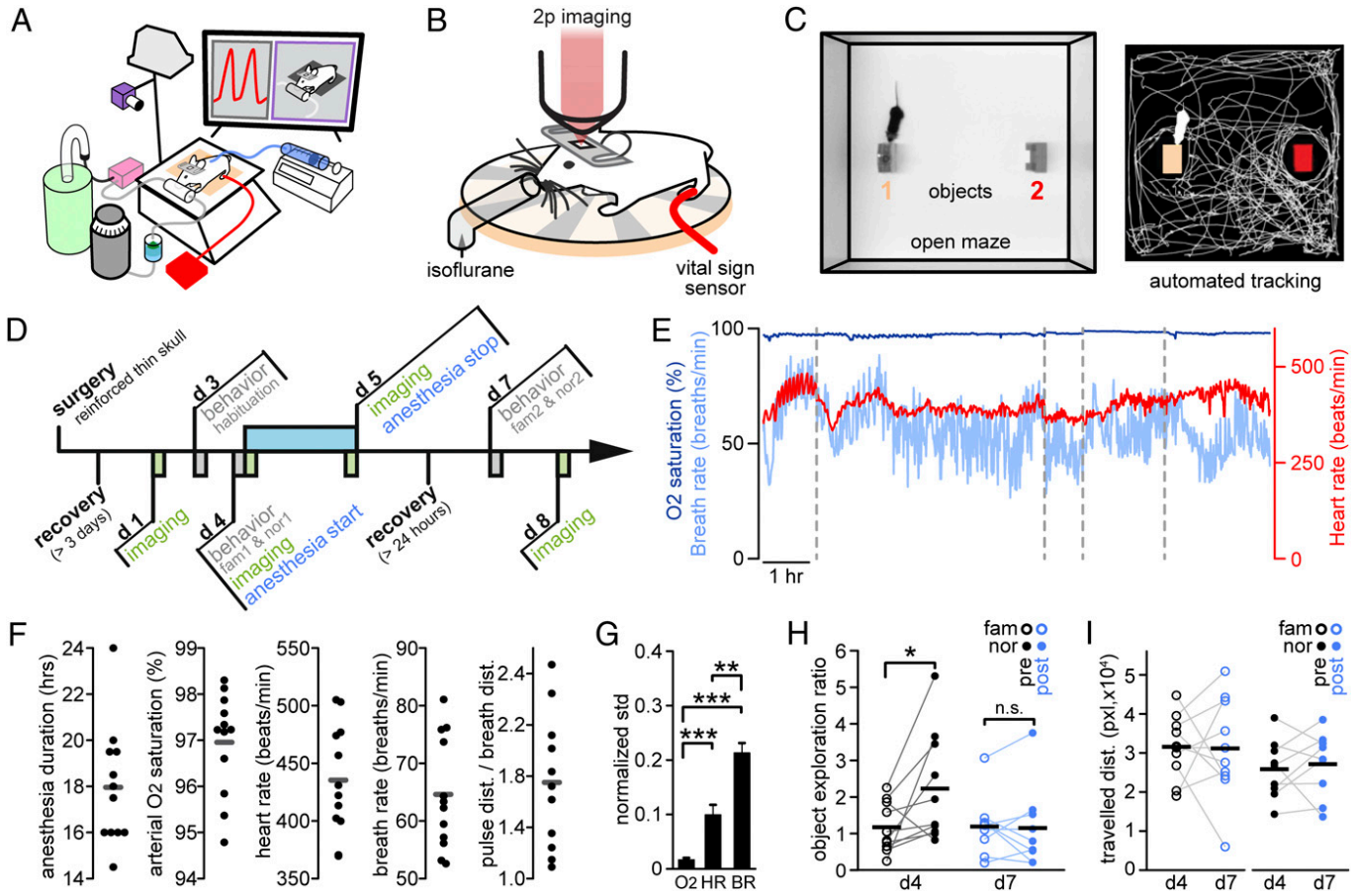

Fig. 1. Experimental design and pMIC-induced behavioral deficits. (*A*) Anesthesia setup. Mice are placed on a warming pad on a tiltable platform. Isoflurane is evaporated (dark gray) and delivered in humidified air/oxygen via a custom nose piece. Waste gas is removed by a suction pump (magenta) and trapped in a charcoal filter (green). Nutritional supply is delivered via a programmable perfusion system (blue, *Right*). An infrared lamp is placed above the setup. A thigh sensor is used for vital-sign monitoring (red). Vital signs and clinical status are live-streamed in a local network (camera, computer display). (*B*) For each imaging session, anesthetized mice are placed under the microscope, on a warming pad, under vital-sign monitoring. (*C*) Open maze for behavioral testing. Videos are recorded during FAM and NOR from above; mouse behavior is automatically tracked. (*D*) Experimental workflow. (*E*) Long-term vital-sign monitoring of an anesthetized mouse with intermittent breaks (dashed lines, e.g., for changing sensor between limbs). (*F*) Vital parameters, mean values ($n = 12$ mice), and overall mean value displayed as gray line. dist., distension. (*G*) Comparison of vital-sign normalized mean SDs ($n = 12$ mice). Unpaired *t* test with Welsh's correction: O2 saturation vs. heart rate, $P = 0.001$; O2 saturation vs. breath rate, $P < 0.0001$; heart rate vs. breath rate, $P = 0.0002$. (*H*) Relative object exploration time ratio (two objects, 50% vs. 50% = 1) during FAM (circles) and NOR (filled circles) measured during baseline (day 4), and post pMIC (day 7). Paired *t* test: FAM (day 4) vs. NOR (day 4) $P = 0.0451$ ($n = 10$ mice), FAM (day 7) vs. NOR (day 7) $P = 0.823$ ($n = 9$ mice). (*I*) Traveled distances (in pixels) prior and post pMIC during FAM (circles) and NOR (filled circles). $^*P < 0.05$, $^{**}P < 0.01$, $^{***}P < 0.001$. All bar plots show mean ± SEM.

more time exploring novel objects post familiarization (FAM) during baseline conditions (Fig. 1 *H*, *Left*). However, this effect was abolished post recovery (>24 h) from pMIC (Fig. 1 *H*, *Right*). Importantly, this could not be explained by postanesthetic reduction of locomotion, as pre- and postanesthetic total distances traveled during FAM and NOR were similar (Fig. 1*I*).

Next, we set out to study whether pMIC affects synaptic architecture. We performed repeated two-photon imaging of yellow fluorescent protein (YFP-labeled dendrites and synapses (up to ~150 µm beneath the pial surface) of layer 5 pyramidal neurons (15) in 6 of 12 adult mice undergoing pMIC (Fig. 2*A*). We used a reinforced chronic cranial window above thinned skull to minimize possible effects from invasive surgery (16). However, this reduces overall imaging fidelity, and we were unable to consistently distinguish between filopodia and dendritic spines across all imaging sessions in all mice. Therefore, we chose to focus on clearly visible synaptic protrusions, regardless of morphological classification. In six mice, we assessed a total of 1,254 synaptic protrusions (209 ± 40 SEM) on 238 dendritic compartments (40 ± 9 SEM). We noticed that, across all anesthetized mice and imaging sessions, dendrites remained stable (Fig. 2 *B* and *C*). However, pMIC-associated synapse dynamics showed considerable alterations (Fig. 2*D*). In comparison to the 1-d total synapse turnover in adult controls ($n = 6$; total synapse count: 1,113 [185.5 ± 50 SEM]), pMIC-associated synapse turnover was more than doubled ($n = 6$, total synapse count: 1,254 [209 ± 40 SEM]) (Fig. 2*E*). Both synaptic gain and loss were significantly enhanced during pMIC, with the gain of synapses outperforming their loss (Fig. 2*F*). When comparing pre- and postanesthetic 3-d synaptic turnover, turnover remained significantly enhanced after pMIC (Fig. 2*G*). In contrast to pMIC itself, the postanesthetic period was dominated by synaptic loss (Fig. 2*H*), while both postanesthetic synaptic gain and loss remained nonsignificantly increased. Intriguingly, a substantial fraction of synapses gained during pMIC remained stable across the 3-d postanesthetic period (42.69 ± 10.87% SEM [total gain: 59 synapses in $n = 6$ mice]). Relating pre- and postanesthetic synaptic turnover with change in NOR performance, we found a significant inverse relationship between increased turnover and decreased test performance (Fig. 2*I*).

Next, we put our findings in adult mice in a developmental context by examining young animals (approximately postnatal day 30). Previous research suggests that short-term MIC (maximum of

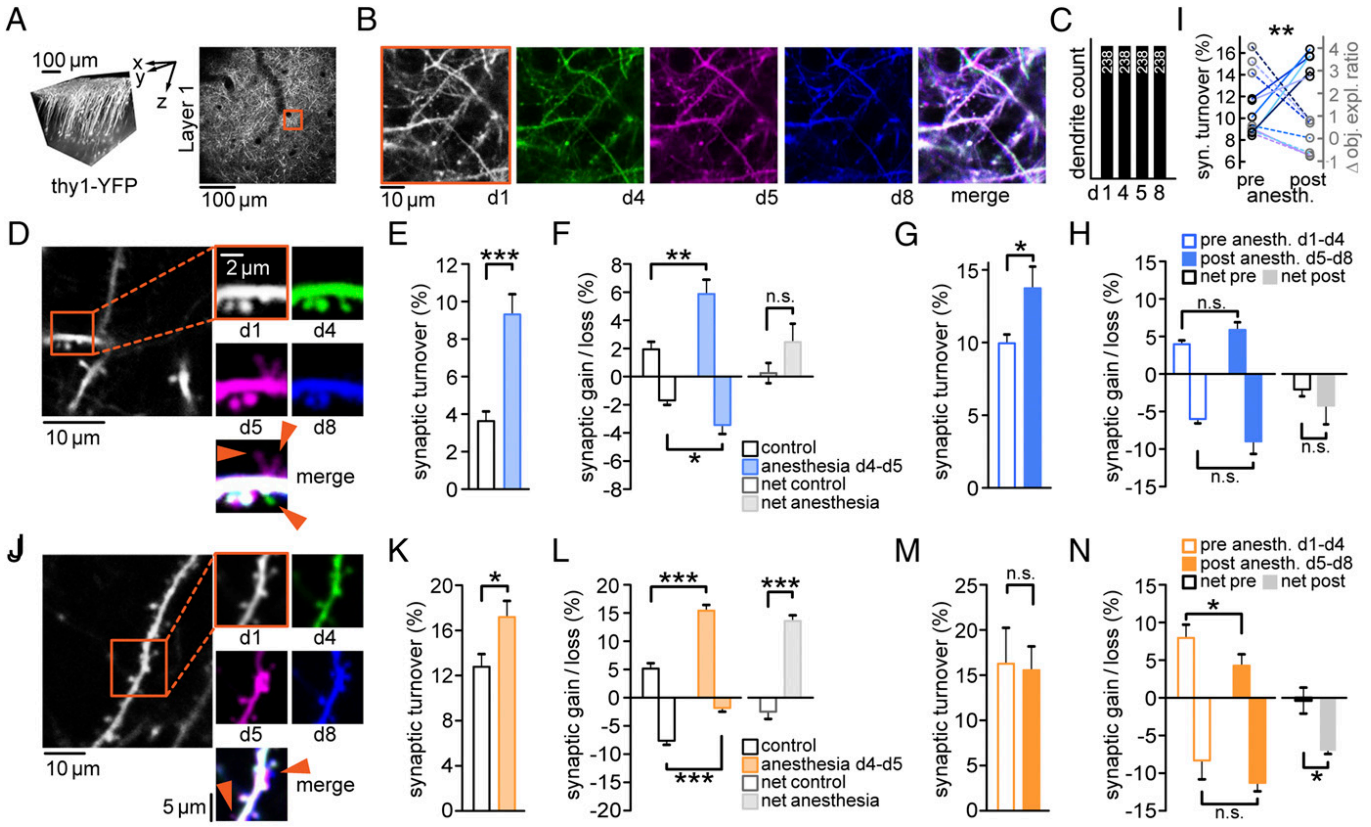

Fig. 2. pMIC leads to synaptic alterations in adolescent and adult mice. (*A*, *Left*) Three-dimensional reconstruction of imaged L5 pyramidal cells. (*A*, *Right*) Axial imaging field of view (FOV) at low magnification to re-identify zoomed-in L1 FOVs across imaging sessions by vascular landmarks. (*B*) Red *Inset* shown in *A*; identical dendritic segments were imaged four times, before pMIC (day 1, day 4), and following pMIC (day 5, day 8) in an adult mouse. (*C*) Quantification of dendritic changes across pMIC in adult mice ($n = 6$); dendritic segments remained stable. (*D*) Exemplary dendritic segment and synaptic changes across pMIC (baseline: day 1 to day 4; pMIC: day 4 to day 5; post pMIC: day 5 to day 8). Two synapses are transiently gained during pMIC (magenta), and one synapse is permanently lost (green). (*E*) Total synaptic turnover during pMIC in adult mice ($n = 6$) vs. 1-d turnover in healthy controls ($n = 6$); unpaired *t* test: $P = 0.043$. (*F*) Synaptic gain, loss, and net effect (gain – loss) during pMIC in adult mice ($n = 6$) vs. healthy controls ($n = 6$); unpaired *t* test: $P = 0.0064$ (gain), $P = 0.1728$ (net effect); Mann–Whitney *U* test: $P = 0.026$ (loss). (*G*) Total 3-d synaptic turnover ($n = 6$ adult mice) during baseline (day 1 to day 4) vs. post pMIC (day 5 to day 8); paired *t* test: $P = 0.0484$. (*H*) Synaptic gain, loss, and net effect ($n = 6$ adult mice) during baseline (day 1 to day 4) vs. post pMIC (day 5 to day 8); paired *t* test: $P = 0.4913$ (gain), $P = 0.16$ (loss), $P = 0.4441$ (net effect). (*I*) Within-mouse ($n = 6$ adult mice, one blue shade per mouse) comparison of change of synaptic turnover (black *y* axis on the *Left*; black circles and solid lines; preanesthetic vs. postanesthetic 3-d turnover) and change of NOR performance (gray *y* axis on the *Right*; gray circles and dashed lines; preanesthetic vs. postanesthetic delta object exploration ratio [FAM vs. NOR]). All mice showed a postanesthetic decrease in NOR performance, while five out of six mice showed a postanesthetic increase in synaptic turnover (Fisher's exact test: $P = 0.0076$). (*J*) Exemplary dendritic segment and synaptic changes across pMIC (baseline: day 1 to day 4; pMIC: day 4 to day 5; post pMIC: day 5 to day 8). Two synapses are gained during pMIC (magenta) and persist post pMIC (blue). (*K*) Total synaptic turnover during pMIC in young mice ($n = 4$) vs. 1-d turnover in healthy controls ($n = 5$); unpaired *t* test: $P = 0.0433$. (*L*) Synaptic gain, loss, and net effect during pMIC in young mice ($n = 4$) vs. healthy controls ($n = 5$); unpaired *t* test: $P = 0.0002$ (gain), $P = 0.0007$ (loss), $P < 0.0001$ (net effect). (*M*) Total 3-d synaptic turnover ($n = 4$ young mice) during baseline (day 1 to day 4) vs. post pMIC (day 5 to day 8); paired *t* test: $P = 0.7099$. (*N*) Synaptic gain, loss, and net effect ($n = 4$ young mice) during baseline (day 1 to day 4) vs. post pMIC (day 5 to day 8); paired *t* test: $P = 0.043$ (gain), $P = 0.1671$ (loss), $P = 0.0386$ (net effect). $^*P < 0.05$, $^{**}P < 0.01$, $^{***}P < 0.001$. All bar plots show mean ± SEM.

6 h tested) at a young age (≤ 1 mo in rodents) is associated with long-term cognitive impairment (7), and increased synapse formation is associated with an age-dependent decreasing effect size (no effect on dendritic spines at age >1 mo) (5, 6, 11).

Similarly to adult mice, pMIC in young mice ($n = 4$, pMIC duration = 18.5 ± 1.26 h SEM) was associated with enhanced 1-d synapse turnover (Fig. 2 *J* and *K*; $n = 4$ mice; total synapse count: 284 [71 ± 12 SEM]). In line with previous results on immature synapses in 1-mo-old mice (isoflurane for 4 h) (11), synaptic loss was significantly reduced during pMIC compared to controls (Fig. 2*L*; $n = 5$ mice; total synapse count: 587 [117.4 ± 15 SEM]). At the same time, consistent with our results for pMIC in adult mice, pMIC-associated synapse formation was strongly increased, resulting in a pronounced net-positive synaptic turnover (Fig. 2*L*). When comparing pre- and postanesthetic 3-d synaptic turnover, total turnover remained unchanged (Fig. 2*M*). Yet, in contrast to adult mice, synaptic formation post pMIC in younger mice was significantly reduced and synapse elimination increased, resulting in a net-negative synaptic turnover (Fig. 2*N*). Again, a substantial fraction of synapses gained during pMIC remained stable during the postanesthetic period (50.57 ± 9.09% SEM [total gain: 36 synapses in $n = 4$ mice]).

Discussion

Our data demonstrate that prolonged general anesthesia in mice alters object recognition and cortical synaptic architecture at all ages. With isoflurane, we find net-positive synapse turnover during pMIC, followed by a net-negative synapse turnover during the postanesthetic period. Across all examined ages, a substantial fraction of newly formed spines during pMIC displayed post-anesthetic stability, suggesting that they may form persistent synaptic connections. Given the relevance of synapses and experience-driven synaptic plasticity for cognitive function and memory (17, 18), our observation of pMIC-associated synaptic dynamics represents

a possible factor contributing to memory impairment following pMIC. The mechanisms underlying these alterations likely play out across multiple anatomical scales (19). On the molecular level, anesthetics target ion channels (20). On the organelle level, anesthetics exert effects, e.g., on a cell's cytoskeleton (21). Ultimately, circuit-level alterations may play a main role in pMIC-associated synaptic dynamics, since prolonged pharmacological circuit inactivation may interfere with physiological synaptic changes associated with intrinsic (e.g., circadian protein expression) (22) and extrinsic environmental parameters (e.g., novel sensory experience) across age (23).

A limitation of this study is whether our synaptic-level findings translate to human pMIC, as such studies do not yet exist. However, recent progress in positron emission tomography imaging of synaptic density in humans using synapse-specific radioligands (24–26) could enable future studies on pMIC-associated synaptic changes even in humans, all other logistical complications of such an enterprise aside. Another possible limitation of the present study is that we examined synaptic plasticity in sensory cortex, but not in higher order cortices. We chose somatosensory cortex for several reasons. In addition to its accessibility for high-resolution imaging, it represents the most extensively studied murine brain area in the field of synaptic plasticity, and thus enables contextualization of our results in light of a prominent body of literature on synaptic stability in adulthood (8–11, 27–30). Furthermore, particularly in mice, somatosensory cortex is important for exploration and tactile learning (31–33), object discrimination, and recognition (34, 35), and thus represents a logical imaging target for pMIC-associated behavioral changes. In addition, sensory cortices contribute to cognitive function (36). Primary sensory and higher-order cortices share reciprocal connections (37–39), and recent work suggests that sensory cortices also implement internal representations of the external environment, even in the absence of specific stimuli (40, 41). Further evidence of the sensory cortex playing a role in working memory (42), social contextualization of conspecifics (43), and reward-related task-relevant anticipation (44) points toward an associative capacity of sensory cortices beyond their immediate sensory function. However, as in addition to basic cognitive impairment (measured e.g. by RBANS assessment) (45), intensive care unit survivors often suffer from impaired executive function (2), the study of higher-level cognitive abilities is of significant interest for further synapse-level research on pMIC. Future steps in this direction will require more specific behavioral testing, and more invasive imaging strategies, e.g. in hippocampus (46, 47) or medial prefrontal cortex (mPFC) (48, 49). In this context, it is important to keep in mind that the longitudinal in vivo synapse dynamics of the hippocampus and mPFC (49–51) are far less well understood than those in sensory cortex. As we imaged somatosensory cortex for the above-mentioned reasons, there is no definitive proof yet that the results reported here extend to other brain areas, too. However, given that anesthetics are administered systemically, and thus distribute throughout the entire brain, it is much rather likely than not that other brain areas will show similar, even if to a different degree, pMIC-associated synaptic changes.

Together, the findings of this pilot study carry important implications for medical care, as they point out significant structural and functional side effects of pMIC. They further indicate that, with regards to pMIC, the synaptic architecture of the adult brain is less stable than previously thought, which has major implications for general anesthesia in intensive care medicine. To date, no standard approach exists to prevent cognitive side effects or alterations of brain architecture during pMIC. For this study, we chose the inhalatory anesthetic isoflurane, which is part of a common class of anesthetics in anesthesiology (52), is widely established in animal research, can be administered non-invasively, does not accumulate in the body, and has a short elimination half-life enabling high controllability of anesthetic depth (53). Partly due to this, inhalatory anesthetics have experienced a renaissance in intensive care medicine using AnaConDa or Mirus systems (53–55). The results of this study make the case for a systematic investigation of synapse-level effects and related cognitive impairment triggered by commonly used anesthetics in intensive care, including propofol and benzodiazepines, and particularly combinations of anesthetics. A better understanding of pMIC-related effects on cortical synapses could allow for more individually tailored anesthetic regimens (52) and could foster research on adjuvant therapeutic strategies to improve cognitive outcomes of ICU survivors.

Materials and Methods

General Information. All experiments were carried out in compliance with the Columbia University institutional animal care guidelines. We used B6.Cg-Tg(Thy1-YFP)HJrs/J mice (15) (Jackson Laboratories; Research Resource Identifier IMSR_JAX:003782), where cortical layer 5 pyramidal neurons are preferentially labeled. For experiments, the postnatal age of mice ranged from 1 to 12 mo (two age groups: postnatal days 30 to 35 [pMIC/imaging: two females, two males; control/imaging: two females, three males], or postnatal days 120 to 360 [pMIC: four females, eight males; pMIC/behavior: three females, seven males; pMIC/behavior/imaging: one female, five males; control/imaging: two females, four males]). Mice were housed at a 12-h light/dark cycle, and food and water were provided ad libitum.

Surgical Procedures. For repeated two-photon imaging of cortical synapses, a reinforced thin skull chronic cranial window was established as described (56). We chose a "thin skull" approach to minimize potential craniotomy-related changes of synaptic plasticity that have been reported previously (16). In brief, mice were anesthetized with isoflurane (initial dose 2 to 3% partial pressure in air followed by reduction to 1 to 1.5%). Prior to surgery, all mice received carprofen subcutaneously (s.c.), enrofloxacin (s.c.), and dexamethasone (intramuscularly). Throughout surgical procedures, proper anesthetic depth was checked intermittently by toe and tail pinching. Under sterile conditions, a small flap of skin above the skull was removed, and a titanium head plate with a central foramen (7×7 mm) was fixed on the skull using dental cement. Then, a dental microdrill was used at low rotation speed to carefully thin a small region (usually <1 mm in diameter) over the left somatosensory cortex. To prevent the skull and brain tissue from heating up by the drilling process, drilling and wetting with sterile artificial cerebrospinal fluid (ACSF) were alternated frequently. At a thickness of around 50 μm, the skull typically began to bend upon gentle pressure and the intracranial vasculature became clearly visible under the moistened skull. In addition, small air bubbles within the thin spongioform part of the thinned skull appeared when ACSF was applied. From here on, the skull was further thinned at an even lower drilling rotation speed and with minimal vertical pressure, down to a thickness of 10 to 20 μm. When thin enough, the small air enclosures in the skull no longer appeared upon ACSF application.

At this point, the skull was allowed to dry completely. Once dry, a small drop of cyanoacrylate glue was applied onto the thinned skull. Immediately following the application of the glue, a thin glass coverslip (3 mm in diameter, no. 0, Warner Instruments) was lowered and gently pressed onto the thinned area, held in place by a stereotactic arm. After glue solidification (several minutes), the edges of the glass coverslip were sealed off by dental cement. Following the surgical procedure, mice received pain medication and were allowed to recover for at least 3 d. The "reinforcement" of the cranial window prevented the skull from growing back, making it possible to image the same cortical structures repeatedly without the need of re-thinning the skull.

Experimental Time Line. The experimental time line is displayed in Fig. 1*D*. Following recovery from surgical establishment of a chronic cranial window, mice were acclimatized to the experimenter until no signs of distress were present (usually approximately three sessions of 30 min each). Then, two imaging sessions were carried out to determine the baseline 3-d synaptic turnover (day 1, day 4). In between baseline imaging sessions, mice were habituated to the open field maze (day 3) and subjected to a first novel object recognition test (14) (NOR1, day 4). Immediately post imaging on day 4, pMIC was initiated. To document synaptic changes occurring during pMIC, a third imaging session was carried out right at the end of pMIC (day 5). After at least 24 h of recovery from pMIC, mice were subjected to a second

NOR (NOR2, day 7). Three days after pMIC termination, mice were imaged once again to determine their postanesthetic 3-d synaptic turnover (day 8).

Prolonged Medically Induced Coma. The tightly controlled and safe pMIC procedure (−24 h) required the continuous presence of an experimenter. Mimicking hospital conditions, remote video and vital parameter monitoring allowed the experimenter to leave the pMIC setup while maintaining the ability to rapidly carry out setup adjustments. Based on a protocol of long-term anesthesia in mice (57), we established a setup that permits continuous general anesthesia of mice for up to several days (Fig. 1*A*). While anesthetized, mice were kept on a warming pad maintaining a body core temperature of 37.5 °C through a rectal probe and closed-loop temperature control system (ATC2000, World Precision Instruments). The warming pad was placed on a tiltable platform whose angle was slightly changed intermittently (maximum 4°) in order to shift the animals' center of mass to reduce pressure pain and bruising. As mice lose body temperature easily due to their anatomy, an infrared lamp was additionally put in place and optionally switched on, if needed. Isoflurane was delivered in humidified air through a custom nose piece (initial dose: 1.5 to 2.5% ppa; steady-state dose: 0.5 to 1.5% ppa). Ventilation air was humidified between the isoflurane vaporizer and the nose piece, and all waste gas was actively removed via a suction pump. With the help of a dual gas flowmeter system (100% O_2 and room air) set up before the isoflurane vaporizer system, the oxygen fraction (FiO_2) in air could be modified seamlessly between 21 and 100%. FiO_2 adjustment depended on the measured peripheral arterial O_2 saturation. During the early period of pMIC, a fraction of inspired oxygenation (FiO_2) of 21% was completely sufficient to maintain high peripheral O_2 saturation in all anesthetized mice, while subsequently (>8 h), FiO_2 was usually slowly increased toward pMIC termination without exceeding 50%. Similarly to human intensive care, we tried to avoid an FiO_2 >50% (13). To provide the animal with sufficient fluid and nutrition during anesthesia, continuous fluid (saline) and nutritional supply (1% glucose solution in PBS) were administered via a programmable perfusion system through a subcutaneous line at a rate of 0.1 to 0.2 mL/h. All throughout anesthesia, basic vital parameters (blood oxygenation, heart rate, breath rate, pulse distension, breath distension) were continuously monitored and recorded by a thigh or paw sensor (mouse ox plus system, Starr Life Sciences). The sensor was periodically moved from one extremity to another to reduce pressure-induced tissue damage. Technically erroneous vital sign data points (e.g. due to visible thigh compression by the sensor clip, confirmed by immediate normalization of vital signs upon moving the clip to another limb) were excluded from analysis. A sustained pulse/breath distension ratio below 1 was sought to be avoided (57), as it indicates that anesthesia is too deep (large inhalatory excursions and gasping in combination with brady- or normocardia) or a lack of intravascular fluid (hypovolemia in combination with tachycardia). The experimenter was continually present in the laboratory to perform imaging immediately prior and post pMIC, and to adjust, for example, anesthetic depth or fluid supply with minimal delay all throughout anesthesia. Real-time streaming of video monitoring (Thorlabs, DCC1645C) and vital parameters through a local network allowed for remote monitoring of anesthetized animals.

Two-Photon Imaging. For chronic surveillance of structural synaptic changes in vivo, dendritic arborization, and dendritic spines of layer 5 cortical neurons expressing YFP (15) were imaged four times (day 1, day 4 [start of anesthesia], day 5 [end of anesthesia], day 8) using a two-photon microscope (Bruker Ultima) and a Ti:Sapphire laser (Chameleon Ultra II; Coherent) at 940 nm through a 25x objective (water immersion, numerical aperture: 1.05; Olympus). Galvanometer scanning and image acquisition was controlled by Prairie View Imaging software. Each imaging session (∼15 to 30 min) included one to four high-resolution z-stacks in different locations (field of view typically ∼50 × 50 μm, 512 × 512 pixels, step size 1.5 μm, stack depth up to 150 μm beneath the pial surface). Imaged z-stacks were precisely coregistered across each imaging session by vascular landmarks and several different optical zoom average images of the cortex. For each imaging session, head-restrained animals were kept under light isoflurane anesthesia (0.5 to 1% partial pressure in air) via a nose piece while body temperature was maintained with a warming pad (37.5 °C).

Novel Object Recognition Test. Before and after anesthesia, mice were subjected to basic cognitive testing by use of a NOR test, a widely used basic measure of cognitive function and recognition memory in mice (14). Following habituation (experimental day 3, Fig. 1*D*) to an open field maze (50 × 50 cm), mice underwent a first NOR (experimental day 4, prior to start of pMIC). Initially, mice were exposed to two identical objects (e.g., cell culture flasks filled with sand or LEGO towers) that were placed in the open field for 10 min ("familiarization", FAM). After FAM, mice returned to their home cage for 4 to 5 h after which they were placed in the open field maze again, yet with one of the two identical objects replaced by a novel object (differently shaped flask or LEGO tower, respectively). After pMIC, FAM and NOR were repeated for each mouse with the complementary, previously unused set of flasks or LEGO tower objects at least 24 h after pMIC termination (experimental day 7), so changes in recognition memory could be evaluated. All behavioral testing was videotaped (7.5 fr/s) from above the open field. We used custom written Matlab code for automated tracking (traveled distance, object exploration time) of mouse exploratory behavior during FAM and NOR (Fig. 1*C*).

Data Analysis. Similarly to previously described procedures for quantifying synapse dynamics (58), stacks were analyzed using the freely available software ImageJ (http://rsbweb.nih.gov/ij/). Individual 3-d stacks for each time point (day 1, day 4, day 5, day 8) and imaged areas (one to four per animal) were analyzed side-by-side by two examiners who were blinded to conditions, except for the reference imaging time point (day 1). Based on consensus between the two blinded examiners, clearly visible protrusions on dendritic segments were classified as synapses. For each dendritic segment analyzed, same synapses were defined as present (1) or absent (0) across stacks (imaging time points). Based on the examiners' consensus, synapses could be defined as stable, gained, or eliminated across (blinded) imaging time points. Once an entire experiment was analyzed, real imaging time points could be revealed and thus reassigned to individual stacks. Upon testing for normality using a Kolmogorov–Smirnov test statistic, statistical differences between synaptic turnover and synaptic gain or loss were examined using paired (pre- vs. postanesthetic) or unpaired (control group vs. anesthetized group) Student's *t* test, unless stated otherwise. The relationship (decrease or increase) between pre- vs. postanesthetic synaptic turnover and pre- vs. postanesthetic NOR performance was statistically analyzed using Fisher's exact test. All statistical analyses were carried out using MATLAB-R2017b (MathWorks) and Prism 5 (GraphPad Software).

Data Availability. All study data included in the paper are available from the corresponding author upon reasonable request. The custom MATLAB code for automated behavioral tracking is available at https://github.com/hanshuting/mnovobj.

ACKNOWLEDGMENTS. We thank R.Y. laboratory members for useful comments and Prof. H.W. Pfister (LMU, Munich) for clinical supervision. This work was supported by the National Eye Institute (R01EY011787) and National Institute of Mental Health (R01MH115900). M.W. is a Hertie Fellow in the Hertie Network of Excellence in Clinical Neuroscience. R.Y. is an Ikerbasque Research Professor at the Donostia International Physics Center.

1. C. E. Cox, S. S. Carson, Medical and economic implications of prolonged mechanical ventilation and expedited post-acute care. *Semin. Respir. Crit. Care Med.* **33**, 357–361 (2012).
2. P. P. Pandharipande *et al.*; BRAIN-ICU Study Investigators, Long-term cognitive impairment after critical illness. *N. Engl. J. Med.* **369**, 1306–1316 (2013).
3. M. Unroe *et al.*, One-year trajectories of care and resource utilization for recipients of prolonged mechanical ventilation: A cohort study. *Ann. Intern. Med.* **153**, 167–175 (2010).
4. J. Kohler *et al.*, Cognitive deficits following intensive care. *Dtsch. Arztebl. Int.* **116**, 627–634 (2019).
5. A. Briner *et al.*, Developmental stage-dependent persistent impact of propofol anesthesia on dendritic spines in the rat medial prefrontal cortex. *Anesthesiology* **115**, 282–293 (2011).
6. M. De Roo *et al.*, Anesthetics rapidly promote synaptogenesis during a critical period of brain development. *PLoS One* **4**, e7043 (2009).
7. R. D. Sanders, J. Hassell, A. J. Davidson, N. J. Robertson, D. Ma, Impact of anaesthetics and surgery on neurodevelopment: An update. *Br. J. Anaesth.* **110** (suppl. 1), i53–i72 (2013).
8. J. Grutzendler, N. Kasthuri, W. B. Gan, Long-term dendritic spine stability in the adult cortex. *Nature* **420**, 812–816 (2002).
9. Y. Zuo, A. Lin, P. Chang, W. B. Gan, Development of long-term dendritic spine stability in diverse regions of cerebral cortex. *Neuron* **46**, 181–189 (2005).
10. J. T. Trachtenberg *et al.*, Long-term in vivo imaging of experience-dependent synaptic plasticity in adult cortex. *Nature* **420**, 788–794 (2002).
11. G. Yang, P. C. Chang, A. Bekker, T. J. J. Blanck, W. B. Gan, Transient effects of anesthetics on dendritic spines and filopodia in the living mouse cortex. *Anesthesiology* **115**, 718–726 (2011).
12. N. Yasuda *et al.*, Kinetics of desflurane, isoflurane, and halothane in humans. *Anesthesiology* **74**, 489–498 (1991).

13. E. de Jonge *et al*., Association between administered oxygen, arterial partial oxygen pressure and mortality in mechanically ventilated intensive care unit patients. *Crit. Care* **12**, R156 (2008).
14. M. Leger *et al*., Object recognition test in mice. *Nat. Protoc.* **8**, 2531–2537 (2013).
15. G. Feng *et al*., Imaging neuronal subsets in transgenic mice expressing multiple spectral variants of GFP. *Neuron* **28**, 41–51 (2000).
16. H. T. Xu, F. Pan, G. Yang, W. B. Gan, Choice of cranial window type for in vivo imaging affects dendritic spine turnover in the cortex. *Nat. Neurosci.* **10**, 549–551 (2007).
17. M. Segal, Dendritic spines: Morphological building blocks of memory. *Neurobiol. Learn. Mem.* **138**, 3–9 (2017).
18. R. Yuste, Dendritic spines and distributed circuits. *Neuron* **71**, 772–781 (2011).
19. P. Århem, G. Klement, J. Nilsson, Mechanisms of anesthesia: Towards integrating network, cellular, and molecular level modeling. *Neuropsychopharmacology* **28** (suppl. 1), S40–S47 (2003).
20. M. D. Krasowski, N. L. Harrison, General anaesthetic actions on ligand-gated ion channels. *Cell. Mol. Life Sci.* **55**, 1278–1303 (1999).
21. S. Kaech, H. Brinkhaus, A. Matus, Volatile anesthetics block actin-based motility in dendritic spines. *Proc. Natl. Acad. Sci. U.S.A.* **96**, 10433–10437 (1999).
22. C. Liston *et al*., Circadian glucocorticoid oscillations promote learning-dependent synapse formation and maintenance. *Nat. Neurosci.* **16**, 698–705 (2013).
23. M. Fu, Y. Zuo, Experience-dependent structural plasticity in the cortex. *Trends Neurosci.* **34**, 177–187 (2011).
24. F. Bretin *et al*., Biodistribution and radiation dosimetry for the novel SV2A radiotracer [(18)F]UCB-H: First-in-Human study. *Mol. Imaging Biol.* **17**, 557–564 (2015).
25. J. Mercier *et al*., Discovery of heterocyclic nonacetamide synaptic vesicle protein 2A (SV2A) ligands with single-digit nanomolar potency: Opening avenues towards the first SV2A positron emission tomography (PET) ligands. *ChemMedChem* **9**, 693–698 (2014).
26. S. J. Finnema *et al*., Imaging synaptic density in the living human brain. *Sci. Transl. Med.* **8**, 348ra96 (2016).
27. A. Holtmaat, L. Wilbrecht, G. W. Knott, E. Welker, K. Svoboda, Experience-dependent and cell-type-specific spine growth in the neocortex. *Nature* **441**, 979–983 (2006).
28. S. B. Hofer, T. D. Mrsic-Flogel, T. Bonhoeffer, M. Hübener, Experience leaves a lasting structural trace in cortical circuits. *Nature* **457**, 313–317 (2009).
29. L. Ma *et al*., Experience-dependent plasticity of dendritic spines of layer 2/3 pyramidal neurons in the mouse cortex. *Dev. Neurobiol.* **76**, 277–286 (2016).
30. C. Liston, W. B. Gan, Glucocorticoids are critical regulators of dendritic spine development and plasticity in vivo. *Proc. Natl. Acad. Sci. U.S.A.* **108**, 16074–16079 (2011).
31. N. J. Sofroniew, K. Svoboda, Whisking. *Curr. Biol.* **25**, R137–R140 (2015).
32. N. Pacchiarini, K. Fox, R. C. Honey, Perceptual learning with tactile stimuli in rodents: Shaping the somatosensory system. *Learn. Behav.* **45**, 107–114 (2017).
33. N. J. Sofroniew, J. D. Cohen, A. K. Lee, K. Svoboda, Natural whisker-guided behavior by head-fixed mice in tactile virtual reality. *J. Neurosci.* **34**, 9537–9550 (2014).
34. M. Antunes, G. Biala, The novel object recognition memory: Neurobiology, test procedure, and its modifications. *Cogn. Process.* **13**, 93–110 (2012).
35. E. Guic-Robles, W. M. Jenkins, H. Bravo, Vibrissal roughness discrimination is barrelcortex-dependent. *Behav. Brain Res.* **48**, 145–152 (1992).
36. D. Mumford, On the computational architecture of the neocortex. II. The role of cortico-cortical loops. *Biol. Cybern.* **66**, 241–251 (1992).
37. D. J. Felleman, D. C. Van Essen, Distributed hierarchical processing in the primate cerebral cortex. *Cereb. Cortex* **1**, 1–47 (1991).
38. G. Minamisawa, S. E. Kwon, M. Chevée, S. P. Brown, D. H. O'Connor, A non-canonical feedback circuit for rapid interactions between somatosensory cortices. *Cell Rep.* **23**, 2718–2731.e6 (2018).
39. S. A. Bedwell, E. E. Billett, J. J. Crofts, C. J. Tinsley, The topology of connections between rat prefrontal, motor and sensory cortices. *Front. Syst. Neurosci.* **8**, 177 (2014).
40. P. Berkes, G. Orbán, M. Lengyel, J. Fiser, Spontaneous cortical activity reveals hallmarks of an optimal internal model of the environment. *Science* **331**, 83–88 (2011).
41. J. E. Miller, I. Ayzenshtat, L. Carrillo-Reid, R. Yuste, Visual stimuli recruit intrinsically generated cortical ensembles. *Proc. Natl. Acad. Sci. U.S.A.* **111**, E4053–E4061 (2014).
42. A. Fassihi, A. Akrami, V. Esmaeili, M. E. Diamond, Tactile perception and working memory in rats and humans. *Proc. Natl. Acad. Sci. U.S.A.* **111**, 2331–2336 (2014).
43. E. Bobrov, J. Wolfe, R. P. Rao, M. Brecht, The representation of social facial touch in rat barrel cortex. *Curr. Biol.* **24**, 109–115 (2014).
44. C. O. Lacefield, E. A. Pnevmatikakis, L. Paninski, R. M. Bruno, Reinforcement learning recruits somata and apical dendrites across layers of primary sensory cortex. *Cell Rep.* **26**, 2000–2008.e2 (2019).
45. C. Randolph, M. C. Tierney, E. Mohr, T. N. Chase, The repeatable battery for the assessment of neuropsychological status (RBANS): Preliminary clinical validity. *J. Clin. Exp. Neuropsychol.* **20**, 310–319 (1998).
46. D. A. Dombeck, C. D. Harvey, L. Tian, L. L. Looger, D. W. Tank, Functional imaging of hippocampal place cells at cellular resolution during virtual navigation. *Nat. Neurosci.* **13**, 1433–1440 (2010).
47. W. Yang *et al*., Anesthetics fragment hippocampal network activity, alter spine dynamics and affect memory consolidation. *bioRxiv* [Preprint] (2021). https://doi.org/10.1101/2020.06.05.135905 (accessed 8 February 2021).
48. R. J. Low, Y. Gu, D. W. Tank, Cellular resolution optical access to brain regions in fissures: Imaging medial prefrontal cortex and grid cells in entorhinal cortex. *Proc. Natl. Acad. Sci. U.S.A.* **111**, 18739–18744 (2014).
49. R. N. Moda-Sava *et al*., Sustained rescue of prefrontal circuit dysfunction by antidepressant-induced spine formation. *Science* **364**, eaat8078 (2019).
50. L. Gu *et al*., Long-term in vivo imaging of dendritic spines in the hippocampus reveals structural plasticity. *J. Neurosci.* **34**, 13948–13953 (2014).
51. T. Pfeiffer, Super-resolution STED and two-photon microscopy of dendritic spine and microglial dynamics. *University of Bordeaux*, https://tel.archives-ouvertes.fr/tel-01967610 (2017).
52. E. N. Brown, K. J. Pavone, M. Naranjo, Multimodal general anesthesia: Theory and practice. *Anesth. Analg.* **127**, 1246–1258 (2018).
53. P. V. Sackey, C. R. Martling, F. Granath, P. J. Radell, Prolonged isoflurane sedation of intensive care unit patients with the Anesthetic Conserving Device. *Crit. Care Med.* **32**, 2241–2246 (2004).
54. M. Bellgardt *et al*., Use of MIRUS™ for MAC-driven application of isoflurane, sevoflurane, and desflurane in postoperative ICU patients: A randomized controlled trial. *Ann. Intensive Care* **9**, 118 (2019).
55. A. Jerath *et al*., The use of volatile anesthetic agents for long-term critical care sedation (VALTS): Study protocol for a pilot randomized controlled trial. *Trials* **16**, 560 (2015).
56. P. J. Drew *et al*., Chronic optical access through a polished and reinforced thinned skull. *Nat. Methods* **7**, 981–984 (2010).
57. A. J. Ewald, Z. Werb, M. Egeblad, Monitoring of vital signs for long-term survival of mice under anesthesia. *Cold Spring Harb. Protoc.* **2011**, pdb.prot5563 (2011).
58. G. Yang, F. Pan, W. B. Gan, Stably maintained dendritic spines are associated with lifelong memories. *Nature* **462**, 920–924 (2009).

Diskussion

Neuronalen Mikronetzwerken kommt wahrscheinlich eine Schlüsselrolle in einer Vielzahl neurologischer und psychiatrischer Erkrankungen zu. Aufgrund technischer Entwicklungen sind neuronale Mikronetzwerke in den letzten drei Jahrzehnten selbst im lebenden Gehirn empirisch zugänglich geworden. Insbesondere die Einführung zellulär auflösender *in vivo* Messmethoden wie MEAs (Bragin et al., 1999; Fried et al., 1999; Schevon et al., 2008; Ulbert et al., 2004) und 2P-Fluoreszenzmikroskopie (Denk et al., 1990) haben in den letzten Jahren fundamentale neue Einsichten in pathophysiologische Hirnprozesse und mögliche therapeutische Zielstrukturen ermöglicht. Die direkte Erforschung neuronaler Mikronetzwerke mittels hochauflösender Messmethoden hat hierbei teils Jahrhunderte währende pathophysiologische Grundkonzepte infrage gestellt und anhaltende Debatten in den jeweiligen Forschungsfeldern ausgelöst.

Als Blaupause hierfür kann die Forschung an den Grundlagen der Epilepsie dienen. Epilepsie ist eine Netzwerkerkrankung, kann jedoch auf der für sie anatomischen Schlüsselebene, jener neuronaler Mikronetzwerke und Ensembles, erst seit wenigen Jahren erschlossen werden. So sind trotz 100 Jahren experimenteller Forschung an der Epilepsie, die größtenteils auf Einzelneuronmessungen oder makroanatomischen Messtechniken (z.B. EEG, fMRT) basierte, selbst fundamentale Aspekte unklar geblieben. Es ist bislang nicht geklärt, wie ein epileptischer Anfall entsteht oder endet, warum er lokal begrenzt bleibt oder sich über das Gehirn ausbreitet und falls er dies tut, nach welchen Gesetzmäßigkeiten. Ebenfalls unklar bleibt, warum Anfälle in der Regel nicht unablässig, sondern intermittierend auftreten. Anerkannt ist derzeit, dass epilepsietypische Aktivität durch eine pathologische Interaktion erregender und hemmender lokaler Neuronenverbände zustande kommt (Jirsa et al., 2014; Khoshkhoo et al., 2017; Paz und Huguenard, 2015; Trevelyan und Schevon, 2013; Žiburkus et al., 2013). Entsprechend dieses Kenntnisstandes konzentrieren sich bisherige antiepileptische Pharmakotherapien zumeist auf eine Erhöhung hemmender, oder Verringerung erregender neuronaler Aktivität (Crepeau und Sirven, 2017; Löscher, 2011). Man könnte nun den Standpunkt vertreten, dass die Klärung der soeben genannten pathophysiologischen Grundaspekte epileptischer Anfälle

einen untergeordneten Stellenwert besitzen, solange man die Epilepsie mit den zur Verfügung stehenden Pharmakotherapien effektiv behandeln kann. Genau dies aber gelingt in einem Drittel der Epilepsiepatienten nicht und nur für einen geringen Teil der Betroffenen kommen epilepsiechirurgische Verfahren in Betracht (Wiebe und Jette, 2012). Daher besitzt die Vertiefung des Wissensstandes über Netzwerkmechanismen auf mikroanatomischer Ebene einen essentiellen Stellenwert für die gegenwärtige Epilepsieforschung.

Der hier vorliegenden Habilitationsschrift liegen eine Reihe an Publikationen zugrunde, die Fragen zu grundsätzlichen Ausbreitungsmustern und -mechanismen epileptischer Anfälle auf mikroanatomischer Ebene nachgingen. Ausgangspunkt bildete hierbei die Frage nach konservierten zeitlich räumlichen Ausbreitungsmustern wiederkehrender epileptischer Anfälle (Wenzel et al., 2017, 2019a). So fundamental diese Frage erscheint und so langjährig die Annahme, dass wiederkehrender iktualer und interiktualer Aktivität dasselbe pathophyiologisch verfestigte neuronale Netzwerk zugrunde liegt, so kontrovers wird diese Frage seit mehreren Jahren durch Resultate hochauflösender Mikronetzwerkstudien im Feld diskutiert. Die Spanne der Resultate reicht hierbei von Stereotypie der iktualen oder interiktualen Rekrutierung neuronaler Populationen (Schevon et al., 2012; Truccolo et al., 2014), bis hin zur vollkommenen Heterogenität, oder Willkür (Bower et al., 2012; Feldt Muldoon et al., 2013). Die Klärung dieser Frage ist von außerordentlicher Relevanz, da die Rationale epilepsiechirurgischer Resektion oder sub-pialer Transsektion auf der Annahme verfestigter, identifizierbarer epileptogener Netzwerkstrukturen fußt.

In Studien zur fokalen Anfallsinitiation und -propagation konnten Wenzel und Kollegen (Wenzel et al., 2017, 2019a) in Modellen akut erzeugter fokaler Anfälle (4-AP, Ptx) erstmals mittels Kombination von Feldelektrophysiologie und zellulär auflösender, intra- und translaminärer *in vivo* 2P-Mikroskopie zeigen, dass der Rekrutierung lokaler Neuronenverbände zu wiederkehrenden Anfällen eine nachvollziehbare zeitliche und räumliche Netzwerkstruktur zugrunde liegt, auch auf Ebene neuronaler Ensembles. Die Struktur konnte hierbei gleichermaßen in der Anfallsursprungszone (Wenzel et al., 2019a) und in Propagationsarealen (Wenzel et al., 2017) identifiziert werden. Gleichsam boten die Untersuchungen, basierend auf der Entdeckung iktualer

„Elasitizität“ (Wenzel et al., 2017), eine Möglichkeit der Konsolidierung der zuvor veröffentlichten, teils gegensätzlichen Ergebnisse (Bower et al., 2012; Feldt Muldoon et al., 2013; Schevon et al., 2012; Truccolo et al., 2014). Die lokale Progression epileptischer Anfälle weist hiernach unter Wahrung der relativen zeitlich räumlichen Rekrutierungsstruktur von Neuronenverbänden (also die Abfolge der Rekrutierung) nach absoluten Zeiteinheiten eine massive Dehnung oder Kompression der zeitlichen Rekrutierung auf (im Bereich von Sekunden). Begreift man einen voranschreitenden Anfall als die Extremform einer Phasensequenz (Carrillo-Reid et al., 2015; Hebb, 1949), dessen zeitliche Struktur durch intrinsische Netzwerkparameter diktiert wird, so ergibt sich durch das Resultat der strukturierten, elastischen Anfallsprogression ein Netzwerkmodell, nach welchem die iktuale Progression zwar zeitlich variieren kann, aber zugrundeliegende neuronale Konnektivität respektieren muss (Übersicht 2, siehe unten). Diesen Ergebnissen zufolge könnte ein Hauptgrund für die in vorherigen Studien disparaten Ergebnisse allein in unterschiedlichen analytischen Herangehensweisen (z.B. festgelegte absolute Zeitfenster vs. populationsbasierte relative Kategorisierung iktualer Rekrutierung) liegen.

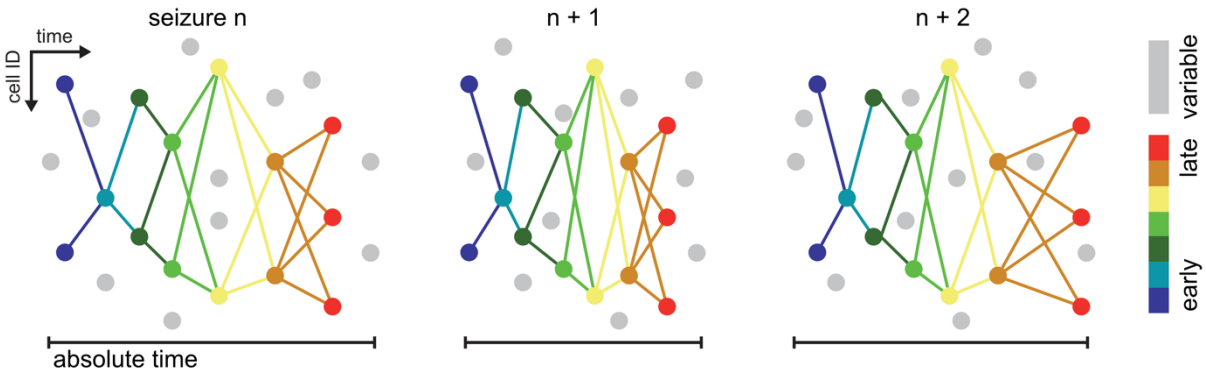

Übersicht 2: Strukturierte, elastische Progression fokaler Anfälle

Schema des Phänomens der elastischen Anfallsprogression. Dargestellt sind drei konsekutive epileptische Anfälle, die die dargestellten Neurone (gefüllte Kreise) eines lokalen Netzwerks rekrutieren. Dem Farbschema entsprechend werden Neurone von frühen zu späten Zeitpunkten rekrutiert, oder variabel (grau). Nach relativen zeitlichen Parametern (frühe Rekrutierung bis späte Rekrutierung), also der zeitlichen Reihenfolge der neuronalen Rekrutierung, lässt sich eine wiederkehrende iktuale Rekrutierungsordnung für einen substantiellen Teil der Neurone des lokalen Netzwerkes feststellen (Die Knotenpunkte des farbigen Netzes haben über Anfälle hinweg eine ähnliche Position zueinander). Die absoluten zeitlichen Rekrutierungszeiträume („absolute time“, schwarze Balken) hingegen variieren von Anfall zu Anfall enorm. Abbildung: M. Wenzel.

Die Konfiguration elastischer iktualer Rekrutierung hing den hier vorgestellten Ergebnissen zufolge kritisch von $GABA_A$-Rezeptor vermittelter kortikaler Inhibition ab (Wenzel et al., 2017). In weiterführender Untersuchung der zellulären Mechanismen

der lokalen Anfallsprogression konnte in aufwändigen multimodalen Experimenten (visuell gesteuerte Einzelzellelektrophysiologie molekular markierter neuronaler Subtypen, Feldelektrophysiologie, translaminäre 2P-Mikroskopie) erstmals mittels neu gestalteter Nanopipetten *in vivo* nachgewiesen werden, dass ein abruptes Versagen interneuronaler Hemmmechanismen in Form eines Depolarisationsblocks mit der lokalen Rekrutierung neuronaler Zellverbände zusammenfällt (Jayant und Wenzel et al., 2019). Dieses Ergebnis steht klar in der Linie vorhergehender Forschungsarbeiten, die der Umgebungshemmung (extrafokal lokalisiert) eine fundamental wichtige Rolle in der Eindämmung fokaler epilepsietypischer Anfälle zugeschrieben haben (Cammarota et al., 2013; Prince und Wilder, 1967; Schevon et al., 2012; Trevelyan et al., 2006). Gleichsam erlaubte in diesem Kontext die optische Messung der Aktivität neuronaler Subklassen auf Populationsebene die Einsicht, dass lokale Interneuronklassen keine homogenen iktualen Aktivitätsmuster aufweisen (Wenzel et al., 2019a). Selbst benachbarte Parvalbumin positive Interneurone zeigten massive Unterschiede in ihrem Antwortverhalten auf einbrechende iktuale Aktivität, was als möglicher Hinweis auf eine iktuale „Hemmung der Hemmung“ (Karnani et al., 2016; Paz und Huguenard, 2015). Diese Ergebnisse auf Populationsebene verdeutlichen eine komplexe Rolle hemmender Interneurone in der mikroanatomischen Progression epileptischer Anfälle.

Ein essentielles Resultat der hier vorgestellten Studien liegt in der mikroanatomischen Kompartmentalisierung und hierdurch Entkopplung lokaler Mikronetzwerkdynamiken von gemessenen Feldpotentialen (Wenzel et al., 2017, 2019a). Für die Grundlagenforschung bedeutet dies, dass die bloße Zuordnung eines Feldpotentials zu einer lokal gemessenen Aktivität keinerlei direkten Zusammenhang bedeuten muss. In den hier vorgestellten Studien zeigte sich mittels 2P-Mikroskopie, dass lokale iktuale Aktivität auf kleinstem Raum (z.B. 100 x 100 μm) mitunter dutzende Sekunden vor dem elektrographischen Anfallsbeginn detektiert werden kann (Wenzel et al., 2019a). Dies ist Ausdruck der vergleichsweise groben räumlichen Auflösung einer Feldpotentialmessung im Vergleich zu einer zellulär auflösenden Messmethode zur Ableitung der Aktivität lokaler Neuronenverbände. Gleichsam bestand, mit wachsender Distanz zwischen mikroskopiertem Mikronetzwerk und Anfallsursprungszone, die Möglichkeit, dass ein elektrographisch detektierter Anfall

vor seiner Termination ausschließlich Interneurone oder gar keine Neuronen im mikroskopierten Sichtfenster rekrutierte (Liou, Ma, Wenzel et al., 2018; Wenzel et al., 2017), weil das abgeleitete Mikronetzwerk schlicht nicht in den andernorts ablaufenden Anfall rekrutiert wurde. Dies unterstreicht nachdrücklich, dass die explizite Berücksichtigung der Lokalisation eines mikroanatomischen Messorts im Vergleich zu einem makroanatomischen Feld-potential für die Interpretation epileptischer Netzwerkdynamiken essentiell ist (Übersicht 3).

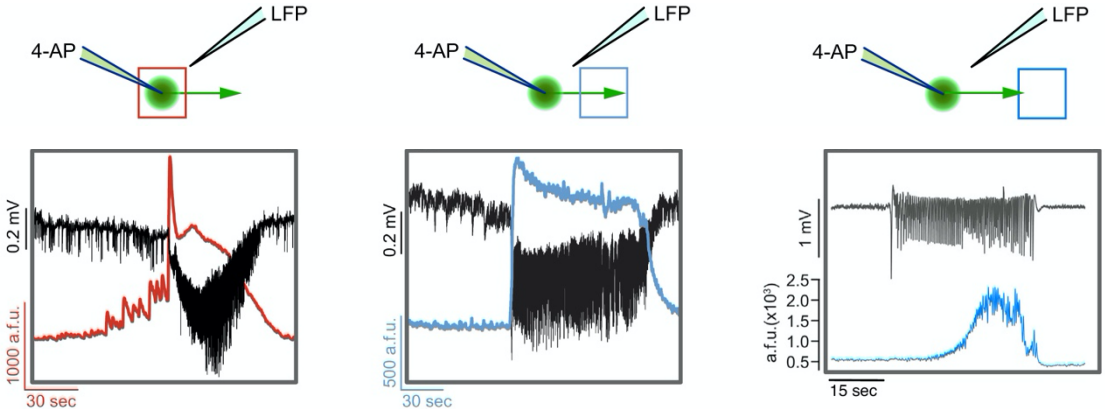

Übersicht 3: Entkopplung des lokalen Feldpotentials von neuronaler Ensembleaktivität

Übersichtsdarstellung der möglichen Konkordanz bzw. Diskonkordanz des lokalen Feldpotentials (LFP), gemessen mittels Glasmikropipette (2-5 MΩ, Distanz zu FOV wenige 100 μm) und lokaler Ensembleaktivität, gemessen mittels 2P-Ca^{2+}-Mikroskopie (FOV ca. 400 x 400 μm, L II/III) im Kontext akut erzeugter fokaler epileptischer Anfälle *in vivo* (Injektion von 7,5 nmol 4-AP in L V).
Links: oben: 2P-Ca^{2+}-Mikroskopie (rotes Quadrat) direkt über der 4-AP Injektionsstelle (intrafokal); unten: zur Messkonfiguration korrespondierendes Ca^{2+}-Populationssignal in rot, LFP in schwarz; bemerke die kontinuierlich eskalierende, bereits iktuale Ensembleaktivität, obwohl elektrographisch noch kein Anfall detektiert wird.
Mitte: oben: 2P-Ca^{2+}-Mikroskopie (blaues Quadrat) außerhalb der 4-AP Injektionsstelle (nah extrafokal, Distanz ~2 mm); unten: zur Messkonfiguration korrespondierendes Ca^{2+}-Populationssignal in blau, LFP in schwarz; bemerke die Konkordanz des elektrographischen Anfalls (LFP) und iktualen Anstiegs der Ensembleaktivität.
Rechts: oben: 2P-Ca^{2+}-Mikroskopie (blaues Quadrat) außerhalb der 4-AP Injektionsstelle (fern extrafokal, Distanz ~3-4 mm); unten: zur Messkonfiguration korrespondierendes Ca^{2+}-Populationssignal in blau, LFP in schwarz; bemerke den im Vergleich zum klar vorliegenden elektrographischen Anfall (LFP) massiv verzögerten (>15 Sek.) iktualen Anstieg der lokalen Ensembleaktivität.
Abbildung adaptiert von Wenzel et al. (2019a) und Wenzel et al. (2017).

Zur Verdeutlichung dieses beachtenswerten Umstands sei hier konkret angeführt, dass in Studien zu epileptischen Mikronetzwerken oft entweder keine Differenzierung stattfand (Miri et al., 2018), oder wiederholt, teils „mit Überraschung“ festgestellt wurde, dass interiktuale oder beginnende iktuale Aktivität im LFP ausschließlich mit interneuronaler Aktivität am Messort korrelierte (Gnatkovsky et al., 2008; Muldoon et al., 2015; Neumann et al., 2017). Hieraus abgeleitet wurde sodann teilweise ein kausaler Zusammenhang dieser Aktivität mit dem gemessenen Feldpotential, zum Beispiel dergestalt, dass interneuronale Aktivität einen epileptischen Anfall bedinge

(Gnatkovsky et al., 2008). Unter Berücksichtigung der soeben erwähnten mikro- und makroanatomischen Parameter jedoch könnte derselbe experimentelle Befund lediglich bedeuten, dass sich der Messort außerhalb der Rekrutierungszone eines ablaufenden fokalen Anfalls befand (Neumann et al., 2017; Wenzel et al., 2019a). Daher wäre, dem klassischen Prinzip der *Feedforward* Hemmung in epileptischen Mikronetzwerken zufolge (Trevelyan et al., 2007), eine Umgebungshemmungsaktivität bei gleichzeitiger Unterdrückung von Pyramidalzellaktivität nicht nur nicht überraschend, sondern zu erwarten (Trevelyan und Schevon, 2013; Wenzel et al., 2019a). Auch für den klinisch epileptologischen Alltag verdeutlicht dies nochmals grundsätzlich, dass die Lokalisation erstmaliger iktualer Rhythmisierungen im Oberflächen-EEG stets mit äußerster Sorgfalt zur vermuteten Anfallsursprungszone sowie der initialen Anfallssemiologie in Bezug gesetzt werden sollte.

Natürlich bestehen für die hier vorgestellten Forschungsarbeiten zu epileptischen Mikronetzwerken mehrere beachtenswerte Limitationen. Zuvorderst angeführt sei das *in vivo* Mausmodell fokaler epileptischer Anfälle, das den hier vorgestellten Arbeiten zugrunde liegt. Da die epileptischen Anfälle jeweils durch lokale Injektion kleiner Mengen 4-Aminopyridin (7,5 nmol) oder Picrotoxin (5 nmol) akut chemoconvulsiv im Gehirn von gesunden Versuchstieren ausgelöst wurden (Jayant und Wenzel et al., 2019; Wenzel et al., 2017, 2019b), erfüllt das experimentelle Rahmenwerk nicht den Bestand einer chronischen Epilepsie und somit auch nicht das Vorliegen eines chronisch transformierten, anfallsproduzierenden Netzwerkes. Ob die erzielten Ergebnisse sich somit ohne Weiteres auf die Anfallsmikroprogression im Rahmen chronisch fokaler Epilepsien übertragen lassen, ist unklar, wenngleich mehrere Aspekte des Modells realweltlichen medizinischen Umständen durchaus ähnlich sind (siehe unten). Die Wahl des Anfallsmodells für die hier vorgestellten Studien, welchen erstmals die systematische Analyse der mikroanatomischen Rekrutierung dicht gepackter lokaler Neuronenverbände zu epileptischen Anfällen mittels *in vivo* 2P-Mikroskopie gelang, hatte jedoch eine Reihe an technischen und prozeduralen Gründen. Die lokale Injektion der Chemoconvulsiva (CC) 4-AP oder Ptx erlaubte die präzise Differenzierung des Anfallsinitiations- gegenüber dem Propagationsareal. Dies ist in Modellen chronischer Epilepsie oder im Epilepsiepatienten nur schwerlich möglich, weil hier die Anfallsursprungszone, welche wie bereits mehrfach erwähnt auf

einen minimalen Raum beschränkt sein kann (Bragin et al., 2000; Schevon et al., 2008; Wenzel et al., 2019a), in der Regel mikroanatomisch unzureichend definiert ist.
Wir definierten das Initiationsareal als den Ort der CC Injektion und verorteten das Propagationsaral in einer Distanz von etwa 1,5 - 2 mm zur Injektion. Mittels Fluoreszenzdiffusionsmessungen konnte in anderen Studien gezeigt werden, dass die lokale 4-AP Diffusion diese Distanz vom Injektionsort im zeitlichen Versuchsablauf der hier vorgestellten Studien (~1 - 2 Stunden) nicht überschreitet (Nagappan et al., 2018). Die hier vorgestellten Experimente bekräftigten dies, zusätzlich mittels gestaffelter Ptx Injektion, dessen diffusionsbedingte Blockade $GABA_A$-vermittelter Hemmung im mikroskopierten Sichtfenster im Propagationsareal erst >1,5 Stunden nach (insgesamt zweimaliger) Injektion festgestellt werden konnte (Wenzel et al., 2017). Gleichsam wurde die Lokalisation der Messung propagierender epileptischer Anfälle nah genug am Anfallsursprung gewählt, um die Möglichkeit zu maximieren, dass propagierende epileptische Anfälle tatsächlich das mikroskopierte Areal miterfassen.

Ein weiterer gewichtiger Grund für die Wahl des Anfallsmodells war die Frequenz der hierdurch ausgelösten Anfälle (mehrere pro Stunde infolge CC Lokalinjektion). In chronischen Epilepsiemodellen ist die Frequenz epileptischer Anfälle in der Regel niedrig (Arida et al., 1999; Ewell et al., 2015; Muldoon et al., 2015). Für die hochauflösende optische Aufzeichnung einer für eine systematischen Analyse suffizienten Anzahl chronisch rekurrenter Anfälle, zusätzlich zur genannten Unklarheit über die genaue Messlokalisation im Vergleich zum Initiationsareal und die iktuale Invasionswahrscheinlichkeit im Sichtfenster (ca. 400 x 400 μm), würde dies unter aktuellen technischen Gegebenheiten ein quasi nicht zu überkommendes Hindernis bedeuten. Da sich die Versuchstiere in der Regel für jede Mikroskopie-Session kopffixiert unter einem 2P-Mikroskop befinden, ist die ethisch vertretbare Aufnahmedauer nachvollziehbar auf wenige Stunden pro Tag begrenzt. Vor dem Hintergrund weniger pro Woche auftretender epileptischer Anfälle in Mausmodellen chronischer Epilepsie reduziert sich so die Möglichkeit, tatsächlich mehrere epileptische Anfälle erfolgreich abzupassen, auf ein Minimum. Selbst wenn längere Aufnahmezeiträume möglich wären, bestünden mit zunehmender Aufnahmedauer experimentelle Einschränkungen, bedingt z.B. durch laserbedingte Fluophor-Bleicheffekte, oder pathologische Gewebserwärmung und hierdurch -schädigung

infolge prolongierter Laserexposition. Vor dem Hintergrund dieser Gegebenheiten erschien das fokale 4-AP Modell als ein geeignetes Modell zur erstmaligen systematischen Erfassung fokaler epileptischer Anfälle mittels *in vivo* 2P-Mikroskopie. Dass die hier vorgestellten Ergebnisse nicht lediglich auf ein spezifisches Anfallsmodell beschränkt sind, wurde durch die Anwendung des fokalen Ptx Modells, welches einen diametral verschiedenen Wirkmechanismus aufweist, sichergestellt.

Schließlich rekapituliert das fokale 4-AP Modell durchaus realweltliche medizinische Gegebenheiten. Die Etablierung eines akut epileptischen Anfallsfokus ähnelt medizinischen Bedingungen wie z.B. intrakranieller Blutung, Schädelhirntrauma oder Schlaganfall, welche sich oft klinisch durch akute epileptische Anfälle manifestieren (Beleza, 2012). Das Modell hat ebenfalls dahingehend Ähnlichkeit mit einer chronisch fokalen Epilepsie, als auch dort iktuale Aktivität während der Anfallsausbreitung in primär unbetroffene, anderweitig voll funktionstüchtige Hirnareale einbricht (Milton et al., 2007). Zuletzt ähneln die fokalen Anfälle, die durch 4-AP oder Ptx ausgelöst werden, klinisch und elektrographisch jenen in chronischen Epilepsiemodellen (Avoli et al., 2002; Szente und Pongracz, 1979). Anstatt ein bestimmtes Epilepsie Krankheitsmodell zu untersuchen, fokussierten sich die hier vorgestellten Arbeiten auf das Verständnis „epileptischer Netzwerkbedingungen“, welche in einer Vielzahl neurologischer Erkrankungen und selbst im gesunden Gehirn zu finden sind (Jirsa et al., 2014).

Dass die explorative Untersuchung pathologisch transformierter Neuronenverbände mittels multimodaler experimenteller Verfahren unter Einbezug zellulär auflösender Messtechniken über medizinische Gegebenheiten hinweg inhaltliche Überlappungen und gar wissenschaftliche Synergien erzeugt, zeigt sich am Beispiel der hier vorgestellten Studien zum medizinisch induzierten Bewusstseinsverlust bzw. Koma (mLOC, MIC). Vor Durchführung der hier zusammengefassten Arbeit am mLOC (Wenzel et al., 2019b) lagen keine Studien vor, die dieses Phänomen auf Ebene neuronaler Ensembles experimentell untersucht hatten. Basierend auf Harry Nyquists Berechnungen zur Telegraphie (Nyquist, 1924) sowie informationstheoretischen Überlegungen, wonach eine sinnvolle Diskrimination und Verarbeitung eines spezifischen Sinnesreizes die zerebrale Fähigkeit erfordert, diesen von einer Vielzahl

alternativer Sinnesreize zu unterscheiden (Tononi, 2008), fanden Wenzel und Kollegen experimentelle Hinweise für eine mikroanatomische Basis des mLOC (Wenzel et al., 2019b). Es ergaben sich einerseits eine anästhesietiefenabhängige reversible Reduktion des Repertoires lokal unterscheidbarer neuronaler Populationsaktivitätsmuster, andererseits eine Fragmentierung lokaler neuronaler Koaktivität, also einen Zerfall neuronaler Ensembleaktivität hin zu Einzelneuronaktivität. Beide Ergebnisse sprechen dafür, dass lokale Neuronenverbände eine Rolle im mLOC spielen, da beide diese Formen neuronaler Aktivität essentiell für kognitive Hirnoperationen und effiziente Aktivierung nachgeschalteter Ensembles im kognitiven Prozess sind (Buzsáki, 2010; Carrillo-Reid und Yuste, 2020; Harris et al., 2003; Hebb, 1949; Hopfield, 1982; Lorente de No, 1938; Yuste, 2015). Die Ergebnisse der Studie legen entgegen der verbreiteten Meinung eines primär makroanatomischen Verlusts der Informationsintegration während mLOC nahe (Barttfeld et al., 2015; Hudetz et al., 2015, 2016; Lewis et al., 2012; Schroeder et al., 2016), dass der Zusammenbruch von Information über makroanatomische Hirnareale hinweg während mLOC eine Folge des Zusammenbruchs lokaler Informationsstrukturen im Gehirn darstellt.

Die Ergebnisse im Mausmodell ließen sich durch zusätzlich implantierte MEAs in Epilepsiepatienten auch im Menschen bestätigen und bieten im Kontext epileptischer Mikronetzwerke synergistisches wissenschaftliches Potential. Da auch epileptische Anfälle oft mit einer Einschränkung oder dem Verlust des Bewusstseins (loss of consciousness [LOC]) einhergehen (Blumenfeld, 2012), bietet das Studium pathophysiologischer Grundlagen der Epilepsie gleichsam ein einzigartiges Fenster zu den neuronalen Mechanismen des Bewusstseinsverlusts, mit welchem sich Epilepsieforscher seit den modernen Anfängen des Forschungsfeldes befasst haben (Blumenfeld und Taylor, 2003; Englot et al., 2010; Jackson, 1931; Lee et al., 2002; Penfield und Jasper, 1954). Vor dem Hintergrund der hier vorgestellten Ergebnisse zum mLOC (Wenzel et al., 2019b) ließe sich nun in einem erweiterten Kontext die Hypothese aufstellen, dass die Anzahl unterscheidbarer neuronaler Aktivitätsmuster während eines epileptischen Anfalls mit LOC in den iktual erfassten Hirnarealen sinkt. Nach informationstheoretischen Gesichtspunkten könnten mLOC und epileptische Anfälle mit LOC diametrale Pole eines Spektrums neuronaler Aktivität (Anfall: maximal,

mLOC [*burst suppression*] minimal) bilden, an welchen die Ähnlichkeit auftretender neuronaler Aktivitätsmuster derartig ansteigt, dass sinnvolle Hirnoperationen nicht mehr möglich sind, mit der Konsequenz des LOC. In der Tat geht die Arbeitsgruppe Wenzel an der Klinik für Epileptologie in Bonn (UKB) dieser Hypothese derzeit unter Zuhilfenahme typischer Similaritäts-Analysen zur Identifikation und Quantifizierung neuronaler Ensembles (Wenzel und Hamm, 2021) in MEA Ableitungen an Epilepsiepatienten über quantitative Bewusstseinsebenen hinweg nach. Auch die letzte hier vorgestellte Studie zum prolongierten medizinisch induzierten Koma (pMIC) führt direkt in die epileptologische Grundlagenforschung zurück. Die hier zusammengefasste Arbeit an pMIC (Wenzel et al., 2021) konnte durch eine experimentelle *Tour de Force* unter maximaler Ausschöpfung der räumlichen Auflösung der 2P-Mikroskopie erstmals eine altersunabhängige Verknüpfung zwischen pMIC-assoziiertem kognitiven Defizit und einer hiermit korrelierenden, nachhaltigen Veränderung der synaptischen Architektur des Gehirns nachweisen. Im Kontext der Epilepsie ist seit langem bekannt, dass epileptische Anfälle Auswirkungen auf die synaptische Plastizität haben (Rensing et al., 2005). Erst kürzlich konnten im Menschen im Rahmen von immunvermittelten Epilepsien gar Autoantikörper nachgewiesen werden, welche direkt an Synapsen binden (Pitsch et al., 2020). Die dynamischen mikroanatomischen Auswirkungen dieser synaptischen Autoantikörperbindung auf die Manifestation epileptogener Netzwerke und ultimativ epileptische Anfälle sind unklar, jedoch zentraler Bestandteil eines DFG-geförderten Projektes (im SFB 1089), in welches die beteiligte Arbeitsgruppe Wenzel ihre Expertise in der chronischen *in vivo* 2P-Mikroskopie synaptischer Plastizität einbringt. So verweist diese Habilitationsschrift abschließend nicht nur auf bereits veröffentlichte Forschungsarbeiten, sondern ebenfalls in die Zukunft der Forschung an epileptischen Mikronetzwerken. Die zellulär auflösende strukturelle und funktionelle Intravital-mikroskopie, welche die Grundlage aller in dieser Habilitationsschrift zusammen-gefassten Forschungsarbeiten bildete, wird hierbei in Kombination mit elektrischen Ableitverfahren und Verhaltensanalysen einen zentralen Stellenwert einnehmen.

Zusammenfassung

Lorente de Nó, ein Schüler des wegweisenden Neuroanatoms Santiago Ramón y Cajal, hypothetisierte in den 1930er Jahren, dass statt einzelner Neurone die kooperative Aktivität afferenter Gruppen von Neuronen eine Antwort in Effektorneuronen auslöse. Spätestens seit Donald J. Hebb 1949 diese Neuronenverbände in seinem Werk *The Organization of Behavior* als *cell assemblies* („neuronale Ensembles“) bezeichnete und postulierte, dass diese das Grundelement kognitiver Prozesse darstellten, gehört die Identifikation und Charakterisierung neuronaler Ensembles zu einer Hauptambition der Neurowissenschaft.

Zur empirischen Erforschung neuronaler Ensembles bedarf es Techniken, die die Erfassung der Aktivität lokaler Neuronenverbände mit zellulärer Auflösung im intakten Gehirn erlauben. Für den Hauptteil des 20. Jahrhunderts aber standen ausschließlich elektrische Einzelzellmessungen (z.B. *Patch-clamp* Technik) oder makroanatomische Messmethoden wie EEG oder fMRT, welche hirnweite neuronale Netzwerkdynamiken erfassen, zur Verfügung. Das Aufkommen hochauflösender Mikroelektroden-Arrays (MEAs) und Bildgebungsverfahren, insbesondere der Zwei-Photonen-Mikroskopie, ermöglichte in den 1990er Jahren plötzlich die direkte Aufzeichnung neuronaler Ensembleaktivität. Seither steigt die Zahl experimenteller Studien, die die Relevanz neuronaler Ensembles in kognitiven Prozessen unterstreichen, stetig an. Auch erscheint zunehmend wahrscheinlich, dass pathologisch transformierte neuronale Ensembles in vielen neurologischen und psychiatrischen Erkrankungen eine tragende Rolle innehaben. Dieser Habilitationsschrift liegen 5 wissenschaftliche Arbeiten zugrunde, die durch kombinierte *in vivo* 2P-Mikroskopie und Elektrophysiologie Mikronetzwerkdynamiken während der epileptischen Anfallsentstehung und -ausbreitung sowie des medizinisch induzierten Bewusstseinsverlusts untersuchten.

Im Kontext einer seit Jahren bestehenden Debatte über interiktuale und iktuale Rekrutierungsmuster lokaler Neuronenverbände wurde hier gezeigt, dass diese in substantiellem Maße verlässlich in einer relativen zeitlichen Ordnung und in räumlichen Clustern zu epileptischen Anfällen rekrutiert werden. Unter Wahrung dieser relativen Rekrutierungsstruktur zeigte sich jedoch von Anfall zu Anfall nach absoluten Zeiteinheiten eine Dehnung oder Kompression der zeitlichen Abfolge neuronaler Rekrutierung im Bereich von Sekunden. Diese „elastische“ Rekrutierung hing dabei

kritisch von der lokalen Aktivität kortikaler Interneurone ab, da deren Kompromittierung in massiv gesteigerter interiktualer und iktualer Rekrutierung primär extrafokaler Neurone sowie enormer Beschleunigung und zeitlicher Uniformität dieser Rekrutierung resultierte. Durch Kombination von 2P-Mikroskopie, LFP und Nanosharp-Einzelzell-ableitungen konnte *in vivo* gezeigt werden, dass Parvalbumin positive Interneurone zeitgleich mit der lokalen iktualen Invasion neuronaler Zellverbände in einen Depolarisationsblock eintreten. Desweiteren wurden differentielle Netzwerkdynamiken während der Anfallsentstehung und -ausbreitung *in vivo* identifiziert. Bereits vor feldelektrographischer Detektion eines Anfalls fanden sich optisch innerhalb der Anfallsursprungszone Dynamiken lokaler Neuronenverbände auf kleinstem Raum (z.B. $<100 \times 100\ \mu$m), die iktuale Merkmale, also pathologisch erhöhte Aktivität, Synchronität sowie räumliche und zeitliche Signalevolution aufwiesen. Durch die hohe räumliche Auflösung und Aufzeichnungsdichte erlaubten die Ergebnisse erstmals eine empirische Rekonstruktion und Charakterisierung der fokalen Anfallsevolution auf mikro-anatomischer Ebene, vom intrafokalen Ursprung bis zur extrafokalen Propagation.

Mit Hilfe derselben Techniken wurden in zwei weiteren Arbeiten funktionelle und strukturelle Mikronetzwerkdynamiken während des medizinisch induzierten Bewusstseinsverlusts bzw. Komas (mLOC, MIC) untersucht. Entgegen der verbreiteten Annahme des Bewusstseinsverlustes durch Zusammenbruch makroanatomischer Konnektivität wurde, basierend auf informationstheoretischen Konzepten, ein möglicher mikroanatomischer mLOC Mechanismus identifiziert. In Mäusen (2P-Mikroskopie) und menschlichen Patienten (MEA) wurde eine anästhesie-tiefenabhängige reversible Reduktion des Repertoires lokal unterscheidbarer neuronaler Populationsaktivitätsmuster festgestellt, sowie ein Zerfall neuronaler Ensembleaktivität hin zu Einzelneuronaktivität. Beides spricht für eine mögliche Rolle lokaler Ensembles im mLOC, da derartige Aktivitätsmuster essentiell für eine effiziente und sinnvolle Aktivierung nachgeschalteter neuronaler Gruppen im kognitiven Prozess darstellen. In der letzten hier vorgestellten Studie konnte unter Vollausschöpfung der räumlichen Auflösung der 2P-Mikroskopie erstmals eine altersunabhängige Verknüpfung zwischen pMIC-assoziiertem kognitiven Defizit und einer hiermit korrelierenden, nachhaltigen Veränderung der - ehemals als im Erwachsenenalter stabil erachteten - synaptischen Architektur des Gehirns nachgewiesen werden.

Alle dieser Habilitationsschrift zugrundeliegenden Publikationen zeichnen sich durch die Kombination zellulär auflösender optischer und elektrophysiologischer Messmethoden im intakten Gehirn aus. Sie illustrieren die technischen Fortschritte der letzten Jahre, insbesondere im Bereich der Optik, Elektrophysiologie, Molekularbiologie und Computertechnologie, welche die experimentelle Erforschung grundsätzlicher Mechanismen pathologisch transformierter lokaler Neuronenverbände in beispielloser Weise möglich gemacht haben.

Inhaltliche Überlappung durch geteilte Autorenschaften

Dieser Habilitationsschrift liegen 5 wissenschaftliche Publikationen zugrunde. Hiervon habe ich drei als alleiniger Erstautor veröffentlicht, zwei als geteilter Erstautor.
Eine der zwei letzteren Arbeiten veröffentlichte ich als geteilter Erstautor mit Dr. Krishna Jayant (Jayant und Wenzel et al., 2019), einem Postdoktoranden und Kollegen an der Columbia University in New York, der zur Zeit der Durchführung des Forschungsprojekts wie ich im Labor von Prof. Rafael Yuste angestellt war. Die komplexen multimodalen *in vivo* Experimente dieser Veröffentlichung wurden von Herrn Dr. Jayant und mir konzipiert und gemeinsam durchgeführt. Das Manuskript der Arbeit wurde von Dr. Jayant und mir verfasst. Sein grundsätzlicher wissenschaftlicher Fokus (*Electrical and Biomedical Engineering*) ist komplementär, nicht überlappend, zu meinem wissenschaftlichen Schwerpunkt.
Eine weitere Arbeit habe ich als geteilter Erstautor mit Dr. Shuting Han und Dr. Elliot H. Smith veröffentlicht (Wenzel, Han und Smith et al., 2019a). Ich konzipierte die Arbeit, plante und führte alle murinen Experimente durch und verfasste das Manuskript der Arbeit. Die humanen Rohdatensätze wurden durch Dr. Smith prozessiert, welcher zur Zeit der Durchführung des Forschungsprojekts als Postdoktorand an der Columbia University angestellt war (Arbeitsgruppe: Prof. Dr. Catherine Schevon). Die Datenanalyse der murinen und humanen Datensätze erfolgte durch mich und Dr. Shuting Han, welche zur Zeit der Durchführung der Durchführung des Forschungsprojekts als Doktorandin im Labor von Prof. Rafael Yuste an der Columbia University in New York tätig war.

Eine Überlappung mit anderen Habilitationsschriften ist nicht gegeben.

Bibliographie

Abeles, M. (1991). Corticonics. Cambridge University Press, MA.

Andermann, M.L., Gilfoy, N.B., Goldey, G.J., Sachdev, R.N.S., Wölfel, M., McCormick, D.A., Reid, R.C., and Levene, M.J. (2013). Chronic Cellular Imaging of Entire Cortical Columns in Awake Mice Using Microprisms. Neuron *80*, 900–913.

Arida, R.M., Scorza, F.A., Peres, C.A., and Cavalheiro, E.A. (1999). The course of untreated seizures in the pilocarpine model of epilepsy. Epilepsy Res *34*, 99–107.

Avoli, M. (1990). Epileptiform discharges and a synchronous GABAergic potential induced by 4-aminopyridine in the rat immature hippocampus. Neurosci. Lett. *117*, 93–98.

Avoli, M., D'Antuono, M., Louvel, J., Kohling, R., Biagini, G., Pumain, R., D'Arcangelo, G., and Tancredi, V. (2002). Network and pharmacological mechanisms leading to epileptiform synchronization in the limbic system in vitro. Prog Neurobiol *68*, 167–207.

Bai, X., Vestal, M., Berman, R., Negishi, M., Spann, M., Vega, C., Desalvo, M., Novotny, E.J., Constable, R.T., and Blumenfeld, H. (2010). Dynamic time course of typical childhood absence seizures: EEG, behavior, and functional magnetic resonance imaging. J. Neurosci. *30*, 5884–5893.

Barttfeld, P., Uhrig, L., Sitt, J.D., Sigman, M., Jarraya, B., and Dehaene, S. (2015). Signature of consciousness in the dynamics of resting-state brain activity. Proc Natl Acad Sci U S A *112*, 887–892.

Beghi, E., Giussani, G., Abd-Allah, F., Abdela, J., Abdelalim, A., Abraha, H.N., Adib, M.G., Agrawal, S., Alahdab, F., Awasthi, A., et al. (2019). Global, regional, and national burden of epilepsy, 1990–2016: a systematic analysis for the Global Burden of Disease Study 2016. Lancet Neurol. *18*, 357–375.

Beleza, P. (2012). Acute symptomatic seizures: a clinically oriented review. Neurologist *18*, 109–119.

Berger, H. (1929). Über das Elektroenkephalogramm des Menschen. Arch. Psychiatr. Nervenkr *87*, 527–570.

Bhandari, R., Negi, S., and Solzbacher, F. (2010). Wafer-scale fabrication of penetrating neural microelectrode arrays. Biomed. Microdevices *12*, 797–807.

Blumenfeld, H. (2012). Impaired consciousness in epilepsy. Lancet Neurol. *11*, 814-26.

Blumenfeld, H., and Taylor, J. (2003). Why do seizures cause loss of consciousness? Neuroscientist *9*, 301–310.

Bower, M.R., and Buckmaster, P.S. (2008). Changes in granule cell firing rates precede locally recorded spontaneous seizures by minutes in an animal model of temporal lobe epilepsy. J Neurophysiol *99*, 2431–2442.

Bower, M.R., Stead, M., Meyer, F.B., Marsh, W.R., and Worrell, G.A. (2012). Spatiotemporal neuronal correlates of seizure generation in focal epilepsy. Epilepsia *53*, 807–816.

Bragin, A., Engel, J., Wilson, C.L., Fried, I., and Buzsáki, G. (1999). High-frequency oscillations in human brain. Hippocampus *9*, 137–142.

Bragin, A., Wilson, C.L., and Engel Jr., J. (2000). Chronic epileptogenesis requires development of a network of pathologically interconnected neuron clusters: a hypothesis. Epilepsia *41 Suppl 6*, S144-52.

Braitenberg, V. (1978). Cell Assemblies in the Cerebral Cortex, In: Heim R., Palm G. (eds) Theoretical Approaches to Complex Systems. Lecture Notes in Biomathematics, vol 21. Springer,

Berlin, Heidelberg. https://doi.org/10.1007/978-3-642-93083-6_9

Briner, A., Nikonenko, I., De Roo, M., Dayer, A., Muller, D., and Vutskits, L. (2011). Developmental stage-dependent persistent impact of propofol anesthesia on dendritic spines in the rat medial prefrontal cortex. Anesthesiology *115*, 282–293.

Buzsaki, G. (2009). Rhythms of the Brain (New York: Oxford University Press).

Buzsáki, G. (2010). Neural Syntax: Cell Assemblies, Synapsembles, and Readers. Neuron *68*, 362–385.

Cai, D.J., Aharoni, D., Shuman, T., Shobe, J., Biane, J., Song, W., Wei, B., Veshkini, M., La-Vu, M., Lou, J., et al. (2016). A shared neural ensemble links distinct contextual memories encoded close in time. Nature *534*, 115–118.

Cammarota, M., Losi, G., Chiavegato, A., Zonta, M., and Carmignoto, G. (2013). Fast spiking interneuron control of seizure propagation in a cortical slice model of focal epilepsy. J Physiol *591*, 807–822.

Campbell, P.K., Jones, K.E., Huber, R.J., Horch, K.W., and Normann, R.A. (1991). A Silicon-Based, Three-Dimensional Neural Interface: Manufacturing Processes for an Intracortical Electrode Array. IEEE Trans. Biomed. Eng. *38*, 758–768.

Carrier, M., Robert, M.È., González Ibáñez, F., Desjardins, M., and Tremblay, M.È. (2020). Imaging the Neuroimmune Dynamics Across Space and Time. Front. Neurosci. *14*, 1–13.

Carrillo-Reid, L., and Yuste, R. (2020). Playing the piano with the cortex: role of neuronal ensembles and pattern completion in perception and behavior. Curr. Opin. Neurobiol. *64*, 89–95.

Carrillo-Reid, L., Kang, J.-E., Hamm, J.P., Jackson, J., Yuste, R., Miller, J.-E.K., Hamm, J.P., Jackson, J., and Yuste, R. (2015). Endogenous sequential cortical activity evoked by visual stimuli. J. Neurosci. *35*, 8813–8828.

Carrillo-Reid, L., Yang, W., Bando, Y., Peterka, D.S., and Yuste, R. (2016). Imprinting Cortical Ensembles. Science. *353*, 691–694.

Carrillo-Reid, L., Yang, W., Kang Miller, J., Peterka, D.S., and Yuste, R. (2017). Imaging and Optically Manipulating Neuronal Ensembles. Annu. Rev. Biophys. *46*, 271–293.

Carrillo-Reid, L., Han, S., Yang, W., Akrouh, A., and Yuste, R. (2019). Controlling Visually Guided Behavior by Holographic Recalling of Cortical Ensembles. Cell *178*, 447-457.e5.

Castaigne, P., Lhermitte, F., Buge, A., Escourolle, R., Hauw, J.J., and Lyon-Caen, O. (1981). Paramedian thalamic and midbrain infarct: clinical and neuropathological study. Ann Neurol *10*, 127–148.

Cavazzuti, M., Porro, C.A., Biral, G.P., Benassi, C., and Barbieri, G.C. (1987). Ketamine effects on local cerebral blood flow and metabolism in the rat. J Cereb Blood Flow Metab *7*, 806–811.

Chen, T.W., Wardill, T.J., Sun, Y., Pulver, S.R., Renninger, S.L., Baohan, A., Schreiter, E.R., Kerr, R.A., Orger, M.B., Jayaraman, V., et al. (2013). Ultrasensitive fluorescent proteins for imaging neuronal activity. Nature *499*, 295–300.

Clausius, R. (1850). Ueber die bewegende Kraft der Wärme und die Gesetze, welche sich daraus fuer die Wärmelehre selbst ableiten lassen. Poggendorffs Ann. *79*.

Constantinople, C.M., and Bruno, R.M. (2011). Effects and mechanisms of wakefulness on local cortical networks. Neuron *69*, 1061–1068.

Cossart, R., Aronov, D., and Yuste, R. (2003). Attractor dynamics of network UP states in the neocortex. Nature *423*, 283–288.

Cox, C.E., and Carson, S.S. (2012). Medical and economic implications of prolonged mechanical ventilation and expedited post-acute care. Semin. Respir. Crit. Care Med. *33*, 357-61.

Crepeau, A.Z., and Sirven, J.I. (2017). Management of Adult Onset Seizures. Mayo Clin. Proc. *92*, 306–318.

Crick, F.C., and Koch, C. (2005). What is the function of the claustrum? Philos Trans R Soc L. B Biol Sci *360*, 1271–1279.

Dana, H., Chen, T.W., Hu, A., Shields, B.C., Guo, C., Looger, L.L., Kim, D.S., and Svoboda, K. (2014). Thy1-GCaMP6 transgenic mice for neuronal population imaging in vivo. PLoS One *9*, e108697.

Dana, H., Mohar, B., Sun, Y., Narayan, S., Gordus, A., Hasseman, J.P., Tsegaye, G., Holt, G.T., Hu, A., Walpita, D., et al. (2016). Sensitive red protein calcium indicators for imaging neural activity. Elife. 5:e12727.

Dana, H., Novak, O., Guardado-Montesino, M., Fransen, J.W., Hu, A., Borghuis, B.G., Guo, C., Kim, D.S., and Svoboda, K. (2018). Thy1 transgenic mice expressing the red fluorescent calcium indicator jRGECO1a for neuronal population imaging in vivo. PLoS One.

Denk, W., Strickler, J.H., and Webb, W.W. (1990). Two-photon laser scanning fluorescence microscopy. Science. *248*, 73–76.

Drew, P.J., Shih, A.Y., Driscoll, J.D., Knutsen, P.M., Blinder, P., Davalos, D., Akassoglou, K., Tsai, P.S., and Kleinfeld, D. (2010). Chronic optical access through a polished and reinforced thinned skull. Nat. Methods *7*, 981–986.

Duemani Reddy, G., Kelleher, K., Fink, R., and Saggau, P. (2008). Three-dimensional random access multiphoton microscopy for functional imaging of neuronal activity. Nat. Neurosci. *11*, 713–720.

Elahian, B., Lado, N.E., Mankin, E., Vangala, S., Misra, A., Moxon, K., Fried, I., Sharan, A., Yeasin, M., Staba, R., et al. (2018). Low-voltage fast seizures in humans begin with increased interneuron firing. Ann Neurol *84*, 588–600.

Englot, D.J., Yang, L., Hamid, H., Danielson, N., Bai, X., Marfeo, A., Yu, L., Gordon, A., Purcaro, M.J., Motelow, J.E., et al. (2010). Impaired consciousness in temporal lobe seizures: Role of cortical slow activity. Brain *133*, 3764–3777.

Ewell, L.A., Liang, L., Armstrong, C., Soltesz, I., Leutgeb, S., and Leutgeb, J.K. (2015). Brain State Is a Major Factor in Preseizure Hippocampal Network Activity and Influences Success of Seizure Intervention. J Neurosci *35*, 15635–15648.

Fang, W.Q., and Yuste, R. (2017). Overproduction of Neurons Is Correlated with Enhanced Cortical Ensembles and Increased Perceptual Discrimination. Cell Rep. *21*, 381–392.

Farrell, J.S., Nguyen, Q.A., and Soltesz, I. (2019). Resolving the Micro-Macro Disconnect to Address Core Features of Seizure Networks. Neuron *101*, 1016–1028.

Feldt Muldoon, S., Soltesz, I., and Cossart, R. (2013). Spatially clustered neuronal assemblies comprise the microstructure of synchrony in chronically epileptic networks. Proc Natl Acad Sci U S A *110*, 3567–3572.

Feng, G., Mellor, R.H., Bernstein, M., Keller-Peck, C., Nguyen, Q.T., Wallace, M., Nerbonne, J.M., Lichtman, J.W., and Sanes, J.R. (2000). Imaging neuronal subsets in transgenic mice expressing multiple spectral variants of GFP. Neuron *28*, 41–51.

Flores, F.J., Hartnack, K.E., Fath, A.B., Kim, S.E., Wilson, M.A., Brown, E.N., and Purdon, P.L. (2017). Thalamocortical synchronization during induction and emergence from propofol-induced unconsciousness. Proc Natl Acad Sci U S A *114*, E6660–E6668.

Frey, B.J., and Dueck, D. (2007). Clustering by passing messages between data points. Science. *315*, 972–976.

Fried, I., Wilson, C.L., Maidment, N.T., Engel, J., Behnke, E., Fields, T.A., Macdonald, K.A., Morrow, J.W., and Ackerson, L. (1999). Cerebral microdialysis combined with single-neuron and electroencephalographic recording in neurosurgical patients: Technical note. J. Neurosurg. *91*, 697–705.

Gavvala, J.R., and Schuele, S.U. (2016). New-Onset Seizure in Adults and Adolescents: A Review. JAMA *316*, 2657–2668.

Gnatkovsky, V., Librizzi, L., Trombin, F., and de Curtis, M. (2008). Fast activity at seizure onset is mediated by inhibitory circuits in the entorhinal cortex in vitro. Ann Neurol *64*, 674–686.

Goldberg, E.M., and Coulter, D.A. (2013). Mechanisms of epileptogenesis: a convergence on neural circuit dysfunction. Nat Rev Neurosci *14*, 337–349.

Golgi, C. (1873). Sulla struttura della sostanza grigia del cervello. Gazz. Med. Ital. *33*, 244–246.

Göppert-Mayer, M. (1931). Über Elementarakte mit zwei Quantensprüngen. Ann. Phys. 273–294.

Gotman, J., Grova, C., Bagshaw, A., Kobayashi, E., Aghakhani, Y., and Dubeau, F. (2005). Generalized epileptic discharges show thalamocortical activation and suspension of the default state of the brain. Proc. Natl. Acad. Sci. U. S. A. *102*, 15236–15240.

Grutzendler, J., Kasthuri, N., and Gan, W.B. (2002). Long-term dendritic spine stability in the adult cortex. Nature 420(6917):812-6.

Hamm, J.P., Peterka, D.S., Gogos, J.A., and Yuste, R. (2017). Altered Cortical Ensembles in Mouse Models of Schizophrenia. Neuron *94*, 153–167.

Hamm, J.P., Shymkiv, Y., Mukai, J., Gogos, J.A., and Yuste, R. (2020). Aberrant Cortical Ensembles and Schizophrenia-like Sensory Phenotypes in Setd1a+/– Mice. Biol. Psychiatry. 10.1016/j.biopsych.2020.01.004.

Hamm, J.P., Shymkiv, Y., Han, S., Yang, W., and Yuste, R. (2021). Cortical ensembles selective for context. Proc. Natl. Acad. Sci. U. S. A. *118*, 14.

Harris, K.D., Csicsvari, J., Hirase, H., Dragoi, G., and Buzsáki, G. (2003). Organization of cell assemblies in the hippocampus. Nature *424*, 552–556.

He, M., and Huang, Z.J. (2018). Genetic approaches to access cell types in mammalian nervous systems. Curr. Opin. Neurobiol. *50*, 109–118.

Hebb, D.O. (1949). The Organization of Behavior (Wiley, New York).

Helassa, N., Podor, B., Fine, A., and Török, K. (2016). Design and mechanistic insight into ultrafast calcium indicators for monitoring intracellular calcium dynamics. Sci. Rep. *6*, 1–14.

Herrera, C.G., Cadavieco, M.C., Jego, S., Ponomarenko, A., Korotkova, T., and Adamantidis, A. (2016). Hypothalamic feedforward inhibition of thalamocortical network controls arousal and consciousness. Nat Neurosci *19*, 290–298.

Holtmaat, A., Bonhoeffer, T., Chow, D.K., Chuckowree, J., De Paola, V., Hofer, S.B., Hübener, M., Keck, T., Knott, G., Lee, W.C.A., et al. (2009). Long-term, high-resolution imaging in the mouse

neocortex through a chronic cranial window. Nat. Protoc. 4, 1128–1144

Hopfield, J.J. (1982). Neural networks and physical systems with emergent collective computational abilities. Proc Natl Acad Sci U S A *79*, 2554–2558.

Houweling, A.R., and Brecht, M. (2008). Behavioural report of single neuron stimulation in somatosensory cortex. Nature *451*, 65–68.

Hu, S., Ciliberti, D., Grosmark, A.D., Michon, F., Ji, D., Penagos, H., Buzsáki, G., Wilson, M.A., Kloosterman, F., and Chen, Z. (2018). Real-Time Readout of Large-Scale Unsorted Neural Ensemble Place Codes. Cell Rep. *25*, 2635-2642.e5.

Huber, D., Petreanu, L., Ghitani, N., Ranade, S., Hromadka, T., Mainen, Z., and Svoboda, K. (2008). Sparse optical microstimulation in barrel cortex drives learned behaviour in freely moving mice. Nature *451*, 61–64.

Hudetz, A.G., Liu, X., and Pillay, S. (2015). Dynamic repertoire of intrinsic brain states is reduced in propofol-induced unconsciousness. Brain Connect *5*, 10–22.

Hudetz, A.G., Vizuete, J.A., Pillay, S., and Mashour, G.A. (2016). Repertoire of mesoscopic cortical activity is not reduced during anesthesia. Neuroscience *339*, 402–417.

Ikegaya, Y., Aaron, G., Cossart, R., Aronov, D., Lampl, I., Ferster, D., and Yuste, R. (2004). Synfire chains and cortical songs: temporal modules of cortical activity. Science *304*, 559–564.

Jackson, J.H. (1931). Selected Writings of John Hughlings Jackson. Volume I: On Epilepsy and Epileptiform Convulsions. J. Am. Med. Assoc.

Jáidar, O., Carrillo-Reid, L., Hernández, A., Drucker-Colín, R., Bargas, J., and Hernández-Cruz, A. (2010). Dynamics of the Parkinsonian striatal microcircuit: Entrainment into a dominant network state. J. Neurosci. *30*, 11326–11336.

Jayant, K., Hirtz, J.J., Plante, I.J., Tsai, D.M., De Boer, W.D., Semonche, A., Peterka, D.S., Owen, J.S., Sahin, O., Shepard, K.L., et al. (2017). Targeted intracellular voltage recordings from dendritic spines using quantum-dot-coated nanopipettes. Nat Nanotechnol *12*, 335–342.

Jayant, K., Wenzel, M., Bando, Y., Hamm, J.P., Mandriota, N., Rabinowitz, J.H., Plante, I.J.-L., Owen, J.S., Sahin, O., Shepard, K.L., et al. (2019). Flexible Nanopipettes for Minimally Invasive Intracellular Electrophysiology In Vivo. Cell Rep. *26*, 266–278.

Jennett, B. (2002). The Vegetative State: Medical Facts, Ethical and Legal Dilemmas (Cambridge: Cambridge University Press).

Jirsa, V.K., Stacey, W.C., Quilichini, P.P., Ivanov, A.I., and Bernard, C. (2014). On the nature of seizure dynamics. Brain *137*, 2210–2230.

Jouhanneau, J.S., and Poulet, J.F.A. (2019). Multiple Two-Photon Targeted Whole-Cell Patch-Clamp Recordings from Monosynaptically Connected Neurons in vivo. Front. Synaptic Neurosci. *11*, 1–13.

Jun, J.J., Steinmetz, N.A., Siegle, J.H., Denman, D.J., Bauza, M., Barbarits, B., Lee, A.K., Anastassiou, C.A., Andrei, A., Aydin, Ç., et al. (2017). Fully integrated silicon probes for high-density recording of neural activity. Nature *551*, 232–236.

Kampa, B.M., Roth, M.M., Göbel, W., and Helmchen, F. (2011). Representation of visual scenes by local neuronal populations in layer 2/3 of mouse visual cortex. Front. Neural Circuits *5*, 18.

Karnani, M.M.M., Jackson, J., Ayzenshtat, I., Tucciarone, J., Manoocheri, K., Snider, W.G.G., and Yuste, R. (2016). Cooperative Subnetworks of Molecularly Similar Interneurons in Mouse Neocortex. Neuron *90*, 86–100.

Kasai, H., Fukuda, M., Watanabe, S., Hayashi-Takagi, A., and Noguchi, J. (2010). Structural dynamics of dendritic spines in memory and cognition. Trends Neurosci. *33*, 121–129.

Khodagholy, D., Gelinas, J.N., Thesen, T., Doyle, W., Devinsky, O., Malliaras, G.G., and Buzsáki, G. (2015). NeuroGrid: Recording action potentials from the surface of the brain. Nat. Neurosci. *18*, 310–315.

Khoshkhoo, S., Vogt, D., and Sohal, V.S. (2017). Dynamic, Cell-Type-Specific Roles for GABAergic Interneurons in a Mouse Model of Optogenetically Inducible Seizures. Neuron *93*, 291–298.

Koch, C. (2012). In which I argue that consciousness is a fundamental property of complex things… (Cambridge, Massachusetts: MIT Press).

Kohler, J., Borchers, F., Endres, M., Weiss, B., Spies, C., and Emmrich, J.V. (2019). Cognitive deficits following intensive care. Dtsch Arztebl Int *116*, 627–634.

Kuchibhotla, K. V., Wegmann, S., Kopeikina, K.J., Hawkes, J., Rudinskiy, N., Andermann, M.L., Spires-Jones, T.L., Bacskai, B.J., and Hyman, B.T. (2014). Neurofibrillary tangle-bearing neurons are functionally integrated in cortical circuits in vivo. Proc. Natl. Acad. Sci. U. S. A.

Laaksonen, L., Kallioinen, M., Langsjo, J., Laitio, T., Scheinin, A., Scheinin, J., Kaisti, K., Maksimow, A., Kallionpaa, R.E., Rajala, V., et al. (2018). Comparative effects of dexmedetomidine, propofol, sevoflurane, and S-ketamine on regional cerebral glucose metabolism in humans: a positron emission tomography study. Br J Anaesth *121*, 281–290.

Lashley, K.S. (1929). Brain Mechanisms and Intelligence: A Quantitative Study of Injuries to the Brain (University of Chicago Press).

Lee, A.K., Manns, I.D., Sakmann, B., and Brecht, M. (2006). Whole-Cell Recordings in Freely Moving Rats. Neuron *51*, 399–407.

Lee, A.K., Epsztein, J., and Brecht, M. (2009). Head-anchored whole-cell recordings in freely moving rats. Nat. Protoc. *4*, 385–392.

Lee, K.H., Meador, K.J., Park, Y.D., King, D.W., Murro, A.M., Pillai, J.J., and Kaminski, R.J. (2002). Pathophysiology of altered consciousness during seizures: Subtraction SPECT study. Neurology *59*, 841–846.

Leger, M., Quiedeville, A., Bouet, V., Haelewyn, B., Boulouard, M., Schumann-Bard, P., and Freret, T. (2013). Object recognition test in mice. Nat. Protoc. *8*, 2531–2537.

Leszczynski, M., Chaieb, L., Reber, T.P., Derner, M., Axmacher, N., and Fell, J. (2017). Mind wandering simultaneously prolongs reactions and promotes creative incubation. Sci. Rep. *7*, 1–9.

Lewis, L.D., Weiner, V.S., Mukamel, E.A., Donoghue, J.A., Eskandar, E.N., Madsen, J.R., Anderson, W.S., Hochberg, L.R., Cash, S.S., Brown, E.N., et al. (2012). Rapid fragmentation of neuronal networks at the onset of propofol-induced unconsciousness. Proc Natl Acad Sci U S A *109*, E3377-86.

Liang, B., Zhang, L., Barbera, G., Fang, W., Zhang, J., Chen, X., Chen, R., Li, Y., and Lin, D.T. (2018). Distinct and Dynamic ON and OFF Neural Ensembles in the Prefrontal Cortex Code Social Exploration. Neuron *100*, 700-714.e9.

Lillis, K.P., Wang, Z., Mail, M., Zhao, G.Q., Berdichevsky, Y., Bacskai, B., and Staley, K.J. (2015). Evolution of Network Synchronization during Early Epileptogenesis Parallels Synaptic Circuit Alterations. J Neurosci *35*, 9920–9934.

Liou, J.-Y., Ma, H., Wenzel, M., Zhao, M., Baird-Daniel, E., Smith, E.H., Daniel, A., Emerson, R., Yuste, R., Schwartz, T.H., et al. (2018). Role of inhibitory control in modulating focal seizure spread. Brain *141*, 2083–2097.

Little, W.A. (1974). The existence of persistent states in the brain. Math. Biosci. *19*, 101–120.

Long, M.A., and Lee, A.K. (2012). Intracellular recording in behaving animals. Curr. Opin. Neurobiol. *22*, 34–44.

Lorente de No, R. (1938). Analysis of the activity of the chains of internuncial neurons. J. Neurophysiol. 207–244.

Löscher, W. (2011). Critical review of current animal models of seizures and epilepsy used in the discovery and development of new antiepileptic drugs. Seizure *20*, 359–368.

Van Der Maaten, L., and Hinton, G. (2008). Visualizing Data using t-SNE. J. Mach. Learn. Res. *9*, 2579–2605.

Margrie, T.W., Brecht, M., and Sakmann, B. (2002). In vivo, low-resistance, whole-cell recordings from neurons in the anaesthetized and awake mammalian brain. Pflugers Arch. Eur. J. Physiol. *444*, 491–498.

Margrie, T.W., Meyer, A.H., Caputi, A., Monyer, H., Hasan, M.T., Schaefer, A.T., Denk, W., and Brecht, M. (2003). Targeted whole-cell recordings in the mammalian brain in vivo. Neuron *39*, 911–918.

Marinković, P., Blumenstock, S., Goltstein, P.M., Korzhova, V., Peters, F., Knebl, A., and Herms, J. (2019). In vivo imaging reveals reduced activity of neuronal circuits in a mouse tauopathy model. Brain *142*, 1051–1062.

Merricks, E.M., Smith, E.H., McKhann, G.M., Goodman, R.R., Bateman, L.M., Emerson, R.G., Schevon, C.A., and Trevelyan, A.J. (2015). Single unit action potentials in humans and the effect of seizure activity. Brain. *138* (Pt 10), 2891-2906.

Mhuircheartaigh, R.N., Rosenorn-Lanng, D., Wise, R., Jbabdi, S., Rogers, R., and Tracey, I. (2010). Cortical and subcortical connectivity changes during decreasing levels of consciousness in humans: a functional magnetic resonance imaging study using propofol. J Neurosci *30*, 9095–9102.

Miller, J.E., Ayzenshtat, I., Carrillo-Reid, L., and Yuste, R. (2014). Visual stimuli recruit intrinsically generated cortical ensembles. Proc Natl Acad Sci U S A *111*, E4053-61.

Milton, J.G., Chkhenkeli, S.A., and Towle, V.L. (2007). Brain Connectivity and the Spread of Epileptic Seizures. Ed. A. R. McIntosh Viktor K. Jirsa (Handb. Brain Connect. Heidelb. Springer).

Minert, A., Yatziv, S.L., and Devor, M. (2017). Location of the Mesopontine Neurons Responsible for Maintenance of Anesthetic Loss of Consciousness. J Neurosci *37*, 9320–9331.

Miri, M.L., Vinck, M., Pant, R., and Cardin, J.A. (2018). Altered hippocampal interneuron activity precedes ictal onset. Elife *7*, e40750.

Mollinedo-Gajate, I., Song, C., and Knöpfel, T. (2019). Genetically encoded fluorescent calcium and voltage indicators. In Handbook of Experimental Pharmacology, pp. 209–229.

Morcos, A.S., and Harvey, C.D. (2016). History-dependent variability in population dynamics during evidence accumulation in cortex. Nat. Neurosci. *19*, 1672–1681.

Moruzzi, G., and Magoun, H.W. (1949). Brain stem reticular formation and activation of the EEG. Electroencephalogr Clin Neurophysiol *1*, 455–473.

Muldoon, S.F., Villette, V., Tressard, T., Malvache, A., Reichinnek, S., Bartolomei, F., and Cossart, R. (2015). GABAergic inhibition shapes interictal dynamics in awake epileptic mice. Brain *138*, 2875–2890.

Nagappan, S., Liu, L., Fetcho, R., Nguyen, J., Nishimura, N., Radwanski, R.E., Lieberman, S., Baird-Daniel, E., Ma, H., Zhao, M., et al. (2018). In Vivo Femtosecond Laser Subsurface Cortical Microtransections Attenuate Acute Rat Focal Seizures. Cereb Cortex. *29*, 8, 3415-3426.

Neumann, A., Raedt, R., Steenland, H.W., Sprengers, M., Bzymek, K., Navratilova, Z., Mesina, L., Xie, J., Lapointe, V., Kloosterman, F., et al. (2017). Involvement of fast-spiking cells in ictal sequences during spontaneous seizures in rats with chronic temporal lobe epilepsy. Brain *Volume 140*, 2355–2369.

Ngugi, A.K., Bottomley, C., Kleinschmidt, I., Sander, J.W., and Newton, C.R. (2010). Estimation of the burden of active and life-time epilepsy: a meta-analytic approach. Epilepsia *51*, 883–890.

Nguyen, Q.T., Callamaras, N., Hsieh, C., and Parker, I. (2001). Construction of a two-photon microscope for video-rate Ca2+ imaging. Cell Calcium *30*, 383–393.

Niediek, J., Boström, J., Elger, C.E., and Mormann, F. (2016). Reliable analysis of single-unit recordings from the human brain under noisy conditions: Tracking neurons over hours. PLoS One *11*, e0166598.

Nikolenko, V., Watson, B.O., Araya, R., Woodruff, A., Peterka, D.S., and Yuste, R. (2008). SLM microscopy: Scanless two-photon imaging and photostimulation with spatial light modulators. Front. Neural Circuits *2*, 5.

Noebels, J., Avoli, M., Rogawski, M., Olsen, R., and Delgado-Escueta, A. (2012). Jasper's Basic Mechanisms of the Epilepsies.

Noguchi, A., Ikegaya, Y., and Matsumoto, N. (2021). In vivo whole-cell patch-clamp methods: Recent technical progress and future perspectives. Sensors *21*, 1–21.

Nyquist, H. (1924). Certain factors affecting telegraph speed. Bell Syst. Tech. J. *3*, 324–346.

Ogawa, S., Lee, T.M., Kay, A.R., and Tank, D.W. (1990). Brain magnetic resonance imaging with contrast dependent on blood oxygenation. Proc Natl Acad Sci U S A *87*, 9868–9872.

Pala, A., and Petersen, C.C.H. (2015). InVivo Measurement of Cell-Type-Specific Synaptic Connectivity and Synaptic Transmission in Layer 2/3 Mouse Barrel Cortex. Neuron *85*, 68–75.

Palm, G., Knoblauch, A., Hauser, F., and Schüz, A. (2014). Cell assemblies in the cerebral cortex. Biol. Cybern. *108*, 559–572.

Pandharipande, P.P., Girard, T.D., Jackson, J.C., Morandi, A., Thompson, J.L., Pun, B.T., Brummel, N.E., Hughes, C.G., Vasilevskis, E.E., Shintani, A.K., et al. (2013). Long-Term Cognitive Impairment after Critical Illness. N. Engl. J. Med. *369*, 1306–1316.

Paninski, L., and Cunningham, J.P. (2018). Neural data science: accelerating the experiment-analysis-theory cycle in large-scale neuroscience. Curr. Opin. Neurobiol. *50*, 232–241.

Pavlov, P.I. (1927). Conditioned reflexes: An investigation of the physiological activity of the cerebral cortex (Oxford University Press).

Paz, J.T., and Huguenard, J.R. (2015). Microcircuits and their interactions in epilepsy: is the focus out of focus? Nat Neurosci *18*, 351–359.

Pedreira, C., Martinez, J., Ison, M.J., and Quian Quiroga, R. (2012). How many neurons can we see with current spike sorting algorithms? J. Neurosci. Methods *211*, 58–65.

Pender, J.W. (1971). Dissociative anesthesia. JAMA *215*, 1126–1130.

Penfield, W., and Jasper, H. (1954). Epilepsy and the Functional Anatomy of the Human Brain (Little,

Brown, Boston).

Pernía-Andrade, A.J., and Jonas, P. (2014). Theta-Gamma-Modulated Synaptic Currents in Hippocampal Granule Cells InVivo Define a Mechanism for Network Oscillations. Neuron *81*, 140–152.

Petersen, C.C.H. (2017). Whole-Cell Recording of Neuronal Membrane Potential during Behavior. Neuron *95*, 1266–1281.

Pilge, S., Jordan, D., Kreuzer, M., Kochs, E.F., and Schneider, G. (2014). Burst suppression-MAC and burst suppression-CP(5)(0) as measures of cerebral effects of anaesthetics. Br J Anaesth *112*, 1067–1074.

Pitsch, J., Kamalizade, D., Braun, A., Kuehn, J.C., Gulakova, P.E., Rüber, T., Lubec, G., Dietrich, D., von Wrede, R., Helmstaedter, C., et al. (2020). Drebrin Autoantibodies in Patients with Seizures and Suspected Encephalitis. Ann. Neurol. *87*, 869–884.

Poerio, G.L., Sormaz, M., Wang, H.T., Margulies, D., Jefferies, E., and Smallwood, J. (2017). The role of the default mode network in component processes underlying the wandering mind. Soc. Cogn. Affect. Neurosci. *12*, 1047–1062.

Polack, P.O., Friedman, J., and Golshani, P. (2013). Cellular mechanisms of brain state-dependent gain modulation in visual cortex. Nat Neurosci *16*, 1331–1339.

Pouget, A., Dayan, P., and Zemel, R. (2000). Information processing with population codes. Nat. Rev. Neurosci. *1*, 125–132.

Prince, D.A., and Wilder, B.J. (1967). Control mechanisms in cortical epileptogenic foci. “Surround” inhibition. Arch Neurol *16*, 194–202.

Progatzky, F., Dallman, M.J., and Celso, C. Lo (2013). From seeing to believing: Labelling strategies for in vivo cell-tracking experiments. Interface Focus *3*, 3.

Quintas, R., Raggi, A., Giovannetti, A.M., Pagani, M., Sabariego, C., Cieza, A., and Leonardi, M. (2012). Psychosocial difficulties in people with epilepsy: a systematic review of literature from 2005 until 2010. Epilepsy Behav *25*, 60–67.

Raichle, M.E., MacLeod, A.M., Snyder, A.Z., Powers, W.J., Gusnard, D.A., and Shulman, G.L. (2001). A default mode of brain function. Proc. Natl. Acad. Sci. U. S. A. *98*, 676–682.

Rensing, N., Ouyang, Y., Yang, X.F., Yamada, K.A., Rothman, S.M., and Wong, M. (2005). In vivo imaging of dendritic spines during electrographic seizures. Ann Neurol *58*, 888–898.

Reznichenko, L., Cheng, Q., Nizar, K., Gratiy, S.L., Saisan, P.A., Rockenstein, E.M., González, T., Patrick, C., Spencer, B., Desplats, P., et al. (2012). In vivo alterations in Calcium buffering capacity in transgenic mouse model of synucleinopathy. J. Neurosci. *32*, 9992–9998.

De Roo, M., Klauser, P., Briner, A., Nikonenko, I., Mendez, P., Dayer, A., Kiss, J.Z., Muller, D., and Vutskits, L. (2009). Anesthetics rapidly promote synaptogenesis during a critical period of brain development. PLoS One *4*, e7043.

Sakmann, B., and Neher, E. (2009). Single-Channel Recording, Second Edition.

Sanders, R.D., Hassell, J., Davidson, A.J., Robertson, N.J., and Ma, D. (2013). Impact of anaesthetics and surgery on neurodevelopment: an update. Br J Anaesth *110 Suppl*, i53-72.

Schevon, C.A., Ng, S.K., Cappell, J., Goodman, R.R., McKhann Jr., G., Waziri, A., Branner, A., Sosunov, A., Schroeder, C.E., and Emerson, R.G. (2008). Microphysiology of epileptiform activity in human neocortex. J Clin Neurophysiol *25*, 321–330.

Schevon, C.A., Weiss, S.A., McKhann Jr., G., Goodman, R.R., Yuste, R., Emerson, R.G., and Trevelyan, A.J. (2012). Evidence of an inhibitory restraint of seizure activity in humans. Nat Commun *3*, 1060.

Schroeder, K.E., Irwin, Z.T., Gaidica, M., Nicole Bentley, J., Patil, P.G., Mashour, G.A., and Chestek, C.A. (2016). Disruption of corticocortical information transfer during ketamine anesthesia in the primate brain. Neuroimage *134*, 459–465.

Schröter, M.S., Spoormaker, V.I., Schorer, A., Wohlschläger, A., Czisch, M., Kochs, E.F., Zimmer, C., Hemmer, B., Schneider, G., Jordan, D., et al. (2012). Spatiotemporal reconfiguration of large-scale brain functional networks during propofol-induced loss of consciousness. J. Neurosci. *32*, 12832–12840.

Scoville, W.B., and Milner, B. (1957). Loss of recent memory after bilateral hippocampal lesions. J Neurol Neurosurg Psychiatry *20*, 11–21.

Segal, M. (2017). Dendritic spines: Morphological building blocks of memory. Neurobiol. Learn. Mem. *138*, 3–9.

Sessolo, M., Marcon, I., Bovetti, S., Losi, G., Cammarota, M., Ratto, G.M., Fellin, T., and Carmignoto, G. (2015). Parvalbumin-Positive Inhibitory Interneurons Oppose Propagation But Favor Generation of Focal Epileptiform Activity. J Neurosci *35*, 9544–9557.

Sharma, G., Annetta, N., Friedenberg, D., Blanco, T., Vasconcelos, D., Shaikhouni, A., Rezai, A.R., and Bouton, C. (2015). Time Stability and Coherence Analysis of Multiunit, Single-Unit and Local Field Potential Neuronal Signals in Chronically Implanted Brain Electrodes. Bioelectron. Med. *2*, 63–71.

Shepherd, G.M. (1991). Foundations of the Neuron Doctrine (Oxford University Press).

Sherrington, C.S. (1906). Observations on the scratch-reflex in the spinal dog. J. Physiol. *34*, 1–50.

Shiri, Z., Manseau, F., Lévesque, M., Williams, S., and Avoli, M. (2016). Activation of specific neuronal networks leads to different seizure onset types. Ann. Neurol. *79*, 354–365.

Siniscalchi, M.J., Wang, H., and Kwan, A.C. (2019). Enhanced Population Coding for Rewarded Choices in the Medial Frontal Cortex of the Mouse - PubMed. Cereb. Cortex *29*, 4090–4106.

Stead, M., Bower, M., Brinkmann, B.H., Lee, K., Marsh, W.R., Meyer, F.B., Litt, B., Van Gompel, J., and Worrell, G.A. (2010). Microseizures and the spatiotemporal scales of human partial epilepsy. Brain *133*, 2789–2797.

Steriade, M. (2003). The corticothalamic system in sleep. Front Biosci *8*, d878-99.

Suzuki, M., and Larkum, M.E. (2020). General Anesthesia Decouples Cortical Pyramidal Neurons. Cell *180*, 666–676.

Svoboda, K., Denk, W., Kleinfeld, D., and Tank, D.W. (1997). In vivo dendritic calcium dynamics in neocortical pyramidal neurons. Nature *385*, 161–165.

Szente, M., and Pongracz, F. (1979). Aminopyridine-induced seizure activity. Electroencephalogr Clin Neurophysiol *46*, 605–608.

Tononi, G. (2008). Consciousness as integrated information: a provisional manifesto. Biol Bull *215*, 216–242.

Tononi, G., Edelman, G.M., and Sporns, O. (1998). Complexity and coherency: Integrating information in the brain. Trends Cogn. Sci. *2*, 474–484.

Tononi, G., Boly, M., Massimini, M., and Koch, C. (2016). Integrated information theory: from consciousness to its physical substrate. Nat Rev Neurosci *17*, 450–461.

Trachtenberg, J.T., Chen, B.E., Knott, G.W., Feng, G., Sanes, J.R., Welker, E., and Svoboda, K. (2002). Long-term in vivo imaging of experience-dependent synaptic plasticity in adult cortex. Nature *420*, 788–794.

Trevelyan, A.J., and Schevon, C.A. (2013). How inhibition influences seizure propagation. Neuropharmacology *69*, 45–54.

Trevelyan, A.J., Sussillo, D., Watson, B.O., and Yuste, R. (2006). Modular Propagation of Epileptiform Activity: Evidence for an Inhibitory Veto in Neocortex. *26*, 48, 12447-12455.

Trevelyan, A.J., Sussillo, D., and Yuste, R. (2007). Feedforward Inhibition Contributes to the Control of Epileptiform Propagation Speed. *27*, 13, 3383-3387.

Truccolo, W., Donoghue, J.A., Hochberg, L.R., Eskandar, E.N., Madsen, J.R., Anderson, W.S., Brown, E.N., Halgren, E., and Cash, S.S. (2011). Single-neuron dynamics in human focal epilepsy. Nat Neurosci *14*, 635–641.

Truccolo, W., Ahmed, O.J., Harrison, M.T., Eskandar, E.N., Cosgrove, G.R., Madsen, J.R., Blum, A.S., Potter, N.S., Hochberg, L.R., and Cash, S.S. (2014). Neuronal ensemble synchrony during human focal seizures. J Neurosci *34*, 9927–9944.

Tye, K.M. (2014). Neural circuit reprogramming: A new paradigm for treating neuropsychiatric disease? Neuron *83*, 1259–1261.

Ulbert, I., Heit, G., Madsen, J., Karmos, G., and Halgren, E. (2004). Laminar Analysis of Human Neocortical Interictal Spike Generation and Propagation: Current Source Density and Multiunit Analysis In Vivo. Epilepsia *45*, 48–56.

Unroe, M., Kahn, J.M., Carson, S.S., Govert, J.A., Martinu, T., Sathy, S.J., Clay, A.S., Chia, J., Gray, A., Tulsky, J.A., et al. (2010). One-year trajectories of care and resource utilization for recipients of prolonged mechanical ventilation: A cohort study. Ann. Intern. Med. *153*, 167–175.

Welch, T.A. (1984). A Technique for High-Performance Data-Compression. Computer (Long. Beach. Calif). *17*, 8–19.

Wenzel, M., and Hamm, J.P. (2021). Identification and quantification of neuronal ensembles in optical imaging experiments. J. Neurosci. Methods *351*, 109046.

Wenzel, M., Hamm, J.P., Peterka, D.S., and Yuste, R. (2017). Reliable and Elastic Propagation of Cortical Seizures In Vivo. Cell Rep. *19*, 2681–2693.

Wenzel, M., Hamm, J.P., Peterka, D.S., and Yuste, R. (2019a). Acute Focal Seizures Start As Local Synchronizations of Neuronal Ensembles. J. Neurosci. *39*, 8562–8575.

Wenzel, M., Han, S., Smith, E.H., Hoel, E., Greger, B., House, P.A., and Yuste, R. (2019b). Reduced Repertoire of Cortical Microstates and Neuronal Ensembles in Medically Induced Loss of Consciousness. Cell Syst. *8*, 467–474.

Wenzel, M., Leunig, A., Han, S., Peterka, D.S., and Yuste, R. (2021). Prolonged anesthesia alters brain synaptic architecture. Proc. Natl. Acad. Sci. *118*, e2023676118.

Wiebe, S., and Jette, N. (2012). Pharmacoresistance and the role of surgery in difficult to treat epilepsy. Nat. Rev. Neurol. *8*, 669–677.

Xin, Y., Zhong, L., Zhang, Y., Zhou, T., Pan, J., and Xu, N. long (2019). Sensory-to-Category Transformation via Dynamic Reorganization of Ensemble Structures in Mouse Auditory Cortex.

Neuron *103*, 909-921.e6.

Xu, H.T., Pan, F., Yang, G., and Gan, W.B. (2007). Choice of cranial window type for in vivo imaging affects dendritic spine turnover in the cortex. Nat. Neurosci. *10*, 549–551.

y Cajal, S.R. (1888). Estructura de los centros nerviosos de las aves. Rev. Trim. Histol. Norm. Pat. *1*, 1–10.

Yang, W., and Yuste, R. (2017). In vivo imaging of neural activity. Nat. Methods *14*, 349–359.

Yang, G., Pan, F., and Gan, W.B. (2009). Stably maintained dendritic spines are associated with lifelong memories. Nature *462*, 920–924.

Yang, G., Chang, P.C., Bekker, A., Blanck, T.J.J., and Gan, W.B. (2011). Transient effects of anesthetics on dendritic spines and filopodia in the living mouse cortex. Anesthesiology *115*, 718–726.

Yuste, R. (2011). Dendritic spines and distributed circuits. Neuron *71*, 772–781.

Yuste, R. (2015). From the neuron doctrine to neural networks. Nat. Rev. Neurosci. *16*, 487–497.

Yuste, R., and Denk, W. (1995). Dendritic spines as basic functional units of neuronal integration. Nature *375*, 682–684.

Zaremba, J.D., Diamantopoulou, A., Danielson, N.B., Grosmark, A.D., Kaifosh, P.W., Bowler, J.C., Liao, Z., Sparks, F.T., Gogos, J.A., and Losonczy, A. (2017). Impaired hippocampal place cell dynamics in a mouse model of the 22q11.2 deletion. Nat. Neurosci. *20*, 1612–1623.

Žiburkus, J., Cressman, J.R., and Schiff, S.J. (2013). Seizures as imbalanced up states: Excitatory and inhibitory conductances during seizure-like events. J. Neurophysiol. *109*, 1296–1306.

Ziv, J., and Lempel, A. (1978). Compression of Individual Sequences Via Variable-Rate Coding. Ieee Trans. Inf. Theory *24*, 530–536.

Zuo, Y., Lin, A., Chang, P., and Gan, W.B. (2005). Development of long-term dendritic spine stability in diverse regions of cerebral cortex. Neuron *46*, 181–189.

Danksagung

Dass der akademische Weg mein Lauf wurde und bislang gelungen ist, verdanke ich vor allen meinen Eltern. Sie waren die ersten Abiturienten und Hochschulabsolventen ihrer Familien, eine Dissertation aber war ihnen allen dreien aus verschiedenen Gründen verwehrt. Zu Ausstellungsbeginn aber war aus einem Fleck etwas Andersgroßartiges geschaffen. Für ihren Scharfsinn, ihren Mut, ihre Leidenschaft und Tragfähigkeit bewundere ich sie. Ich bin auf diesem vor allem die Fortführung ihres Weges und ihnen für ihre liebende Unterstützung, ihren Geist, zutiefst dankbar. Wissenschaftlich laufe ich nicht in ihren Fußstapfen - wie auch - ich stehe auf ihren Schultern.

Das Fundament systematischen wissenschaftlichen Arbeitens entstand unter Simon Rothenfußer in Stefan Endres' *Klin-Pharm*. Ich hatte im Studium keine Probleme - und keinen Kompass. Simon schrieb später: „ […] It was a pleasure seeing him turn from a medical student half-heartedly looking for a thesis project into an enthusiastic scientist […]". Stefan Endres förderte uns Doktoranden von Natur aus mit aller Kraft: „[…] Dann eben alles oder nichts, ***stiftung! […]". Beide formten meinen Weg in diesen Jahren, wofür ich ihnen und der damaligen *Klin-Pharm* Truppe besonders verbunden bin. Nach der Promotion waren es Uwe Ködel und Hans-Walter Pfister in Großhadern, die diesem Fundament neben der intensiven Klinikzeit weiter Raum verliehen, meinen Sprung als Post-doc nach New York unterstützten und das Tor zurück geduldig offen ließen, wofür ich ihnen herzlich danke.

Die Zeit in Rafael Yustes Labor war, umgeben von Hirnforschern aller Disziplinen, transformativ. Sie war einzigartig und immens lehrreich, führte zu Freundschaften und Kollaborationen, die bis heute anhalten und wachsen. Rafa gab mir alle Freiheit, meine Ideen zu entwickeln und zu verfolgen. Darcy Peterka, Reka Recinos, Shuting Han, Angeles Rabadan und Yuki Bando bildeten in dieser Zeit den Kern, mit Jordan Hamm und Krishna Jayant entstand ein freundschaftliches Trio wissenschaftlicher Schlagkraft. Erwähnt seien dazu Manhattan überspannende Projekte mit Cathy Schevon (CUMC) und Ted Schwartz (Cornell Weill MC). Ich bin voll des Dankes, diese außergewöhnlichen Menschen getroffen zu haben, sie sind für meine persönliche und wissenschaftliche Entwicklung entscheidend gewesen.

Dass diese Entwicklung seit meinem Post-doc weiter Auftrieb hat, liegt zuvorderst an Heinz Beck. Bei unserem Aufeinandertreffen in Girona bei der *Gordon Research Conference* verstand ich mich auf Anhieb mit ihm und kam auf diese Weise nach Bonn, als ich wieder Fuß auf deutschen Boden setzte. Durch seine Gelassenheit und Großzügigkeit bezüglich wissenschaftlicher Infrastruktur und sein maximales Interesse an der Sache, nicht an Politik, gelang mir mit weiterer Unterstützung von Christian Elger die Gründung meiner Nachwuchsgruppe. Dass diese seither an Fahrt aufnimmt und grundlegenden Fragestellungen zur Epilepsie mit klinisch epileptologischer Rückbindung nachgehen kann, liegt auch am Zusammenwirken mit Florian Mormann sowie der kontinuierlichen und wegweisenden Unterstützung durch Rainer Surges und Randi von Wrede in der Klinik für Epileptologie, wofür ihnen mein aufrichtiger Dank gilt. Juergen Bauer ist auf seine ganz eigene Art - „Na, Herr Wenzel, lebt die Zelle noch?“ - für mich wissenschaftlicher Ansporn.

Ohne meine Familie bin ich nicht denkbar. Leva hat mich seit New York entlang ihres eigenen steilen Weges mit hierher getragen. Zwischen Rausch und Intensität, maßlosem Glück und enormer Anstrengung musste ich in den letzten Jahren abseits neuronaler Netzwerke und Neuronotfallzentren vieles lernen. Dass wir hier sind, dass es uns gelungen ist, unsere Leichtigkeit zu heben und Schwingen an sie hin zu fügen, erfüllt mich mit tiefer Demut, Dankbarkeit und Stolz. Dass mein Weg an der Habilitation vorbeiführen würde, mag irgendwann vorstellbar geworden sein. Dass wir zu uns würden, war kaum zu erahnen. Wir sind schon viele tausend Kilometer zusammen, ja aber gerade am Beginn! Danke, Ginster, ich liebe Dich!